Università degli Studi di Ferrara

DOTTORATO DI RICERCA IN

"SCIENZE DELL'INGEGNERIA"

CICLO XVII

COORDINATORE Prof. Stefano Trillo

An innovative methodology for the analysis of micro-particle deposits in transonic and subsonic blades for the assessment of compressor degradation

Settore scientifico disciplinare ING-IND/08

Dottorando

Alessio Suman

Tutori

Prof. Michele Pinelli

Prof. Pier Ruggero Spina

Anni 2012/2014

this page was intentionally left blank

this page was intentionally left blank

this page was intentionally left blank

Abstract

Solid particle ingestion is one of the principal degradation mechanisms in the compressor section of heavy-duty gas turbines. Usually, foulants in the ppm range not captured by the air filtration system cause deposits on blading and result in a severe performance drop of the compressor. It is of great interest to the manufacturer and industry to determine which areas of the compressor airfoils are affected by these contaminants as a function of the location of the power unit. The aim of this work is the estimation of the actual deposits on the blade surface in terms of location and quantity.

Particle trajectory simulations use a stochastic Lagrangian tracking method which solves the equations of motion separately from the continuous phase. Then, a transonic rotor and subsonic rotor are considered as a case study for the numerical investigation. The compressor rotor numerical model and the discrete phase treatment have been validated against the experimental and numerical data available in literature.

The size of the particles, their concentrations and the filtration efficiency are specified in order to perform a realistic quantitative analysis of the fouling phenomena in an axial compressor. This study combines the impact/adhesion characteristic of the particles obtained through a Computational Fluid Dynamics (CFD) numerical simulation and the real size distribution of the contaminants in the air swallowed by the compressor.

The kinematic characteristics (velocity and angle) of the impact of micrometric and sub-micrometric particles with the blade surface of an axial transonic and subsonic rotor are shown. The blade zones affected by particle impact are extensively analyzed. This work has the goal of combining the kinematic characteristics of particle impact on the blade with fouling phenomenon through the use of a quantity called ‘sticking probability’ adopted from literature.

The analysis shows that particular fluid-dynamic phenomena such as separation, shock waves and tip leakage vortex strongly influence pattern deposition. The combination of the smaller particles (0.15 — 0.25) µm and the larger ones (1.00 — 1.50) µm determines the highest amounts of deposits on the leading edge of the compressor airfoil. The blade zones affected by deposits are clearly reported by

using easy-to-use contaminant maps realized on the blade surface in terms of contaminant mass per unit of time.

From these analyses, some guidelines for proper installation and management of the power plant (in terms of filtration systems and washing strategies) can be drawn.

Sommario

Uno dei principali meccanismi di degradazione delle prestazioni nelle turbine a gas è determinato dall'ingresso di particelle nei compressori. Molto spesso, i contaminanti presenti in intervalli di pochi ppm nell'aria, non vengono catturati dai sistemi di filtraggio causando depositi sulle pale che determinano pesanti perdite di prestazioni del compressore. E' interesse primario per i costruttori e per l'industria determinare quali aree del compressore sono interessate dai contaminanti in funzione dell'ambiente di lavoro dell'unità di potenza. Lo scopo di questo lavoro è la stima dei depositi che realmente si verificano in termini sia di zone di preferibile deposizione sia in termini quantitativi.

Le traiettorie delle particelle sono state calcolate attraverso l'utilizzo dell'approccio Lagrangiano che risolve le equazioni del moto separatamente rispetto a quelle della fase continua. Con questo approccio, un rotore transonico e un rotore subsonico sono stati considerati per questo studio. Il modello numerico e la modellazione della fase discreta sono stati validati attraverso dati sperimentali e numerici presenti in letteratura.

La dimensione delle particelle, la loro concentrazione e l'efficienza di filtraggio sono stati definiti secondo dati reali per ottenere un'analisi quantitativa del fenomeno del fouling all'interno di compressori assiali. Questo studio combina le caratteristiche di impatto/adesione della particelle ottenute attraverso simulazione numeriche CFD, con reali distribuzioni dei contaminanti presenti nell'aria aspirata dai compressori.

Vengono riportate le caratteristiche cinematiche (velocità e angolo) dell'impatto di particelle micrometriche e sub-micrometriche con le superfici palari di rotori transonici e subsonici. Dettagliate analisi sono state condotte riguardo alle zone della pala affette da impatti. Questo lavoro ha come l'obiettivo di collegare le caratteristiche cinematiche delle particelle impattanti la pala con il fenomeno del fouling attraverso l'utilizzo di una grandezza chiamata probabilità di adesione ottenuta dalla letteratura.

L'analisi mostra che particolari fenomeni fluidodinamici come separazioni, onde d'urto e vortici all'apice della pala dovuto al gap, influenzano la deposizione delle particelle. La combinazione delle particelle di dimensione più piccole (0.15 – 0.25) µm con quelle di dimensione più grande (1.00 – 1.50) µm, determinano la più alta quantità di depositi sul bordo d'attacco delle pale. Le zone della pala affette dalla

deposizione di particelle sono mostrate mediante l'utilizzo di mappe di facile comprensione che riportano i valori della massa depositata per unità di tempo.

Da queste analisi possono essere anche definite linee guida sulla corretta installazione e gestione dell'impianto (in termini di sistemi di filtraggio e lavaggio del compressore).

Index

Chapter 3

Chapter 4

Chapter 5

Chapter 6

Chapter 7

List of symbols

Appendix I

Appendix II

Appendix III

Appendix IV

Appendix V

this page was intentionally left blank

List of Figures

Chapter 1

Chapter 2

Chapter 3

Chapter 4

Chapter 5

Chapter 6

Chapter 7

Appendix I

List of Tables

Chapter 1

Chapter 3

Chapter 4

Chapter 5

Chapter 6

Appendix II

Appendix III

Appendix IV

Appendix V

Introduction

Air is a continuous medium that contains and carries a large number of particles (contaminants). The contaminants in the air are different in composition, size (pollen 50 µm, spores 3 µm — 10 µm and exhaust particle < 0.1 µm) and quantity (industrial environment, urban or country atmosphere, in/off-shore locations).

Particle dispersion is related to natural sources (such as desert, forest, ocean, etc.) and to human sources (domestic heating, transport vehicles, plumes, etc.). The dimension of the particle influences the dynamic characteristics of the particle. In particular, small particles have a random movement similar to gas while large particles are influenced by air velocities, gravitation and shape effects (spherical particles, irregular particles, etc.).

Gas turbines ingest a large amount of air during operation. For example, a 25 MW gas turbine ingests 68 kg/s of air compared to the 24 kg/day breathed by an adult. The quality and purity of the air entering the turbine is a significant factor in the performance and life of the gas turbine. In particular, the fouling of the axial compressor is a serious operating problem and its control is of critical importance for operators of gas turbine-driven power plants, compressor stations and pump stations in on/off-shore applications.

In order to minimize the particles entering industrial gas turbines, an adequate filtration system that can limit the ingestion of contaminants by the power unit is required. For industrial gas turbines, highly effective filtration systems exist. Because modern inlet filtration systems are effective in removing particles larger than about 1 µm to 2 µm, compressor erosion is not a problem frequently found in industrial gas turbines. However, depending on the type of filtration system used, smaller particles can enter the engine. These smaller particles are too small to cause erosion issues, but they do cause compressor fouling.

Although 99 % of the particles in the atmosphere are less than 1 µm in size, 70 % of the weight is due to particles which have a diameter greater than 1 µm. In order to capture these different types of particles, filtration systems use many different mechanisms. Each filter in fact has various different mechanisms working together to remove the particles. The first step in selecting an inlet

filtration system is to define the expected operating environment. This includes determining which potential contaminants could be present at the installation site. Once the expected contaminants have been defined, the filters can be selected. The locations where a gas turbine is installed are classified into two main areas: (i) coastal/marine/offshore and (ii) land-based applications. The main difference between these areas is the high concentration of salt in the atmosphere which is present in coastal/marine/offshore applications. An extensive report and analysis of the salt deposits in heavy-duty compressors exists in literature. However, these works focus on the land-based gas turbines for which the surrounding air is characterized by sand and soil carried by winds and/or storms. These areas commonly have poor vegetation such as dry lakebeds, deserts, and loess (areas of fine-grained soil made from particles of silt and clay deposited by the wind). Levels of precipitation and vegetation also have strong effects on the levels of solid contaminants.

All gas turbine work environments can be characterized by their typical weather patterns and air quality, but short term or seasonal variations must also be considered. Several land-based environments in which gas turbines can operate include deserts, arctic locations, tropical sites, rural countryside, large cities and industrial areas in which heating, plumes and transport vehicles play a key role.

The details on how the small particles entering the gas turbine reach the blade surface and stick there are not fully and quantitatively understood. Particle adhesion on the blade surface is a complex phenomenon that includes many aspects which can be summarized as follows:

- the material of the body in contact (blade and particle): density, ultimate strength and elastic yield limit (in order to define an elastic or plastic collision);
- the surface conditions: roughness, presence of added materials (water, oil, grease), presence of electrostatic charges or their generation by contact (bounces or slips) with the particles;
- the particle size: inertia force and some energy whose effects are directly related to particle size;
- the impact velocity: directly related to kinetic energy. This energy is transferred into the contact zone between two bodies and determines deformation, bounce and sometimes particle breakage;
- the impact angle: represents the most important quantity for impact kinematics and consequent impact effects (bounce, adhesion or slip).

All these phenomena can be studied from many points of view: (i) kinematic (velocity and direction), (ii) dynamic (velocity and mass) and (iii) energy

(deformations or breaks). At the same time it is possible to consider both microscopic (e.g. atom attraction and molecular bonds) or macroscopic (e.g. adhesion, rebounds and deformations) effects. In almost all cases the phenomena mentioned above occur at the same time during contact between two bodies and the result of the contact depends on the combination of these effects.

Particle sticking on blade surfaces results in an increase of the thickness of the airfoil and the surface roughness. Both of these events change the flow-path inside the passage vanes. This leads in particular to: (i) an increment of boundary layer thickness, (ii) a decrement of the flow passage area and (iii) modifications of three-dimensional fluid dynamic phenomena. These phenomena determine a reduction of the compressor mass flow rate and a consequent reduction in the functioning of a turbine. This, in turn, results in a drop in the overall gas turbine output of 5.5 MW in the case of a 40 MW class gas turbine. Estimates have cited fouling as being responsible for 70 % to 85 % of all gas performance losses accumulated during operation. Output losses between 2 % (under favorable conditions) and 15 % to 20 % (under adverse conditions) have been experienced.

Evaluation of fouled compressors has revealed contamination both on the suction side and the pressure side of the compressor blades and, in general, only small particles can stick to the blade surface and thus cause fouling. Numerous reports are present in literature in which the deposits on axial compressors are described in order to study the cause and, at the same time, to realize a better washing strategy.

The question that still requires research is the mechanism that allows particles to actually reach the suction surface. Particles that deviate from the streamlines will readily impact on the pressure side of the blades, but the mechanism that can deposit particles on the suction side of the blade is not fully understood. The experimental applications related to the fouling phenomenon and the consequent results are affected by numerous problems, summarized as follows: (i) actual conditions of the contaminants and the work environment of the compressor, (ii) size of the experimental test bench since even if the cascade and the velocities are scalable, the particle dimensions are not scalable and their ratio with respect to the cascade and the velocities is not the actual one, (iii) rotational velocity of the cascade (neglected in nearly all experimental apparatus) influences the dynamic and the kinematic characteristics of the particle impact, (iv) the modification of the interface between the particle and the blade in order to accelerate the fouling process limits the validity of the results, and finally, (v) the lack of particle count, in particular, the lack of ratio between the injected particles and the stuck particles.

For these reasons, it is possible to understand the mechanisms which determine the fouling phenomenon, not only by using experimental applications.

After the particle deposition on the blade surface, the only method for recovering the performance of the compressor is a washing operation. Experimental results have demonstrated that the process of washing has been assumed to recover the output power by up to 99.5 %. Fouling can be removed by off-line washing and slowed down by on-line washing. The decision to shut the engine down for off-line washing is a balance between lost production due to the lower power versus the lost production due to shutting the engine down for a certain amount of time. Since the engine needs to be shut down for washing, it will not produce revenue for a day.

Aim of the Thesis

The lack of comprehension of fouling mechanisms related to particle impact is the major theme of this work.

The objective of this work is to determine the fouled region on the compressor rotors and provide an estimation of the fouling rate for transonic and subsonic rotor blades.

The objective is developed according to the following points:

- determine the proper set up and boundary conditions of the numerical models by reviewing literature;
- determine the position and the quantity of the ingested particles that impact the blade surface of a transonic and subsonic axial compressor rotor;
- determine which characteristics of the compressor influence its capability of collecting air contaminants during operation;
- determine which characteristics of the particle influence its sticking capability and develop a combined approach in order to extract this parameter from numerical simulations;
- determine the relationship between power plant characteristics (location and filtration system) and the fouling rate of the rotor blades.

this page was intentionally left blank

Limitations

This work is limited by the following issues:

- the uncertainty of the numerical models. In particular, the uncertainty: (i) of the representation of the compressor's performance, (i) of the three-dimensional fluid dynamic phenomena that characterize compressor operation and (iii) of the particle's trajectory representation. These uncertainties are strongly related to the boundary layer calculation and representation provided by the turbulence model;
- the relation between capture efficiency and design parameter of the compressor rotor should be validated using a higher number of compressor rotors. The fouling rate data should also be validated against more data obtained from a greater number of compressor rotors;
- the sticking probability data are limited to a silica carbide which has a high value of hardness compared to the classical materials involved in the fouling phenomenon;
- the sticking probability data are limited to only a few particle diameters but they are also used to calculate the sticking probability for particles of different diameters;
- the lack of experimental data that relates sticking probability to particle tangential velocity.

this page was intentionally left blank

Thesis Outline

The thesis provides the background for the papers, details the numerical setup and summarizes the results.

Chapter 1 defines the main influences regarding the issue of fouling.

Chapter 2 reports the different approaches used to study particle-surface interaction.

Chapter 3 describes the numerical models for the Eulerian and Lagrangian phases.

Chapter 4 contains the results of the particle impact and the relation between the rotor's performance and capture efficiency.

Chapter 5 contains the results of the particle adhesion in the compressor rotors.

Chapter 6 reports the estimation of the deposition and shows the deposition pattern on the blade surfaces.

Chapter 7 summarizes the differences in terms of particle impact and deposition between the two rotors and provides some conclusions and perspectives for the future in order to improve knowledge regarding the fouling issue.

Appendix I contains the overall representation of airfoil contamination.

Appendix II contains the values of particle impacts for the transonic rotor.

Appendix III contains the values of particle impacts for the subsonic rotor.

Appendix IV contains the values of the Dangerous Index for the transonic rotor.

Appendix V contains the values of the Dangerous Index for the subsonic rotor.

this page was intentionally left blank

Originality and Contributions by Other

This work combines numerical results and the fluid dynamic analyses typical of fluid machinery research with particle experimental data obtained in aerospace research.

Its originality is represented by the use of numerical tools to generate the contaminants dispersion in the compressor rotor and particle experimental data to link the numerical results with fouling phenomenon. The interdisciplinary approach is concluded by using realistic data for air contaminants and filtration efficiency to calculate the actual fouling rate.

Several people have contributed to this study and the following paragraphs outline their contributions.

The initial hint was provided by Dr. Rainer Kurz who inspired the application of the Eulerian-Lagrangian approach to improve the knowledge of fouling phenomenon. Dr. Rainer Kurz revised all of the results and, in association with Dr. Klaus Brun, provided me with the impetus to improve the readability of the results in order to link the numerical results with the actual power plant.

My advisors, Professor Michele Pinelli and Professor Pier Ruggero Spina revised the results and proposed the strategy to relate the numerical results to the compressor's design characteristics.

The close collaboration with Dr. Mirko Morini provided the algorithm which allowed the calculation of the particle's dynamic characteristics in order to calculate the sticking probability. Finally, Mr. Nicola Aldi provided the Eulerian numerical models comprising the numerical mesh and geometry generation.

this page was intentionally left blank

Chapter 1

Problem Statement

In this chapter a global overview of all aspects and contributions of the compressor fouling is reported. Air contaminant, filtration system, particle adhesion and compressor washing are studied for improve the knowledge in the compressor fouling. The effects of the deposits on the blade surface are briefly analyzed in order to better comprise the following results.

1.1 Air contaminant

The atmospheric aerosols are constituted by a suspension of solid (smoke, fumes, fly ash, dust, etc.) or liquid (mist, fog, etc.) in the atmosphere. The particle sizes can be categorized into seven classes:

- Coarse solid (5 – 100) mm
- Granular solid (0.3 – 5) mm
- Coarse powder (100 – 300) μm
- Fine powder (10 – 100) μm
- Super fine powder (1 – 10) μm
- Ultra-fine powder ~1 μm
- Nano Particles ~1 nm

In general, fine particles refer mainly to a man-made action while the coarse particles refer mainly to a natural phenomenon.

The particle size could be link to some proprieties as reported in Fig. 1.1 provided by Fuchs (1964). Some properties are strongly related to the particle size, while in some case, there is a threshold limits that divided the particle size into two range. For example, the particle movement refers to Brownian motion for particle radius less than 10^{-5} cm and to gravitational motion (settling) for particle radius higher than 10^{-4} cm.

The aerosols assume a very wide range of concentrations (from 1 $\mu g/m^3$ to 100 $\mu g/m^3$) according to site location and time. In particular, the following relations

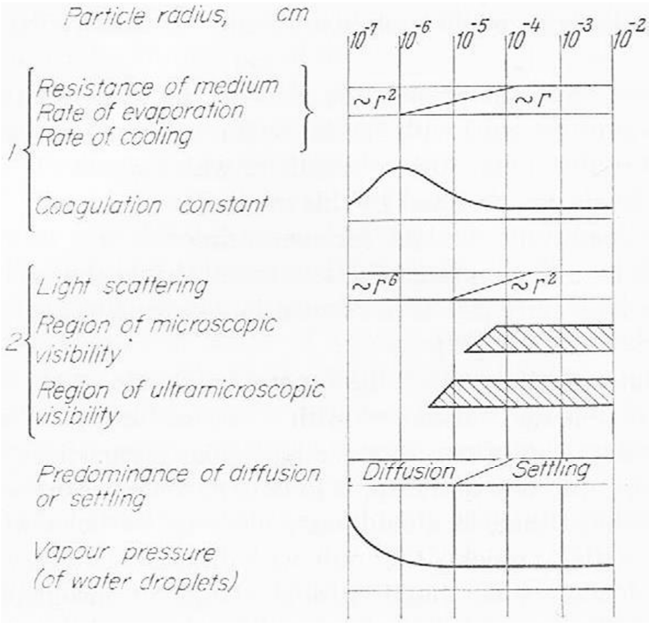

Figure 1.1 – Some properties of aerosol in relation to particle size (Fuchs, 1964)

summarize the general rules. Equation (1.1) reports the relation for the spatial ranges

desert > urban area >ocean surface> pole (1.1)

Eq. (1.2) reports the daily temporal ranges and Eq. (1.3) reports the weekly temporal ranges

morning > evening (1.2)

weekday > non-working (1.3)

and finally, Eqs. (1.4) and (1.5) report the relation for the seasons

winter > summer (caused heating system) (1.4)

summer > winter (caused organic matter) (1.5)

This work refers in particular to the power plant located inshore called land based applications. In this areas, the solid contaminants are widespread and influence the compressor operation. An extensive report for this application can be found in Wilcox *et al.* (2010) were the authors have highlighted numerous critical aspects that influence the compressor and turbine fouling as a function of the environment. Solid contaminants are spread from their source carried by the wind. Heavier and larger particles drop out of the air stream quickly, while smaller particles will remain airborne until they fall out due to air turbulence dropping off or the particles settling out of the air. Particles less than 10 µm will stay airborne the longest. Some common examples of solid particles are sand, silica, road dust, dust from fertilizer and animal feed, airborne seeds, alumina, rust, calcium sulfate and vegetation.

There are three physical processes by which solid contaminants move from their source: creep, saltation and suspension. Figure 1.2 reports these three physical processes (Wilcox *et al.*, 2010).

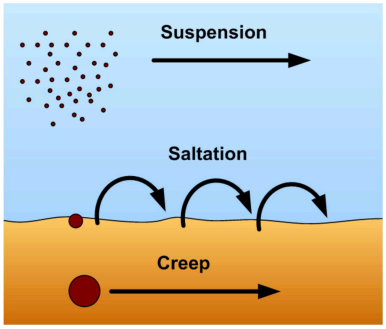

Figure 1.2 – Solid contaminant transportation processes (Wilcox *et al.*, 2010)

Suspension describes the process where particles are carried by the wind (the size of the particle must be compared to the wind intensity). Saltation is when the particles move forward on the ground through a series of leaps and jumps. Creep is when the particle will travel across the ground during heavy winds. These contaminants are not lifted into the air but move through rolling or sliding action.

In order to define which physical process influence the motion of the particle, the particle settling rate must be introduce. The settling rate is the rate at which the particle falls to the earth. Larger and heavier particles will have a faster settling rate, where smaller particles will have a lower settling rate and can remain suspended in the air for days at a time.

In addition to the settling rate, the critical velocity and the powder dispersibility are also considered. The critical velocity is the air velocity at which the particle are carried away by the wind. In Fig. 1.3 the critical velocity for sand particle as a function of the particle radius is reported (Fuchs, 1964).

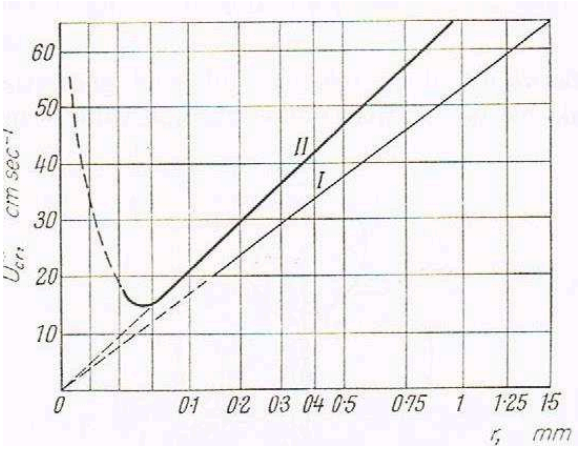

Figure 1.3 – Critical flow velocity for sand (Fuchs, 1964)

Dispersibility of powder is an important property. Dispersibility depends primarily on the cohesive force between particles and improves as the particle size increases while depending very much upon the moisture content of the powder. Hydrophobic powders, such as talc, are easier to disperse than hydrophilic ones like quartz and limestone (Fuchs, 1964). Experimental data on the dispersibility of various powder are scarce in literature. Fuchs (1964) reported some results provided by Andreasen (1939) obtained by experimental tests. Two cubic centimeters of powder was poured through a narrow slit into a vertical tube of height 250 cm and diameter 4.5 cm. The particles were separated to some extend as they fell through the air and the percentage of powder which had not settled on the bottom of the tube in 6 s was determined. Since individual particles could not have reached the bottom in this time the author assumed that his figures represented the percentage of dispersed powder, which his called the dispersibility. Some results are reported in Fig. 1.4.

	Particle radius limits (μ)	Dispersibility (%)
Lycopodium	12	100
Wood charcoal dust	0–25	85
Wood charcoal dust	0 7	23
Aluminium powder	0 15	66
Talc	0-20	57
Carbon black	0 15(?)	47
Potato starch	0 35	27
Graphite dust	0 25	17
Pulverized slate	0 25	13
Cement	0-45	5·5
Prepared chalk	0 6	1·5
Polydisperse silica dust (coarse)	–	21
Polydisperse silica dust (fine)	–	8
Isodisperse silica dust	11·5	68
	8	83
	5·6	45
Porcelain dust with fine fractions removed	7	50
	2·7	52
	1·1	21
	0·45	12
Porcelain dust without fine fractions removed	–	5

Figure 1.4 – Dispersibility of some powders (Fuchs, 1964)

Start from the results reported in Figs. 1.3 and 1.4, areas with very fine solids and sand are more likely to be potential source regions for dust storms or high dust concentration in the air. These areas commonly have poor vegetation such as dry lakebeds, deserts, and loess (areas of fine-grained soil made from particles of silt and clay deposited by the wind). Levels of precipitation and vegetation also have strong effects on the levels of solid contaminants.

Given the information related to the particle transport, is easy to understand that the particles are carried by the wind and not only the geographic area close to the

power plant influences the air contamination ingested by the power unit. As reported in Zender *et al.* (2003) the natural particles were carried by the intercontinental winds that spread the particles as a function of the wind intensity and direction. Zender *et al.* (2003) report the results of a global simulation that comprises natural mobilization and deposition tendency in the all world areas.

Figure 1.5 shows the predicted annual mean mobilization and deposition tendencies. In general, entrainment occurs in regions with a combination of high winds, low vegetation, no snow cover, and large upstream area. The strongest sources are in North Africa and Asia. The predicted dust deposition in Fig. 1.5b shows that mass transport affects extensive areas downwind of the source regions. Figures 1.5c and 1.5d decompose the total deposition into dry and wet deposition fluxes. As expected, dry deposition dominates source regions because of large particle sedimentation. Dry deposition operates continuously, so the dry deposition patterns are an excellent proxy for atmospheric dust loading (Fig. 1.6). Wet deposition removes most dust far from source regions. It accounts for 41 % of global deposition, and for 89 % of oceanic deposition.

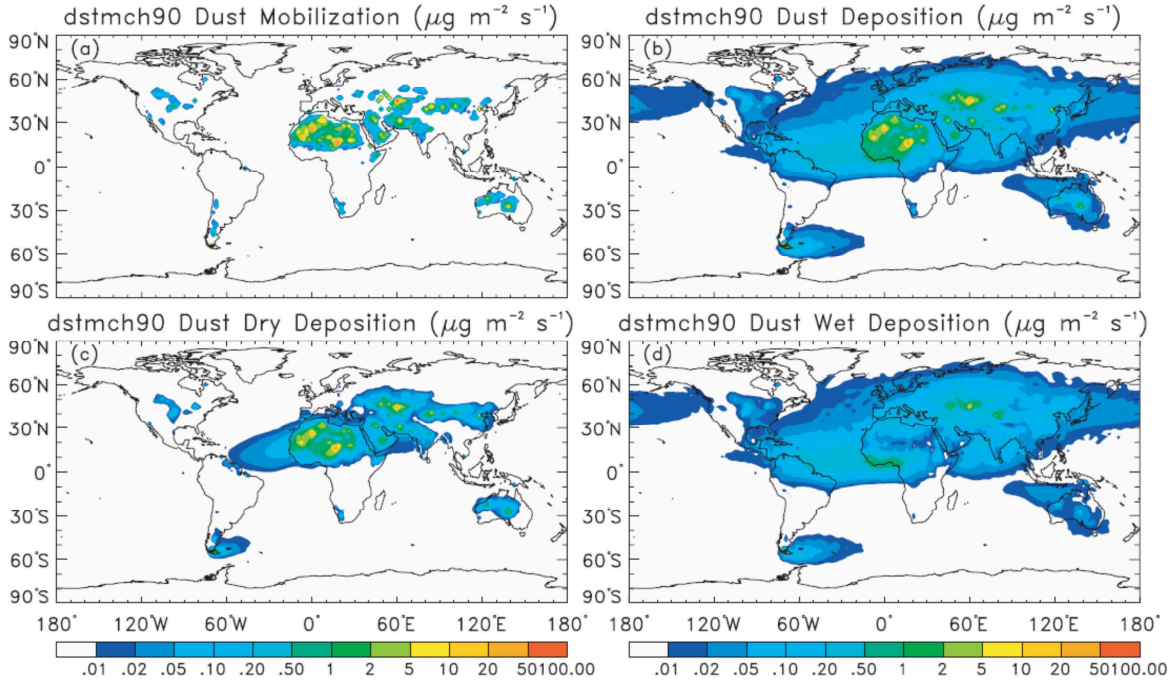

Figure 1.5 – Predicted annual mean dust source and sink fluxes in μg/m^2 s^1 for (a) mobilization, (b) total deposition, (c) dry deposition, (d) wet deposition. Scale is logarithmic (Zender *et al.* 2003)

Figure 1.6 shows the predicted annual mean mass burden in mg/m^2. Strong dust burdens are apparent over source regions, where large particles have not yet sediment. Source regions in North and South America and South Africa show no persistent dust burden, contrary to what might be expected on the basis of Fig. 1.5a. Emissions in these mid-latitude source regions are very susceptible to wet

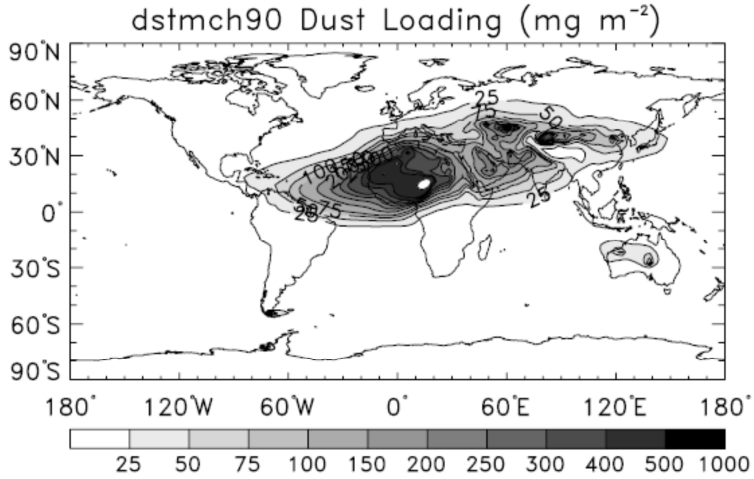

Figure 1.6 – Predicted annual mean dust mass burden in mg/m^2. Scale is nonlinear (Zender *et al.* 2003)

scavenging and so have a relatively short lifetime. The analysis relates to the particle sources and dispersion highlight that the analysis of the air contaminant is fundamental for a proper management of the filtration systems and then, of the entire power unit. An useful example reported by Brake (2007) explain more in detail the issue related to the contaminant transportation. A 20 µm particle will fall at around 350 m/h. If the particle has been lofted to 2,100 m, it would take six hours to fall back to earth. A wind speed of 20 km/h would give this particle a range of 120 km. However, a 5 µm particle in the same situation, would settle at around 35 m/h, meaning it would take 60 h to fall back to earth, giving it a range of 1,200 km under the same circumstances.

The natural air contaminants represent a single part of the total amount of the air contaminant in the air. The human activities strong influence the particle concentration and could be overturn the general rules mentioned above. Human activities, such as: domestic heating, vehicle emission and industrial process emit particles and contaminant continuously. In general, larger particles refer to the nature behavior (coarse and micro particles) while smaller particles refer to the artificial behavior (micrometric and nanometric particles). Table 1.1 summarize the global emissions of major atmospheric aerosols (Brice).

Reports related to the particles concentrations and their analysis in terms of size and material are widespread in literature. Many authors provided the detection of the contaminant in particular location characterized by different source of pollution.

In Liu and Harrison (2011) the authors have reported the properties of coarse particles in the United Kingdom atmosphere and have highlighted, after a sensitivity analysis, that coarse and fine particles show very different behavior as a result of their different sources and properties. In particular the coarse particles have a lower

Table 1.1 – Global emissions of major atmospheric aerosols (Brice)

			%	Size	Composition
Natural	**–**	soil dust	48.1	> 1 µm	Si, Al, Fe, Ca
		sea salts	41.7	> 1 µm	Na, Cl, S
		volcanic dust	1.0	> 1 µm	Si, Al, Fe
		biological debris	1.6	> 1 µm	C
	=	sulfates from biogenic gases	4.2	< 1 µm	S
		sulfates from volcanic SO_2	0.6	< 1 µm	S
		organic matter from biogenic cause	1.9	< 1 µm	C
		nitrates	1.0	> 1 µm	Na
	Total Natural < 1 µm		6.7	< 1 µm	C, S
Man-made	**–**	industrial particulates	9.5	> 1 µm	C, Si, Al, Fe, heavy metals
		dusts	57.1	> 1 µm	C, N, Si, Al, Fe, Ca
		soot	1.0	< 1 µm	C
		biomass burning	8.6	< 1 µm	S
	=	sulfates from SO_2	18.1	< 1 µm	C, K, metals
		nitrates from NO_x	4.8	< 1 µm	N
		organic matter from man-made cause	1.0	< 1 µm	C, N
	Total Man-made < 1 µm		33.3	< 1 µm	C, S, K, N, metals

spatial homogeneity and for their, no spatial trend or correlation can be done. For example, plots of particle concentration versus wind speed show a monotonic decline of concentration with increasing wind speed for fine particles but an initial decline and an increase at higher wind speeds for coarse ones. Results related to the fine and ultrafine particles were reported in Birmili *et al.* (2013). This study, relates to Dresden (Germany) urban atmosphere shows that particle concentrations in the size range (5 – 300) nm are proved to be significantly influenced by the local urban sources and showed an increasing variability with decreasing particle size.

The local source and weather condition influence the air contaminant distribution and concentration. Recently, Zhu *et al.* (2011) have reported the concentration and size distribution of ultrafine particles in the vicinity of major highways. The study was related to the fine particles (< 0.1 µm) and the results showed that both atmospheric dispersion and coagulation contributed to the rapid decrease in particle number concentration and change in particle size distribution with increasing distance from the freeway. Ultrafine particle number concentration measured 300 m downwind from the freeway was indistinguishable from upwind background concentration. Together to the human-made sources (e.g. highways) also the natural source are investigated. Wang *et al.* (2013) reports the Impact of Gobi desert dust on aerosol chemistry of the urban ground surface and the mountain atmosphere. Particular attention was put on the massive dust storm event that has carried a large amount of coarse particles.

As stated above, air contaminants are very different in material, shape, dimension and source. In Lü *et al.* (2012) there are detailed SEM pictures that report the shape of typical aerosols dispersed in the Shanghai urban summer atmosphere. Some SEM micrographs are reported in Fig. 1.7. The authors have reported a detailed chemical analysis related to the air contaminant, and have emphasized the characterization of the *ultra-fine* particles. The results demonstrated that the Shanghai urban area is dominated by a *fine* particle (from 0.1 μm to 2.5 μm) constituted by soot aggregates and fly ashes.

In order to link the air contaminant data to the characteristic of the filtration systems and then to the fouling issue, the mass characterization of the air contaminant must be done. Lü *et al.* (2012) report a mass characterization of the different size airborne particles. The mass level characterization is reported in Fig. 1.8. This characterization will be used in this work to analyze the mass deposits on a compressor blade surface in a configuration named Urban (U).

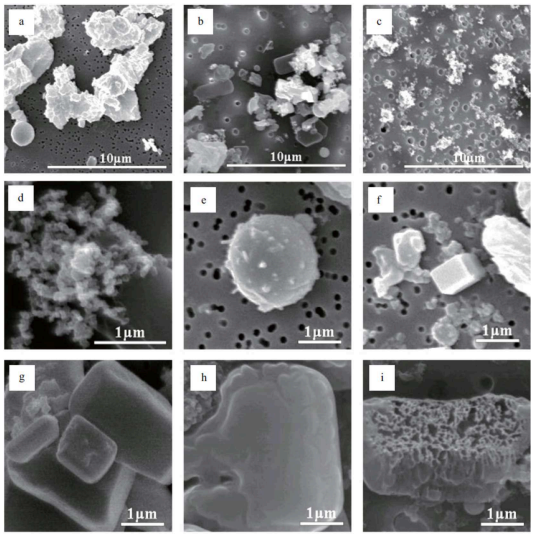

Figure 1.7 – SEM micrographs of size-segregated particles: a) coarse particles, b) fine particles, c) ultrafine particles, d) soot aggregates, e) fly ash, f), g) mineral particles and h), i) irregular particles (Lü *et al.*, 2012)

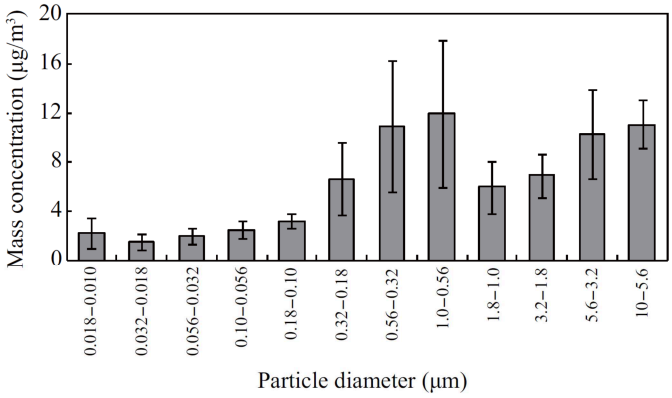

Figure 1.8 – Mass concentrations of size-segregated particles collected in the Shanghai atmosphere (Lü *et al.*, 2012)

The mass percentage of the 20 elements in coarse, fine and ultrafine particles in the Shanghai atmosphere is depicted in Fig. 1.9. The coarse particles are dominated by Si, Ti and Sr elements, while the ultrafine particles are dominated by the V element.

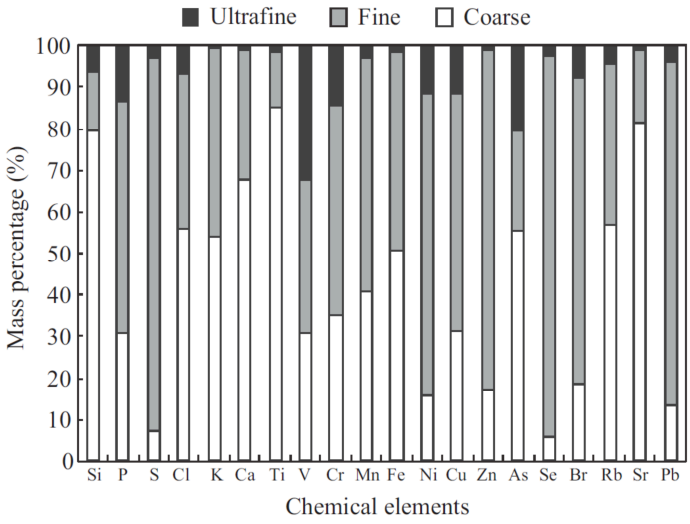

Figure 1.9 – Mass percentage of the 20 elements in coarse, fine and ultrafine particles in the Shanghai atmosphere (Lü *et al.*, 2012)

In order to realize as wide a fouling sensitivity analysis as possible, not only the mass level characterizations reported in Fig. 1.9 are considered in this work. In some cases, the power units work in highly contaminated areas, due to local chimney, plumes and/or soils. For these reasons, the mass level characterization reported in Lü *et al.* (2013) is also taken into account. The authors reported air contaminant characterization of the Xuanwei, Yunnan province, China divided into two periods: spring season and winter season. This area is characterized by pollutants emitted by local coal combustion. The mass level characterization, as a function of the season, is reported in Fig. 1.10.

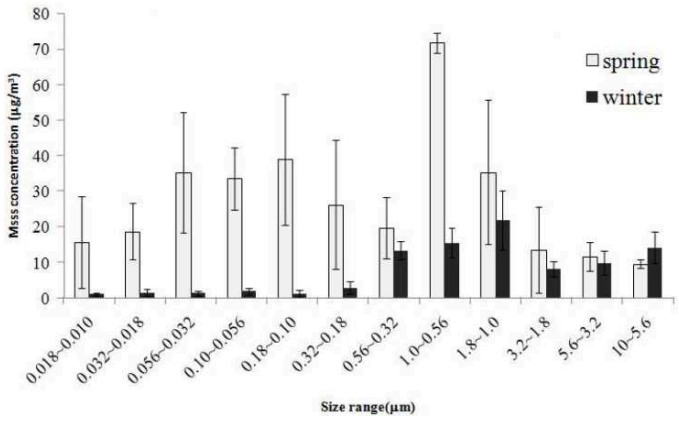

Figure 1.10 – Mass concentrations of size-segregated particles collected in the Xuanwei atmosphere (Lü *et al.*, 2013)

Lü *et al.* (2013) have found that the total mass concentrations of the size-resolved particles collected in spring were higher than those in early winter. The high concentration found in the spring time is not affected by the spore because the spore diameter is equal to 50 µm and, therefore, out of the sampled range. These characterizations will be used in this work to analyze the mass deposits on a compressor blade surface in a configuration named Industrial Spring (IS) and Industrial Winter (IW).

The mass percentage of the 22 elements in coarse, fine and ultrafine particles in the Xuanwei atmosphere is depicted in Fig. 1.11. Zn and K could be found in the major chemical element category in winter particles. Sulfur was the most abundant element in spring and winter particles. This element mainly distributed in fine particles, while Si, Ca, Al and Fe largely found in coarse particles.

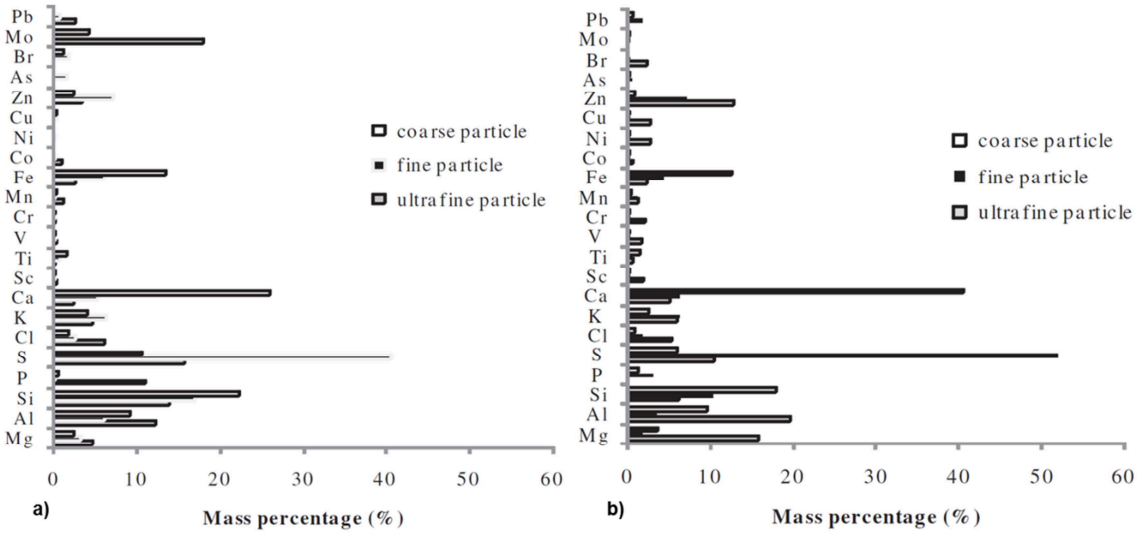

Figure 1.11 – Mass percentage of the 22 elements in coarse, fine and ultrafine particles in the Xuanwei atmosphere: a) IS, b) IW (Lü *et al.*, 2013)

1.2 Filtration systems

The filtration system protects the gas turbine from harmful debris in the ambient air, which can lead to issues such as FOD, erosion, fouling, and corrosion. As reported by Schroth and Cagna (2008) a gas turbine with an intake volume flow of 1.5 million cubic meters per hour will swallow up to 30 trillion particles of 0.5 µm and larger in size per hour. Inlet air can significantly impact the operation, performance, and life of the gas turbine. The selection of the proper inlet filtration system cover the following aspects: (i) characteristics of filters and filter systems, (ii) characteristics of different environments where the gas turbine can operate, (iii) evaluation of the site where the gas turbine will be or is installed and (iv) evaluation of the combined effect

due to the increment in filter pressure drop compared to the increasing in filter efficiency. In this paragraph a summary of the filtration system world is reported.

The filter efficiency is the ratio of the weight, volume, area, or number of particles captured in the filter to the weight, volume, area, or number of the particles entering the filter, respectively. As reported by Wilcox *et al.* (2011), a general efficiency calculation is reported in Eq. (1.6), where *W* is the variable for which efficiency is being calculated.

$$\eta_{\mathrm{f}} = \frac{W_{entering} - W_{leaving}}{W_{entering}} 100\,\% \tag{1.6}$$

Many filters have poor performance against small particles at the beginning of their lives, but as the filter media becomes loaded with particles, it is able to catch smaller particles. In this case, the average efficiency would actually be higher than the initial efficiency. Some of the filters will never reach the quoted maximum efficiency before they are replaced. The filter efficiencies vary with particle size, typically being lower for small particles and higher for large particles. They also vary with operational velocity. Filters designed for medium and low velocities will have a poor performance at higher velocities and vice versa. Therefore, a particle size range and flow velocity must be associated with the stated efficiency.

In order to capture different types of particles, filtration systems use many different mechanisms. Each filter in fact has various different mechanisms working together to remove the particles. The filter media, fiber size, packing density of the media, particle size, and electrostatic charge influence how the filter removes particles. The consolidated mechanism used in the air filtration systems are: (i) inertial impaction, (ii) diffusion, (iii) interception, (iv) sieving and (v) electrostatic charge.

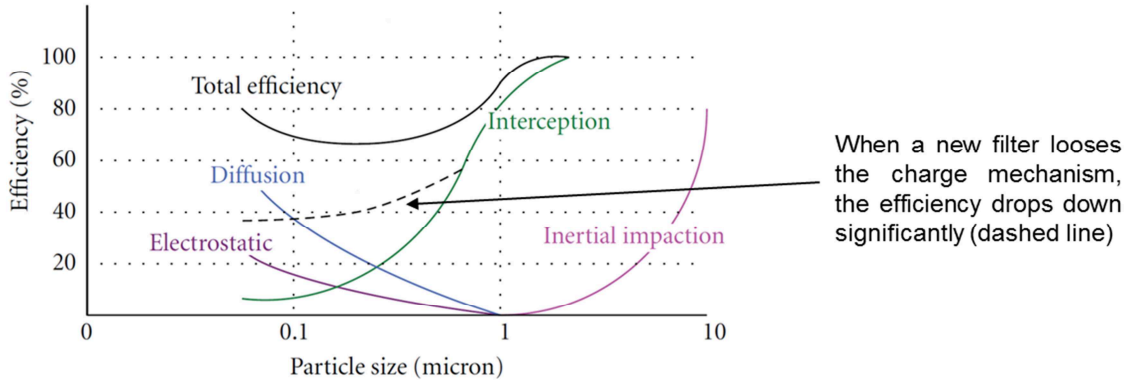

Figure 1.12 – Combination of filtration mechanism to obtain filter efficiency at various particle sizes Wilcox *et al.* (2011)

Figure 1.12 shows a comparison of a filter's total efficiency based on the various filtration mechanisms that are applied as a function of the particle diameter. The

inertial impaction is applicable to particles larger than 1 µm in diameter. The inertia of the large heavy particles in the flow stream causes the particles to continue on a straight path as the flow stream moves around a filter fiber. The diffusion mechanism is effective for very small particles typically less than 0.5 µm in size. Particularly in turbulent flow, the path of small particles fluctuates randomly about the main stream flow. As these particles diffuse in the flow stream, they collide with the fiber and are captured. Interception occurs with medium sized particles that are not large enough to leave the flow path due to inertia or not small enough to diffuse. The particles will follow the flow stream where they will touch a fiber in the filter media and be trapped and held. Sieving is the situation where the space between the filter fibers is smaller than the particle itself, which causes the particle to be captured and contained. A simplified sketch of these four mechanism is depicted in Fig. 1.13.

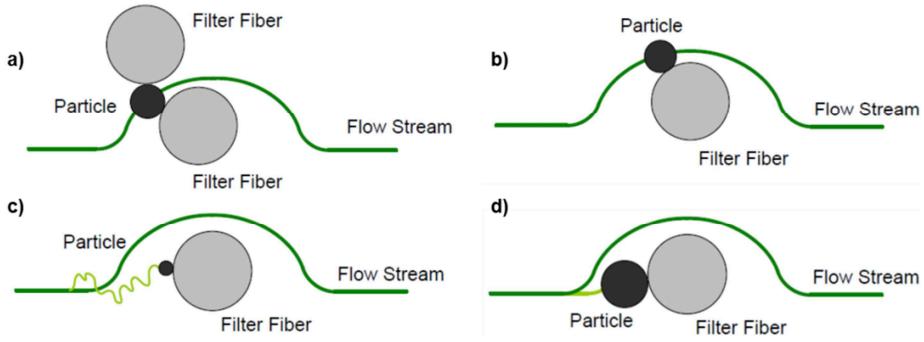

Figure 1.13 – Common filtration mechanism: a) sieving, b) interception, c) diffusion, d) inertial impaction Wilcox *et al.* (2011)

The last mechanism is related to the electrostatic charge. The filter works through the attraction of particles to a charged filter. Filters always lose their electrostatic charge over time because the particles captured on their surface occupy charged sites, therefore neutralizing their electrostatic charge. In Fig. 1.12, the difference between the filter's efficiency curve as a function of the electrostatic charge is reported. A simplified sketch is depicted in Fig. 1.14.

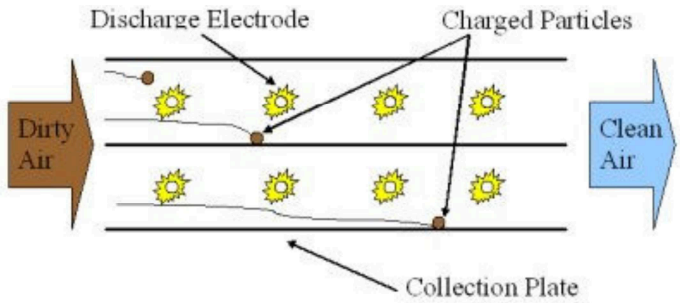

Figure 1.14 – Electrostatic precipitators Brake (2007)

As reported by Wilcox *et al.* (2011) several filtration devices are used in order to protect the compressor inlet from the airborne debris. Modern filtration system

comprises all or only a part of these devices:

- weather protection and trash screens: remove large objects or contaminants carried in the flow stream. Weather hoods are sheet metal coverings on the entrance of the filtration system. Weather hoods and louvers are used on the majority of inlet filtration systems, and they are essential for systems in areas with large amounts of rainfall or snow. Trash screens capture large pieces of paper, cardboard, bags, and other objects. Screens that are installed specifically for preventing insects entering the filtration system are referred to as insect screens. These screens will have a finer grid than trash screens;
- anti-icing protection. anti-icing protection is used in climates with freezing weather. Freezing climates with rain or snow can cause icing of inlet components, which can result in physical damage to inlet ducts or to the gas turbine compressor. Heaters, compressor bleed air, or self-cleaning filters are often used in the inlet system in frigid environments to prevent the build-up of ice on the inlet bell mouth or filter elements;
- inertial separators: inertial separation takes advantage of the physical principles of momentum, gravity, centrifugal forces, and impingement, and the physical difference between phases to cause particles to be moved out of the gas stream in such a way that they can be carried off or drained;
- moisture coalescers: catches the small water droplets in its fibers. As the particles are captured, they combine with other particles to make larger water droplets;
- pre-filters: are used to increase the life of the downstream high efficiency filter by capturing the larger solid particles. Therefore, the high efficiency filter only has to remove the smaller particles from the air stream which increases the filter life. Pre-filters normally capture solid particles greater than 10 μm;
- high-efficiency filters: removes smaller particles which lead to corrosion, fouling, and cooling passage plugging. These types of filters have average separations greater than 80 %. In order to achieve the high filtration efficiency, the flow through the filter fiber is highly restricted which creates a high pressure loss, unless the face velocity is kept low. High efficiency filters are rated under various standards. The filters used in gas turbines are rated with ASHRAE 52.2:2007 and EN 779:2002.

As reported in the previous paragraph, the selection of the inlet filtration system should be primarily dependent on the environment where it operates. Vegetation, weather events, local emissions, temporary emissions, and seasonal changes must be considered for a proper design and manage of the power unit. This thesis refer to the land-based power unit and, for this reason, only this location will be treated.

The land-based environment is very diverse. It can be classified in many different ways depending on weather patterns, vegetation, and local emission sources.

Several land-based environments are described below but an extensive description can be found in Wilcox *et al.* (2010).

- desert: is classified as an area with a dry and hot climate. Large amount of dust is present and there is little vegetation. The particles can range from large (500 µm) to very fine (submicron size). The filtration systems in deserts are usually solely designed for dust removal. Dust loads in the desert can range from mild (low wind) to fairly high (dust storms). There are three typical conditions that exist in the desert: clean air, dust haze, and sand storms. Table 1.2 summarized the typical desert conditions;

Table 1.2 – Typical desert conditions (Wilcox *et al.*, 2010)

Condition	Contaminant level [ppm]	Average contaminant level [ppm]	Particle size [µm]
sand storm	3 – 118	59	5 – 15
dust haze	0.15 – 3	1.5	1 – 3
clean air	0.15	0.15	0 – 1

- artic: is characterized by freezing weather (below 0 °C) for an extended period of time. To prevent the formation of ice from the depression of cool humid air requires an anti-icing system. In addition to ice, warm season contaminants must be considered for the design of the inlet filtration system. These contaminants can be similar to any of the other land-based environments;
- tropical: is characterized by hot climate, high humidity, monsoons, high winds and insect swarms. Due to the extensive vegetation, it is considered a low-dust environment. Typhoons, dust, insects and the remoteness of systems in the tropics should be considered when choosing the correct system. The filtration systems for tropical environments are specifically built to handle large amounts of rain. Weather hoods are used as a primary defense. Extended area insect screens are used for blocking insects. These filters should also be selected for the expected contaminants such as pollen and road dust;
- rural: depending upon where the gas turbine is located in this environment, it can be subjected to hot, dry climate, rain, snow and fog throughout the year. The contaminants in this environment vary depending on the season. This climate has one of the most diverse filtration requirements as compared to other environments. These systems are typically comprised of three stages: weather hood, pre-filter and high-efficiency filter;
- large city: can experience all the types of gas turbine degradation: corrosion, erosion and fouling. Contaminants from many different sources ensure the requirement of a multi-staged filtration system. The filtration system is composed of a pre-filter and a high-efficiency filter;
- industrial area: there are several emission sources in an industrial location, which

contribute to the contaminants that must filtered out. The most prevalent contaminant in industrial areas is contaminants from exhaust stacks. These can be in the form of particles, gases and aerosols. Many of the particles emitted by the exhaust stack are in the submicron size range. Many of these aerosols are sticky and when they are not removed by the filters, they stick to compressor blades, nozzles and other surfaces. If the gas turbine is near a petrochemical plant, the air may be contaminated with specific chemicals. One contaminant that is often in the air at industrial locations is sticky aerosols. These aerosols can be from oil vapors from lubrication systems or unburned hydrocarbons emitted from exhaust stacks. These aerosols are very difficult to remove from the air and often lead to blade fouling. High efficiency filters should be used to minimize the aerosol's effect on the gas turbine, but a compressor washing scheme is needed to keep the compressor blades clean and to minimize the effects of fouling on gas turbine performance.

Normally, the filtration system pressure loss will increase with an increase in filtration efficiency. As filters become more efficient, less dust penetrates through them. Also, the air flow path is more constricted with higher efficiency filters. This leads to higher pressure loss. Studies have shown that a higher pressure loss due to using a high efficiency filter has a lower effect on gas turbine power degradation than poor inlet air quality. As reported by Wilcox *et al.* (2011), a 50 Pa reduction of pressure loss can result in a 0.1 % improvement in power output. Typical pressure losses on inlet filtration systems can range from 500 to 1,500 Pa.

Modern day filtration systems are comprised of multiple filtration stages. Each stage is selected based on the local operating environment and the performance goals for the gas turbine. Figure 1.15 shows a generalized view of a filtration arrangement. This arrangement is not correct for all cases due to the fact that the filter stages are highly influenced by the environment they are operating in.

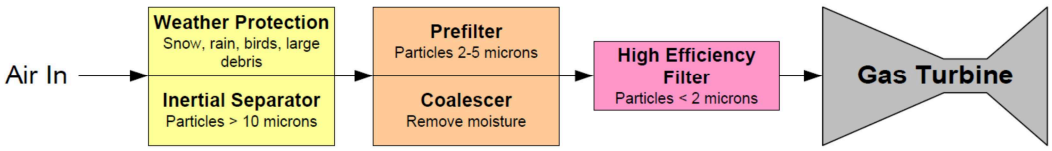

Figure 1.15 – Multistage filtration system (Wilcox *et al.*, 2010)

In three stage arrangement, a pre-filter or weather louver can be used first to remove erosive particles, rain and snow. The second may be a low to medium-performance filter selected for the type of finer-sized particles present or a coalescer to remove liquids. The third filter is usually a high-performance filter to remove smaller particles less than 2 µm in size from the air. In Table 1.3 the comparison in terms of number of particle at the compressor inlet is reported for the 2-stage and

3-stage filtration system.

Schroth and Cagna (2008) have reported also the differences in term of pressure drop between the two filtration method. The comparison is depicted in Fig. 1.16. The curves marked with “2-stage system“ and “3-stage system“ respectively, represent the total pressure drop of the 2-stage or 2-stage systems. The significantly lower pressure drop in the two-stage filter system can be seen, with the average pressure drop over the entire year being approximately 300 Pa less compared to the 3-stage system.

Table 1.3 – Comparison of the filter collection efficiencies of 2-stage and 3-stage filter systems (Schroth and Cagna, 2008)

#-stage filtration	Particle size [µm]	Particle in the atmosphere [#/m^3]	Initial efficiency filtration [%]	Particle penetration [#/m^3]
2-stage filtration	0.3 – 0.5	20,000,000	64	7,200,000
	0.5 – 1.0	4,000,000	80	800,000
	1.0 – 2.0	300,000	95	15,000
3-stage filtration	0.3 – 0.5	20,000,000	98.9	220,000
	0.5 – 1.0	4,000,000	99.9	4,000
	1.0 – 2.0	300,000	99.999	3

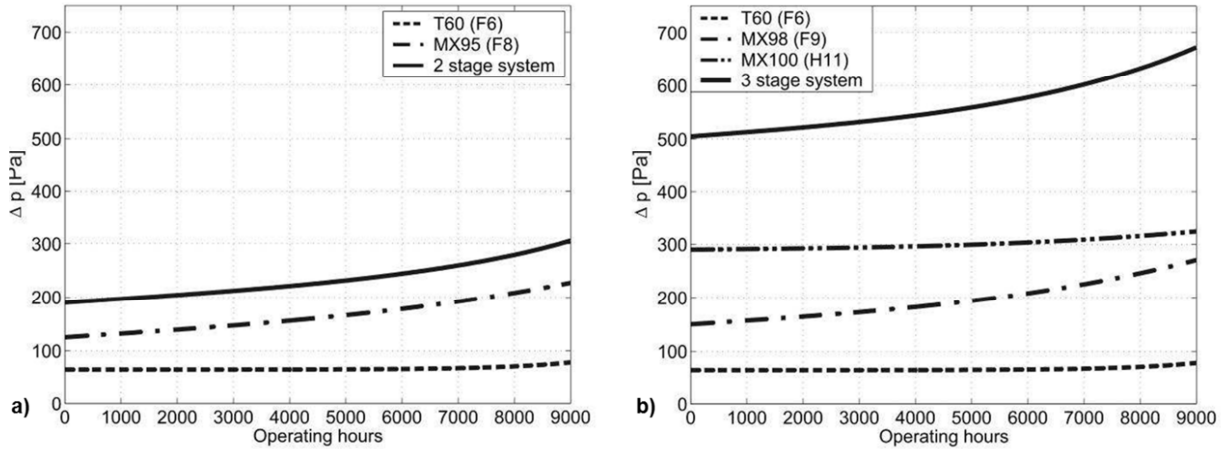

Figure 1.16 – Pressure drop curve at 4250 m^3/h volume flow rate per filter element: a) 2-stage filter, b) 3-stage filter (Schroth and Cagna, 2008)

1.3 Deterioration in axial compressor

The fouled axial compressor has deteriorated aerodynamic qualities, which causes

the decrease in the air mass flow through the axial compressor and in the axial compressor efficiency, the surge margin also decreases. Simultaneously there is a decrease in the compressor pressure ratio due to reduced gas mass flow through the turbine. This, all together, leads to decrease in the gas turbine unit output and to increase in the specific fuel consumption. The correlation between these variables for the General Electric gas turbine unit, reported by Hoeft (1993), is shown on Fig. 1.17, from which one can see that in case the axial compressor is fouled to a degree that the pressure ratio decreases by 5.5 % (the vertical line on the fouling curves), the gas turbine unit output decreases by 13 % and the specific fuel consumption increases by 6 %. As reported by Nicholson (1990) and Schurovsky and Levikin (1986) the axial compressor fouling increases during the first 1,000 operation hours. The gas turbine unit output and efficiency losses decrease as the operation time increases, according to an exponential curve, and they will tend to stabilize after 1,000 – 2,000 operation hours.

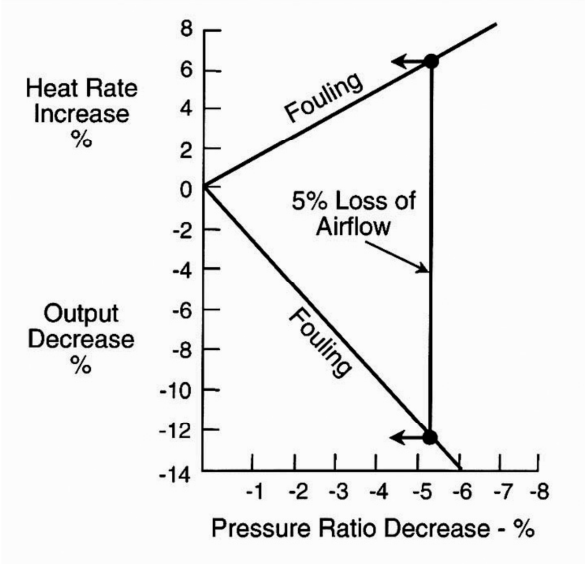

Figure 1.17 – Deterioration of gas turbine performance due to compressor blade fouling (Hoeft, 1993)

Even under normal power unit operating conditions, with a proper filtration system and fuel, the engine flow path components will become fouled, eroded, corroded, covered with rust scale, damaged, etc. As reported by Diakunchak (1992) types of engine performance deterioration may be listed under the following point:

- permanent performance deterioration, which is not recoverable after an overhaul and the refurbishment of all clearances, replacement of damaged parts;
- performance deterioration non-recoverable with cleaning/washing operations;
- performance deterioration recoverable with cleaning/washing operations.

Gas turbines involved in oil and gas production have a large economic potential to keep performance and availability at the highest level possible. All gas turbine

experience loss performance over time. Performance deterioration is caused by many different factors such as erosion of blade surfaces due to particle ingestion, fouling due to airborne pollution or oil vapors, blocking of cooling holes and labyrinth seals, and foreign object damage. Deterioration is generally referred to as either recoverable by routine maintenance actions or non-recoverable except by replacement of degraded engine components.

This thesis refers to the recoverable deterioration especially due to the fouling phenomenon in the compressor sections but, in order to report a wide overview of the gas turbine operation issue, all of these aforementioned points are briefly explain in this paragraph. In particular, the report focuses on the three main families that cause degradation in compressor gas turbine: (i) corrosion, (ii) erosion and (iii) fouling. In general, corrosion and erosion are classified as non-recoverable with cleaning/washing operations while the fouling is classified as recoverable with cleaning/washing operations. Diakunchak (1992) estimates the extent of this type of unrecoverable deterioration to be usually less than 1 %. The extent of the unrecoverable loss will be greater if heavy fuels are being utilized. Hepperle *et al.* (2011) summarize the performance trend affected by the degradation and the effect of the following action in order to reach the maximum available performance. Figures 1.18 and 1.19 report these concept.

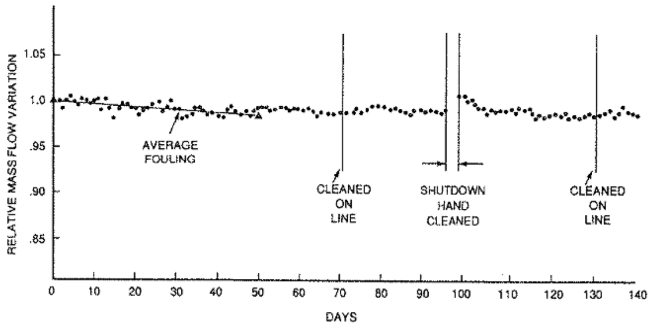

Figure 1.18 – Relative with mass flow variation with time (Diakunchak, 1992)

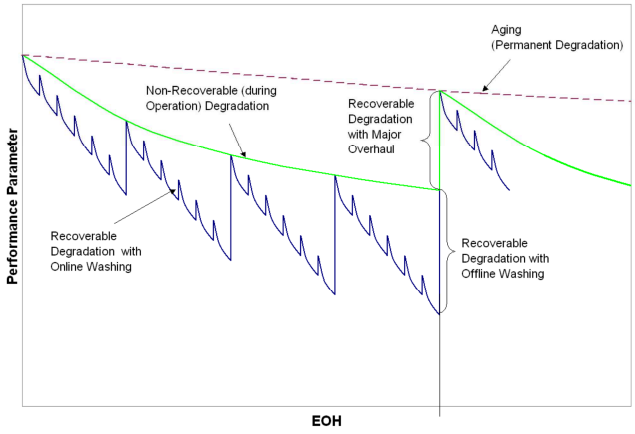

Figure 1.19 – Recoverable and non-recoverable degradation (Hepperle, 2011)

Corrosion is the loss of material from flow path components caused by chemical reactions between the component and certain deposits, such as salts, mineral acids or reactive gases. Corrosion is caused both by inlet air contaminants and by fuel and combustion derived contaminants. The contaminant enter in the gas turbine with the inlet air, fuel or injected water/steam. Corrosion that occurs in the compressor section is referred to as “cold corrosion” and is due to wet deposits of salts, acid and aggressive gases such as chlorine and sulfides. Corrosion in the combustor and turbine sections is called “hot corrosion”.

Cold corrosion could be eliminated by coating the compressor airfoil that protect the compressor sections against the wet corrosion. Hot corrosion is the loss or deterioration of material from flow path components caused by chemical reactions between the component and certain contaminants, such as salts (for example sodium and potassium), mineral acids or reactive gases (such as hydrogen sulfide or sulfur oxides). Hot corrosion requires the interaction of the metal surface with another chemical substance at elevated temperatures. Hot corrosion is a form of accelerated oxidation that is produced by the chemical reaction between a component and molten salts deposited on its surface. A sample of the effects due to the hot corrosion is reported in Fig. 1.20.

Figure 1.20 – Hot corrosion on turbine blades after about 1,000 h of operation on distillate fuel containing 2 ppm sodium from sea water contamination (Kurz *et al.* 2012)

Erosion is a non-reversible process; therefore, the gas turbine components must be replaced in order to regain their original condition. Erosion is the abrasive removal of blade material by hard particles or incompressible particles such as sand fly ash and water, usually greater than 10 μm in diameter. These particles will impact the surface and remove tiny particles of metal which eventually lead to changes in the geometry of the surface. This change in geometry causes deviations in the air flow path (changes in the inlet metal angle), roughening of smooth surfaces, alteration of clearances and reduction of cross-sectional areas of metal components possibly in high stressed regions. Thinning of the trailing edge is detrimental to the fatigue

strength and can result in blade failure even if this damage may be beneficial to performance (Diakunchak, 1992). A significant loss in tip solidity can promote compressor surge. The typical area of metal loss for a rotor blade is at the tip while for a stator it is near the root. Typically, the erosive particles are centrifuged to the outer diameter of the compressor. This usually increases radial tip clearances or sealing gaps and results in higher leakage flows.

The material removal will typically increase seal or tip gaps. Part of this is also age related, as bearings tend to become softer (reduction in stiffness) due to an increase in clearance over time that causes an increase in journal orbital amplitude. Damage may also be caused by foreign objects striking the flow path components. These objects may enter the engine with the inlet air, or the gas compressor with the gas stream or are the result of broken off pieces of the engine itself. Pieces of ice breaking off the inlet or carbon build up breaking off from fuel nozzles can also cause damage.

Bons (2010) have reported a review of the state of the art of the study related to the effects due to erosion in compressor and turbine sections. He pointed out that the roughness effects in the compressor and turbine are dependent on Reynolds number, roughness size and to a lesser extent Mach number. At low Re, roughness can eliminate laminar separation bubbles (thus reducing loss) while at high Re (when the boundary layer is already turbulent), roughness can thicken the boundary layer to the point of separation (thus increasing loss). In the turbine, roughness has the added effect of augmenting convective heat transfer. While this is desirable in an internal turbine coolant channel, it is clearly undesirable on the external turbine surface.

Also in Hamed *et al.* (2006) it is possible to found a complete review of erosion and deposition research in turbomachines and the associated degradation in engine performance caused by particulate matter ingestion. In particular, the authors reported a large number of investigations on the particle deposition on the blade turbine surface, in which the characteristics of the particle motion, size and deposition rate of the particle were highlighted. The reported results show that in the particle size range of (0.5 – 3.0) μm there is a combined action of two mechanisms called diffusion and inertia. For the turbine blade, there are specific experimental and numerical analyses in order to link the impact angle, impact velocity and particle size to the erosion rate and surface roughness (Hamed *et al.,* 2005). One of the experimental results reported by Hamed *et al.* (2005) is depicted in Fig. 1.21.

Erosion is more a problem for aero engine applications, because state of the art filtration systems used for industrial applications will typically eliminate the bulk of the larger particles. Erosion can become a problem for engines using water droplets for inlet cooling or water washing. For this reason, some experimental and numerical

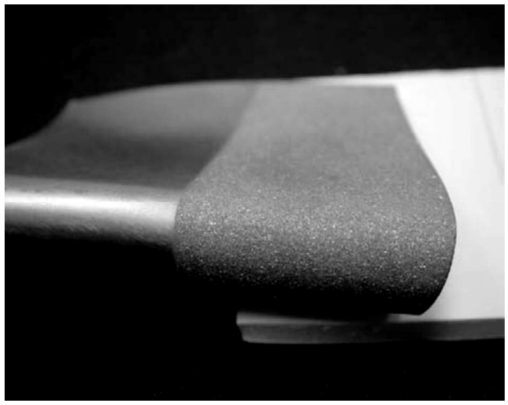

Figure 1.21 – Vane subjected to 1,500 µm particles, 91.4 m/s (300 ft/s), 30° incidence. Erosion rate 5 mg/g of particles (Hamed *et al.*, 2005)

studies related in particular to the compressor section are reported below.

Regarding the erosion in the compressor section some experimental and numerical results can be found in literature. Balan and Tabakoff (1984) report an experimental investigation on two dimensional compressor cascade. The results showed that: (i) the leading edge were flattened and the erosion is clearly visible both in pressure and suction side, (ii) the pressure surface of the airfoils were eroded severely associated with the increase in surface roughness and (iii) the suction side surface remain unaffected except for the erosion that occurs in the leading edge and the increased surface roughness of a small region immediately following the leading edge. A schematic blade erosion is shown in Fig. 1.22. Probabilistic study conducted by Kumar *et al.* (2005) pointed out that pressure losses could be increase up to 5 % for an eroded compressor fan blades.

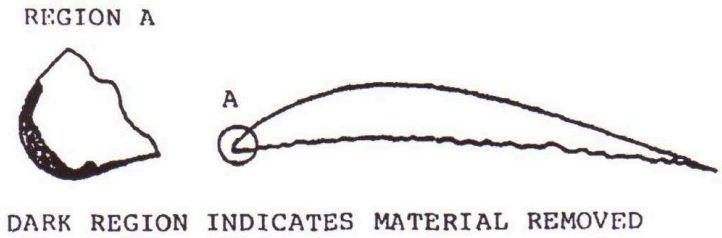

Figure 1.22 – Schematic of erosion damage (Balan and Tabakoff, 1984)

Suzuki *et al.* (2008) performed a study of the erosion effects in an axial compressor stage. The particles have a diameter equal to 165 µm and the results were obtained with the following assumption: (i) non-rotating spherical particle, (ii) the particle-particle collision was neglected, (iii) the particle-phase had no influence on the gas-phase and (iv) the drag-force was the only force that influenced the particle-phase. The authors took into account the effect of the rebounded particles and the

results show that the first impact of the particle determines the most important erosion on the blade surface, in particular at the leading edge. With the same axial compressor and nature of the particles, Suzuki and Yamamoto (2011) show the performance drop and the modification of the flow path inside the stage caused by the erosion.

Ghenaiet (2012) studied the particle dynamics and erosion of the front compression stage of a turbofan PW-JT8-D17. Particle trajectory simulations used a stochastic Lagrangian tracking code and the sand particle size varied from 0 μm to 1,000 μm. The numerical simulations show different trajectories for different particle diameters. After the initial impact, the larger particles were affected by inertia and centrifugal force and some of these re-impacted the blade surface at the pressure side. Some particles crossed the blade through the tip clearance and induced erosion of the blade tip. Small size particles (i.e. ≈ 10 μm) tended to follow the flow path closely and were strongly influenced by the flow turbulence, secondary flows and flow leakage above the blade tip and induced erosion of the blade tip and shroud. Particles with a diameter less than 10 μm have not been taken into account for the erosion analyses.

Hamed *et al.* (1998) have presented the results of a simulation of compressor performance deterioration due to blade erosion. The simulation was based on a mean line row by row model, which incorporates the effects of blade roughness and tip clearance. The results indicated a pronounced effect of blade erosion on the compressor adiabatic efficiency and a lesser effect on the pressure ratio. The loss in performance is mainly caused by the increased blade surface roughness and was highest at 100 % speed. A loss in adiabatic efficiency of (3 – 4) % was predicted under the combined effects of increased blade surface roughness and tip clearance due to erosion.

Particles and drops smaller than 10 μm do not determine erosion issue but, in determinate circumstance, cause fouling issue. Compressor fouling is due to the size, amount, and chemical nature of the aerosols in the inlet air flow, dust, insects, organic matter such as seeds from trees, rust or scale from the inlet ductwork, carryover from a media type evaporative cooler, deposits from dissolved solids in a water spray inlet cooling system, oil from leaky compressor bearing seals, ingestion of the stack gas, or plumes from nearby cooling towers (Kurz and Brun, 2012). Fouling can be controlled by appropriate air filtration system and often reversed to some degree by detergent washing of components. Some example of deposits in axial compressor in Fig. 1.23 and gas turbine in Fig. 1.24.

The result of fouling is buildup of material, which changes the shape of airfoil, changes the airfoil inlet angle, increases surface roughness and reduces the airfoil throat opening. The end result is reduced component performance, such as: (i)

Figure 1.23 – Low Solubility Deposits on Compressor Blades (Kurz *et al.*, 2012)

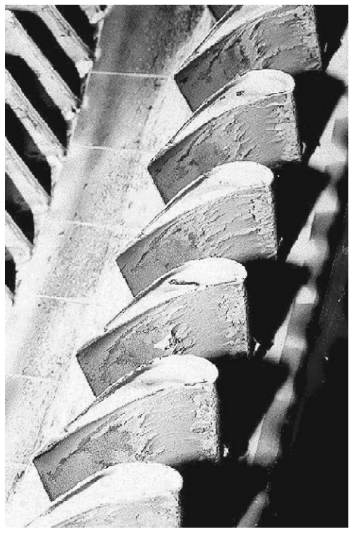

Figure 1.24 – Gas turbine operating on heavy fuel, showing blading fouled with ash deposits (Meher-Homji and Bromley, 2004)

reduced compressor discharge pressure, (ii) reduced compressor efficiency, (iii) increased compressor discharge temperature, (iv) reduced power output, (v) slowing of shaft speed in multi-spool engines and (vi) onset of compressor stall or surge.

In particular, for the compressor section, the change in surface roughness determines an important variation in the performance. As reported by Bammert and Woelk (1980) the rough blading not only causes shifting of the operating points to smaller suction volumes but also narrowing of the characteristic field from the throttling line and rotating stall line. Recently, Morini *et al.* (2010a) reported the actual modification of compressor and turbine performance maps due to blade deterioration by using a stage-by-stage models of the compressor and the turbine. The results for the case of fouling are reported in Fig. 1.25b in terms of non-dimensional pressure ratio and efficiency against non-dimensional corrected mass flow rate. As can be noticed, fouling causes a shift of the pressure ratio curve toward

a lower corrected mass flow rate value. The same occurs for efficiency curves reported in Fig. 1.25a.

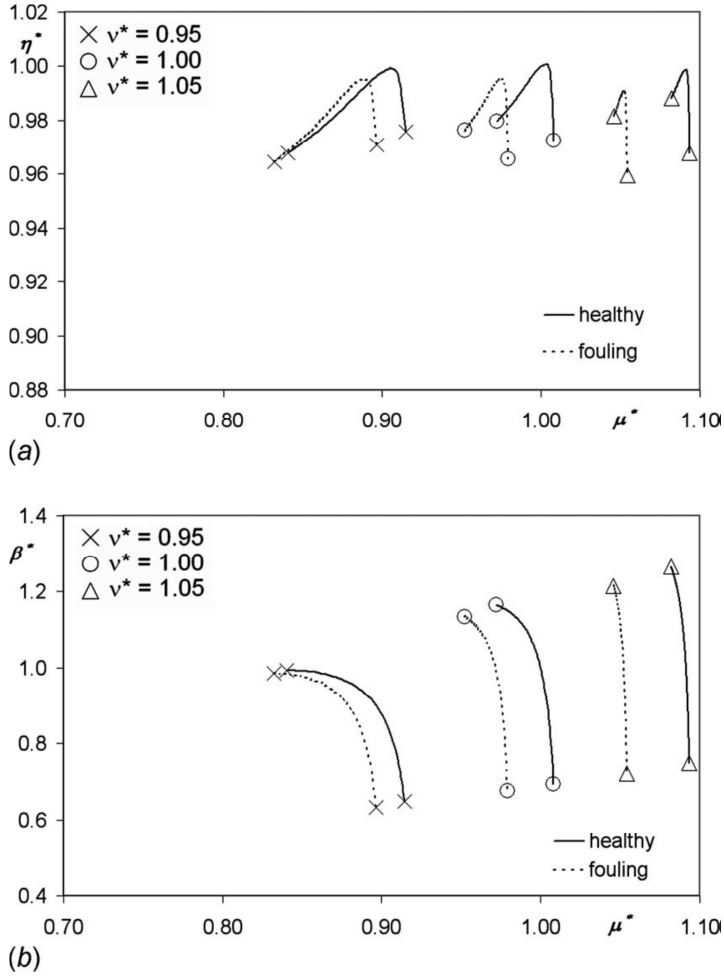

Figure 1.25 – Effect of gradual fouling on all the stages: a) efficiency vs corrected mass flow rate, b) non-dimensional pressure ratio vs corrected mass flow rate (Morini *et al.*, 2010a)

Compressor fouling is more common and has the more serious effect on engine performance. Typically about 70 % to 85 % of all gas turbine engine performance loss accumulated during operation is attributable to compressor fouling (Diakunchak, 1992). In fact, one of the first on-field fouling detection was proposed by Scott (1979), using a simple manometer of intake depression which gives an indication of airflow. It was found that 3 % decrease in intake depression was suitable level for cleaning action. Compressor cleaning at this stage was found to restore the intake depression to its original level.

Fouling restricts flow and causes increased boundary layer thickness both on the blades and along the endwalls of the annulus and hub. Blockage of the air path and increased frictional losses reduce the compressor head and flow, causing an overall reduction in the power capacity and an increase in the specific fuel consumption.

All compressors are susceptible to fouling. The degree of fouling, the rate of fouling and the effect on performance depend on the following: compressor design, compressor airfoil loading, airfoil incidence, airfoil surface smoothness/coating, type and condition of the air-borne contaminants, the site environment and the climatic conditions (high humidity increases the rate of fouling). Dry particles in dry atmospheres are likely to deposit in different areas depending on the location of sticky material and oily compounds. At high inlet humidity, the drop in static pressure during acceleration of the air through the compressor will increase dust adhesion on the blades because of the condensing water (Zaba, 1980, Meher-Homji *et al.*, 2001).

Studies on fouling phenomena are widespread in literature: (i) reports on fouling issue by using on-field data, (ii) experimental test on single cascade and (iii) analytical-numerical analysis related to the fouling effects on gas turbine performance. Some of these works comprise more than one point of view in order to better understand the fouling issue and try to extrapolate general rule from experimental and numerical analyses.

As mentioned above one of the fouling effects is the variation of the surface roughness. In particular, the deposits on blade surfaces increase the surface roughness.

Kind *et al.* (1998) have reported an experimental analysis relates to the surface roughness on turbine blade. The experimental tests are conducted with a variation of the surface roughness pattern: spanwise-oriented bands of roughness was placed at various locations on the suction and pressure surfaces of the blades. The authors have varied roughness height, spacing between roughness elements and band width. Roughness was found to have little effect on static pressure distribution around the blades and on deviation angle, provided that it does not precipitate substantial flow separation. Roughness on the suction surface can cause large increases in profile losses. Roughness height and location of the leading edge of the roughness band are particularly important. Loss increments due to pressure surface roughness are much smaller than those due to similar roughness on the suction surface.

The impact of surface roughness compared to the Reynolds number on turbine blade aerodynamics was evaluated through experimental tests by Hummel *et al.* (2005). With a Reynolds number in the range of 600,000 to 1,200,000 the authors have performed some measurement related to the pressure losses through a heavy-duty turbine blade cascade. The results show that maximum loss increase due to surface roughness occurs at the highest Reynolds number tested (maximum surface roughness equal to Ra = 11.80 µm). Similar results can be found in Boyle (1994) that found for a two stage turbine efficiency losses of 2.5 % for a 10.2 µm surface roughness when compared to the smooth blades.

The influence of the surface roughness and the increased thickness of the airfoil is reported by Samsher (2007). The author has performed experiments with smooth, smooth-thickened and rough-thickened turbine blades. The emery paper was positioned on suction side and pressure side separately and over both surfaces. The roughened surface represented the erosion effects while the rough-thickened blades represent the effect of the surface roughness induced by the deposits. For the same roughness level, roughness caused by the deposition is more detrimental than that by erosion. The performance deterioration and non-uniformity of flow is more for rough-thickened blades.

Three major effects determine the performance deterioration of the compressor: (i) increased tip clearance, (ii) changes in airfoil geometry and (iii) changes in airfoil surface quality. While the first two effects typically lead to non-recoverable degradation, the latter effect can be at least partially reversed by washing operation. The degradation will force all stages after the first one to work at off optimum surge margins and lower than design efficiency. This will not only lower the overall efficiency and the pressure ratio than can be achieved, but also the operating range.

Literature reports a widespread type of analyses and studies relates to fouling in axial compressor. Some of these, report the effects of the fouling in the axial compressor performance or in more in general in the power unit performance, other, are related to better comprises the fouling phenomenon, in particular, which are the favorable locations and which are the resulting blade surfaces. The first type are conducted in two manner: (i) the first one refers to the experimental application while (ii) the second one refers to the numerical simulation of the axial compressor performance in which the effect of fouling are modeled.

Tarabrin *et al.* (1998b) reported an investigation of compressor blade contamination for a Nuovo Pignone MS5322 R(B) gas turbine engine. This power unit operated for a long time without blade washing but only the first 5 to 6 stages of 16 are subjected to blade fouling due to deposits. Figure 1.26 depicted the weight distribution of deposits for rotor blades (Fig. 1.26a) and stator blades (Fig. 1.26b). The inlet guide vane blades, as well as the rotor and stator blades of the first stage have more deposits on the blade convex side. The deposits masses on blades of the other stage are approximately equal for the convex and concave side. The deposits masses decrease from the first to the sixth stage. From the seventh stage, the amount of deposits on blades is insignificant. The authors pointed out that the deposits amount is greater on the stator blades, than on the rotor blades due to the cleaning effects provided by the centrifugal forces on a dirt particles.

Back *et al.* (2010) reported an experimental investigation for characterize the influence of surface roughness location and Reynolds number on compressor cascade performance. In addition to the entirely smooth and entirely rough blade

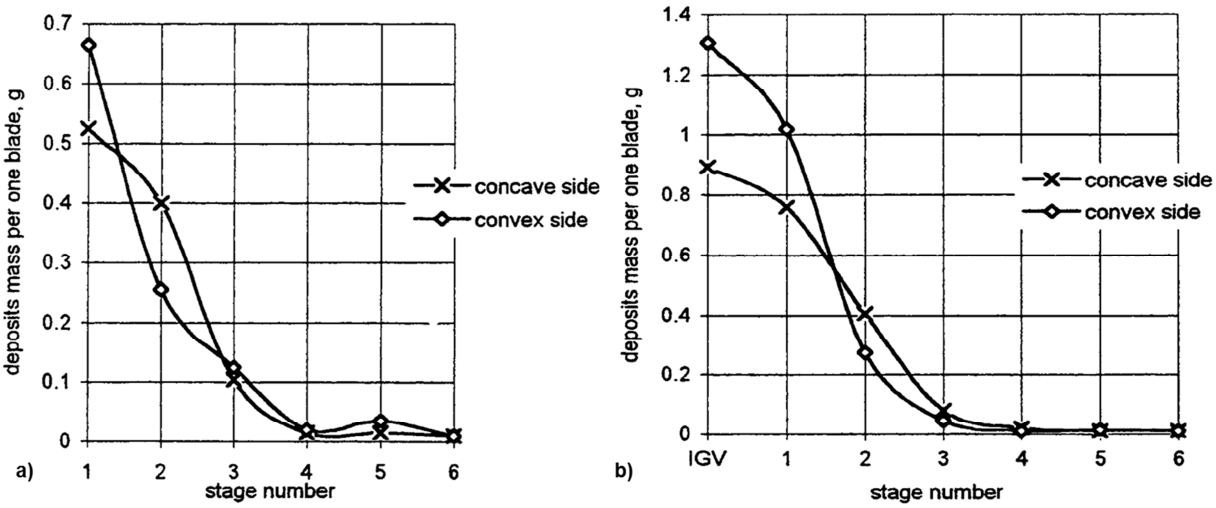

Figure 1.26 – Weight distribution of deposits on the convex and concave sides of the axial compressor blades: a) rotor, b) stator (Tarabrin *et al.*, 1998b)

cases, blades with roughness covering the leading edge, pressure side and 5 %, 20 %, 35 %, 50 %, and 100 % of suction side from the leading edge have been studied. The roughened surface is obtained by using paint or glue that realized an surface roughness equal to 2.89 µm. The cascade performance is more sensitive to the suction side roughness and the roughness near the trailing edge of suction side increases loss more than that near the leading edge. The suction side partially covered (20 %) in the near leading edge area is reported in Fig. 1.27.

Figure 1.27 – Suction side partially covered (20 %) by a paint/glue (Back *et al.*, 2010)

Syverud *et al.* (2005) reported the location of salt deposits in General Electric J85-13 axial compressor. The experimental tests have shown that the salt deposits were mainly found along the leading edge of the first four stages and on the pressure side of the stator vanes along the hub. The salt deposits were generated by the salt carried by the water droplets and for this reason, significantly less deposit were

observed on the rotor blades compared to the stator vanes due to the centrifugal force.

Gbadebo *et al.* (2004) presented the results of experiments and numerical simulations performed on a large-scale single-stage low-speed compressor by imposing a roughness value established in Ra = 25 μm. They found that for a single stator, roughness in mid-chord position and near the trailing edge on the suction side surface had negligible effect, while surface roughness applied from the leading edge to peak suction induced a significant performance drop.

Suder *et al.* (1995) analyzed the performance deterioration of a high-speed axial compressor rotor, the NASA Rotor 37, due to artificially imposed alterations in terms of surface roughness and airfoil thickness variations. In particular, a quasi-3D Navier-Stokes flow solver was used to simulate these alterations and the comparison to the experimental data was reported. With regard to non-uniform roughness, they found that pressure surface roughness has little impact on performance degradation and that performance degradation is triggered by additional thickness and/or roughness at the leading edge.

Parker and Lee (1972) studied fouling patterns on rotating blades for very fine (0.13 μm and 0.19 μm) particles. Results show high deposition rates at the blade leading edge, relatively low deposition on the pressure side and a higher deposition rate on the suction side toward the trailing edge. The deposition rates on the suction surface near the trailing edge are where the boundary layer is thick and turbulent. Analogous results can be found in Silingardi *et al.* (2013) where field data regarding the deposition of foulants on a transonic blade compressor are reported. Silingardi *et al.* (2013) reported the blade surface condition after 25,000 operation hours and the authors highlighted that three-dimensional flow features cause small particles to be deposited in zones where secondary flows and vortices are dominant. Figure 1.28 depict the areas interested by the deposits both in pressure and suction side for the Ansaldo AE94.3A4 axial compressor.

Figure 1.28 – Compressor first rotor blade visual appearance after 25,000 operating hours, pressure side on the left and suction side on the right (Silingardi *et al.*, 2013)

Vigueras Zuniga (2007), and Erol and Bettner (1983) reported some experimental measurements with regard to the deposition on the axial compressor blade surface. In particular, Vigueras Zuniga (2007) documented the formation of deposits on the gas turbine compressor rotor and stator, both on the suction and on the pressure surface. There is evidence of increased deposits in the leading edge region of the rotor blade suction side. The experiments document deposit formation on the blade surface, in particular near the hub and tip regions. Moreover, a clean zone near the leading edge, that is larger at the mid-span than at the tip and hub, is noticed. Erol and Bettner (1983) reported a comparison of the performance of gas turbine axial compressors for different shroud roughness levels.

Meher-Homji *et al.* (2009) introduced the important distinction between susceptibility and sensitivity to fouling. Susceptibility is the amount of fouling a compressor incurs under a specified contaminant load, while sensitivity describes the effect on compressor efficiency, or, in a wider sense gas turbine power output capability and efficiency, of a certain amount of compressor fouling. This thesis refers to the analysis of the fouling susceptibility of transonic and subsonic axial compressor rotors. Regarding the fouling sensitivity some analyses can be found in literature. These analyses, relates the effect of the fouling phenomenon to the compressor performance degradation. The fouling phenomenon is modeled in order to reproduce the fouling effects with the numerical models.

Relates of this, Morini *et al.* (2011), by using an already validated numerical model reported by Morini *et al.* (2010b), have investigated the effect of non-uniform surface roughness on both rotor and stator blades. In particular, different non-uniform combinations of surface roughness levels on rotor and stator blades were imposed, both on the pressure side and on the suction side. This made it possible to highlight how the localization of fouling on compressor blades affects compressor performance, both at an overall and at a fluid-dynamic level. In this numerical model the effects of fouling are modeled by increasing the airfoil thickness (0.3 mm) and by imposing the surface roughness. A roughened rotor showed the greatest performance drop, mainly due to suction surface roughness.

The same computational strategy was adopted by Aldi *et al.* (2014). The authors have investigated the effect of different spanwise distributions of roughness on the rotor, to simulate operating conditions characterized by non-uniform fouling. This type of deterioration can be found in practice and may be attributed both to normal operation under varying conditions and to the non-uniform action of compressor washing. The results highlighted that, for all the considered roughness distributions, the shape of the performance maps was similar and in agreement with the computationally smooth baseline case. In addition to overall performance drop, the results showed a significant redistribution of blade loading may occur, the location being a function of actual surface roughness distribution. Moreover, the losses at

blade hub seem to be independent of the roughness at the same location.

The last numerical method to study the fouling phenomena is represented by the analysis of the particle trajectories and particle deposition in the compressor flow path. Borello *et al.* (2012) develop a numerical model to simulate the trajectories of adhesive particles in order to identify deposit formation in a 3D linear compressor cascade. The unsteady flow field is calculated by means of an hybrid Large-Eddy Simulation (LES)/Reynolds-Averaged Navier-Stokes (RANS) computation. Deposits are observed to form near the casing and the hub where there are strong vortical structures originating from the tip leakage and hub vortices, respectively. The numerical results showed good agreement with the experimental results reported by Vigueras Zuniga (2007). Figure 1.29 reports the comparison. It is important to highlight that in this case, the diameter of used particles (25 μm) are larger than the diameter of particles responsible of the fouling issue.

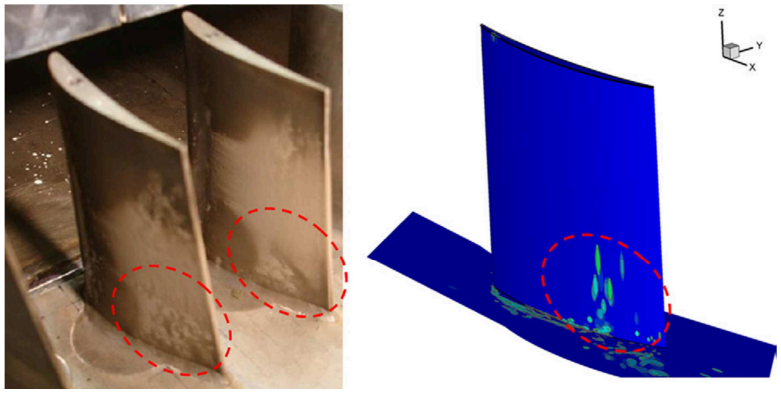

Figure 1.29 – Deposit on the suction surface: experiments by Vigueras Zuniga (2007) (left), simulation by Borello *et al.* (2012) (right); the circles show the deposit induced by the presence of large recirculation due to the development of hub vortex

1.4 Compressor washing

The degradation caused by the adherence of particles on the compressor airfoil and annulus surface can be partially recovered by compressor cleaning. Compressor cleaning is realized by some procedure and strategies summarized as washing method.

The state of the art method for removing fouling is a liquid wash in which a wash fluid is injected at the front end of the gas turbine. The wash fluid penetrates the gas path where it dissolves and removes the fouling. There are presently two washing methods in use for liquid washing: offline wash and online wash.

In offline washing the gas turbine is run at sub-idle shaft speeds while a cleaning

solution is injected into the engine. This method is well-proven and effective in removing deposits not only in the axial compressor but also on the interior surfaces of the entire gas path. Before an offline wash, the gas turbine unit must be shut down and cooled to avoid excessive thermal loading of the internal gas turbine components. This causes loss of availability and possibly production losses.

Online washing is done during gas turbine operation by injecting the cleaning solution into the compressor section while the engine is running in normal operation, hence avoiding the associated down-time cost. The potential savings that can be gained from efficient online compressor cleaning have led a number of companies to install such systems. Online washing is often combined with off-line washing to optimize uptime while maintaining an acceptable thermal efficiency. Cost of fuel and lost production are the predominant economic factors in determining the time between off-line washes.

The decision to shut the engine down for off-line washing is a balance between lost production due to the lower power versus the lost production for shutting the engine down for a certain amount of time. Stalder (2001) reported a complete overview of the washing operation. Stalder (2001) reported also the result of the long term test on the combined effect of online and offline washing. Typical effects of different washing strategies are reported in Fig. 1.30.

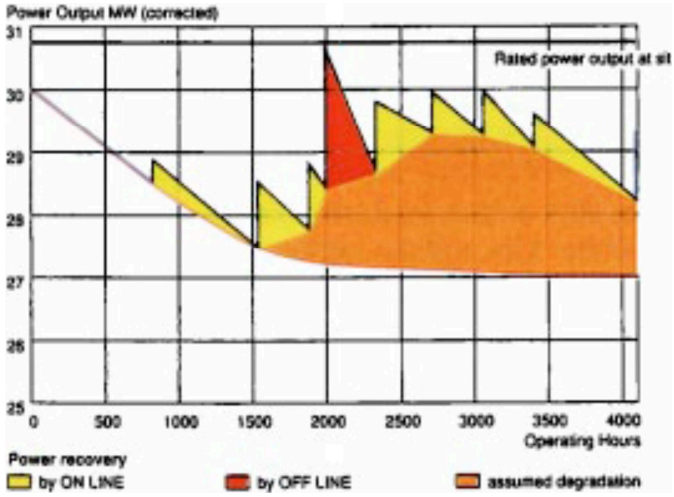

Figure 1.30 – Typical effect of on line and off line compressor wet cleaning (Stalder, 2001)

Another extensive report on the effect of the different methods of compressor washing is provided by Zaba (1980). The effects of cleaning are shown in the Fig. 1.31. Different cleaning methods determine different behavior in the compressor:

- dry cleaning using nut shells reduces the losses due to compressor fouling by only approximately (20 – 30) %. If this cleaning procedure is repeated, the situation is only slightly improved (Fig. 1.31, points 7-8, 9, 10, 11-12). The

modest cleaning effect is attributable to the fact that, due to the flow pattern, the suction side of the blade profile is only slightly cleaned by the nut shells;
- an experiment with wet steam cleaning, carried out at full load, showed a somewhat better result than the nut shells, but was still un-satisfactory; it is possible that, with this type or cleaning, the compressor efficiency is only slightly improved, because the later stages may become more heavily fouled during the washing procedure (Fig. 1.31, points 13-14);
- an experiment with water injection at full rotational speed had an effect similar to that of blowing in saturated steam (Fig. 1.31. points 16-17);
- very good results were obtained by washing the compressor blading after the machine had been stopped and allowed to cool. Washing was carried out using deposit-dissolving agents, as the rotor was turned over by the starting motor (Fig. 1.31, points 3-4, 14-15, 17-18);
- if the machine is opened and the blading is thoroughly cleaned the original acceptance test output is almost attained.

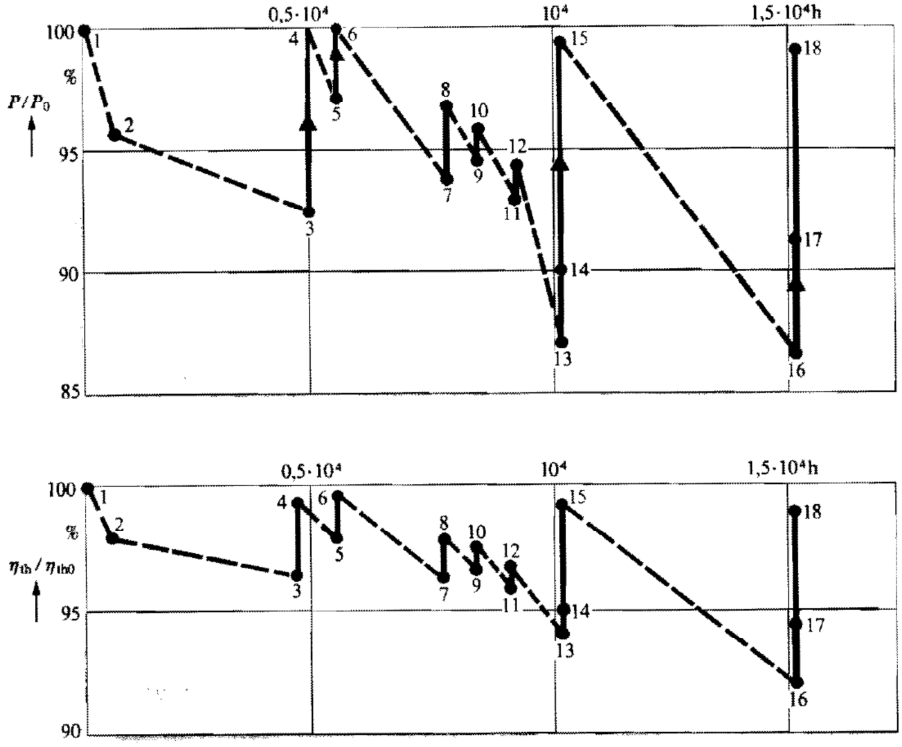

Figure 1.31 – Variations in output and thermal efficiency as functions of lime when compressor is fouled, and recovery obtained by cleaning (Zaba, 1980)

Mund and Pilidis (2006) reported the summary of advantages and disadvantages for each washing method. Table 1.4 summarized their overview. The authors reported also the state of the art of the washing patent in terms of nozzle disposition and washing strategies. They remarked the fact that the washing system must be designed for a specific operating condition and it is not possible to generalized the

Table 1.4 – Advantages and disadvantages of compressor cleaning methods (Mund and Pilidis, 2006)

Method	Advantages	Disadvantages
Manual cleaning (brushes, washing agent)	Very effective	Shut down the engine Laborious
Grit blasting (charcoal, rice, nut shell, synthetic resin particles)	Simple and fast No engine downtime Effective in cold environments	Less effective at rear stages and for oily deposits Clogging of internal cooling passage Erosion Increased in surface roughness Damage of blade coating
Soak, crank, offline washing	Very effective	Shutdown of engine
Fired, online washing (demoralized water, washing agent)	No interference with load profile Extends intervals of crank washes	Less effective Cannot replace offline washing (complementary)

washing systems and strategies.

The success of online cleaning appears to depend on site-specific issues such as the gas turbine operating profile and the nature of the deposits. Brun *et al.* (2013) reported an experimental investigation in which the cleaning agent, redeposit issue and online washing strategy are considered. Their results can be summarized as: (i) the blade cleaning is primarily a mechanical (droplet impact) function and does not depend on the fluid used for cleaning, and then the type of fluid used did not have a significant impact on the cleaning effectiveness, (ii) dirt removed from the blades will redeposit in downstream stages as the cleaning fluid is evaporated, in particular in the recirculation zones and (iii) blade erosion was not found to be a significant issue for the short durations that online water-washing is performed.

Improper use of online cleaning may further deteriorate gas turbine performance and increase fouling, both in the gas path and in the cooling air passages. In literature can be found analysis related in particular to the droplet size developed by using numerical simulation.

Mustafa *et al.* (2006) investigate droplet flow pattern during fluid injection into an axial compressor. The range of droplet sizes used in their simulations (from 50 µm to 300 µm) is representative of the droplet dimensions used during online washing. The droplet dispersion and flow pattern inside the compressor is strongly influenced by the initial conditions of the droplets during online compressor washing. Larger

droplets migrate towards the casing of the compressor and impinge on it, causing shrink due to the added cooling effect of the local liquid flow, thereby reducing the blade clearances. The authors emphasize the use of a range of droplet size, in this way in fact, the first few stages of an axial compressor, which are known to be more prone to fouling than the back stages, can preferentially receive lower sized particles, while bigger droplets, which are less likely to evaporate, can be injected with the cleaning of the back stages as their main target.

The injection of droplets in the scale of the larger size is undesirable due to its potential to cause blade erosion and induce rotor rubs. Additionally large size droplets are more likely to adopt a more marked radial migration towards the casing due to the greater centrifugal body forces due to their larger mass.

The erosion effects of the water droplets are reported by Khan and Wang (2011). The authors found that the erosion occurs in the leading edge area and in the trailing edge areas in the suction side. The droplet diameter used in this analysis is equal to 10 µm, and, the authors remark that the erosion rate is very low. The metal thickness lost only 14 µm. The erosion that afflict the leading edge is clearly reported by Kurz *et al.* (2008). The eroded leading edge area are reported in Fig. 1.32. The tendency of water droplet to surround the leading edge was also highlighted by Day *et al.* (2008).

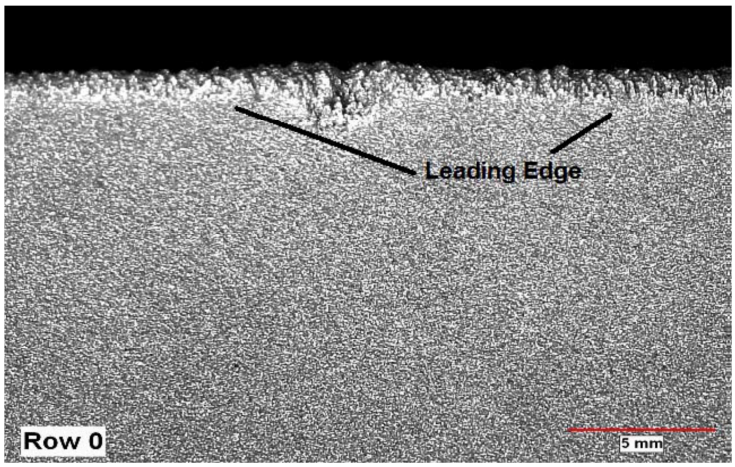

Figure 1.32 – Eroded leading edge of a the rotor blade of a the first stage of a compressor. The picture shows a section at midspan (but the other parts of the blade show similar damage) of a heavy duty industrial gas turbine (Kurz *et al.*, 2008)

Unfortunately, erosion that afflict the leading edge has great impact on the performance degradation. As reported by Reid and Urasek (1973), the shape of the leading edge influence the compressor performance. In their tests, the shorter leading edge (that results in a double thickness of the leading edge with respect to the original shape) determines a reduction in a compressor efficiency equal to 3.5 % at the design speed.

Chapter 2

Particles: Impact, Adhesion and Rebound

In this chapter a global overview of the wide horizon of the micro-particle analysis is reported. Micro-particles, carried by the air or, more in general, every type of micro-particles that became in contact to each other or with a surface show different behavior as a function of their material, size, surface conditions, impact velocity and impact angle. All these aspects can be studied from many points of view: (i) kinematic (velocity and direction), (ii) dynamic (velocity and mass) and (iii) energy (deformations or breaks). At the same time it is possible to consider microscopic effects (e.g. atoms attractions, molecular bonds) or macroscopic (e.g. adhesion, rebounds, deformations). Given that background, in this chapter will report some of the most important analytical models, experimental results and CFD numerical application related to the particle studies. Finally, this chapter, will focus on the analysis of the particle behavior inside the turbomachine, in particular, turbines sections and compressors cascades.

2.1 Historical overview: analytical models

Particles impinging onto the surface of a solid body can be reflected off the surface, stick to the surface or penetrate into the bulk. Often, the impact of a particle on a surface causes a deformation or destruction of both, the particle and the solid body. The first applications and studies related to the particle refer to the impact and/or adhesion during the contact between two particles and/or particle and surface. Particles are attracted to substrates (or other particles) via different types of interactions. These interactions create stresses between the materials. These stresses, in turn, create strains that may be large or small, elastic or plastic. Only by understanding both the interactions and the mechanical response of the materials to these interactions can adhesion be understood.

The bond between two generic bodies (such as the first particle with the surface and the following particles with the particle that is already contact with the surface) is ruled by (i) the physico-chemical properties of the body, (ii) the type and characteristic of the impact (velocity and angle) and (iii) the presence of a third substance at the point of impact (called bridges). The phenomenon of the impact

between two bodies, however, may not always result in an adhesion and bond between the two bodies. In fact, after impact, in some cases the two bodies can change energy and directions of motion with respect to those possessed before the impact. In this case, the phenomenon can be described by the introduction of some parameters called coefficients of restitution. Coefficient of restitution indicates the impact force ratio of the contact decompression (restitution) phase after impact and the contact compression phase during impact. For perfect plastic impact the coefficient of restitution is equal to 0 while for perfect elastic impact the coefficient of restitution is equal to 1.

Before entering into the description of analytical models, by using the comprehensive and detailed report provided by Tomas (2006), some preliminary definitions are reported. Figure 2.1, reports the surface and field forces at direct contact and the material bridge between contacts.

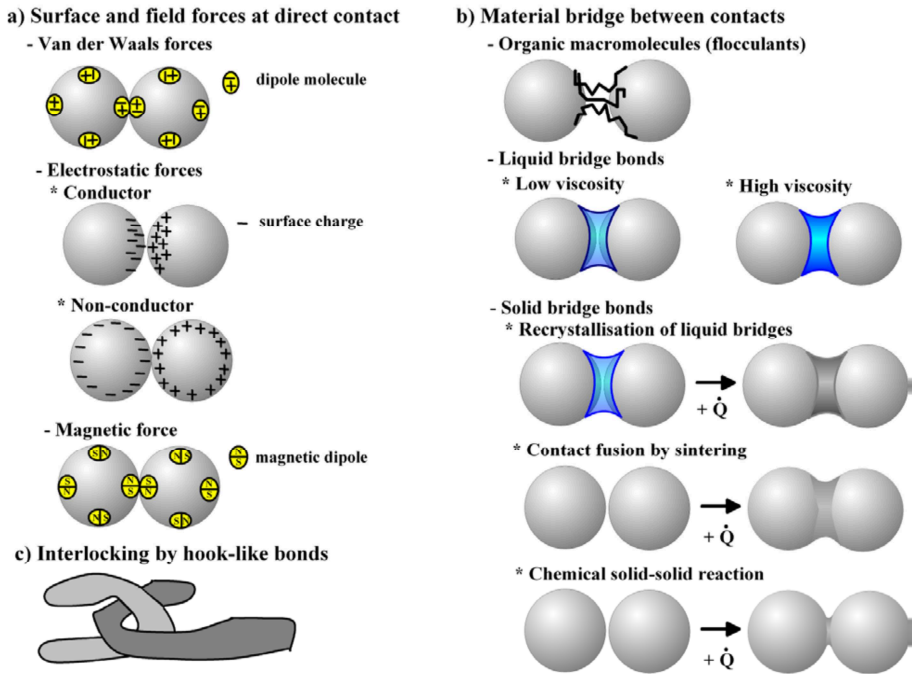

Figure 2.1 – Particle adhesion and micro-processes of particle bond effects in contact (Tomas, 2006)

The bond effects reported in Fig. 2.1 determine the adhesion force. These effects can work together or the adhesion could be the results of different phenomena that occur at the same time. Figure 2.2 summarize this issue for the adhesion between particle and flat smooth surface. Instead of the smooth surface can also consider a coarse smooth particle with a large radius of surface curvature. Figure 2.2 link the adhesion force with the particle diameter and the distance between flat smooth surface and the closest particle point to the surface.

Hertz (1896) proposed that a rigid indenter, acting under a compressive load,

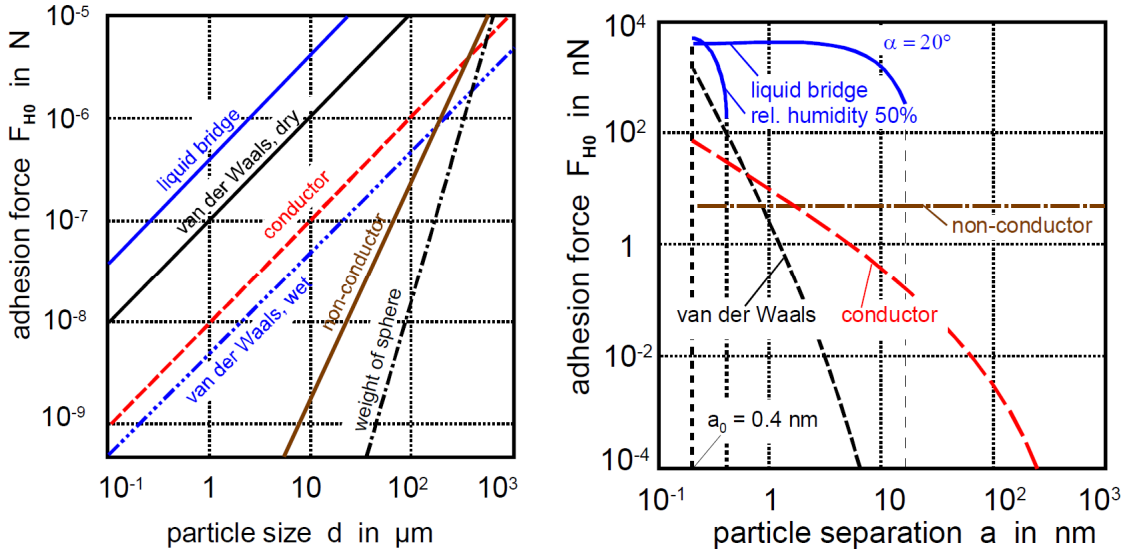

Figure 2.2 – Adhesion forces between stiff particle and smooth surface according (Tomas, 2006)

would cause a deformation of finite radius in a substrate having a specific Young modulus and a Poisson ratio. The classic approach to this type of problem consists in most cases of description of the impact (usually normal impacts) phenomena which involves two bodies (usually sphere-sphere or sphere-surface) made from a ductile material that has a defined yield load. In this case the deformation of the bodies plays a key role during contact and determines the result of the impact. Figure 2.3 depicts two deformations that occur during the particle impact: particle deformation and surface deformation.

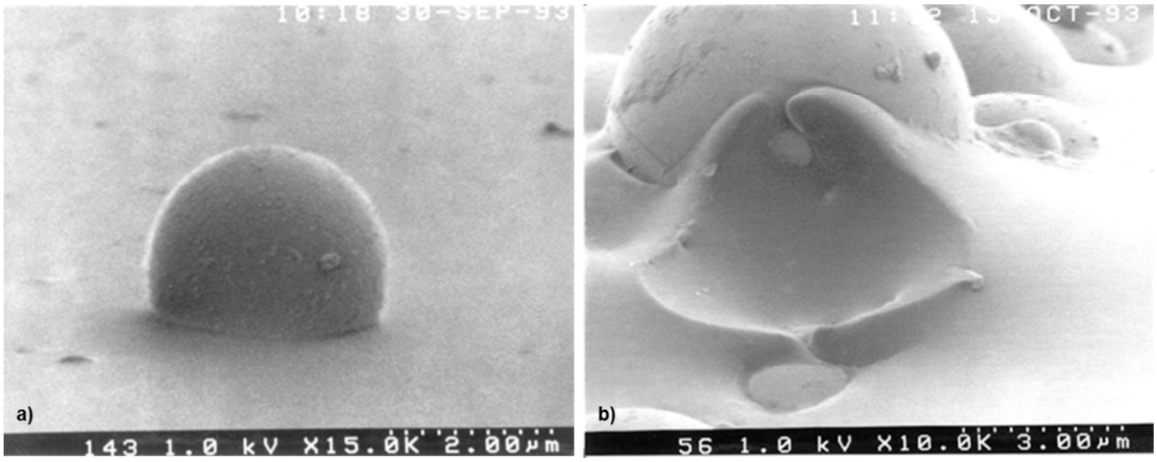

Figure 2.3 – Example of adhesion induced deformation: a) particle deformation, b) surface deformation

Starting from the Hertz's theory, numerous models have been proposed. Hamaker (1937), proposes that surface forces were related to the density of atoms in

the particle and substrate. Derjaguin *et al.* (1975) developed the Hamaker's model through the use of the Hertz's theory and in this way they proposed an equation that link the contact radius with the particle size. Krupp (1967) proposes adhesion-induced plastic deformations. He proposed that the adhesion induced stresses between a particle and a substrate could exceed the yield strength of at least one of the contacting materials.

One of the major contributions to this field has been provided by Johnson *et al.* (1971). The Johnson, Kendall and Roberts (JKR) theory recognized that both tensile and compressive interactions contribute to the total contact radius. The JKR model describes the phenomena that occurs between two bodies in contact demonstrating that even if there is not an external force maintaining two bodies in contact, there is a well-defined contact area at the body interface and it requires a force greater than zero to separate it.

Based on JKR model, Muller *et al.* (1980) propose a general model that take into account the particle size and material. In particular they pointed out that the JKR are suitable for larger particle, lower modulus, higher surface energy while the Derjaguin-based (1975) model is more suitable for small particle, high modulus and low surface energy systems due to the tensile interaction. Finally Maugis and Pollock (1984) generalize the JKR theory to include adhesion-induced plastic deformations.

Thorton and Ning (1998), have formulated a model of rebound/adhesion which takes into account impact velocity, capture velocity and yield velocity. Capture velocity represents the particle velocity limit below which contact becomes adhesion and above which contact becomes rebound. Yield velocity represents the material particle velocity limit below which impact can be considered elastic and above which a plastic deformation occurs in the contact zone. Yield velocity is a function of the materials (Young's module, Poisson's ratio and density). The authors also performed a study on the influence of the energy at the interface and demonstrated that for the highest velocity impact the energy interface does not affect the bounces characteristics. Confirming the relationship between the particle size and the attraction force, Heim and Blum (1999) by using the principles of atomic force microscopy (AFM), measured directly the adhesion and rolling-friction forces between individual silica microspheres of radii between 0.5 μm and 2.5 μm. It showed that the linear dependence of the pull-off force on the particle radius is still valid for micron-sized particles as reported in Fig. 2.4.

Unfortunately, most of the models and the results reported in literature do not provide a full understanding of the adhesion phenomena which is responsible for the fouling mechanism. This limit is largely due to: (i) different particle sizes, (ii) different material characteristics (some particle materials do not show the elastic yield limit) and (iii) the different impact velocity. In fact, if the model reported in

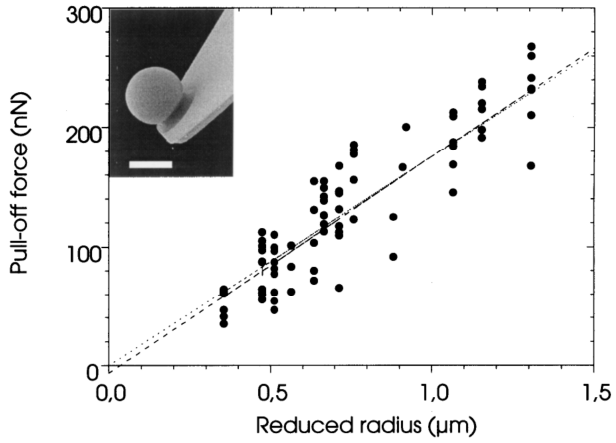

Figure 2.4 – Pull-off force versus reduced particle radius obtained from direct force measurements between silica microspheres (Heim and Blum , 1999)

Thorton and Ning (1990) is applied to a metallic micro-sized particle with Young's Module equal to 72 GPa, Poisson's ratio equal to 0.17 and a surface energy equal to 0.2 J/m^2, the capture velocity is approximately 1 m/s. By using these results for fouling phenomena and considering that the sub-micrometric and micrometric particles follow the streamline with a velocity of about 350 m/s, all of these particles must bounce on the blade surface and the fouling phenomena would not exist. For this reason, in the following paragraph, some experimental results are reported in order to better approach the fouling phenomenon.

To recap the different behavior of the particle-surface impact, an useful summary was proposed by Klinkov *et al.* (2005). Figure 2.5 shows the relationship between particle size and impact velocity.

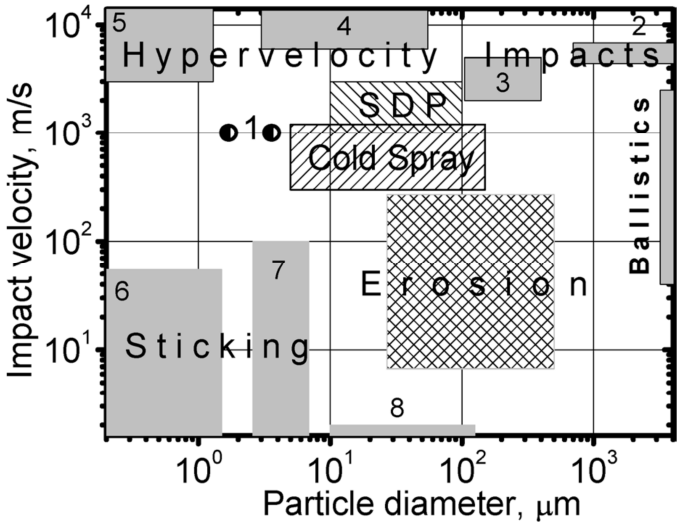

Figure 2.5 – Particle impact on a solid surface: Influence of impact velocity and particle size on features of the interaction. Regions characteristic of certain impact phenomena are shown (Klinkov *et al.*, 2005)

The classification is based on two important dimensional parameters: (i) impact velocity and (ii) diameter of impinging particles (size of a particle). Regions characteristic of certain impact phenomena, according to the Fig. 2.5, could be identified as (Klinkov *et al.*, 2005):

- low-velocity impacts: at low impact velocities (from 1 m/s to 100 m/s) small particles (from 0.1 μm to1.0 μm) can stick to the surface after impact. Adhesion is governed by van der Waals and electrostatic forces. Sticking is characterized by two critical velocities: (i) if the impact velocity is below the first critical velocity, particles are collected by the surface and (ii) if the impact velocity is above the second critical velocity, impinging particles rebound. In the intermediate range there is a probability of sticking (or rebound) of particles, which depends on the impact velocity. Larger particles (so called macro-particles, from 1 mm to 10 mm) impinging with velocities up to about 40 m/s on semi-infinite solid bodies typically rebound from the surface without disintegrating but leaving plastic prints on both the particle and the impacted surface. Rebound happens because some part of the initial kinetic energy is stored as elastic energy in the interacting bodies, and then transferred back into kinetic energy of the rebounding particle;
- ballistic impacts: when the impact of macro-bodies (from 1 mm to 10 mm) occurs at higher velocities (in the range of approximately from 50 m/s to 3,000 m/s) this corresponds with ballistic impacts. Due to the high kinetic energy, values of plastic strain and strain rate considerably increase during the impact;
- hypervelocity impact: at impact velocities greater than 2,000 m/s stresses arising in bodies on impact considerably exceed the yield point of materials. Under these conditions solids behave like liquids. Locally, arising flow velocities are comparable to and can exceed the sound speed of the material. Hypervelocity impacts of micro-bodies have extensively been studied in connection with orbital debris impact damage and in order to simulate large scale impacts on a small scale in the laboratory;
- super-deep penetration: particles of a hard powder have been accelerated up to velocities of about (1 – 3) km/s and interact with a metal body some particles of diameters up to 100 μm penetrate far into the metal body;
- erosion: at moderate and low impact velocities (from 5 m/s to 300 m/s) a repeated impact of intermediate-sized particles (in the range from 30 μm to 500 μm) on the same part of a surface results in an erosion (deformation and destruction of the surface causing a loss of mass);
- cold spray: when particles impinge on a surface at intermediate velocities of about (400 – 1,200) m/s they can become strongly attached to the surface generating the cold spray deposition practice (Alkhimov *et al.*, 1990 and Alkhimov *et al.*, 1992). The essence of the phenomenon is that particles of ductile metals or alloys, having diameters of approximately in the range (10 – 100) μm, become deformed and strongly attached to a surface when they

impinge on the surface of metals, ceramics or glasses at impact velocities in the range of about (400 – 1,200) m/s. In this manner coatings can be formed on a substrate. The substrate formation is a function of: material, impact velocity, temperature and impact angle. Exist a minimum critical velocity necessary to achieve the deposition, because sufficient kinetic energy must be available to plastically deform the solid material (Dykhuizen and Smith, 1998).

Alkhimov *et al.* (1990) reported the influence of velocity and materials on the deposition efficiency. The dependence is depicted in Fig. 2.6 where it is clearly visible the critical velocity after that the deposition efficiency rapidly increase. Different materials show different deposition efficiency as a function of the particle velocity due to the its hardness and yield strength.

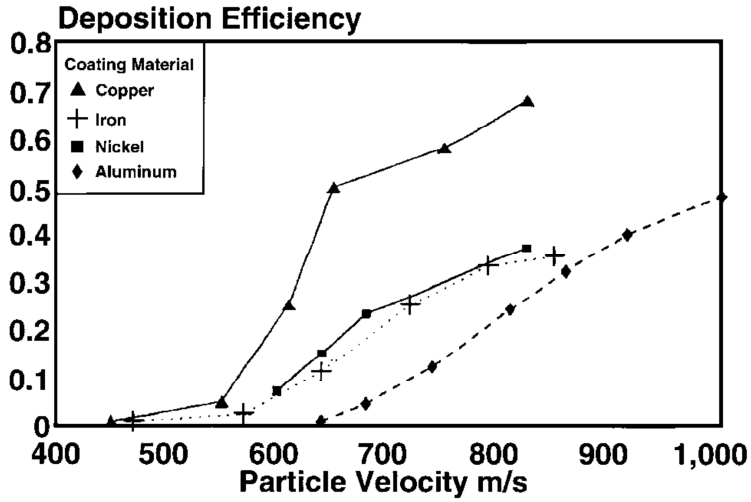

Figure 2.6 – Deposition efficiency versus particle velocity

2.2 Experimental applications

Different types of effects and testing techniques that provide information on the forces between particles and surfaces. Figure 2.7 reports a wide overview of the adhesion conditions (Tomas, 2006).

As reported in Fig. 2.7, the adhesion effects could be summarized as:

a) adhesion measurements (practical applications: xerography, particle adhesion, powder technology and ceramic processing);
b) peeling measurements (practical applications: adhesive tapes, materials fracture and crack propagation);
c) direct measurements of force as a function of surface separation (practical applications: testing theories of intermolecular forces);

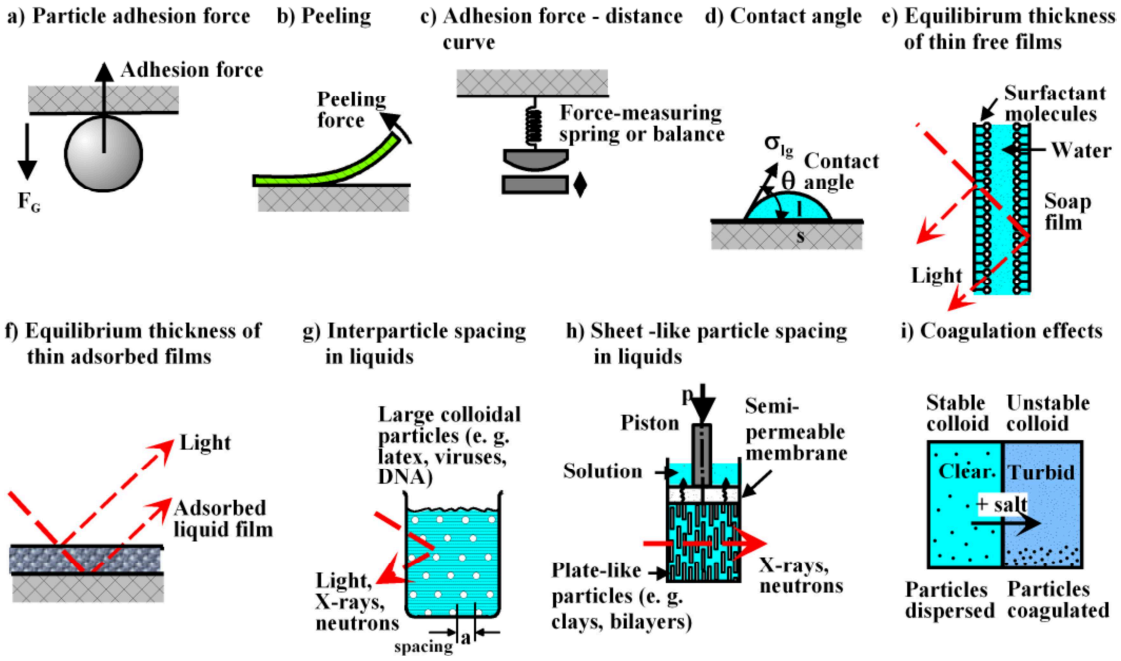

Figure 2.7 – Adhesion effects between particles and surfaces by intermolecular forces (Tomas, 2006)

d) contact angle measurements (practical applications: testing wettability and stability of surface films, detergency);
e) equilibrium thickness of thin free film (practical applications: soap films and foams);
f) equilibrium thickness of thin adsorbed films (practical applications: wetting of hydrophilic surfaces by water, adsorption of molecules from vapor, protective surface coatings and lubricant layers, photographic films);
g) interparticle spacing in liquids (practical applications: colloidal suspensions, paints and pharmaceutical dispersions);
h) sheet-like particle spacing in liquids (practical applications: clay and soil swelling behavior, microstructure of soaps and biological membranes);
i) coagulation studies (practical application: basic experimental technique for testing the stability of colloidal preparations).

Since these adhesion effects, exist some principles of measuring the adhesion force, which are based in applying external force on the particles. Figure 2.8 summarize these principles reported by Gotoh *et al.* (1997).

The interacting force between two microscopic bodies is measured by the spring balance method as a function of the elongation of the spring when they are separated. In the centrifugal method, the plate on which particles are deposited is put on a centrifuge to press particles on the surface by a compressive force and after this so-called contact pre-consolidation, to detach the particles. The centrifugal force where half of the deposited particles are removed is measured to evaluate the average adhesion force. When one turns the plate perpendicular to the axis of

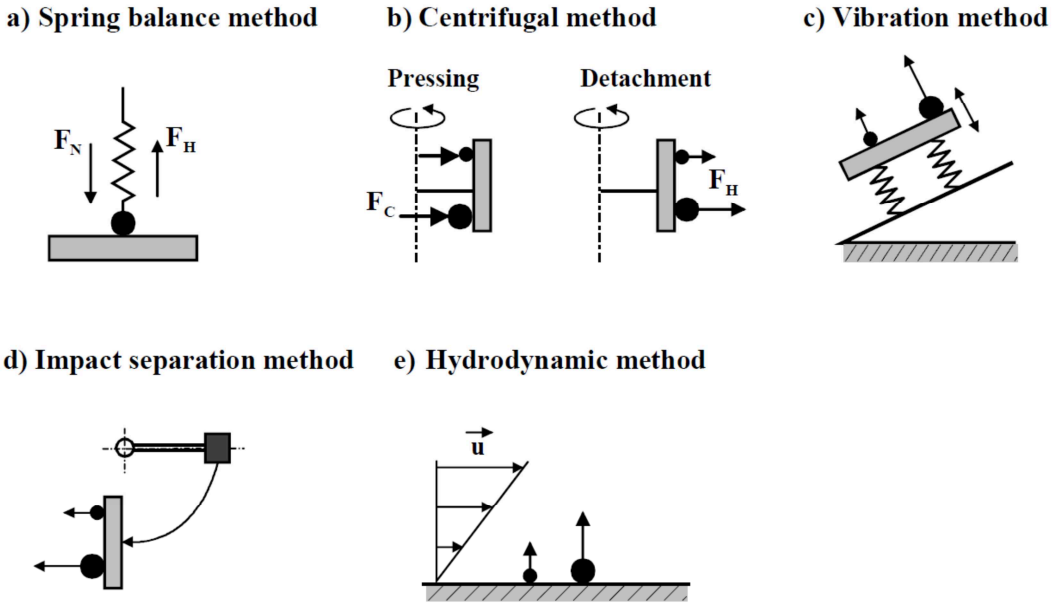

Figure 2.8 – Testing the adhesion force between particle and surface (Gotoh *et al.*, 1997)

revolutions, the tangential or shear force distribution of the contacts can be measured by the cumulative mass fraction of detaching particles. The vibration method is based on particle detachment from a vibrating surface caused by its inertia at a certain acceleration. Thus, the vibration does not only yield a detachment or pull-off force to compensate the adhesion force, but also causes compressive normal forces between particles and surface of the same order. The impact separation method uses an acceleration generated by the bullet or hammer impact. When a fluid flow field is applied to particles adhered on a plate, the particles suffer a force caused by the flow. At a certain flow velocity, particles start to detach from the plate. Then, the adhesion force can be obtained as a function of flow velocity and/or stress.

One of the most important experimental reports was provided by Wall *et al.* (1990). The authors have performed a number of experiments with ammonium fluorescein microspheres (with diameters equal to 2.58 µm, 3.44 µm, 4.90 µm and 6.89 µm) impacted normally against smooth, flat surfaces of polished molybdenum, silicon, cleaved mica and a fluorocarbon polymer over an initial velocity range of (1 – 100) m/s. The main results shown in this work can be summarized as follows: (i) at low velocity (< 20 m/s), the ratio of rebound to impact velocity was sensitive to target material, decreasing with impact velocity due to the adhesion surface energy, (ii) the kinetic energy recovered in low velocity impacts was found to depend on particle size, (iii) no such particle size dependence was observed for impact velocities near 20 m/s and (iv) above 40 m/s, the velocity ratio was insensitive to the target material, indicating that the particle has a lower elastic yield limit than the material target. Finally, the authors have highlighted that the plastic deformation was a significant component of energy loss at all impact velocities and the knowledge of

interface energy plays a key role for the proper description of particle impact.

By using the results reported by Wall *et al.* (1990) and Brach and Dunn (2007) developed a model for the low velocity impact of microspheres with surfaces based upon classical impact dynamics and Hertzian theories. A unique feature of the model is that energy losses due to material deformation are included through the use of the coefficient of restitution. The authors pointed out that the nature of rebound depends not only on the usual effects (restitution and adhesion), but also on the approach angle, the friction coefficient and its effect on the impulse ratio (which depends upon whether or not sliding ends before contact ceases).

Not only the particle size and material influence the results of the impact, but also the surface roughness and the particle asperity play an important role. As reported by Adi *et al.* (2013), the particle slip is related to the surface roughness. Greater roughness causes more slip resistance and therefore easier adhesion or easier breaking away of particles. Results showed that the impaction causes significantly better deagglomeration in corrugated particles than smooth particles.

Abd-Elhady *et al.* (2006) through use of laser measurement tecniques, showed the interaction of an incoming micron particle with already deposited particles. This aspect is an important factor in fouling phenomenon. By using a numerical model, validated by experimental results, they found that the time required for a particle to be ejected out of a bed of particles due to an incident particle impact is proportional to the interacting particles diameter and to the square root of the number of bed layers (Fig. 2.9). As reported in Fig. 2.10, there are velocity regimes at which the incident particle sticks, bounces off or removes particles from the bed of particles. The regimes overlap due to the impact angle effect. The effect of particle removing by incident particle are reported in Fig. 2.10.

Some very interesting results and detailed analysis of micro-particle adhesion can

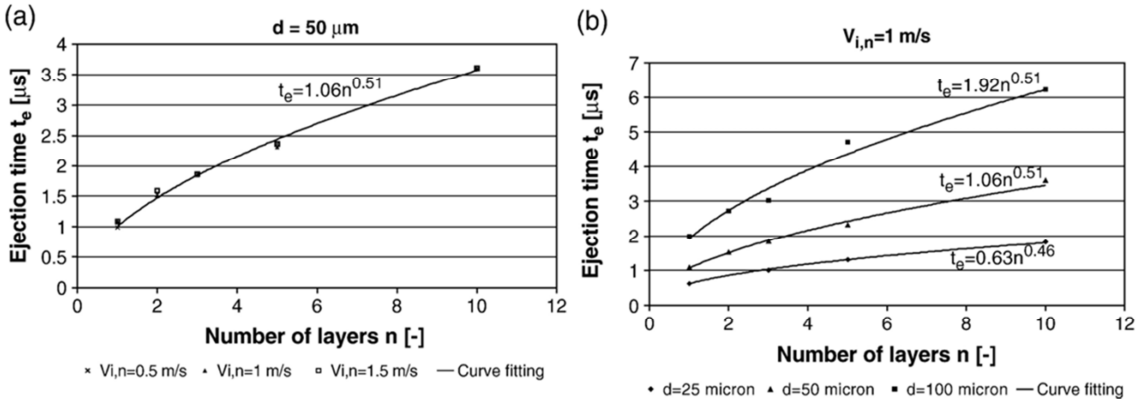

Figure 2.9 – The ejection time for an orthorhombic bed of copper particles due to an incident particle as a function of number of bed layers and (a) incident particle diameter or (b) impact speed. The bed's particles and the incident particle are made of the same material and are of the same size (Abd-Elhady *et al.*, 2006)

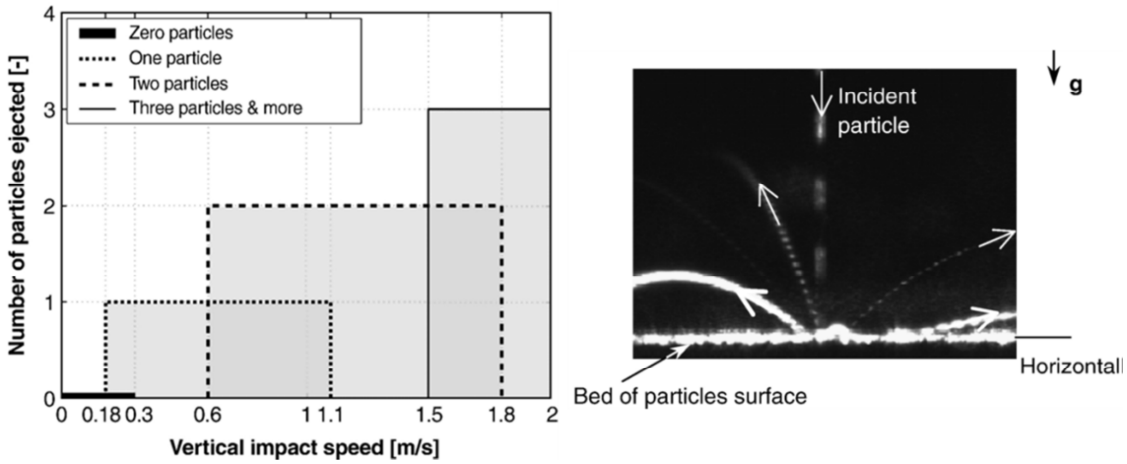

Figure 2.10 – Particle falling vertically onto a bed of particles and ejecting particles out of the bed (Abd-Elhady *et al.*, 2006)

be found in astrophysics applications related to the research of pre-planetary dust dynamics. The particles, in most cases consisting of sub-micrometric silica spheres, are the basis of the planets' origin. These space-dispersed particles collide with each other and if the impact allows for adhesion, the particles generate an agglomerate. The difference between these mechanisms, not yet fully understood and the fouling phenomenon, is due to the type of motion. In fact, the pre-planetary particles move in cosmic space, characterized by high Knudsen numbers (molecular motion), while in the case of fouling, and more generally of motions in the Earth's atmosphere, the transportation of the particles takes place with very small Knudsen numbers (viscous motion). This aspect must not diminish the importance of the results highlighted in this research field because the experiments are conducted only in some cases under vacuum and the results are often in line with the more classical theories mentioned above. The uniqueness and usefulness of these studies is that the particle velocities, materials and dimensions are in the same range as those responsible for the fouling phenomenon.

In this field of research, Poppe *et al.* (2000) proposed one of studies closest to the fouling phenomena. They have reported an experimental evaluations of perfectly spherical and irregular particles impacting a smooth surface (smooth as the particle surface). Figure 2.11, reports the silica spherical particles and the irregular small silicon carbide grains shapes. Different combinations of particle size and materials have been tested. The particle diameters are very close to 1 μm and in some cases the experiments were conducted with sub-micrometric particles. The material (silica in some cases) has a density of about 2,000 kg/m^3.

The major results reported by Poppe *et al.* (2000) can be summarized as follows:

- for impact velocities in the range (1 – 10) m/s, the kinetic energy is typically

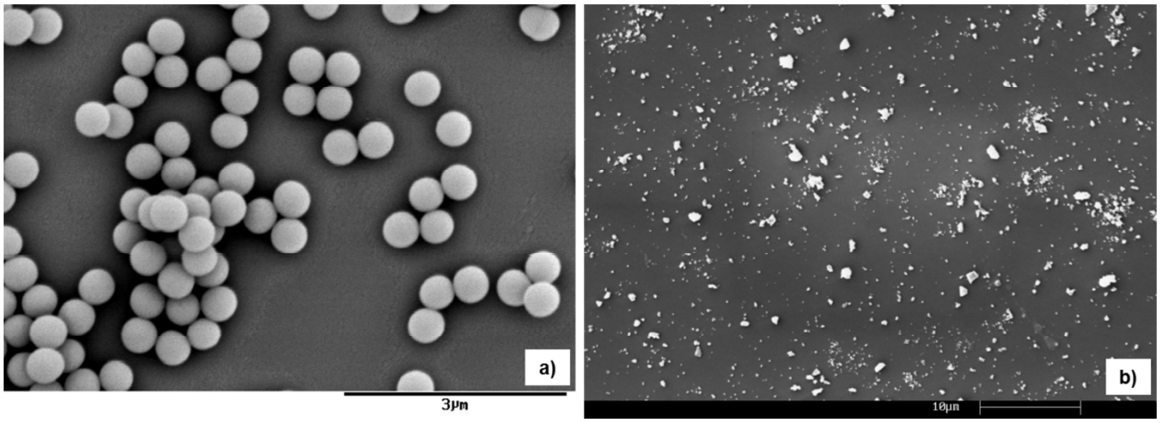

Figure 2.11 – SEM pictures: a) silica dust and b) irregular small silicon carbide grains (Poppe *et al.*, 2000)

reduced to one-half for the 1.2 µm and to one-quarter for the 0.5 µm;
- for impact velocities exceeding 10 m/s, the bouncing collisions reduce the kinetic energy by more than one order of magnitude;
- for the 1.2 µm diameter silica spheres the capture velocity is independent of the target surface tilt angle (0° – 60°);
- electrostatic effects occur during the test and the action of the electrostatic field is observed up to 40 µm from the surface. The same effect can be found in Poppe *et al.* (1997);
- experimental results obtained with irregular shaped particles show a higher capture velocity and, at the same time, a higher sticking probability.

The sticking probability is the one of the most interesting quantities used in this type of study. The sticking probability was evaluated by a statistical approach. It compares the impact that results in sticking with the total amount of impacts. For the sticking probability, the most common threshold limit is equal to 0.5. If more than 50 % of the sampled impact results in sticking between the particle and surface, the final results will be sticking or, vice versa, if less than 50 % of the sampled impact results in sticking, the final result will be bounce. With this approach the authors wish to emphasize that the particle impacts are different from each other and, in order to provide a macroscopic evaluation of the results, a statistic/probabilistic approach is the best way.

The same approach was adopted by Ahluwalia *et al.* (1989). Sticking probability was used to establish the sticking coefficient that relates the sticking probability and the mass of incident particles. The mass of incident particles depends on the particle diameter and density. Therefore, the sticking coefficient, is the mass fraction of incident particles to a surface that are retained on that surface. In this case, the influence of temperature play a key role. Ahluwalia *et al.* (1989) in fact, studied the particle adhesion for the hot turbine section where the particle gas and temperature

are much higher than 1,000 °C. Interesting results are related to the different deposits buildup between suction surface and pressure surface. The authors pointed out that in the deposition dominates (due to high delivery rates) for particle diameters larger than about 1 µm unless sticking fractions for the pressure surface are much smaller than for the suction surface. In fact, the rate of deposit buildup decreases with particles larger than 1 µm because the inertial deposition takes a place on the pressure surface mostly. Pressure surface and suction side surface are affected by different phenomena, such as inertial deposition for the pressure surface and diffusive deposition for suction surface.

Fouling and particle adhesion in the hot section of gas turbine have recently gained attention. Reagle *et al.* (2014), reported a study where Arizona road dust was injected into a hot flow field to measure the effects of high temperature and velocity on particle rebound from a polished 304 stainless steel coupon. The effects of increasing temperature and velocity led to a 12 % average reduction in coefficient of restitution at 533 K (47 m/s), 15 % average reduction at 866 K (77 m/s) and 16 % average reduction at 1,073 K (102 m/s) compared with ambient results. The decrease in coefficient of restitution appeared to be almost entirely a result of increased velocity that resulted from heating the flow. Delimont *et al.* (2014) reported a similar study related to the near-melting particle temperature. In this case, the coefficient of restitution of the particles decreases slightly as some of the particles approach their glass transition point and start to become molten. Other particles, which do not become molten due to different particle composition, rebound and maintain a relatively high coefficient of restitution. The results show an increase in deposition as the temperature approaches the melting temperature of sand. Finally, Mangwandi *et al.* (2007) reported a study on coefficient of restitution related to the molten granulate. The results show a lower bounce capability at high impact velocities and then, low coefficient of restitution values.

From the reported literature, it is easy to understand that for the total comprehension of the fouling phenomena it must be known how the contaminants hit the blade surface. In this context the word how refers to the impact velocity and the impact angle for each particle. This thesis, will report the kinematic characteristics of the particle impact on the axial compressor blades by means of a CFD numerical simulation. For this reason, in the last part of this chapter, an overview of the CFD approaches presented in literature for study the particle motion and adhesion is reported.

2.3 CFD approaches

There are two approaches commonly used to predict gas-particle flows: Eulerian and Lagrangian formulations.

The Eulerian formulation treats both gas and particulate flows as continua and the phases are regarded as two mutually interacting fluids. The main advantage of using the Eulerian method is to make computation fairly economical for flows with relatively high concentrations of particles and for the purpose of engineering designs. In addition, effects of interactions, particularly turbulence, between two phases (two-way coupling) are more easily considered by using the Eulerian approach. However, some difficulties in using the Eulerian method exist in the prediction of particle erosion and deposition because the Eulerian approach gives mean values of the particulate phase over a small control volume where both incident and reflected particles contribute to this mean value near wall surface.

In the Lagrangian formulation, the motion of a single particle is considered and relevant variables are calculated along the particle trajectory. Lagrangian method emphasizes the individual behavior of each particle and determines particle trajectories based on the equation of motion. One disadvantage of this approach is that it is computationally expensive for engineering applications because of the great number of particles which are required to determine the average behavior of the relatively high particle loading. The Lagrangian formulation, however, is a more fundamental procedure to describe the particle-wall collision process and can yield a detailed physical description of individual particle motion. Lagrangian method is found to be efficient in simulating dilute two-phase flows where the particle to fluid volumetric loading ratio is very small. In the Lagrangian approach, the airflow field is first simulated as a Eulerian phase, and then the trajectories of individual particles are tracked by integrating a force balance equation on the particle (drag and lift forces due to the particle size, shear stress, rotation, diffusion and flow temperature). A vast amount of information can be extracted from this type of simulation due to its discrete and instantaneous treatment of particle motion.

Results reported by Lee *et al.* (2002) show that both approaches are successful in predicting the main features of particulate flow near wall, however, the Eulerian approach is much less expensive than the Lagrangian approach in obtaining the flow solution of impacting particles. The particulate flow predictions using both approaches have been applied for predicting tube erosions: good agreement between predictions using the two approaches and between the predicted and measured erosion results are observed.

Regarding the evaluation of the possibility to study and simulate the Lagrangian phase with a one-way or two-way coupling method, Gupta and Pagalthivarthi (2006) demonstrated through the use of experimental results that the CFD numerical simulation with an Eulerian-Lagrangian one-way coupling strategy well fit with the experimental data. This evidence allow the simplification of the numerical problem reducing the computational efforts.

One of the main mechanisms that control particle movement is the turbulent diffusion by which the particles in the turbulent boundary layer migrate to the surface under the influence of random flow fluctuations. Theoretical approaches to particle dispersion use random walk models to represent the effect of turbulent fluctuation velocity on particle movement. As a consequence, the turbulence model has a significant effect on the particle trajectory. As reported in the previous paragraph, particle sticking probability depends upon the particle impact velocity. Moreover, the wall shear stress that is calculated from the turbulence model is the main cause of particle detachment from the surface and smaller particles tend to accumulate in the near-wall region due to the damping of fluid turbulence provided by wall function. For these reasons some authors focus their study in modeling the interaction between the particle motion and the turbulent models.

Tian and Ahmadi (2007) report an extensive sensitivity analysis of the relationship between the turbulence models, mesh refinement close to the wall and particle dimensions expressed by the non-dimensional particle relaxation time τ^+. Tian and Hamadi (2007) highlighted the effect of a different turbulence model on the velocity deposition for particles in a horizontal and vertical tube. Their study has shown that the *k-ε* with STandrad Wall Function (STW) turbulence model over-predicts the deposition velocity for particles in a *Brownian* ($\tau^+ < 10^{-2}$) and *transition* ($10^{-2} < \tau^+ < 10$) region and it does not allow the estimation of the real trend of the particle velocity deposition. For the *inertial* ($\tau^+ > 10$) region, the *k-ε* STW turbulence model over-predicts the deposition velocity but in a minor way compared to the other regions and the trend of the deposition velocity curve is in agreement with the other results. This results can be obtained if the dimensionless wall distance y^+ is higher than 5. Quite different results was reported by El-Batsh and Haselbacher (2000). The authors concluded that the STW should not be used when solving the flow field near the wall for particle deposition. However, in this case, the dimensionless wall distance y^+ is less than 2 in each point of the numerical model. This difference with respect to the results reported by Tian and Hamadi (2007) explain the differences in the final results and observations. A comprehensive review related to the transport and deposition of particles in turbulent and laminar flow is performed by Guha (2008). Guha (2008) reports also the influence of the surface roughness on the predicted deposition rate. The surface roughness is in some case neglected, but, as reported by Guha (2008) in the case of particle with low non-dimensional relaxation time the values of surface roughness play a key role in the deposition rate values.

Vortex phenomena, due to obstacles, or more in general, due to the flow deviation influence the particle deposition. Studies relates to these effects are widespread in literature. For example, Song *et al.* (2013) studied the particle deposition in a bent shape tube while Zhang and Chen (2006) studied the particle transport and distribution in ventilated rooms. Particle tracking and more in general Lagrangian

approach can studies a wide range of problems.

In the case of high temperature of the phases (gas and particles), the coefficient that drive the Lagrangian model must be calibrated for each application. Casaday *et al.* (2014) studied the effect of hot streaks on deposition in a high pressure turbine vane passage by experimental and computational method. A computational model was developed to simulate both the flow and deposition. The critical viscosity model was used to determine particle sticking upon impact with vane surfaces. Computational simulations confirm the migration of the hot streak and locations susceptible to enhanced deposition. Results show that the deposition model is overly sensitive to temperature and can severely overpredict deposition.

Brun *et al.* (2012) developed a CFD-empirical software tool that allows a probabilistic analysis of the kinematic and impact behavior of solid particulates in the near-field of turbomachinery blades and impellers surfaces. The method and tool employ a commercially available CFD solver to calculate the machine's steady-state flow field. The model then uses the output to determine a set of non-dimensional coefficients in a set of empirical functions to predict the statistical probability of a given weight and size or distribution of solid particles, impacting on a specified rotating or stationary surface. The method was tested by using experimental data obtained through PIV techniques. The authors highlighted the importance to use a probabilistic approach for particle analysis: zone with highest probability of particle impact will be more affected by erosion or fouling phenomenon.

Chapter 3

Numerical Models: Eulerian and Lagrangian Phases

In this chapter the numerical models of compressor rotors are reported. Details related to rotor compressor geometries, computational meshes, boundary conditions and compressor rotors performance are presented. All the parameters used for modeling the Eulerian and Lagrangian phase can be found in this chapter.

3.1 Geometries and numerical domains

The geometry and performance of the transonic rotor were taken from Reid and Moore (1978). The NASA Rotor 37 is a transonic rotor test case chosen for this analysis. Rotor 37 is composed of 36 multiple circle arc blades and the tip clearance at design speed is 0.356 mm (0.45 % of the blade span). The hub to tip ratio is equal to 0.705. The transonic rotor is studied at its nominal rotational speed equal to 17,188 rpm and the peripheral velocity at the blade tip is equal to 454 m/s that corresponds to a rotor tip Mach number equal to 1.34. Figure 3.1 reports the rotor blade geometry and three representative airfoils at hub, mid-span and blade tip. The airfoil shape is characterized by very thin leading edge and the airfoil at the blade tip is characterized by a very low curvature of the mean line.

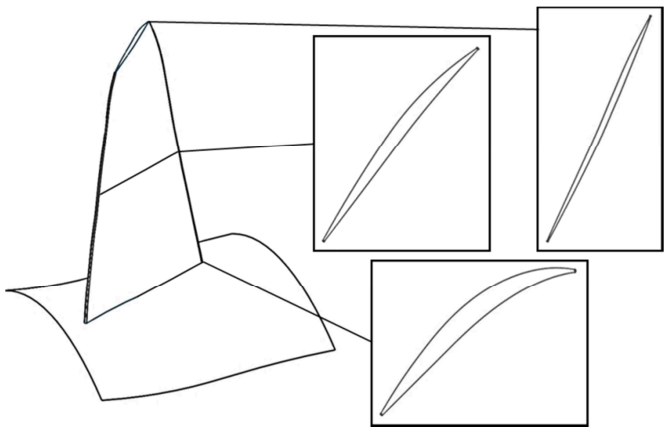

Figure 3.1 – CAD geometry of the NASA Rotor 37

The subsonic rotor is the first stage of a multi-stage axial compressor used in an industrial application. Subsonic rotor is composed of 31 blades. The hub to tip ratio is equal to 0.739, while the tip clearance is 0.382 mm (0.45 % of the blade span). The subsonic rotor is studied at the nominal rotational speed equal to 6,054 rpm and the peripheral velocity at the blade tip is equal to 206 m/s that corresponds to a rotor tip Mach number equal to 0.62. Figure 3.2 reports the rotor blade geometry and three representative airfoils at hub, mid-span and blade tip. The airfoil shape is characterized by thicker leading edge compared to the transonic one. From hub to blade tip the airfoil shape change in minor way with respect to transonic rotor.

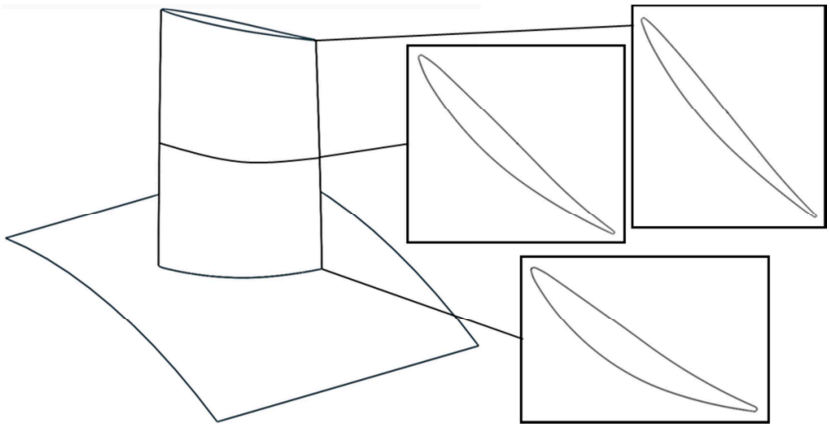

Figure 3.2 – CAD geometry of the subsonic rotor

All the simulations are performed in a steady multiple frame of reference in order to take into account the contemporary presence of moving and stationary domains. The rotating and stationary frames are coupled using a frozen rotor interface with the appropriate frame transformation occurring across the interface. The numerical domain is composed by three domains: two stationary domains (inlet and outlet duct) and one rotating domain (rotor). For each numerical domain only a single passage vane was modeled as can been seen in Fig. 3.3.

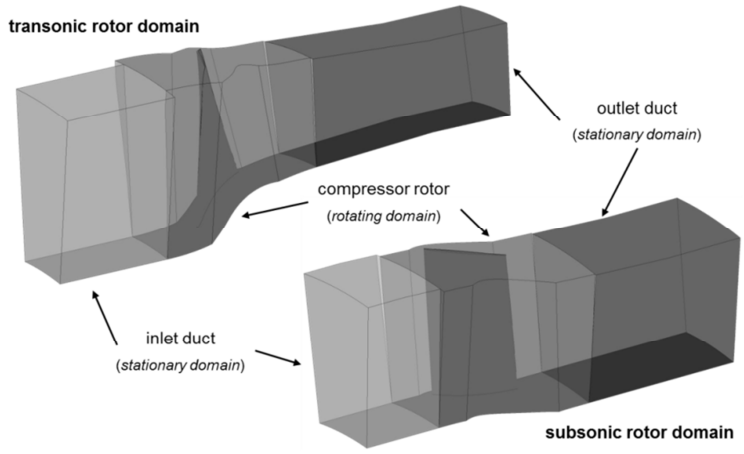

Figure 3.3 – Numerical models

The meridian flow-paths are reported in Fig. 3.4. Since only the rotor section is under investigation, the meridian flow-paths was design in order to allow the easy implementation of the Lagrangian phase. Figure 3.4 reports the flow-paths for both rotors whit the dimension of the inlet and outlet duct in terms of blade chord. Meridian flow-paths show that Rotor 37 has both endwalls (hub and shroud) that develop along the streamwise direction with different diameters, while for subsonic rotor, the endwall hub develops at constant diameters.

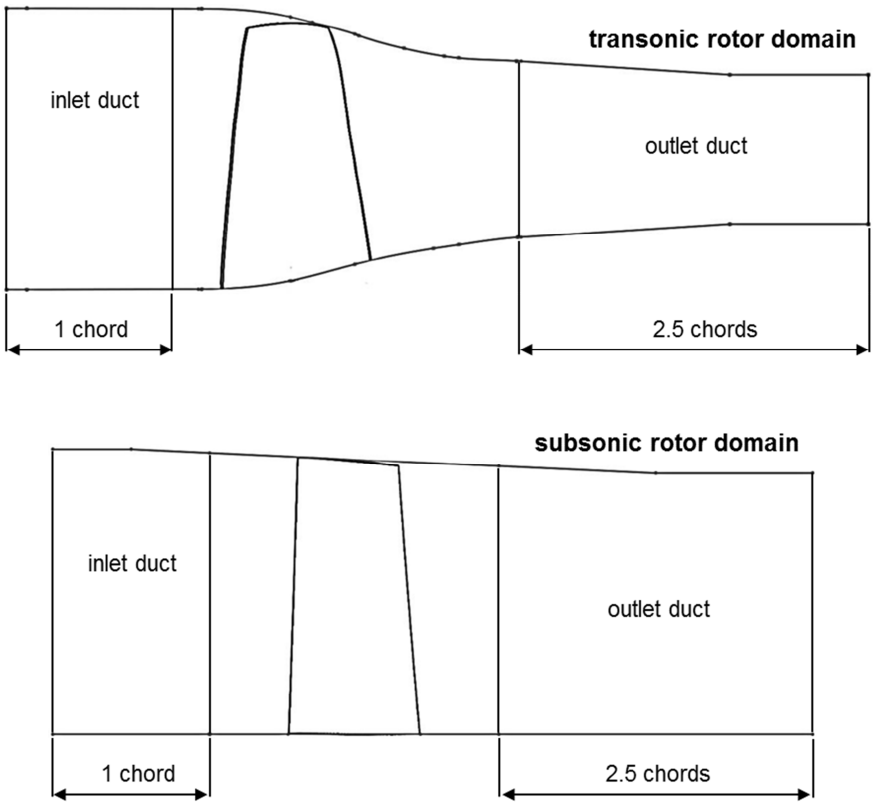

Figure 3.4 – Meridian flow paths

3.2 Meshes

For the transonic rotor, a multiblock hexahedral grid with a total number of 1,131,063 elements is used with refinements in the vicinity of the leading and trailing edges of blade, near hub and shroud and in tip clearance. Figure 3.5 depict the mesh on the blade surface with the aforementioned refinements in the vicinity of the leading edge and of the hub. Regarding the near walls, the nodes are positioned in such a way that the values of y^+ are within 5 – 65.

For the subsonic rotor, the same strategy is adopted. A multiblock hexahedral grid with a total number of 1,007,800 elements is used. Figure 3.6 depict the mesh used

in this analysis. Mesh refinements can be found in the vicinity of the leading and trailing edges of blade, near hub and shroud and in tip clearance. Regarding the near walls, the nodes are positioned in such a way that the values of y^+ are within 5 – 71.

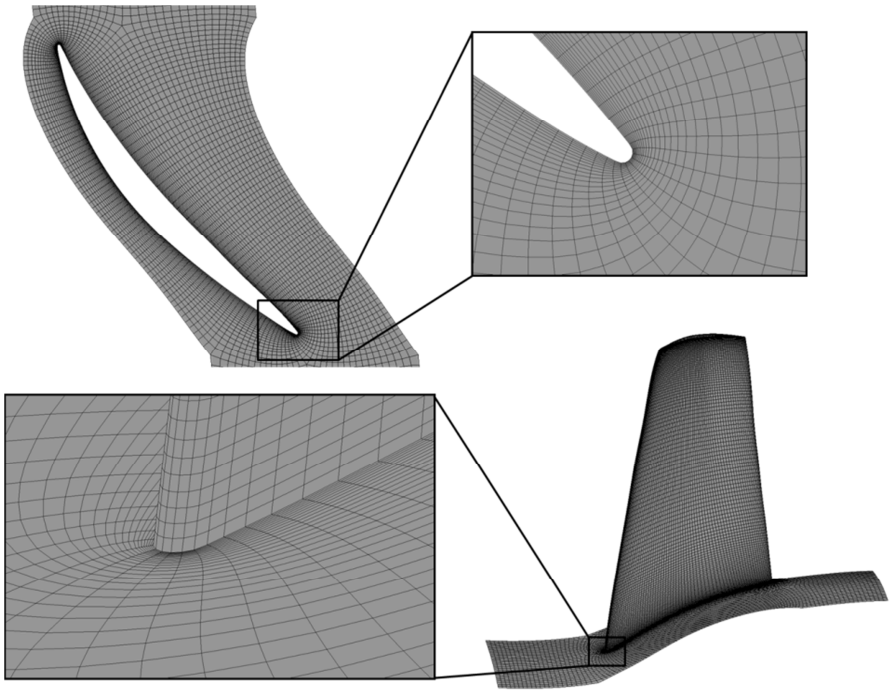

Figure 3.5 – Transonic rotor mesh

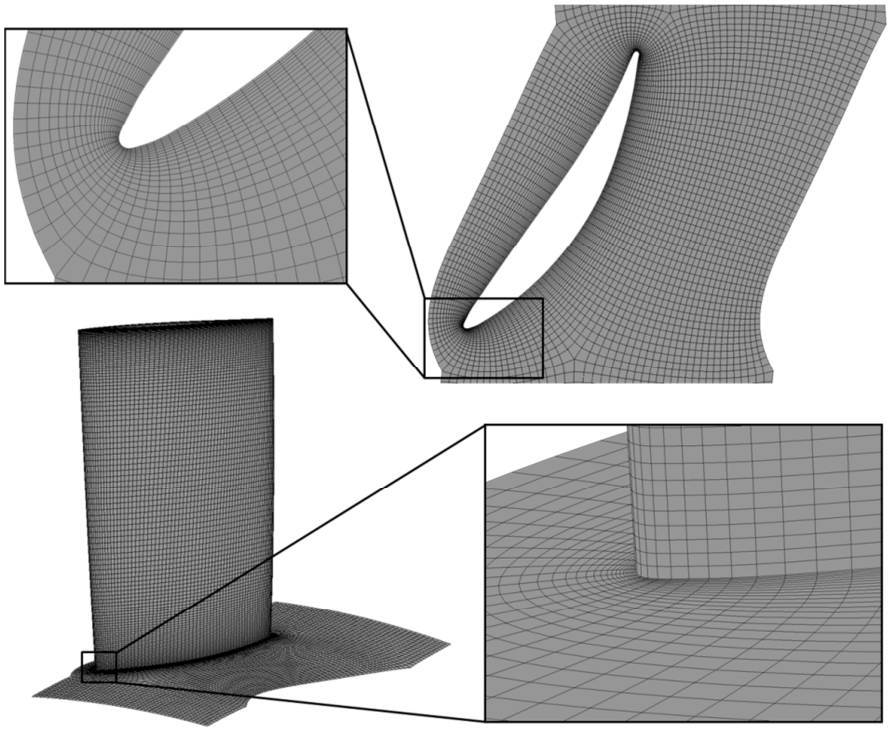

Figure 3.6 – Subsonic rotor mesh

The last mesh feature is related to the node distribution at the inlet of the numerical domain. The inlet surface mesh (inlet duct) has every single element with the same size in order to guarantee a uniform node distribution on the surface. The uniform distribution of grid nodes allows the realization of a uniform particle injection from this surface. The particles in fact, will be released from the node of the inlet surface and only the uniform node distribution can ensure the uniformity of the particle distribution. Thanks to this arrangement, the particle impact concentration and deposition that will detected on the blade surfaces will be due only to the fluid dynamic phenomena and the blade shape. For the transonic rotor, an inlet surface mesh of 1,888 hexahedral elements was created while, for the subsonic rotor, an inlet surface mesh of 2,596 hexahedral elements was created. Figure 3.7 reports the inlet surface meshes. The differences in the number of node will be compensate by the proper number of injected particles. Further information will be reported in the next chapter. The injection surface (inlet surface) is positioned at about 1.5 chords far from the rotor in both numerical domains.

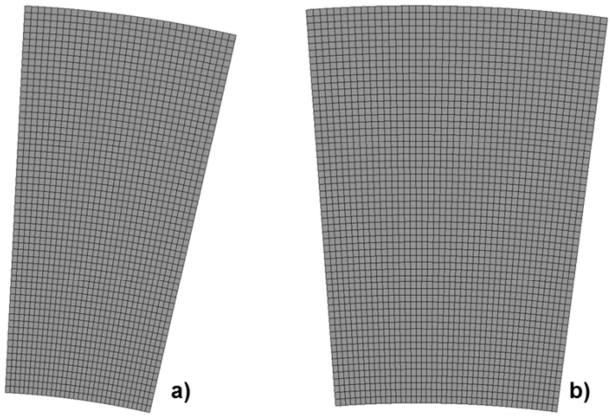

Figure 3.7 – Inlet surface meshes: a) transonic rotor (1,888 elements), b) subsonic rotor (2,596 elements)

The computational meshes used for transonic and subsonic rotor are comparable in terms of mesh refinement and element distribution along the domain allowing the direct comparison of the results. In the next chapter, the size of the mesh element on the blade surface is evaluated compared to the particles track in order to ensure the best representation of the particle impact on the blade surface.

3.3 Eulerian phase set-up

The numerical simulations were carried out by means of the commercial CFD code ANSYS Fluent 13.0 (2012). The code solves the 3D Reynolds-averaged form of the Navier-Stokes equations by using a finite-element based finite-volume method. An implicit Roe-FDS formulation was adopted with a Green-Gauss Node Based

spatial discretization.

For both rotors, the total pressure, total temperature and flow angle were imposed at the inflow boundary. The inlet total pressure and total temperature were imposed at 101,325 Pa and 288.15 K, respectively. An relative static pressure p_2 was imposed at the outflow boundary, both in the near-choked flow region and in the near-stall region. The outflow pressure was progressively increased (from near-choked flow region to near-stall region) in order to perform the entire performance trends.

Since only a section of the full geometry has been modeled, rotational periodic boundary conditions were applied to the lateral surfaces of the flow domain. Since the inlet surface mesh is built by an uniform node distribution, it does not provide the node refinement in the flow region close to the endwalls (hub and shroud) of the inlet duct. For this reason, for the hub and shroud surfaces of the inlet duct, a free-slip condition (wall shear stress equal to 0 Pa) was imposed.

For the analyses reported in this work, the standard k-ε turbulence model with a STandard Wall function (STW) is used. As reported above the turbulence model play a key role in the particle deposition analysis and further analysis will be reported in the following chapters according to the literature data and results reported in the Chapter 2. For the solution step, a secondo order Upwind scheme was chosen for the flow solution, while a first order Upwind scheme was adopted for the turbulence terms.

3.4 Eulerian solution and performance of the compressors

In order to ensure an adequate CFD analysis the numerical models should be validated against experimental performance data. For the transonic rotor the experimental performance data is taken from Reid and Moore (1978). Figure 3.8a reports the trend of compression ratio β and total-to-total efficiency η_{TT}. It can be noticed that the shape of both the experimental performance maps is correctly reproduced by the numerical code. The numerical values are in fairly good agreement with the experimental data. The numerical pressure ratio and the total-to-total efficiency always underestimate the experimental data but in a very consistent way. The deviation in terms of mass flow rate at the choked-flow condition is about 1.87 %. Since the aim of the validation was to obtain a compressor model, the numerical model can be considered reliable. Regarding the subsonic rotor, no experimental data is available. Considering that the subsonic numerical model and its set-up is realized in agreement with those provided for the transonic rotor, it can be state that also the CFD numerical solution obtained for the subsonic rotor is suitable for the aim of the study. Figure 3.8b reports the numerical performance trends of the subsonic rotor.

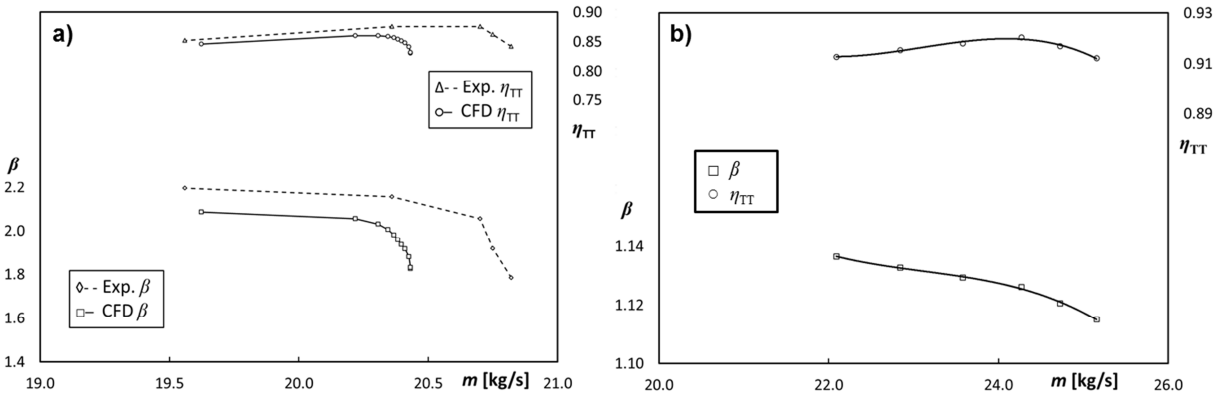

Figure 3.8 – Performance: a) transonic rotor with the comparison between experimental data taken from Reid and Moore (1978), b) subsonic rotor

Figures 3.9 and 3.10 report the overall fluid dynamic phenomena that characterize the transonic rotor operation. Figures depicted the velocity field and wall shear stress at the best efficiency point, characterized by an pressure coefficient Ψ = 0.431 and a flow coefficient Φ = 0.427. In details, Fig. 3.9 reports the velocity field in the blade-to-blade view for different blade span. Clearly visible is the shock wave that occurs in the blade passage vanes, after which the velocity fall down and the flow separation (blue area close to the suction side of the airfoils) takes a place. In the leading edge zone the velocity field is characterized by local normal shock waves due to the local curvature of the airfoil (Cumpsty, 1989) that determines the reduction of the velocity to zero (stagnation point). Fig. 3.10 reports the wall shear stress for suction and pressure side. The flow separation in the suction side determines a reduction of the wall shear stress (blue areas in the second part of the airfoil chord).

Figures 3.11 and 3.12 report the overall fluid dynamic phenomena that characterize the subsonic rotor operation. Figures depicted the velocity field and wall shear stress at the best efficiency point, characterized by an pressure coefficient Ψ = 0.310 and a flow coefficient Φ = 0.754. Figure 3.11 reports the velocity field in the blade-to-blade view for different blade span. Clearly visible is the separation that occurs in the corner region of the blade passage. This flow separation is common (Gbadebo *et al.*, 2005) and affected only the first 25 % of the blade span. Fig. 3.12

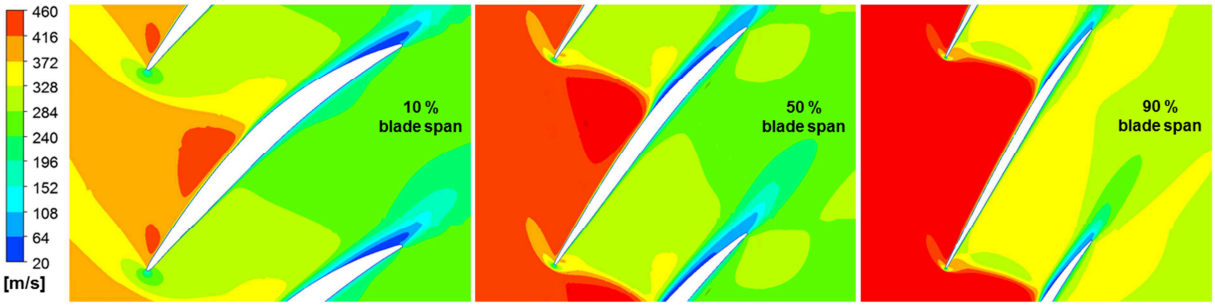

Figure 3.9 – Blade-to-blade velocity field at the best efficiency point (transonic rotor)

reports the wall shear stress for suction and pressure side. Also in this case, flow separation in the suction side determines a reduction of the wall shear stress (blue areas in the second part of the airfoil chord).

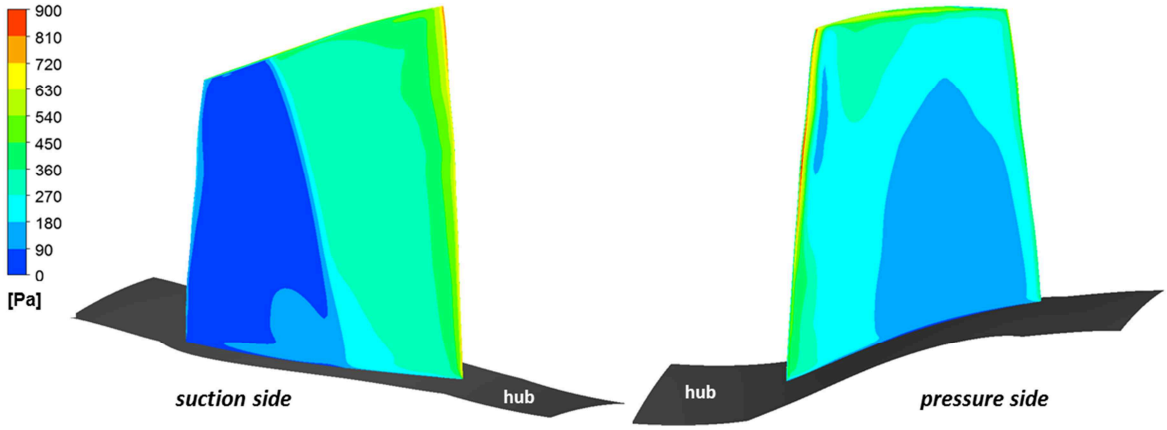

Figure 3.10 – Wall shear stress for suction and pressure side at the best efficiency point (transonic rotor)

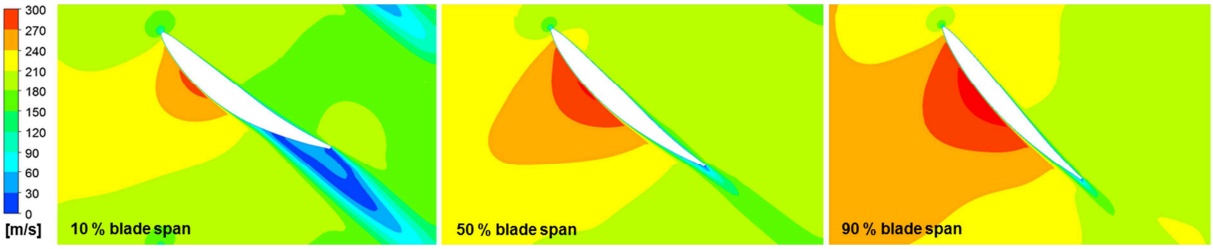

Figure 3.11 – Blade-to-blade velocity field at the best efficiency point (subsonic rotor)

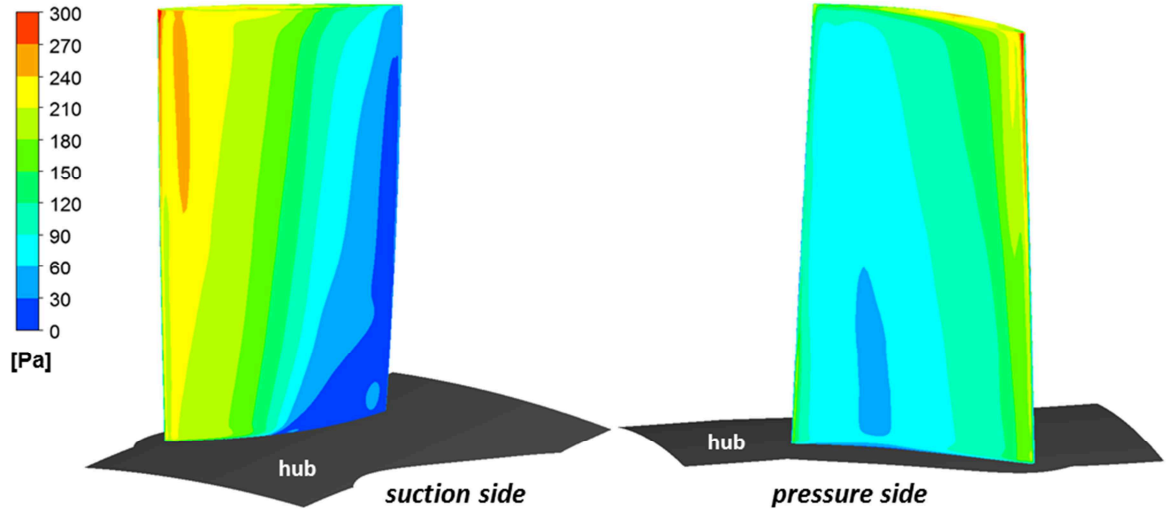

Figure 3.12 – Wall shear stress for suction and pressure side at the best efficiency point (subsonic rotor)

3.5 Lagrangian model

A comprehensive study of the phenomenon of ingestion of contaminants by a turbomachine must contain the resolution of particle adhesion and particle rebound described in the previous chapter. The transport of contaminants (particles) is resolved by coupling the Eulerian and Lagrangian approaches while, for the resolution of particles that impact the surfaces, two strategies were adopted, i.e. the ideal adhesion and reflection. In this paragraph the numerical set-up of the discrete phase is reported.

In this paper the solution approach is based on a mathematical model with Eulerian conservation equations in the gas phase and a Lagrangian frame to simulate a discrete phase. Therefore, the airflow field is first simulated and then the trajectories of individual particles are tracked by integrating a force balance equation on the particle, which can be written as

$$\frac{du_\mathrm{p}}{dt} = F_\mathrm{D} + \frac{g(\rho_\mathrm{p} - \rho)}{\rho_\mathrm{p}} + F_\mathrm{S} + F_\mathrm{B} \tag{3.1}$$

the left-hand side represents the inertial force per unit mass and u_p is the particle velocity. The first term on the right-hand side is the drag term (F_D is the inverse of relaxation time) and the second term represents the gravity and the buoyancy contribution, where ρ and ρ_p are the density of air and the particles, respectively. The last two terms F_S and F_B represent the additional contributions (per unit mass) called Saffman's lift and Brownian force, respectively. These last contributions are generally at least two magnitudes smaller than the drag force. However, some of these forces may occasionally become comparable in magnitude to the drag force within the turbulent boundary layer.

The choice of the proper formulation of the drag terms represents the most important step because the particles that are ingested by the rotor add the following characteristics: (i) spherical, (ii) eventually dragged by a high Mach number air flow and (iii) its diameters are, in some cases, less than 1 μm. The software provides three types of drag model that are described below. The drag term for spherical smooth particles is

$$F_\mathrm{D} = \frac{18\mu}{\rho_\mathrm{p} d_\mathrm{p}^2} \frac{C_\mathrm{D} Re_\mathrm{p}}{24} (u - u_\mathrm{p}) \tag{3.2}$$

where μ is the fluid viscosity, d_p is the particle diameter and Re_p is the particle Reynolds number defined as

$$Re_\mathrm{p} = \frac{\rho d_\mathrm{p} |u_\mathrm{p} - u|}{\mu} \tag{3.3}$$

and C_D is the drag coefficient defined as

$$C_{\mathrm{D}} = a_1 + \frac{a_2}{Re} + \frac{a_3}{Re^2} \tag{3.4}$$

where a_1, a_2 and a_3 are the coefficients defined by Morsi and Alexander (1972). If the particle Mach number is greater than 0.4 and the Reynolds particle number is greater than 20, for the proper resolution of the particle motion the spherical drag law must be corrected by the proper high Mach number term provided by ANSYS Fluent in agreement with Cliff *et al.* (1978). For the sub-micron size particles, the Stokes law was corrected by the Cunningham correction term. The drag term for spherical sub-micron particles follows the Stokes drag law

$$F_{\mathrm{D}} = \frac{18\mu}{\rho_{\mathrm{p}} d_{\mathrm{p}}^2 C_{\mathrm{c}}} (u - u_{\mathrm{p}}) \tag{3.5}$$

where C_{C} is the Cunningham correction factor defined as

$$C_{\mathrm{C}} = 1 + \frac{2\lambda}{d_{\mathrm{p}}} \left(1.257 + 0.4\, e^{-(1.1 d_{\mathrm{p}} / 2\lambda)} \right) \tag{3.6}$$

where λ is the molecular mean free path. The last two contributions are Saffman's lift force (Saffman, 1965) and Brownian force. Saffman's lift force is defined as

$$F_{\mathrm{S}} = \frac{2K\upsilon^{1/2} \rho\, d_{\mathrm{ij}}}{\rho_{\mathrm{p}} d_{\mathrm{p}} (d_{\mathrm{lk}} d_{\mathrm{kl}})^{1/4}} (u - u_{\mathrm{p}}) \tag{3.7}$$

where $K = 2.594$, d_{ij} is the deformation tensor and v is the air kinematic viscosity. This contribution is intended for small particle Reynolds numbers. Also Re_{p} based on the particle-fluid velocity difference must be smaller than the square root of the particle Reynolds number based on the shear stress Re_{sh} defined as

$$Re_{\mathrm{sh}} = \frac{d_{\mathrm{p}}^2 \left| du / dy \right|}{\upsilon} \tag{3.8}$$

The Brownian term is intended only for laminar simulations and its contribution has not been taken into account in this paper.

The dispersion of particles in the fluid phase can be predicted using a stochastic tracking model. The time-averaged flow field determines the mean path of particles, while the instantaneous flow field governs each particle's turbulent dispersion from the mean trajectory. By computing the trajectory in this manner for a sufficient number of representative particles (named *number of tries*), the random effects of turbulence on the particle dispersion can be included. This investigation used the Discrete Random Walk (DRW) model to simulate the stochastic velocity fluctuations in the airflow. The DRW model assumes that the fluctuating velocities follow a Gaussian probability distribution. The DRW model may give nonphysical results in

strongly nonhomogeneous diffusion-dominated flows, where small particles should become uniformly distributed. Instead, the DRW will show a tendency for such particles to concentrate in low-turbulence regions of the flow. In this case, a specific analysis conducted by the author shows that the interaction between the wall, with its boundary layer and the discrete phase is characterized by the inertial law. For this reason the diffusion phenomena can be neglected and the DRW model can be considered reliable. The analysis is related to the value of the y^+ and the specific results are reported in the following paragraphs.

The turbulence model plays a key role in the resolution of the particle trajectory near the wall. Through the use of *k-ε* STW turbulence model, there is anisotropic treatment of the turbulence near the wall and this implies, in the case where the values of y^+ are less than 5, that both the stream-wise mean velocity and the turbulence kinetic energy will be overestimated. Tian and Ahmadi (2007) report an extensive sensitivity analysis of the relationship between the turbulence models, mesh refinement close to the wall and particle dimensions expressed by the non-dimensional particle relaxation time τ^+ defined as

$$\tau^+ = \frac{(\rho_p / \rho) d_p^2 u^2}{18\nu^2} \tag{3.9}$$

where the u is the flow shear velocity defined as

$$u = \sqrt{\frac{\tau_W}{\rho}} \tag{3.10}$$

and τ_w is the wall shear stress. Their study has shown that the *k-ε* STW turbulence model over-predicts the deposition velocity for particles in a *Brownian* ($\tau^+ < 10^{-2}$) and *transition* ($10^{-2} < \tau^+ < 10$) region and it does not allow the estimation of the real trend of the particle velocity deposition. For the *inertial* ($\tau^+ > 10$) region, the *k-ε* STW turbulence model over-predicts the deposition velocity but in a minor way compared to the other regions and the trend of the deposition velocity curve is in agreement with the other results. In the following paragraphs the non-dimensional particle relaxation time for all particle diameter used in this analysis will report.

The number of particles tracked was selected in order to satisfy statistical independence since turbulent dispersion is modeled based on a stochastic process. In the present study, all the injections take place on the inlet surface. As state above, the inlet surface was made by uniform distributed elements that have the same size. This particularity allows the achievement of the maximum uniformity of the injected particles at the inlet of the rotor. All the injections of a single run, were characterized by 1,500 trajectories for the transonic rotor and 1,100 trajectories for the subsonic rotor. Every single analysis was carried out with 3 different runs. With these settings, eight million and half particles are used for each analysis with a fixed particle

diameter. For the tracking scheme the Runge-Kutta model was chosen. Finally, according to Wang and Dhanasekaran (2008), the time constant used in stochastic tracking was imposed equal to 0.15 for all the simulations.

Considering the dynamic movement and the subsequent contact of a particle with a surface (as may be the impact of a grain of dust and the rotor blade) the characteristics and phenomena that take place in the area of impact are directly related to the characteristics of the particle, the characteristics of the surface and the impact force, which can be represented by the impact velocity between the two bodies. The goal of this analysis is to provide an estimation of the presence of particles on the blade surfaces of the two considered rotors. As described above, the problem of the impact/adherence between two bodies is highly complicated and it is hard to be solved without using simplifications and assumptions. For this reason, the following conditions have been adopted: (i) not deformable spherical particles, (ii) ideal adherence condition (named *trap*) on the blade surface and (iii) non-adherence condition (named *reflect*) on the hub and shroud surfaces.

In a generic way for the turbomachine applications, it can be possible to describe three types of resulting conditions for the contact between a particle and a surface: (i) a large particle bounces on a dry surface, (ii) a small particle sticks to a dry surface and (iii) large and small particles stick to a wet surface. The condition of the ideal adherence set on the surface of the rotor blade, reflects a real heavy operating condition, which is found in reality in cases where the compressor works in very humid environments and/or with the presence of oily substances which promote sticking (such as transmission oil, grease, etc.), as reported in Kurz and Brun (2012) and Meher-Homji *et al.* (2009). The wall boundary conditions allow the evaluation of the position where the contaminants hit the blade surface for the first time, avoiding the introduction of the inaccuracies due to the use of restitution models not fully representative of the real conditions. This strategy is adopted by Tarabrin *et al.* (1998a) for estimation of the inertial deposition of particles on an axial compressor cascade. The assumption to consider the particle that impacts the surface how stuck particles was proposed for the first time by Fuchs (1964) that formulates the collection efficiency as the ratio between the number of particles colliding with the surface of the body and the number of particles that could fall on the body surface if the streamlines were not deviated by the body.

The condition of non-adherence set on the hub and shroud allows the analysis only on the blade surfaces. The authors have implemented a specific functions and restitution coefficient for the near-wall particle behavior. The model functions are defined in agreement with the Ahlert model (Ahlert, 1994) where the impact angle function *f(α)* is defined as

$$f(\alpha) = 17.9\alpha - 33.4\alpha^2 \tag{3.11}$$

for the range 0 – π/12. However the function *f(α)* as defined as

$$f(\alpha) = 2.1843 + 1.0362\ \alpha + 0.5777\ \alpha^2 - 2.8201\ \alpha^3 + 1.4242\ \alpha^4 + 0.0618\ \alpha^5 - 0.1041\ \alpha \quad (3.12)$$

for the range π/12 – π/2. The impact angle *α* is expressed in radians. The other model constants are: (i) the coefficient for the relative particle velocity $b(v_p)$ equal to 1.73 and (ii) the coefficient of the particle diameter $C(d_p)$ equal to 1.85e-8. These coefficients are based on direct impingement tests at various angles and impingement velocities provided by Ahlert (1994). The coefficients were calculated through the erosion rate calculation. Ahlert (Ahlert, 1994) proposed the relationship between the erosion rate and some characteristics related to the materials and particle's dimensions and shapes. The functions *f*, *b* and *C* are related to the property of the materials.

The theory of collision indicates that the coefficient of restitution, or the ratio of relative velocities (particle velocity after collision divided by particle velocity before collision), may have any value from one, for completely elastic collision, to zero, depending on the material, size, shape and relative velocity of the colliding bodies. In elastic collision the maximal stress in the region of the contact, should be less than a certain critical value which is many time larger than the elastic limit of the material under static load owing to the rapidity with which the load is applied. Coefficient of restitution depends not only to the material of the particle but also depends on the direction of the collision. Oblique collision generates friction force and if the particle has a rotational velocity, the combination of particle rotation with the oblique direction changes the particle trajectories after the collision. Fuchs (1964) have reported some of experimental results provided by different tests.

In this analysis, the restitution coefficient was in agreement with the results reported by Forder *et al.* (1998). In their study, the authors found the restitution coefficients for sand particles impacting steel plates. The restitution coefficient is dependent on the particle impingement angle *α* and both the perpendicular and tangential components of the restitution coefficient should be considered. Forder *et al.* (1998) provided the following correlations for both perpendicular e_n, and tangential e_t, restitution coefficients based on impingement testing using AISI 4130 carbon steel and sand

$$e_n(\alpha) = 0.988 - 0.780\ \alpha + 0.190\ \alpha^2 - 0.024\ \alpha^3 + 0.027\ \alpha^4 \quad (3.13)$$

$$e_t(\alpha) = 1.000 - 0.780\ \alpha + 0.840\ \alpha^2 - 0.210\ \alpha^3 + 0.028\ \alpha^4 - 0.022\ \alpha^5 \quad (3.14)$$

where the impact angle *α* is expressed in radians. In a general applications, restitution coefficients could depend on (i) impact velocity, (ii) pressure and (iii) temperature (Zohdi, 2004). In this case, only the velocity could be represent an obstacle through the correct representation of the particle bounce. The restitution coefficients used in this work (Forder *et al.*, 1998) resulting from a study of an oilfield

control valves with a flow velocity almost equal to 80 m/s. This value of velocity added to the locations where the restitution coefficients are imposed determine the validity of the assumption to considered, in this study, the restitution coefficients independent from the velocity.

Regarding the variation of the restitution coefficients due to the presence of a third material at the interface between surface and particle (such as liquid water due to the combination of high humidity > 60 % and the inlet depression) data are not available in literature. Poppe *et al*. (2001) pointed out that the presence of hydrophobic silane coating did not change the collisional behavior with respect to another test in which the surface was only cleaned with alcohol and subsequently dried with pressurized air. Generally, in the actual compressors, the presence of a third substance (such as oil, grease, etc.) on the blade surface could decrease the restitution coefficients (and then increase the sticking probability) of the particle, but, at the moment, there are no specific studies that allow the quantification of this effect. Based on the adhesion force theory and measurement, Tomas (2006) reported the influence of a liquid bridge (and then the humidity) on the adhesion force. The influence of liquid bridge is reported in Fig. 2.2 where it is clearly evident as the presence of the water at the particle-wall interface increment the adhesion force of a two or three order of magnitude.

The model functions and the restitution coefficients reported above were implemented on the Ansys Fluent solver in order to describe the interaction between sand particles and blade surface well. Table 3.1 summarizes the wall-particle interaction setup. In order to take into account the real composition of the ultra-fine powder, a density equal to 2,560 kg/m^3 was chosen. This assumption is due to the nature of the air contaminants that make up a large part of sand, pollen and very small particles of soil. The variation of the particle diameter, d_p, is in the range of (0.15 – 2.00) μm, while the Stokes number *St* (calculated at the inlet of the numerical model) defined as

$$St = \frac{\rho_p d_p^2}{18\mu} \frac{U_1}{d_h} \tag{3.15}$$

Table 3.1 – Wall-particle interaction settings

Location	DPM wall condition	Erosion model function $f(\alpha)$, $B(v)$, $C(d_p)$	Restitution coefficients e_n, e_t
Inlet duct	Reflect	✓	✓
Outlet duct	Reflect	✓	✓
Rotor (hub & shroud)	Reflect	✓	✓
Blade surface	Trap	✓	×

is in the range of 0.0004 – 0.0630.

All the analyses refer to injections having particles with the same diameter, the same material and therefore the same Stokes number. On the contrary, the total flow rate of the discrete phase m_p, is linked to the work environment of the compressor and the efficiency of the filtration system. In fact, the particle concentration in the air, χ, depends on the working area of the turbomachine and the filtration efficiency (there is a connection between the filtration efficiency η_f and the particle diameter as reported in previous chapters). For this reason, the total flow rate of contaminants is defined as

$$m_p = \chi q M_p (1-\eta_f) \tag{3.16}$$

where M_p represents the particle mass, the particle concentration χ refers to the typical city side working area with 100,000,000 particles/dm^3, as reported by camfil FARR (2013) and the filtration efficiency η_f refers to the good (but not optimal) charge conditions of the filter. All the simulation characteristics are reported in Table 3.2 and Table 3.3 for the transonic and subsonic rotor respectively. As can be seen in Tables 3.2 and 3.3, the non-dimensional particle relaxation time τ^+, defined by Eq. (3.9), is in the range 1 – 410 which corresponds to the transition and inertial region. However, the values in the transition region are close to the inertial region and thanks to the analyses mentioned above (values of y^+ and τ^+) the k-ε STW turbulence model used for all the analyses was considered suitable for studying the real deposition phenomenon that occurs in the axial compressors under investigation.

In order to achieve the uniform particle concentration assumption, particles were released at the same velocity as the freestream (≈ 170 m/s for the transonic rotor and ≈ 140 m/s for the subsonic rotor). It is assumed that the particles will not affect the fluid flow (one-way coupling) as the volume fraction of the particles was very low (<< 10 %). The continuum flow property refers to the non-contaminated flow conditions at the inlet of the compressor at the maximum efficiency point. All injections take place on a previously solved flow field, at the best efficiency point. All results presented in this paper were obtained from convergent simulations with all

Table 3.2 – Characteristics of the injections for the transonic rotor

Case	**1**	**2**	**3**	**4**	**5**	**6**
Particle diameter, d_p [μm]	0.15	0.25	0.50	1.00	1.50	2.00
Stokes number, St	4e-4	0.0010	0.0039	0.0158	0.0355	0.0630
Nondim. relax. time, τ^+	2	6	26	103	231	410
Filtration eff., η_f [%]	61	60	65	85	96	99
Mass flow rate, m_p [kg/s]	3.5e-6	2.5e-5	8.4e-5	7.6e-5	4.5e-5	3.5e-6

residual values less than 10^{-4} and a variation of the residues of the motion and turbulent equations close to zero.

Table 3.3 – Wall-particle interaction settings for the subsonic rotor

Case	**1**	**2**	**3**	**4**	**5**	**6**
Particle diameter, d_p [μm]	0.15	0.25	0.50	1.00	1.50	2.00
Stokes number, *St*	3e-4	8e-4	3e-3	1e-2	3e-2	5e-2
Nondim. relax. time, τ^+	1	3	13	52	117	209
Filtration eff., η_f [%]	61	60	65	85	96	99
Mass flow rate, m_p [kg/s]	9.8e-7	4.7e-6	3.3e-5	1.1e-4	1.0e-4	6.0e-5

Chapter 4

Particle Impact

In this chapter the analyses of the particle impact on the transonic rotor are shown. The results will show the position and the quantity of the ingested particles that affected the blade surface.

4.1 Capture efficiency

In this paragraph the analyses of the particle impact on the two rotors are reported. Only a portion of particles injected from the inlet surface of the numerical model impacts on the blade surface and, due to the imposed surface condition (ideal adherence), the contact results in a permanent adherence. For the comparison between the different particle diameters the ratio η_{hit} can be used. The ratio η_{hit} is defined as the ratio between the number of particles that hit the blade and the total number of injected particles.

The trends of the η_{hit} as a function of the particle diameter d_p for the two rotors are shown in Fig. 4.1. It is possible to notice that the percentage of the particles that hit the blade surface increases with the diameter of the particles (solid lines) like a Stokes number (dashed lines) for the two considered rotors. The same result, not shown for brevity, is obtained by comparing these two trends with the trends of the non-dimensional particle relaxation time τ^+, defined in Eq. 3.9. The increase of impacting particles with increasing non-dimensional relaxation time is consistent with the indications given in Tian and Hamadi (2006). In Fig. 4.1, the total number of particles injected and the absolute number of impacting particles on the blade surface are also reported for all studied cases.

Starting from the total number of injected particles, it is possible to evaluate the ratio between the number of injected particles and the number of mesh elements on the blade surface. Transonic rotor has 21,349 computational cell on the blade surface compared to the 8 million and a half injected particles then the ratio is equal to 398 particles for each cell. Since each cell is about 0.35 mm^2 the transonic rotor analysis is carried out by using 1,137 particles/mm^2. Subsonic rotor has 17,118 computational cell on the blade surface compared to the 8 million and a half

injected particles then the ratio is equal to 497 particles for each cell. Since each cell is about 0.49 mm^2 the transonic rotor analysis is carried out by using 1,014 particles/mm^2.

From this first analysis it is clearly evident that the transonic rotor could be more affected by the fouling phenomenon because it is more impacted by the particles. As can be seen in Fig. 3.8, the mass flow rates swallowed by the two rotors are in the same order of magnitude as well as the amount of the contaminant (see Tables 3.2 and 3.3). The higher blade contamination showed by the transonic rotor could be due to (i) higher peripheral velocity that leads to higher values of a shear stress on the blade surfaces and to (ii) different fluid dynamic phenomena (such as a separation) that leads to different patterns of shear stress on the blade surfaces. Considerations about the influence of the shear stress on the fouling phenomena are reported by Kurz and Brun (2012).

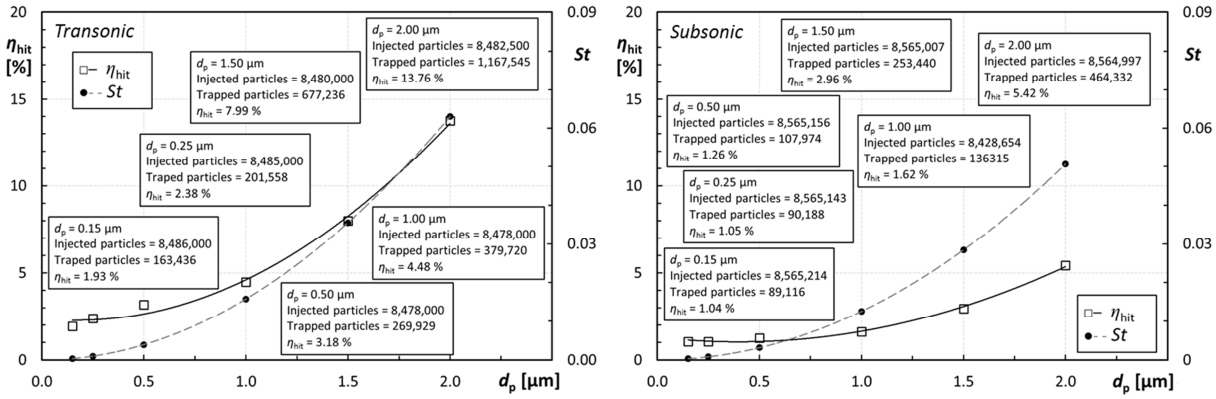

Figure 4.1 – Capture efficiency and Stokes number as a function of particle diameter

Due to the wall-particle interaction settings, the particles do not stick to the hub and shroud. Particles bounce on these surfaces following the rules imposed by the restitution coefficients reported in Eqs (3.13) and (3.14). In Tables 4.1 and 4.2, the global count of the bounces is reported. The values of N_b represent the number of particles that bounce on the hub or shroud, the values of n_b represent the ratio between the number of particles that bounce on the hub or shroud and the total number of injected particles and finally, the values of b represent the average number of bounces of each particle.

From Table 4.1, related to the transonic rotor, it can be noticed that the number of bouncy particles increases with the increase of particle diameter but, conversely, the number of average bounces decreases with the increase of particle diameter. This implies that for the smaller diameters, the particles that hit the blade may have had more frequent multiple impacts on the hub or shroud before the impact with the blade. Thus, the smaller particles could have a better chance of sticking to the hub or shroud surface compared to the bigger ones. However, this phenomenon is related

to a much smaller number of particles compared to the number of injected particles (less than 2.00 %) and does not influence the overall results.

Table 4.1 – Particles bounces on the hub and shroud (transonic rotor)

d_p [µm]	Hub			Shroud		
	N_b	n_b [%]	b	N_b	n_b [%]	b
0.15	40,551	0.48	4.1	44.406	0.52	4.5
0.25	66,186	0.78	4.4	66,216	0.78	6.8
0.50	71,154	0.84	2.5	76,236	0.90	6.7
1.00	53,082	0.63	1.3	94,218	1.11	6.4
1.50	63,357	0.75	1.1	122,811	1.45	5.4
2.00	66,186	0.78	4.4	66,216	0.78	6.8

In similar manner, Table 4.2 reports the values of the bouncing particles in the case of subsonic rotor. Also in this case, the smaller particles have a higher values of average bounces. This phenomenon is related to a much smaller number of particles compared to the number of injected particles (less than 1.00 %) and does not influence the overall results.

Table 4.2 – Particles bounces on the hub and shroud (subsonic rotor)

d_p [µm]	Hub			Shroud		
	N_b	n_b [%]	b	N_b	n_b [%]	b
0.15	40,551	0.47	4.1	47064	0.52	4.5
0.25	41,133	0.48	4.1	47,064	0.55	4.6
0.50	46,053	0.54	3.7	56,208	0.66	4.5
1.00	41,730	0.50	2.1	5,6478	0.67	3.0
1.50	34,143	0.40	1.2	53,241	0.62	2.2
2.00	28,659	0.33	0.7	53,205	0.62	1.8

4.2 Fouling susceptibility

Capture efficiency showed in the previous paragraph represents the ratio between the number of particles that hit the blade and the total number of injected particles. This definition is in agreement with the definition of the collection efficiency provided

by Fuchs (1964) that modeled the mechanism of entrainment of particles by a surface of a body situated in the stream of the air-aerosol mixture. The collection efficiency is the ratio between the number of particles colliding with the surface of the body and the number of particles that could fall on the body surface if the streamlines were not deviated by the body. In this work, the latter term corresponds to the particles that belong with the single rotor passage vane, as reported by Tarabrin *et al.* (1998a), the collection efficiency for a cascade is represented by the ratio between the number of particle that sticking to the surface and the number of particles in the flow for one pitch of the cascade.

In this paragraph some considerations was reported in order to link the capture efficiency with compressor's performance. Meher-Homji *et al.* (2009) split the fouling deterioration in two aspects: (i) the susceptibility of a gas turbine to fouling, i.e. the compressor's propensity to foul given a certain environment and foulants and (ii) the sensitivity of the gas turbine to the impact of fouling on its performance. According to these definitions, some analysis can be found in literature. One of the most important and complete is presented by Tarabrin *et al.* (1998a) in which, starting to the a cascade collection efficiency (that refers to a susceptibility scenario) the authors create the Index of compressor Sensitivity to Fouling (ISF) that allow the evaluation of the fouling sensitivity for different axial compressor. ISF depends on: (i) mass flow rate, (ii) specific heat, (iii) average total pressure rise per stage, (iv) hub to tip ratio for the first stage and (v) tip diameter. The authors underline that the sensitivity of the compressor stage to fouling depends mainly on the: (i) chord to tip diameter ratio, (ii) axial component of absolute velocity, (iii) circumferential velocity, (iv) theoretical head, (v) tip diameter and (vi) degree of reaction. Tarabrin's model (Tarabrin *et al.*, 1998a) started from particle deposition on an endless cylindrical surface developed for a cascade, in similar manner to those reported by Fuchs (1964). In these models there are two main assumption: (i) the deposition is purely inertial, and then, influenced only by a Stokes number and (ii) to consider the particle that impacts the surface how stuck particles. This implies that the only parameter that influence the particle adhesion is the Stokes number.

Starting from the numerical results reported in the previous paragraph it possible to correlates the capture efficiency with Stokes number, in line with the Tarabrin's model. Figure 4.2 reports the capture efficiency as a function of the Stokes number in a logarithmic scale for both rotors.

As can be seen from Fig. 4.2, exponential trends well fit with the data and for both rotors, the coefficient of relation is equal about (or higher) than 0.95. Trends reported in Fig. 4.2 shows a different relation between capture efficiency and Stokes number as a function of the rotor type. Transonic rotor shows an exponential trend with higher values of coefficients compared to those show by subsonic rotor. In this case, the Stokes number is calculated at the inlet of the compressor and no cascade

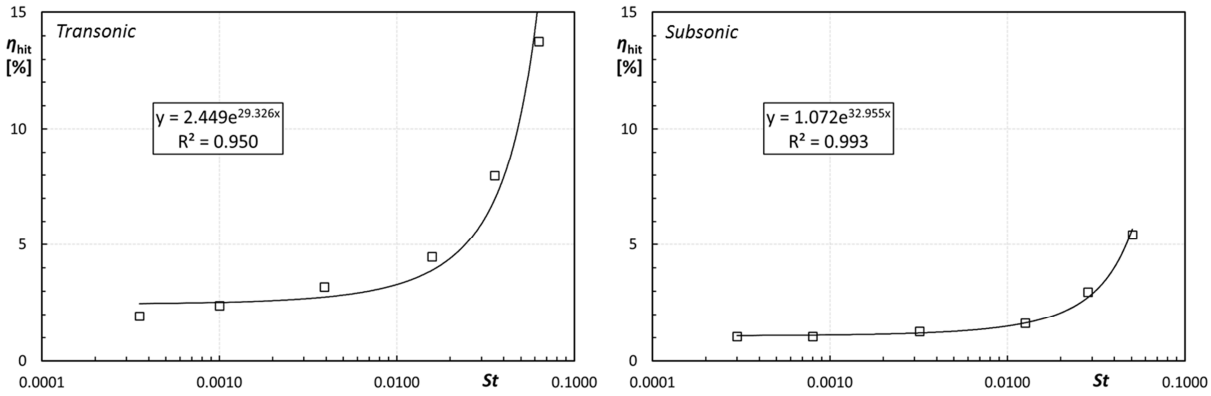

Figure 4.2 – Capture efficiency as a function of Stokes number

parameters must be known for its determination. The numerical results used for determine the capture efficiency are affected only by the numerical resolution of the discrete phase, but, no hypothesis related to type of motion (such as inertial) or type of obstacle are imposed. For these reasons, the results reported in Fig. 4.2 have a great important. Two different axial compressor rotors with very different pressure and flow coefficients show a similar exponential trend that link the capture efficiency and Stokes number.

Tarabrin *et al.* (1998a) reports some conclusion related to the stage design and fouling issue. In particular, the authors pointed out that: (i) on condition of keeping the aerodynamic and geometrical similarity, the compressor of a smaller size (a model) is more sensitive to fouling than a full-scale one, (ii) high-head stages are more sensitive to fouling than low-head ones and (iii) the degree of the particles deposition on the blades increases when the angle of attack grows. Starting from these hints, the differences in terms of exponential coefficient shown in Fig. 4.2 could be due to the different stage-head or other cascade features. The transonic rotor shows higher pressure coefficient (Ψ = 0.431 at best efficiency point) compared to the subsonic one (Ψ = 0.31 at best efficiency point) and the stage total head is equal to 104,504 Pa (equal to about 10.66 m) for the transonic rotor, compared to the subsonic stage total head that is equal to 12,779 Pa (equal to about 1.30 m). Therefore, the capture efficiency is greater in the case of higher head, as reported by Tarabrin *et al.* (1998a).

Since these considerations, in the following, by applying the Buckingham Pi Theorem (Buckingham, 1914), the relationship between the capture efficiency and some parameter related to particles and compressor characteristics is reported. Thanks to this theorem, it is possible to express the capture efficiency as a function of the dimensionless and independent quantities (Π_j).

Firstly, through the evaluation of the particle behavior, based on theory and literature background, will identify which are the main variables of interest. In this

case the question is: Which are the independent variables that influence the capture efficiency? From the results and the literature reported above, seven independent variables are identified. The set of independent variables are reported in Table 4.3 where they are express in terms of its fundamental dimensions among {kg m s}.

Table 4.3 – Independent variables

#	Independent variables	Symbols	{kg m s}
1	Particle density	ρ_p	$\{kg^{-1}\ m^{-3}\}$
2	Particle diameter	d_p	{m}
3	Axial component of absolute velocity	V	$\{m\ s^{-1}\}$
4	Dynamic viscosity	μ	$\{kg\ m^{-1}\ s^{-1}\}$
5	Dimensional characteristic of compressor	L	{m}
6	Angular velocity of compressor rotor	ω	$\{s^{-1}\}$
7	Rotor head	He	{m}

The first five variables refer to the Stokes number (see Eq. 3.15), while the latter two refer to the compressor characteristics and performance. The dimensional characteristic of compressor L, indicates only that also the geometrical feature could influence the particle deposition. For example, in the definition of the Stokes number, L corresponds to hydraulic diameter, d_h, but in this general evaluation L could be also the tip diameter (or radius), the average diameter (or radius), etc.

The number of Π groups will be equal to the difference between the independent variables and the fundamental dimensions. In this case the number of Π groups will be 4. A generic dimensionless number Π will be a function of the seven independent variables as

$$\Pi = \{kg^0\ m^0\ s^0\} = \rho_p^{\,a}\ d_p^{\,b}\ V^c\ \mu^d\ L^e\ \omega^f\ He^g \tag{4.1}$$

by substituting the independent variable with their fundamental equation can be obtain

$$\Pi = \{kg^0\ m^0\ s^0\} = \{kg^1\ m^{-3}\}^a\ \{m\}^b\ \{m\ s^{-1}\}^c\ \{kg\ m^{-1}\ s^{-1}\}^d\ \{m\}^e\ \{s^{-1}\}^f\ \{m\}^g \tag{4.2}$$

In this step, the equations related to each fundamental dimension are written. In this case, the system of equation is made by three equations, related to kg, m and s

$$\begin{aligned}
&\text{equation for kg} \rightarrow\ 0 = a + 0 + 0 + 0 + d + 0 + 0 + 0 \\
&\text{equation for m:} \rightarrow\ 0 = -3a + b + c - d + e + 0 + g \\
&\text{equation for s:} \rightarrow\ 0 = 0 + 0 - c - d + 0 - f + 0
\end{aligned} \tag{4.3}$$

Now, it is possible to fix four coefficients and calculates the other three obtaining the dimensionless group Π.

The first one will obtained by fixing: b = 2, e = -1, f = 0 and g = 0. Consequently, the other three coefficients, calculate by using the Eq. (4.3), are: a = 1, c = 1 and d = -1. The first dimensionless group Π_1 is

$$\Pi_1 = \rho_p \, d_p^2 \, V \, \mu^{-1} \, L^{-1} \tag{4.4}$$

as expected, one of the dimensionless group is related to the Stokes number.

The second one will obtained by fixing: b = 2, c = 2, f = -3 and g = 1. Consequently, the other three coefficients, calculate by using the Eq. (4.3), are: a = -1, d = 1 and e = -7. The second dimensionless group Π_2 is

$$\Pi_2 = \rho_p^{-1} \, d_p^2 \, V^2 \, \mu \, L^{-7} \, \omega^{-3} \, He \tag{4.5}$$

reorganizing the Eq. (4.4) it is possible to highlight some relation with compressor's characteristics, in particular

$$\Pi_2 = (L^{-3}) \, (\rho_p^{-1} \, d_p^2 \, V \, \mu \, L) \, (L^{-2} \, \omega^{-2} \, He) \, (V_a \, L^{-1} \, \omega) \tag{4.6}$$

where the second bracket is proportional to the Stokes number, the third bracket is proportional to the pressure coefficient Ψ and fourth bracket is proportional to the flow coefficient Φ. Therefore the second dimensionless group Π_2 is directly proportional to the *St*, Ψ and Φ.

The third one will obtained by fixing: a = 0, b = 1, e = 0 and g = 1. Consequently, the other three coefficients, calculate by using the Eq. (4.3), are: c = 2, d = 0 and f = -2. The third dimensionless group Π_3 is

$$\Pi_3 = d_p \, V^2 \, \omega^{-2} \, He \tag{4.7}$$

considering the relation

$$\omega^{-2} \, He \propto \Psi \, L^2 \tag{4.8}$$

the dimensionless group Π_3 become

$$\Pi_3 \propto d_p \, V \, \Psi \, L^2 \tag{4.9}$$

Therefore the third dimensionless group Π_3 is directly proportional to particle diameter d_p, pressure coefficient Ψ and axial component of absolute velocity *V*.

The fourth one will obtained by fixing: a = 0, b = 0, e = 1 and f = -1. Consequently, the other three coefficients, calculate by using the Eq. (4.3), are: c = 1, d = 0 and g = -2. The third dimensionless group Π_3 is

$$\Pi_4 = V \, \omega^{-1} \, He^{-2} \tag{4.10}$$

considering the relation (related to flow coefficient)

$$V \, \omega^{-1} \propto \Phi \, L \tag{4.11}$$

substituting Eq. (4.11) in the Eq. (4.10) the dimensionless group Π_4 become

$$\Pi_4 \propto L^2\, He^{-2}\, \Phi \tag{4.12}$$

and considering the relation (related to pressure coefficient)

$$He^{-2}\, L^{-4} \propto \omega^4\, \Psi^2 \tag{4.13}$$

substituting Eq. (4.13) in the Eq. (4.12) the dimensionless group Π_4 become

$$\Pi_4 \propto \Phi\, L^{-2}\, \Psi^{-2}\, \omega^{-4} \tag{4.14}$$

Therefore the fourth dimensionless group Π_4 is directly proportional to flow coefficient Φ and inversely proportional to pressure coefficient Ψ and angular velocity of the rotor ω.

Summarizing the four dimensionless groups obtained by applying the Buckingham Pi Theorem the capture efficiency η_{hit} is a function of the following terms

$$\eta_{hit} = f \left\{ \begin{array}{ll} \Pi_1 & \rho_p\, d_p^2\, V\, \mu^{-1}\, L^{-1} \propto St \\ \Pi_2 & (L^{-3})\, (\rho_p^{-1}\, d_p^2\, V\, \mu\, L)\, (L^{-2}\, \omega^{-2}\, He)\, (V\, L^{-1}\, \omega) \propto (L^{-3})\, St\, \Psi\, \Phi \\ \Pi_3 & d_p\, V^2\, \omega^{-2} \propto d_p\, V\, \Psi\, L^2 \\ \Pi_4 & V\, \omega^{-1}\, He^{-2} \propto \Phi\, L^{-2}\, \Psi^{-2}\, \omega^{-4} \end{array} \right\} \tag{4.15}$$

This preliminary analysis shows how the rotor's performance (thus the rotor design) influence the fouling rate on the blade surfaces. Dimensional characteristic of compressor, pressure and flow coefficient are linked to the capture efficiency of the rotor. Starting with this relationship and this methodology, by using a wider sample of transonic and subsonic rotor, in the future could be define a general trends and correspondence between design parameter of the axial compressor rotors and the capability of the rotor to collect contaminant.

4.3 Particle concentrations

The first analysis of the results refers to the quantity defined as DPM concentration χ_{DPM}, which allows the concentration of contaminant on a specific surface, defined as kg/m^3, to be determined. The χ_{DPM} allows the combined effects between the trajectories of the particles and the total mass flow rate m_p calculated according to Eq. (3.16) to be highlighted. In this analysis, the χ_{DPM} allows the evaluation of the combined effects of: (i) the particle trajectories, (ii) the contamination intensity of the working compressor place χ and (iii) the filtration efficiency η_f. The selected surface to evaluate the χ_{DPM} was obtained by a transformation of the blade surface. In particular, the new control surface was positioned at a constant distance from the blade surface of 50 µm for each point as reported in Fig. 4.3. In this way, it is

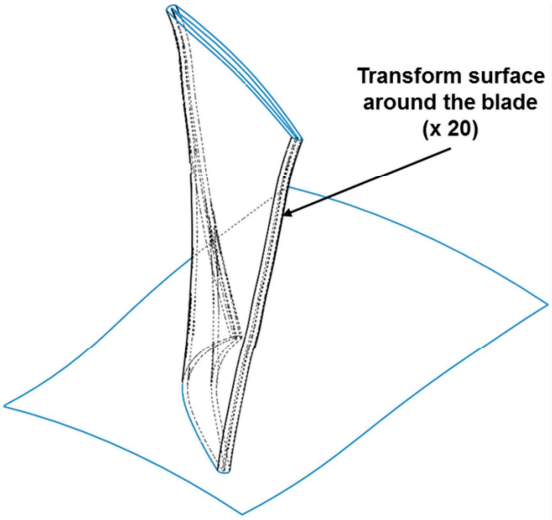

Figure 4.3 – Control surface positioned at a constant distance from the blade

possible to evaluate the presence of contaminants in the portion of fluid that is located very close to the blade surface.

Figure 4.4 shows the contour plot of χ_{DPM} on the transform surface for Pressure Side (PS) and Suction Side (SS) of the transonic blade. From these contour plots it is

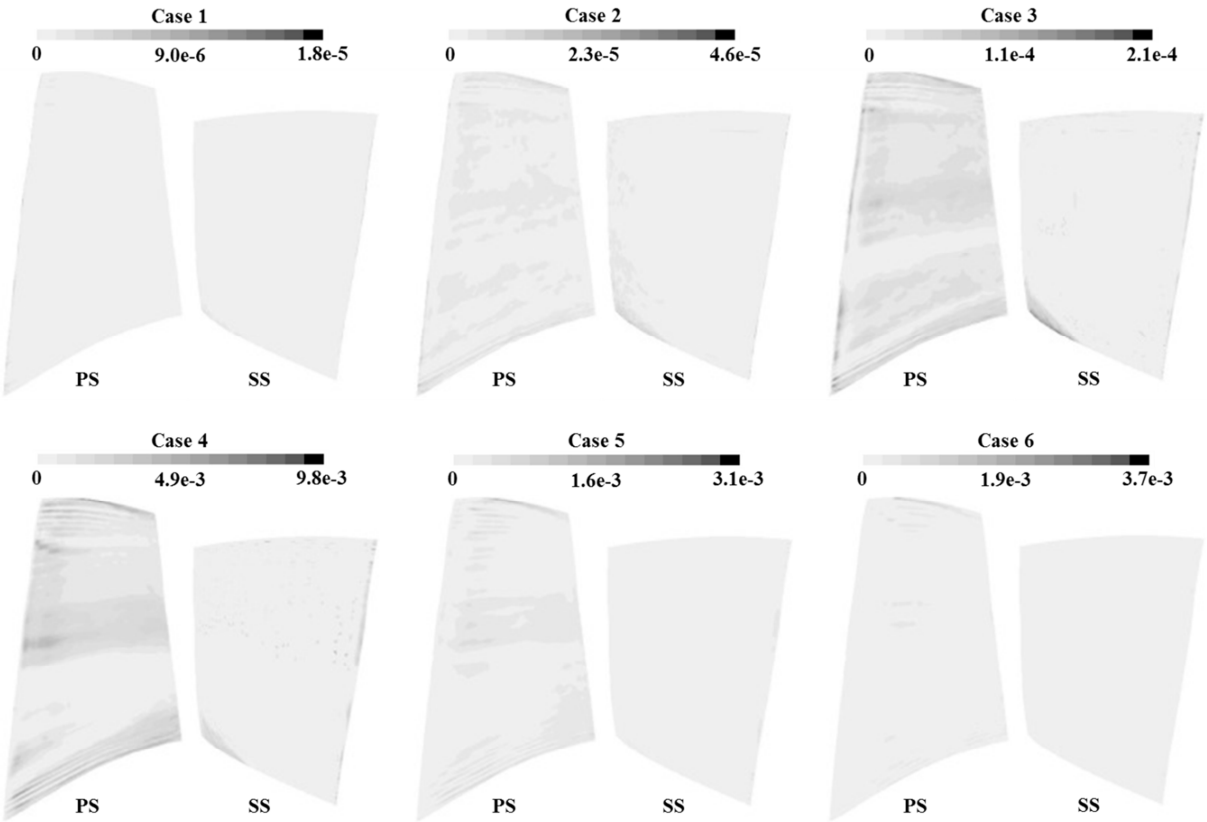

Figure 4.4 – DPM Concentrations, PS and SS (transonic rotor)

possible to notice that:

- the peak of the contaminants concentration is found in correspondence to the Leading Edge (LE);
- the pressure side is more contaminated than the suction side;
- the injections with the smaller particle (d_p = 0.15 µm and d_p = 0.25 µm) show a more distributed contaminant concentration on the pressure side;
- the injections with the larger particle (d_p = 1.50 µm and d_p = 2.00 µm) show a relevant concentration of contaminants only on the pressure side, while in the suction side, it is possible to see a very small quantity of contaminants close to the hub and the top of the blade.

Figure 4.5 shows the contour plot of χ_{DPM} on the transform surface for pressure side and suction side of the subsonic blade. From Fig. 4.3 it is possible to notice that:

- the peak of the contaminant concentration is found in correspondence to the leading edge;

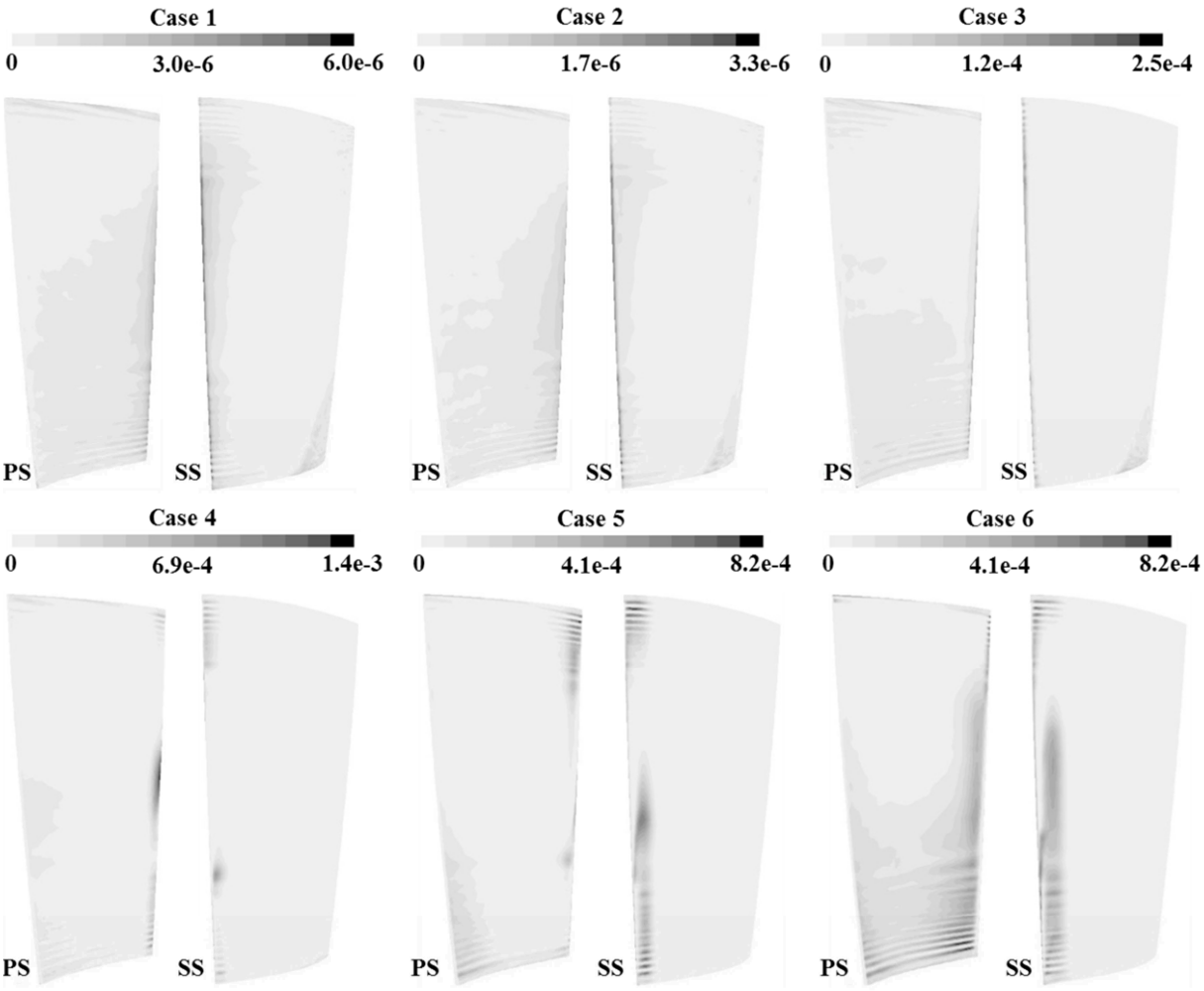

Figure 4.5 – DPM Concentrations, PS and SS (subsonic rotor)

- the pressure side is more contaminated than the suction side;
- the injections with the smaller particles (d_p = 0.15 µm and d_p = 0.25 µm) show a more distributed contaminant concentration on the pressure side. The contaminant concentration in the corner region close to Trailing Edge (TE) in the suction side is clearly visible;
- the injections with the larger particles (d_p = 2.00 µm) show a relevant concentration of contaminants only on the PS and in a blade portion close to the leading edge in suction side.

These distributions are in line with those reported in literature regarding (i) fouling characterized by particles with dimensions less than 2 µm and (ii) erosion of rotor blades which is characterized by larger particles (Kurz and Brun, 2012). In fact, the fouling phenomenon is characterized by a wider distribution of the particle on the blade surfaces with respect to erosion, which shows a higher percentage of impacts on the pressure side and leading edge than on the suction side. A detailed analysis of the particle impact zones on the blade surface will be carried out in the following paragraphs.

The DPM concentration shown in Figs. 4.4 and 4.5 refers to one of the three runs. In fact, as mentioned above, every case was repeated for three different runs in order to avoid the problems caused by statistical resolution of particle tracking. In Tables 4.4 and 4.5 the values of the DPM concentration peak χ_{DPM}^{*}, and the values obtained by a weight-area average of the DPM concentration $\tilde{\chi}_{DPM}$ for all of the executed runs are reported. From the values of Tables 4.4 and 4.5 it is possible to note that the values obtained for the three runs of each case are very close to each other, confirming the independence of the results from the statistical dispersion. Due to this evidence, it is possible to define an average value $\overline{\tilde{\chi}}_{DPM}$ of the $\tilde{\chi}_{DPM}$ among the three runs for each case.

The values reported in Table 4.4 and 4.5 are higher compared to the values

Table 4.4 – DPM concentrations [µg/m^3] and fouling index (transonic rotor)

d_p [µm]	1st run		2nd run		3rd run		Average	*H*
	χ_{DPM}^{*}	$\tilde{\chi}_{DPM}$	χ_{DPM}^{*}	$\tilde{\chi}_{DPM}$	χ_{DPM}^{*}	$\tilde{\chi}_{DPM}$	$\overline{\tilde{\chi}}_{DPM}$	
0.15	1.5e4	3.0e2	1.5e4	3.0e2	1.5e4	3.0e2	3.0e2	0.21
0.25	4.6e4	1.9e3	4.6e4	1.9e3	4.5e4	2.0e3	1.9e3	0.29
0.50	2.2e5	1.5e4	2.2e5	1.4e4	2.1e5	1.4e4	1.4e4	0.31
1.00	9.8e6	5.0e5	1.0e7	5.0e5	9.6e6	4.9e5	5.0e5	3.09
1.50	3.1e6	7.4e4	3.0e6	7.5e4	3.1e6	7.4e4	7.4e4	0.51
2.00	3.7e6	5.3e4	3.6e6	5.3e4	3.7e6	5.3e4	5.3e4	0.61

Table 4.5 – DPM concentrations [µg/m^3] and fouling index (subsonic rotor)

d_p [µm]	1st run		2nd run		3rd run		Average	H
	χ_{DPM}^{*}	$\tilde{\chi}_{DPM}$	χ_{DPM}^{*}	$\tilde{\chi}_{DPM}$	χ_{DPM}^{*}	$\tilde{\chi}_{DPM}$	$\bar{\chi}_{DPM}$	
0.15	5.6e3	3.6e2	6.1e3	3.6e2	6.0e3	3.5e2	3.5e2	0.25
0.25	3.3e4	1.9e3	3.2e4	1.9e3	3.2e4	1.9e3	1.9e3	0.28
0.50	2.5e5	9.3e3	2.5e5	9.2e3	2.5e5	9.3e3	1.4e4	0.20
1.00	1.4e6	2.9e4	1.4e6	2.8e4	1.4e6	2.8e4	5.0e5	0.17
1.50	8.5e5	2.4e4	8.2e5	2.4e4	7.7e5	2.4e4	7.4e4	0.16
2.00	4.8e5	3.4e4	4.8e5	3.4e4	4.6e5	3.4e4	5.3e4	0.39

characteristic of actual air contaminant concentration (< 500 µg/m^3). This fact is due to the previous assumption of particle size, distribution and matter density: actual air contaminants are a distribution of particles of different sizes and materials as widely reported in the first chapter, and not particles with a homogenous size and density as assumed in the numerical simulations.

Figure 4.6 shows the trends of the m_p and $\bar{\chi}_{DPM}$ as functions of the particle diameter d_p. It is possible to note that for Case 4, for both rotors, corresponding to particles with a diameter equal to 1.00 µm, the operating condition for the compressors is the most affected by the contaminants. In fact, for this case the highest values of m_p are associated with the highest values of $\bar{\chi}_{DPM}$. Two rotors show different peak values. Subsonic rotor swallow more air at the best efficiency point, and for this reason, the contaminant mass flow rate is higher.

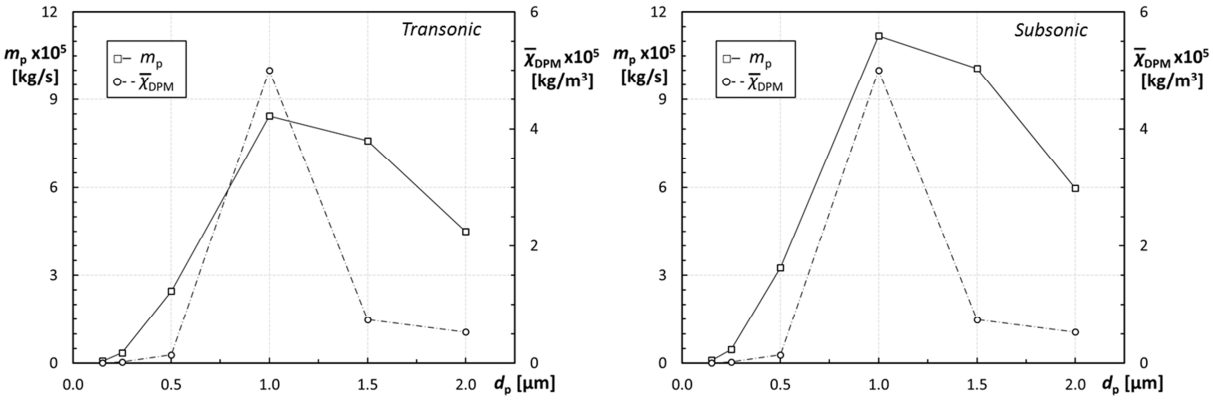

Figure 4.6 – Average DPM concentration and total mass flow as a function of particle diameter

In order to compare the different rotors, or, more in general, different compressors, a new ratio can be defined. From the $\bar{\chi}_{DPM}$, the ratio H can be defined as

$$H = \frac{\overline{\chi}_{\mathrm{DPM}}}{\chi M_p (1-\eta_{\mathrm{f}})} \tag{4.16}$$

This represents the dimensionless index of the compressor's capacity to concentrate the contaminants in the vicinity of the blades. For the studied cases, this particular index assumes the values reported in Tables 4.4 and 4.5 This ratio is a representative index of a real fouling condition in which the compressor operates. In fact, from this index it is possible to link the characteristics of (i) the amount of contaminants, (ii) the type of contaminants, (iii) the filtration efficiency and (iv) the flow pattern inside the axial compressor. The most severe fouling condition that affected the transonic rotor, at the best efficiency point, is Case 4 (H = 3.09, d_{p} = 1.00 µm) while for the subsonic rotor, is the Case 6 (H = 0.39, d_{p} = 2.00 µm). The subsonic rotor swallow more contaminants but its fluid dynamic characteristics determines a lower contaminant concentration in the vicinity of the blade surface.

The index H is very similar to the mass transfer coefficient h_{f} found in Parker and Lee (1972), which defines the ratio of the mass deposited per unit area per unit time and the mass concentration in air per unit volume. While the mass concentration in air per unit volume is the denominator in the Eq. (4.16), the numerator of the h_{f} can be obtained by the quantity called *Accretion Rate* provided by the software. In this analysis, through the use of the ratio H, the result appears to be independent of time for two reasons: (i) the trap conditions on the blade surface implies unrealistic values of the quantity *Accretion Rate*, in contrast to those obtained from experimental tests reported by Parker and Lee (1972) and (ii) the ratio H defined in Eq. (4.16) can be used to compare different types of machine considering only the capacity of the compressor to concentrate the air contaminants around the blade surface (due to the shape of the hub, shroud, airfoil, etc.).

The absolute values of the Accretion Rate (AR) are not representative of the particle deposition because the sticking phenomena changes during the particle deposition due to the different characteristics between the blade surface and the deposited particle layer. Rather, they are representative of the total amount of contaminants which hit the blade. Accretion rate allows the identification of contaminant deposition intensity in terms of kg/m^{2}s. The values of the AR are obtained in the same way as the values of DPM Concentration: values of the peak AR^*, values obtained by a weight-area average $\widetilde{AR}$ for all of the executed runs and the average value $\overline{AR}$ of the $\widetilde{AR}$ for the three runs in each case. These values are reported in Tables 4.6 and 4.7 for transonic and subsonic rotor, respectively.

With these values the amount of contaminants that affected the blade surface during the operation can be evaluated. In fact it is possible to calculate the contaminant mass M_{c} on the blade surface as

Table 4.6 – Accretion Rate values [kg/m^{2}s] (transonic rotor)

d_p [µm]	1st run		2nd run		3rd run		Average
	AR^*	$\widetilde{AR}$	AR^*	$\widetilde{AR}$	AR^*	$\widetilde{AR}$	$\overline{AR}$
0.15	1.3e-2	3.8e-5	1.2e-2	3.4e-5	1.3e-2	3.6e-5	3.6e-5
0.25	4.1e-3	1.1e-5	1.3e-2	3.3e-5	2.1e-2	5.6e-5	3.e-5
0.50	4.7e-2	1.1e-4	1.4e-1	3.1e-4	2.4e-1	5.2e-4	3.1e-4
1.00	3.0e0	1.0e-2	4.5e0	1.5e-2	7.6e0	2.5e-2	1.7e-2
1.50	5.6e-1	3.1e-3	4.4e-1	2.4e-3	7.4e-1	4.0e-3	3.2e-3
2.00	1.8e-1	8.3e-4	5.2e-1	2.5e-3	8.5e-1	4.1e-3	2.5e-3

Table 4.7 – Accretion Rate values [kg/m^{2}s] (subsonic rotor)

d_p [µm]	1st run		2nd run		3rd run		Average
	AR^*	$\widetilde{AR}$	AR^*	$\widetilde{AR}$	AR^*	$\widetilde{AR}$	$\overline{AR}$
0.15	9.5e-3	8.3e-5	9.5e-3	8.5e-5	9.5e-3	8.8e-5	8.5e-5
0.25	7.2e-4	5.9e-6	1.8e-3	1.8e-5	2.6e-3	2.9e-5	1.8e-5
0.50	7.0e-1	2.9e-3	7.2e-1	3.0e-3	7.5e-1	3.1e-3	3.0e-3
1.00	1.0e1	1.1e-2	1.1e1	1.1e-2	1.1e1	1.2e-2	1.1e-2
1.50	7.3e0	2.6e-2	7.5e0	2.7e-2	7.7e0	2.8e-2	2.7e-2
2.00	4.6e0	2.1e-2	4.8e0	2.2e-2	4.9e0	2.3e-2	2.2e-2

$$M_c = \overline{AR}\, A_b\, t \tag{4.17}$$

where A_b is the blade surface and t is the operating time. Tables 4.8 and 4.9 summarizes the mass of contaminants on the blade surface for different operation

Table 4.8 – Mass contaminant on the blade [kg] (transonic rotor)

d_p [µm]	Operating time t			
	1 hour	1 day	2 days	1 week
0.15	0.001	0.023	0.047	0.164
0.25	0.001	0.022	0.043	0.151
0.50	0.008	0.203	0.404	1.421
1.00	0.453	10.861	21.721	76.025
1.50	0.086	2.054	4.107	14.375
2.00	0.067	1.601	3.203	11.210

Table 4.9 – Mass contaminant on the blade [kg] (subsonic rotor)

d_p [µm]	Operating time t			
	1 hour	1 day	2 days	1 week
0.15	0.003	0.061	0.123	0.429
0.25	0.001	0.013	0.025	0.089
0.50	0.091	2.176	4.352	15.233
1.00	0.342	8.209	16.418	57.463
1.50	0.805	19.331	38.662	135.318
2.00	0.665	15.960	31.920	111.721

times. The blade contamination is very noticeable with a very high contaminant mass on the blade surface (up to 76 kg for the transonic rotor and 135 kg for the subsonic rotor) even after one operation week. These values illustrate the reason of the definition of the *H* ratio.

4.4 Particle impact locations

Theoretically, zones with a high number of impacts will be more affected by the fouling phenomena, but, actually, the fouling phenomena depends on the sticking characteristic of the particles. In this paragraph an overall analysis of the impact location of the particles on the blade surface is carried out.

For the transonic rotor, it can be notice that by increasing particle diameter d_p, the suction side is less affected by the impacts. There is a greater number of impacts on the pressure side. In Fig. 4.7 the trends of the impacting particles on the blade (for both sides) for all the cases, can be seen. The η_{hit} values reported for the pressure side $\eta_{hit,PS}$ and suction side $\eta_{hit,SS}$ refer to the percentage of particles that hit the pressure side or suction side compared to the total number of injected particles. As can be seen from Fig. 4.7, the particles tend to hit the pressure side in increasing quantities as the particle diameter increases. These distributions are very important from operators' points of view, because the capability of the compressor to collect air contaminant is directly related to the power unit performance drop. In Fig. 4.7 the η_{side} values are reported in pie charts. These values refer to the percentage of particles that hit the blade on pressure side or suction side compared to the total number of particles that hit the blade. This result is in line with those reported in literature regarding (i) fouling characterized by particles with dimensions close to the unit of micron (Kurz and Brun, 2012) and (ii) erosion of rotor blades which is characterized by larger particles (Ghenaiet, 2012). In fact, the fouling phenomenon is characterized by a wider distribution of the particle on the blade surfaces with respect

to erosion that shows a higher percentage of impacts on the pressure side than on the suction side.

For the subsonic rotor, the results are reported in Fig. 4.8. From the analysis of

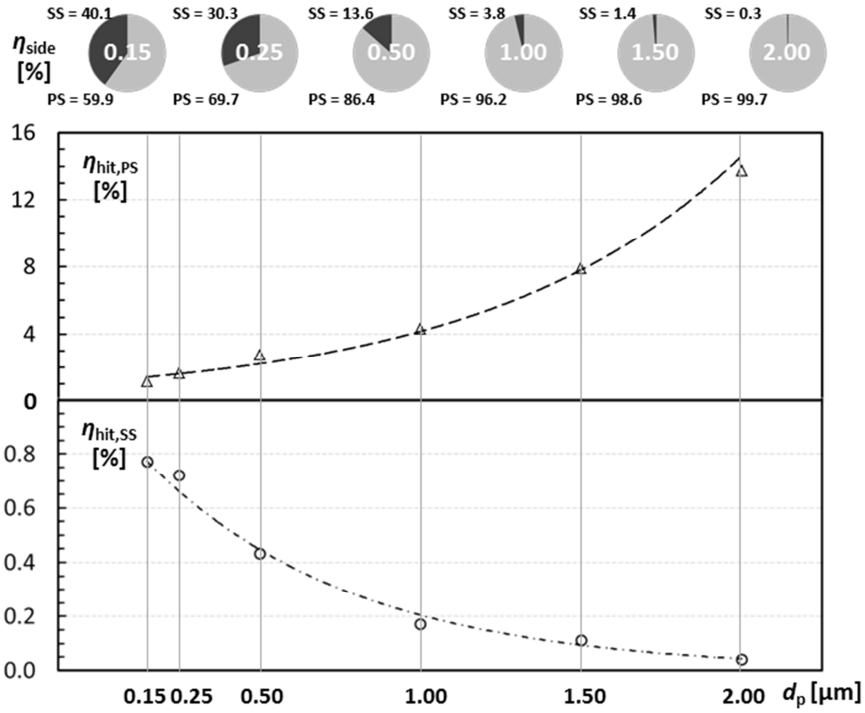

Figure 4.7 – Particle impact distributions, PS and SS (transonic rotor)

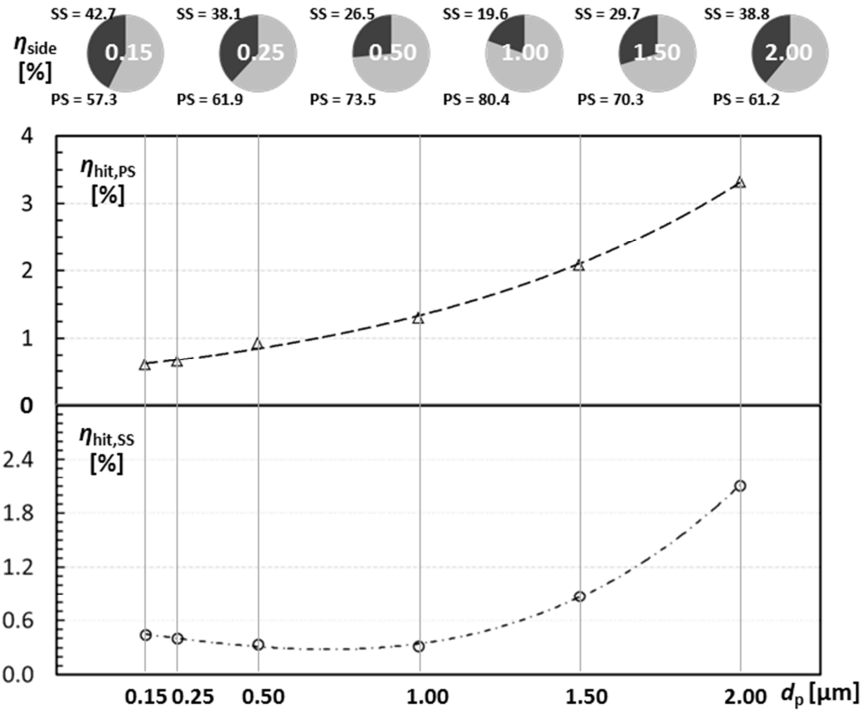

Figure 4.8 – Particle impact distributions, PS and SS (subsonic rotor)

Fig. 4.8 it can be seen that by increasing the particle diameter, the number of particles that hit the pressure side increases (like in the transonic rotor). In the suction side, the number of particles that hit the blade decreases to d_p = 1.00 µm, while the number of impacts that takes place on the suction side increases from d_p = 1.00 µm to d_p = 2.00 µm. The particles that hit the suction side are especially concentrated at the leading edge, but more details on particle impact location could be found in the following. The transonic rotor is more affected by particle impact than impact in greater quantity on the pressure side, whereas the subsonic rotor shows a more distributed particle impact pattern.

In order to show the obtained results in a general form, useful for comparative analysis, a new quantity is introduced. The new quantity refer to the impact concentration on the blade surface. Thanks to a very fine discretization of the blade surface obtained through the use of eleven divisions (strips) along the spanwise direction, and twelve divisions (slices) along the chordwise direction, it is possible to clearly represent the deposits on the blade surface. The new quantity is defined as

$$X_{\mathrm{SLICE}} = \left[\frac{N° \, impacts \; @ \; slice}{N° \, impacts \; @ \; strip} 100 \right] \frac{1}{A_{\mathrm{SLICE}}} \tag{4.17}$$

referring to the amount of impacts in a single slice obtained by a chordwise division of the strip with respect to the total number of particles that impact the entire considered strip. The quantity A_{SLICE} refers to the area of the slice obtained by a chordwise division of the strip. The adopted chordwise division is reported in abscissa for each distribution.

Figure 4.9 shows the impact distributions in terms of X_{SLICE} for the 2nd, 6th and 10th strips for the transonic rotor (Case 1). From Fig. 4.9 the high percentage of impacts on the leading edge can be noted which, in relative terms to the impacts on the strip, reaches a peak for the 6th strip (i.e. at midspan). A similar phenomenon can also be found in the experimental measurements reported by Parker and Lee (1972) where the authors provided some deposition tests for a turbine blade. The strip closest to the hub (2nd strip), shows a more uniform impact distribution on the blade surface, affecting the suction side more than the pressure side. In the strip at the top of the blade (10th strip), there is a high impact concentration on leading edge and a low impact concentration on trailing edge if compared to the other two strips. For all the shown impact distribution trends on the strips, a different decreasing trend of the number of impacts between pressure side and suction side can be noticed. In fact, in the pressure side at the portion of the chord immediately after the leading edge, there is a number of impacts comparable what occurs in the remaining slices. On the contrary, in the suction side there is a non-uniform decreasing trend of the number of impacts. In fact, there is a smaller number of impacts in the slice immediately next to the leading edge with respect to slices corresponding to higher chords. In particular, the peak of impacts for the trailing edge in the 2nd and 6th strip are highlighted. This is

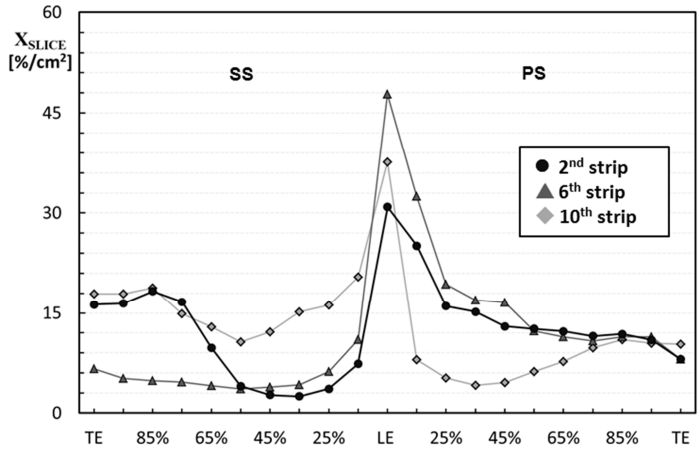

Figure 4.9 – Particle distributions 2nd, 6th and 10th strip, Case 1 (transonic rotor)

due to a thicker boundary layer generated by the flow separation that occurs after the shock wave. Particles reach this blade area because they sweep downstream from the leading edge area due to higher values of shear stress (Kurz and Brun, 2012).

Figure 4.10 show the impact distributions in terms of X_{SLICE} for the 2nd, 6th and 10th strips for the subsonic rotor (Case 1). The high percentage of impacts on the leading edge can be noted which, in relative terms to the impacts on the strip, reaches a peak for the 6th strip (i.e. at mid-span). The strip at mid-span (6th strip), shows a more uniform impact distribution on the blade surface, affecting the suction side more than the pressure side. For the other two strips the impact distribution is quite different. For the 2nd strip (close to the hub), the impact distribution in suction side shows an increment from 50 % of the airfoil chord. The same phenomenon, even if smoother, can be noticed for the 10th (close to the blade tip), while in the pressure side the decreasing trend for the 10th strip shows an increment from 50 % of the airfoil chord. These impact patterns show that there is not a blade area completely free from particle impact and, as a consequence, the blade surface could be completely affected by deposits.

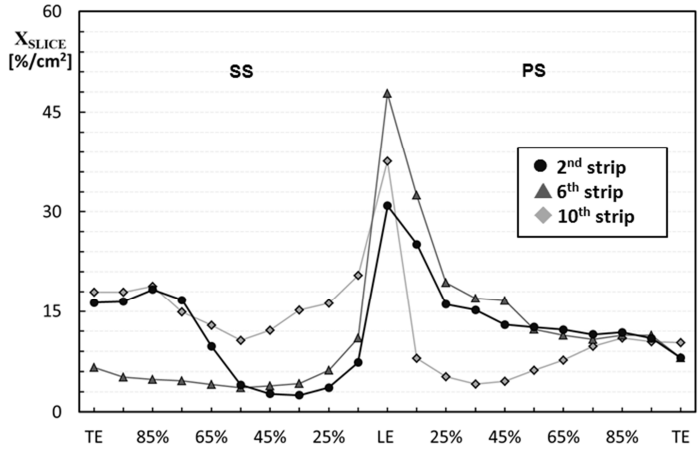

Figure 4.10 – Particle distributions 2nd, 6th and 10th strip, Case 1 (subsonic rotor)

Thanks to the general form of the quantity X_{SLICE} it possible to compare the particle distribution along the airfoil chord of the two rotors. Figure 4.11 reports the comparison for the 2nd, 6th and 10th strips. The two trends, for a fixed strip, are very similar to each other. The major differences can be found in the suction side of the 6th and 10th strip. The shock wave that takes a place in the transonic rotor determines the different particle impact pattern on the suction side blade surface. For the 2nd strip the separation that influence the subsonic rotor suction side induces a particle impact distribution trend very similar to that found for the transonic rotor, while at mid-span only the separation due to the shock wave in the transonic rotor can be found. Jacobs *et al.* (2012) have created computer simulations of the dispersion of particles as a result of moving shocks, pointing toward the shock-particle interaction as means of creating particle velocity components perpendicular to the main flow. So, particle transport perpendicular to the stream lines is greatly promoted by the shock wave.

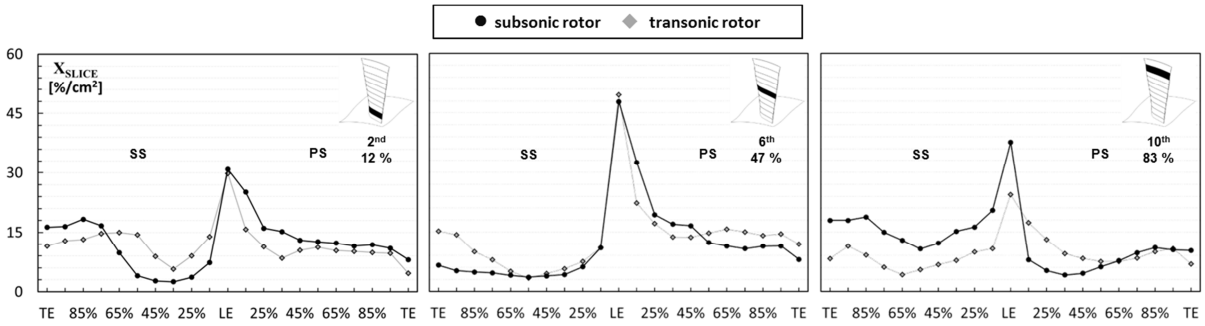

Figure 4.11 – Comparison between particle distributions 2nd, 6th and 10th strip, Case 1

4.5 Airfoil contamination

A graphic representation of the particle impact pattern on the blade surfaces is reported in Fig. 4.12. Each pattern represents the projection of the fouled airfoil into a perpendicular plane with respect to the spanwise direction. On the upper corner in the left side the spanwise station and the correspondent percentage of the blade span can be seen. The blades were divided into 11 strips along the spanwise direction and each dot on the graph represents a single particle that has hit the blade surface. The upper surface is the suction side, while the lower surface is the PS, for each picture.

For both rotors, in the cases with smaller particles (up to 0.50 µm), the contamination comprises the entire height of the blade in the suction side, while, in all cases, particles impact at least the first 25 % of the span in the suction side. This phenomenon, noticeable in particular for the bigger particles, is due to the flow separation and consequent three-dimensional vortex that drags the contaminants into the vicinity of the hub. Flow separation in the corner region of the blade passage

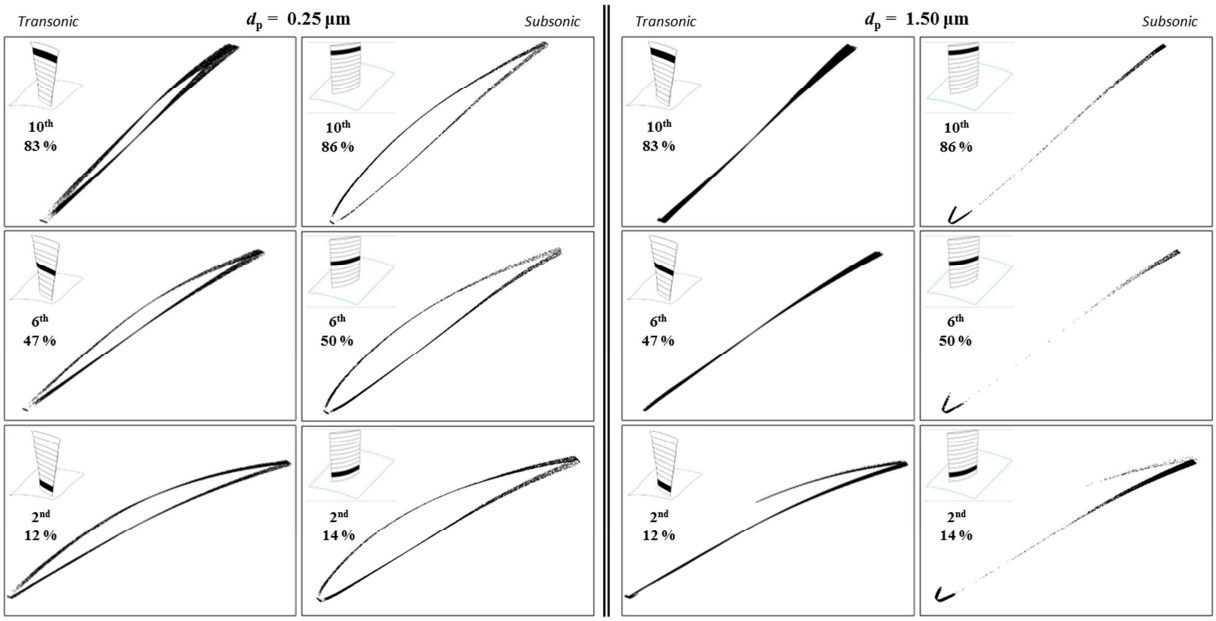

Figure 4.12 – Airfoil impact patterns, d_p = 0.25 µm and d_p = 1.50 µm

is common (Gbadebo *et al.*, 2005) and strongly influences the particle impact pattern. The differences in the particle impact pattern are more evident for the cases with bigger particles (d_p > 0.50 µm), while for the smaller particles the airfoil contamination of the two rotors is similar.

Analogous results can be found in Silingardi *et al.* (2013) where field data regarding the deposition of foulants on a transonic blade compressor are reported. The authors reported the blade surface condition after 25,000 operation hours and the authors highlighted that three-dimensional flow features cause small particles to be deposited in zones where secondary flows and vortices are dominant. The major differences in the particle impact pattern between the rotors are localized in the leading edge zone. For the two rotors, the effect of the stagnation (and the inertial particle impact) determines the high presence of impacting particles on the leading edge and, by contrast, there are no particles in the area immediately downstream. The phenomenon is more evident in the transonic rotor, where the velocity field could be characterized by local normal shock waves due to the local curvature of the airfoil (Cumpsty, 1989). In this blade areas there is also a very different values of shear stress. Particles that reach areas of high shear stresses have a high chance of being swept downstream, and then, fewer deposits take a place downstream of the suction side leading edge. The differences in the shape and size of the leading edge, determine differences in the particle impact pattern. The particles can surround the subsonic leading edge because it is thicker than the transonic leading edge. In this manner, the subsonic suction side appears more contaminated than the pressure side in particular in the case of bigger particles. These results can clarify the differences highlighted for the trends reported in Figs. 4.7 and 4.8. The deposition on

the leading edge represents a key aspect, because the changes in the leading edge area (shape, size and surface roughness) represent one of the most important causes of the performance degradation due to fouling (Suder *et al.*, 1995) and erosion (Balan and Tabakoff, 1984).

There are particular impact patterns in the first portions of the chord, where there is a high presence of impacting particles on the leading edge and, by contrast, there are no particles in the area immediately downstream. This effect, highlighted in Fig. 4.13 for the transonic rotor, is due to the phenomena of stagnation and normal shock waves induced from the nose of the airfoil. In Fig. 4.13 it is possible to observe the pattern of impact (Case 2), for the 6th strip (47% of span) and the contour plot of the airflow velocity of an blade-to-blade surface superimposed. In Fig. 4.13, for both the suction side and pressure side, this phenomena that influences particle impact on the blade surface can be seen. In the Appendix I, an overall representation of the impact zone is reported for both of rotors.

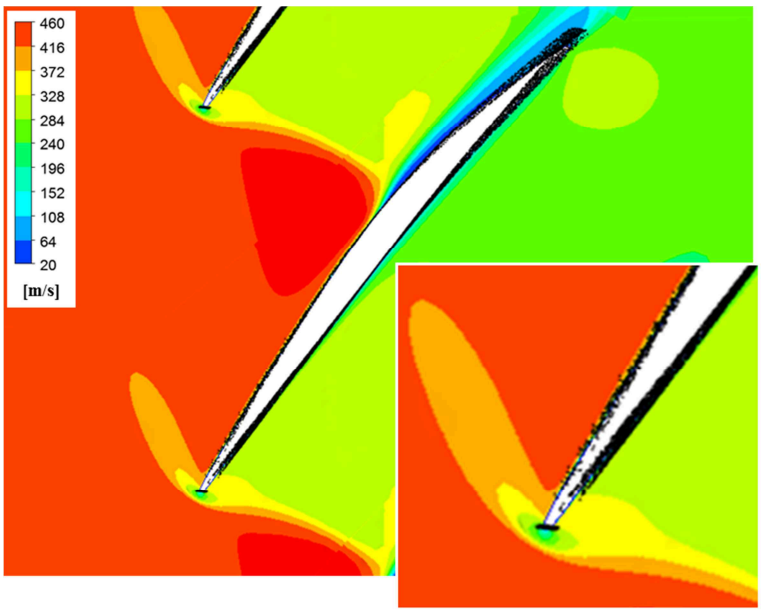

Figure 4.13 – Blade-to-blade airflow velocity contours and impact patterns superimposed, 6th strip, Case 2 (transonic rotor)

4.6 Particle trajectories

Figures 4.14 and 4.15 report the particle trajectories at the root and at the top of the blade for the transonic and subsonic rotor respectively. At the end walls (hub and shroud) the particle trajectories and, in the same way, the fluid dynamic phenomena are quite similar for the two rotors. At the hub, the separation generates a three-dimensional vortex that drags the contaminants into the vicinity of the hub, as

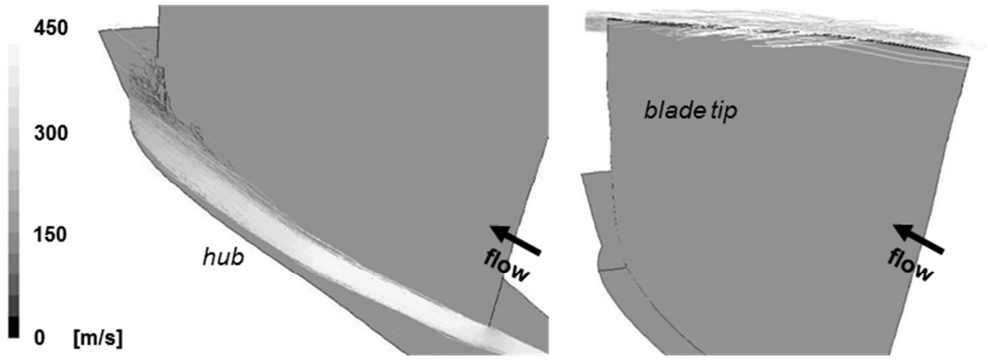

Figure 4.14 – Particle trajectories at the hub and at the blade tip, d_p = 0.25 µm (transonic rotor)

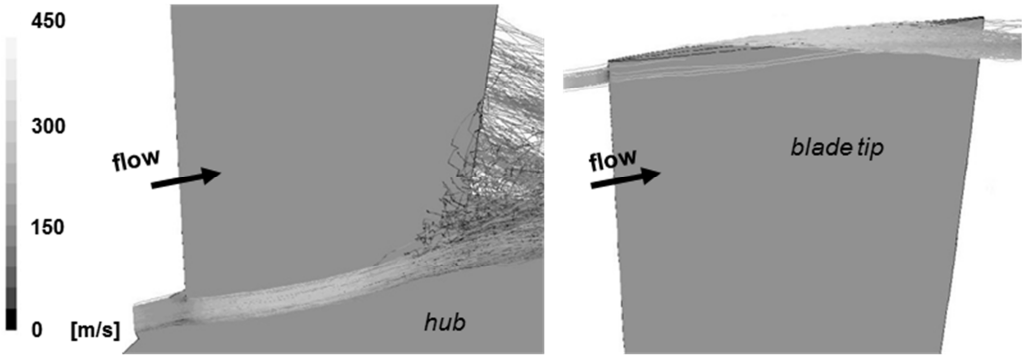

Figure 4.15 – Particle trajectories at the hub and at the blade tip, d_p = 0.25 µm (subsonic rotor)

mentioned above. At the blade tip the tip leakage vortex drags the particles from the pressure side to the suction side of the blade. These three-dimensional flow features cause small particles to be deposited in zones where secondary flows and vortices are dominant. The deposits at the blade tip, especially on the suction side, determine the greater performance drop of the compressor. As reported by Aldi *et al.* (2014), the increased surface roughness and thickness of the airfoil at the blade tip determines a significant work redistribution and greater performance losses.

4.7 Particle impact: observations

The results presented in this chapter refer to particular particle-wall interaction conditions. The ideal-adherence condition imposed on the blade surfaces determines that each particle that impacts with the blade surface sticks there. These conditions, actually representative of very humid or glue-contaminated conditions, have been used in some experimental applications. Vigueras Zuniga (2007) simulated artificial blade fouling with a real dust sample by using a stationary cascade whose blades were impregnated with a thin layer of UW40 oil used as a glue-agent. This thin layer increased the particle deposition on the blade surfaces. The dust used in the

experimental tests was collected from Inchon Power Plant and represents real dust that determines fouling issues. The author also reported some blade pictures resulting from an inspection at Didcot Power Plant (UK) where one of the units was opened to overall maintenance.

In this paragraph a qualitative comparison between the CFD results reported in this chapter and the experimental results presented by Vigueras Zuniga (2007) is reported. First of all, the comparison between the compressor's flow field is necessary in order to judge the successive particle impact comparison. Figure 4.16 shows the velocity values and some fluid dynamic phenomena such as the peak of velocity on the suction side, the low-velocity bubble close to the leading edge and the wake after the airfoils. The shape of the airfoils is quite different yet in a qualitative way the two flow fields are quite similar allowing the particle deposition comparison.

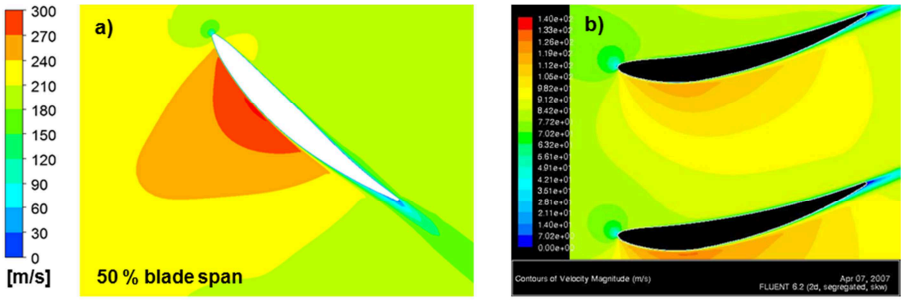

Figure 4.16 – Flow field comparison: a) Blade-to-blade velocity field at the best efficiency point at 50 % of the blade span (subsonic rotor), b) velocity distribution in the 3rd passage (Vigueras Zuniga, 2007)

Figure 4.17 shows the overall impact pattern obtained through the CFD simulations. Black regions or in some cases, only black dots, refer to particles that have impacted on the blade surface. The impact pattern (black) is superimposed with respect to the mesh node that provides the blade shape (grey dots). Since Vigueras Zuniga's results (Vigueras Zuniga, 2007) do not report the particle diameter that composes the real dust used in the experimental tests, for the qualitative comparison only one case (that which fits best) is considered.

In the stationary cascade tests, the impact pattern and deposition are not affected by centrifugal forces because the cascade is a stationary test facility. In addition, the experimental results are not affected by three dimensional fluid dynamic phenomena. As reported by Fottner (1989) and depicted in Fig. 4.18, a clearance vortex due to the tip gap (close to the shroud) and corner vortex (close to the hub) determines the three-dimensional flow structure of the flow field inside an axial compressor. In a three-dimensional flow field, secondary flows, driven by the flow through tip clearances and the imbalance between the pressure field and the kinetic energy of the air in the boundary layer, have to be considered in the particle impact/deposition analysis. This means in particular, that particles can be deposited in places that

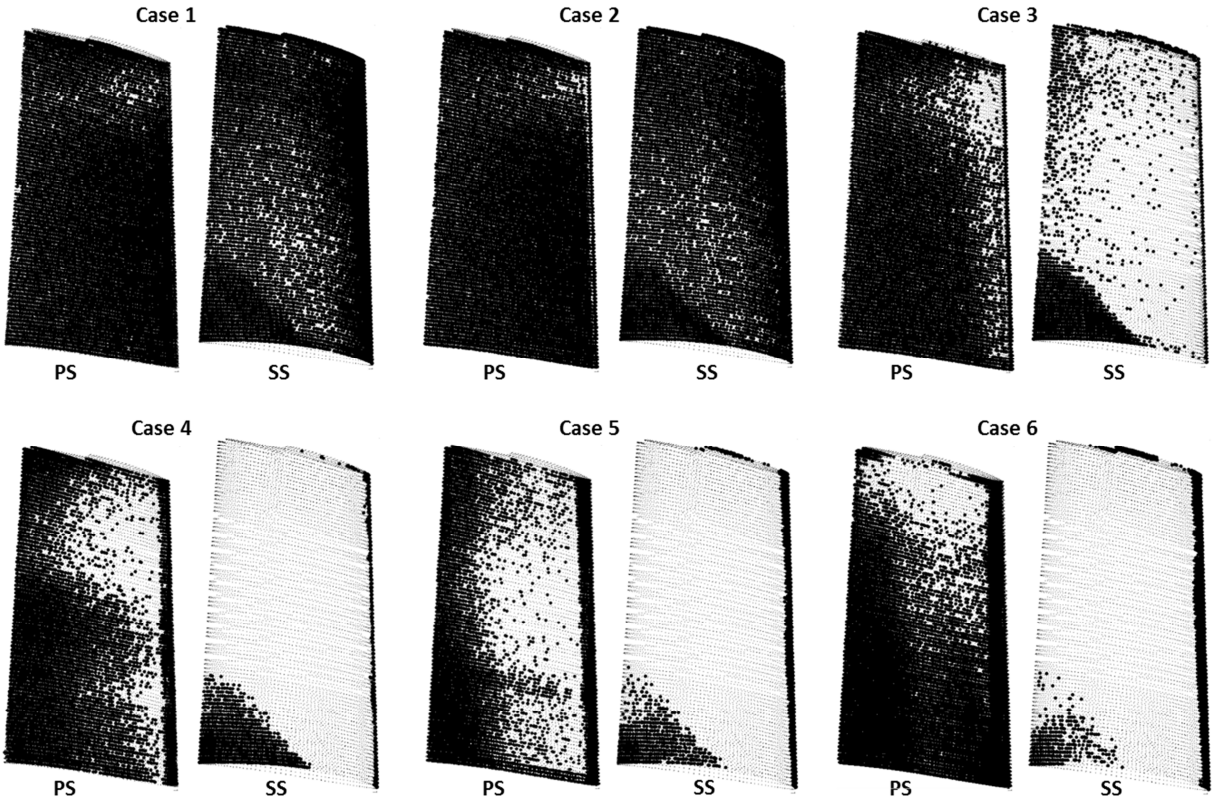

Figure 4.17 – Overall impact pattern (subsonic rotor)

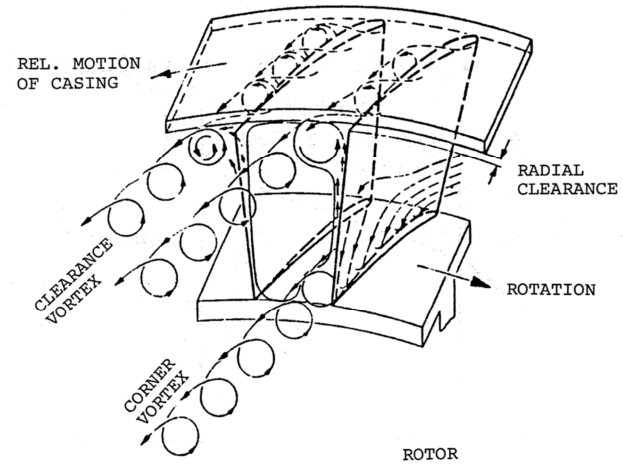

Figure 4.18 – Secondary flow regions in rotor and stator of an axial flow compressor (Fottner, 1989)

would not be reachable for particles in two-dimensional flow.

The comparison is made by using two photographic sources reported by Vigueras Zuniga (2007): (i) the experimental results obtained from the stationary cascade and (ii) the report obtained from the inspection at Didcot Power Plant (UK). Figures 4.19 and 4.20 report the qualitative comparison of: (i) the stationary cascade results after 5 h of real dust sample injection at a rate of 100 g/h, (ii) the deposits on

the 1st rotor blade pressure surface (Didcot Power Plant, UK) and (iii) the particle impact pattern of Case 5.

Figure 4.19 reports the pressure side comparison. Particle impact on the rear zone of the pressure side is clearly visible in the stationary cascade results as well as in the CFD impact pattern. Differences are due to the centrifugal force action and to the different composition and size of the dust. Leading edge deposits are in strong agreement between the CFD impact pattern and the real compressor one. The thickness of the leading edge determines higher particle deposition in this blade zone.

Figure 4.20 reports the suction side comparison. Particle impact on the rear zone of the suction side is clearly visible in the stationary cascade results as well as on the CFD impact pattern. The subsonic rotor used in this thesis shows a bubble separation in the corner region, close to the hub. These fluid dynamic phenomena influence the particle impact pattern. Leading edge deposits are in strong agreement between the CFD impact pattern and the real compressor one. The leading edge area is also involved in particle deposition in the cascade test.

Regarding the transonic rotor, a specific analysis can be conducted for the suction

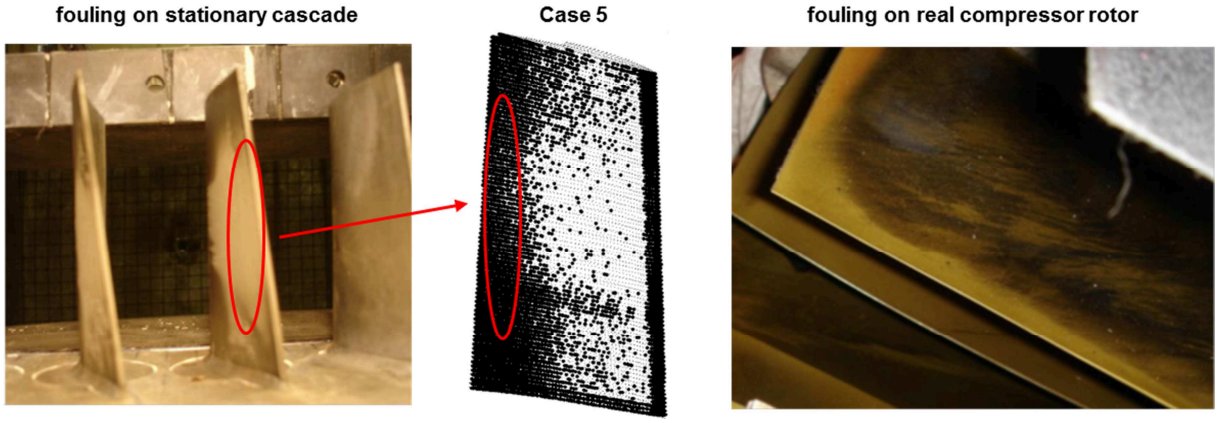

Figure 4.19 – Comparison, pressure side

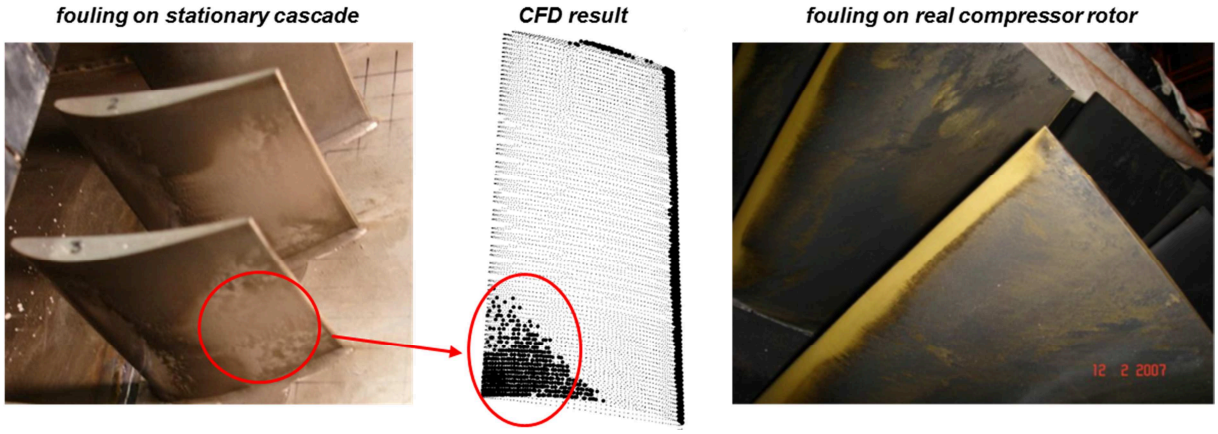

Figure 4.20 – Comparison, suction side

side. Particle impact on the suction side could be highly detrimental because the deposits on the suction side have a greater influence on the compressor performance degradation as reported by Morini *et al.* (2011). For this reason, a specific analysis regarding particle impacts on the suction side, obtained from the results of Case 2 (dp = 0.25 µm), is reported.

In Fig. 4.21 the impact distributions on the entire suction side in the case of the transonic rotor can be seen. The quantity used to represent the results is the same as the one used in Fig. 4.9 and defined by the Eq. (4.17). To improve the reading of the contour, the values of leading edge and trailing edge have been omitted. The greatest suction side impact concentration takes place at the front (close to the leading edge) and at the rear (close to the trailing edge). In fact, the peaks of the impact concentration are carried out at the end of the profiles at the 2nd and 8th strip. Only a small portion of the suction side, in correspondence to the 6th strip and approximately at half chord is almost completely free from impacts. The impact pattern of the suction side shows a peculiarity due to a specific fluid dynamic phenomenon. As reported by Parker and Lee (1972), the collision of the particles takes place in the areas preceding and following the area (line) of flow separation from the blade. As shown in Fig. 4.21 the overlapping (qualitative because of the projection on the plane) of the impact contour and the separation line (obtained by the shear stress contour plot) shows the correspondence of the two effects. From Fig. 4.21 the chordwise coordinates at which the flow separation from the blade surface occurs can be distinctly identified. In particular: (i) for the 2nd strip the separation occurs at 30 — 35 % of the chord, (ii) for the 6th strip the separation occurs at 50 % of the chord and finally (iii) for the 10th strip the separation occurs at 65 % of the chord.

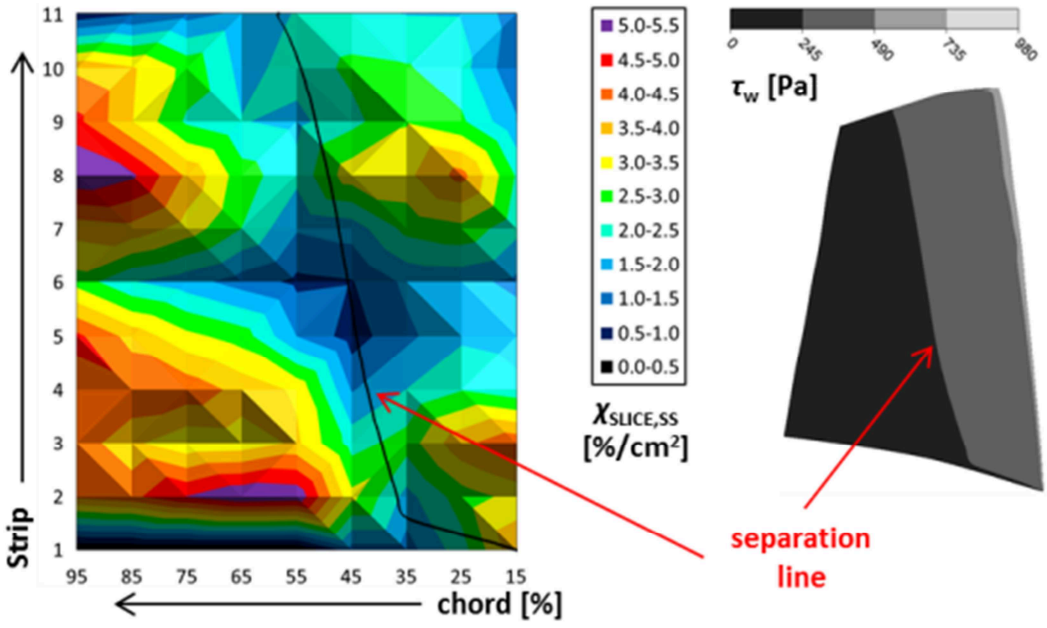

Figure 4.21 – Shear stress and deposition contour plots with the separation line superimposed, Case 2 (transonic rotor)

Chapter 5

Particle Adhesion

In order to establish which particles are dangerous from a fouling point of view the following analyses will be related to (i) impact velocity, (ii) impact angle and finally (iii) sticking probability. As mentioned above, the particle impact becomes adhesion only under specific conditions related to kinematic impact and material characteristics.

5.1 Impact velocity

The first analysis is related to the particle impact velocity v_i. The velocity values refer to the vector sum of the three velocity components u along the coordinate axes x, y and z at the impact point on the blade surface. Figure 5.1 reports the overall representation of the impact velocity for the transonic rotor. Each dots is colored by the impact velocity and it is superimposed with respect to the mesh node that provide the blade shape. Clearly visible is the effect of the separation that occurs in the suction side and the velocity impact peaks that take place at the blade tip area.

Figure 5.2 reports the overall representation of the impact velocity for the subsonic rotor. Again, each dots is colored by the impact velocity and it is superimposed with respect to the mesh node that provide the blade shape. The separation that occurs in the corner region in the suction side generates the decreasing of the particle impact velocity. Clearly visible is the high number of particles that impact the leading edge. In particular, in the case of the biggest particles (Case 6) the leading edge is completely surrounded by the particles.

The modules of the particle impact velocity for the transonic rotor in the case of particles with diameter equal to 0.15 µm (Case 1), are reported in Fig. 5.3. where the most representative strips are depicted: 2^{nd}, 6^{th} and 10^{th} (12 %, 47 % and 83 % of the blade span respectively) divided into pressure side and suction side. Each dot on the graph corresponds to the impacting particle on the blade. From Fig. 5.3 it can be noticed that:

- the impact velocity increases with the height of the blade and this phenomenon is due to the peripheral velocity;
- the lowest impact velocity can be found on the leading edge and on the trailing edge of the suction side;

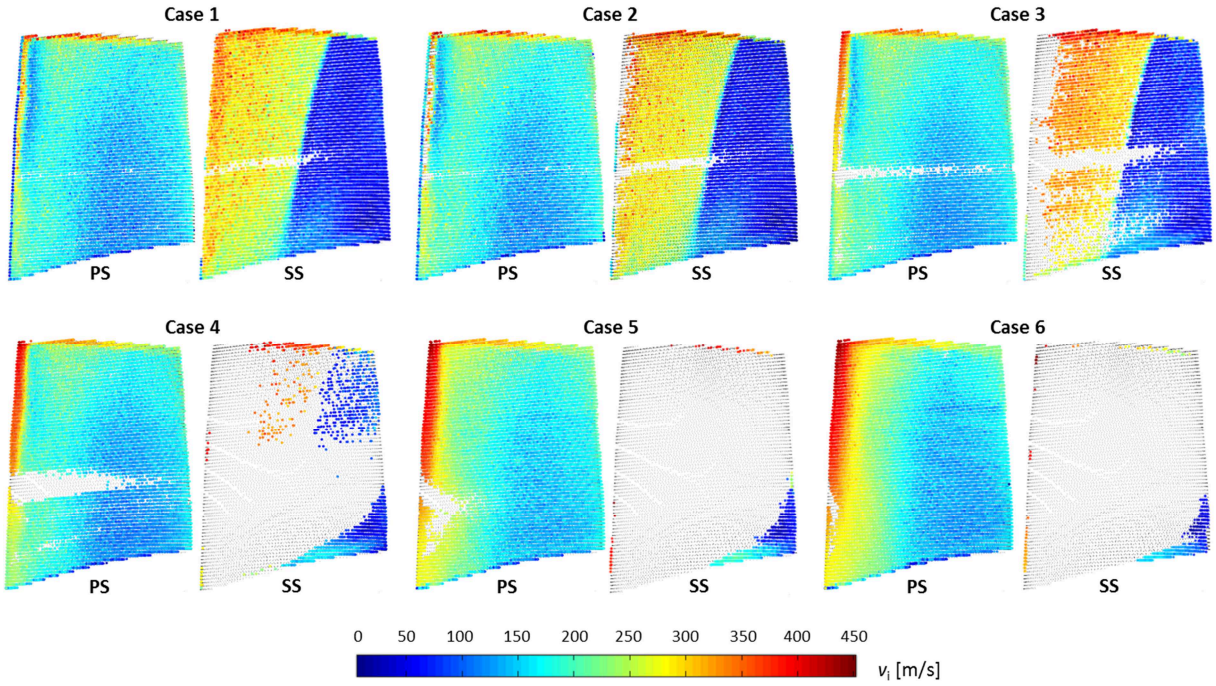

Figure 5.1 – Impact velocity (transonic rotor)

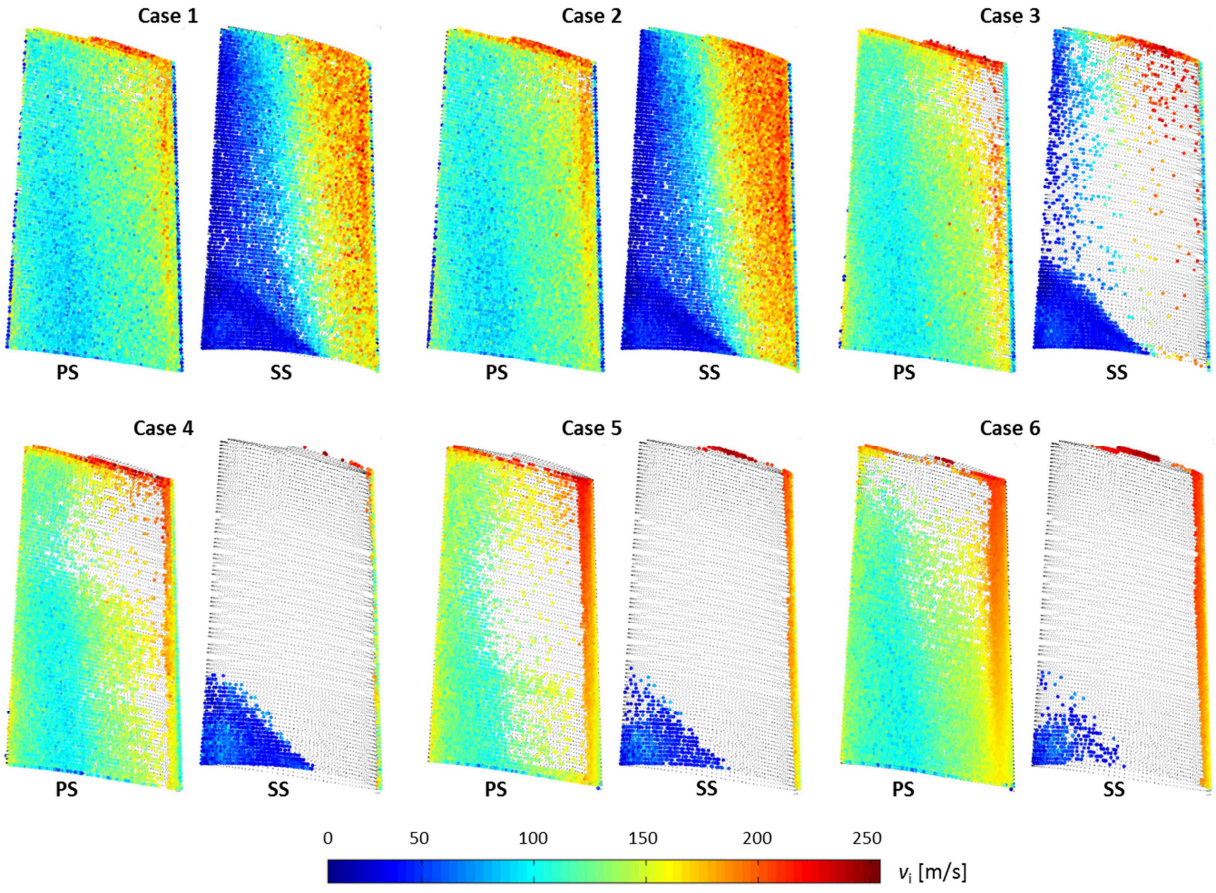

Figure 5.2 – Impact velocity (subsonic rotor)

- the highest impact velocity can be found on suction side, in particular on the first part of the airfoil chord;
- the effects of flow separation (due to the shock wave) can be clearly seen on the suction side. This phenomenon causes the drop of the particle impact velocity and at about 50 % of the chord we find the lowest impact velocity;
- on the pressure side the velocity trend is very similar for all the strips. On the first part of the chord the particles reach the peak of impact velocity while at about the 60 % of the airfoil chord the impact velocity reaches a minimum.

The analysis of Fig. 5.3 shows that the particle impact velocity is very different on the same side of blade. This difference is due to the shape of the blade (e.g. the blade height) and the fluid dynamic phenomena (e.g. flow separation). Another fluid dynamic phenomenon that influenced the particle impact velocity at the top of the blade, is the tip leakage vortex due to the blade tip gap as reported in the previous chapter through the impact location analysis. As is shown for the suction side in Fig. 5.3, the rear part of the airfoil chord is impacted by particles with a very low impact velocity while for the 11th strip, reported in Fig. 5.4, this is not quite the case.

The rear part of the airfoil chord of the 11th strip is impacted at the same time by

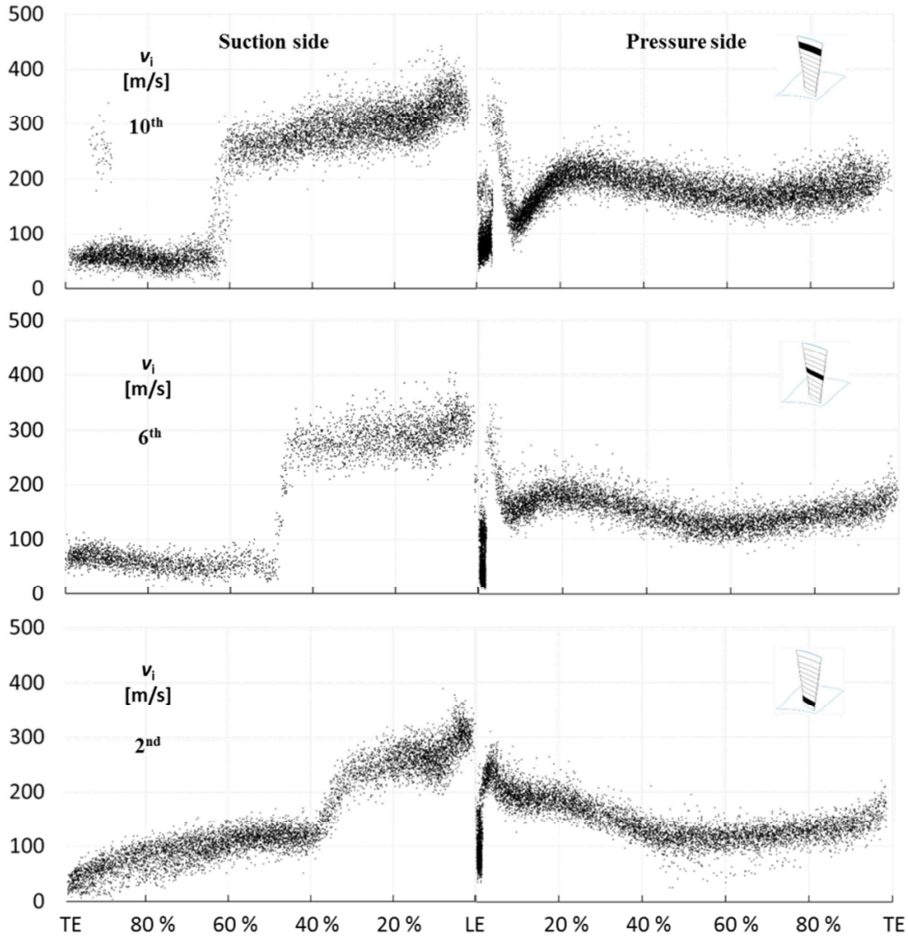

Figure 5.3 – Impact velocity 2nd, 6th and 10th strip, Case 1 (transonic rotor)

particles with very low and very high impact velocity. The particles with the highest impact velocity are the particles dragged by the tip leakage vortex from the pressure side to the suction side. In this specific case, the wall condition imposed on the blade (trap) determines a smaller amount of particles that are dragged from the pressure side to the suction side. Under real conditions, some particles bounce off the pressure side and could reach the other side of the blade through the tip gap. This effect plays a key role in the erosion problem not considered in this work due to the small particle sizes. In fact, the erosion phenomena require a particle diameter larger than 10 µm as reported by Hamed *et al.* (2006), Ghenaiet (2012) and Kurz and Brun (2012).

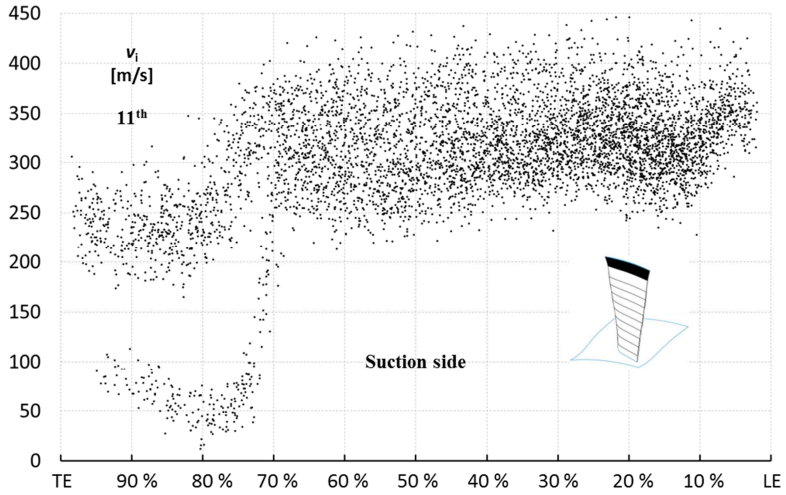

Figure 5.4 – Impact velocity 11th strip, Case 1 (transonic rotor)

In similar manner of the transonic rotor, in Fig. 5.5 three representative strips are reported: 2nd, 6th and 11th (14 %, 50 % and 95 % of the blade span blade respectively) divided into pressure side and suction side for the subsonic rotor. Each dot on the graph corresponds to the impacting particle on the blade. From Fig. 5.5 it can be noticed that the trends of the impact velocity are very similar to those found for the transonic rotor. The impact velocity are lower than the transonic case, but the same widespread velocity values can be found at the leading edge. On the pressure side the velocity trend is very similar for all the strips. At the leading edge and trailing edge the particles reach the peak of impact velocity while in the mid-chord the impact velocity reaches a minimum. In the case of subsonic rotor, there is not the effect of the shock wave in the suction side but, close to the hub, is clearly evident the effects of the separation in the corner region. In this case, flow separation influenced, not only the particle impact pattern but also the particle dynamic. The peak of the impact velocity remains at the first part of the airfoil chord as well as in the transonic rotor and the effects of the tip leakage vortex are clearly visible also in this type of compressor. The tip leakage vortex due to the blade tip gap (0.382 mm, 0.45 % of the blade span) influenced the particle impact at the top of the blade. The rear part of

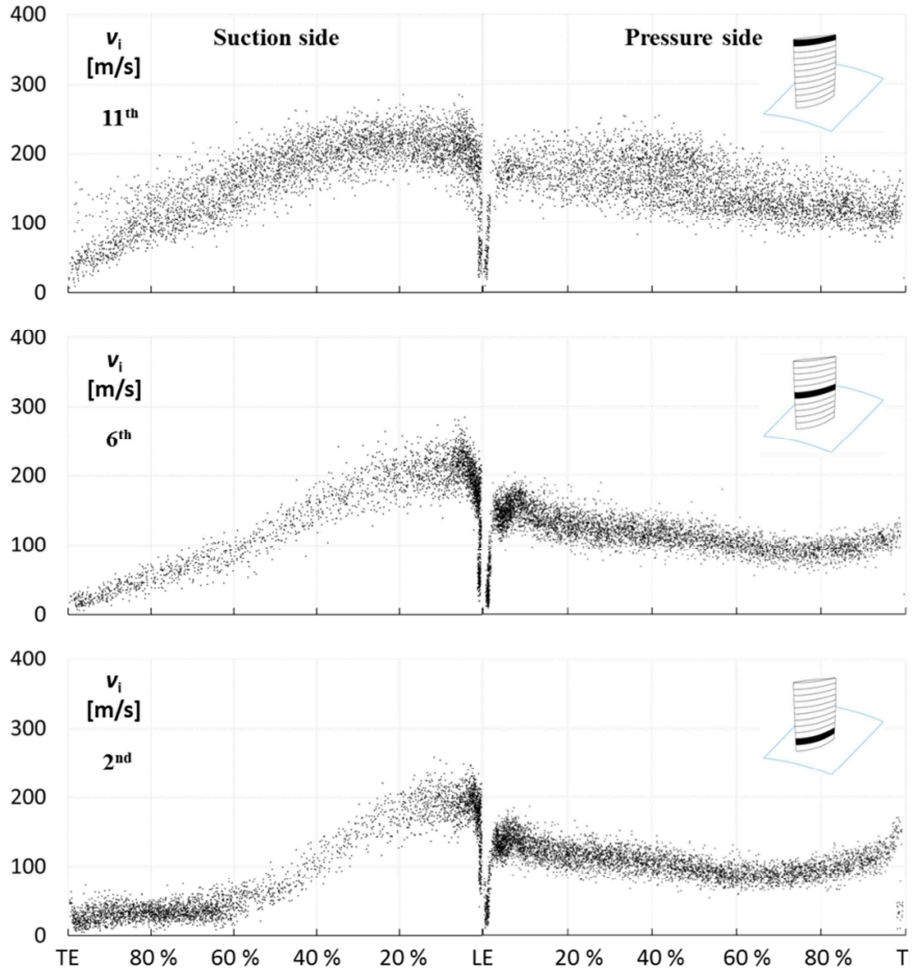

Figure 5.5 – Impact velocity 2nd, 6th and 11th strip, Case 1 (subsonic rotor)

the airfoil chord is impacted by particles with a very different impact velocity with respect to those in the other strips. The particles with the highest impact velocity are the particles dragged by the tip leakage vortex from the pressure side to the suction side.

5.2 Particle kinematic post-process

As can be seen from the previous analysis, the particle impact velocity changes from the hub to the shroud, from the pressure side to the suction side and along the airfoil chord. However, the impact velocity v_i, is not the only parameter needed to determine particle adhesion on the blade surface. As mentioned above, particle adhesion is due to a combination of an number of effects, but the most important parameters are the normal v_n and tangential v_t velocity components. In this paragraph the analysis of the particle impact angle are provided in order to better

understand the particle kinematic impact.

The impact velocity was obtained by a vector sum of the three velocity components u_x, u_y and u_z along the axes x, y and z respectively. The impact velocity was decomposed with respect to the normal (v_n) and tangential (v_t) direction. Thus, the impact angle α is the angle between the surface normal vector n and the impact velocity vector v_i. The representation of the vectors velocity is reported in Fig. 5.6.

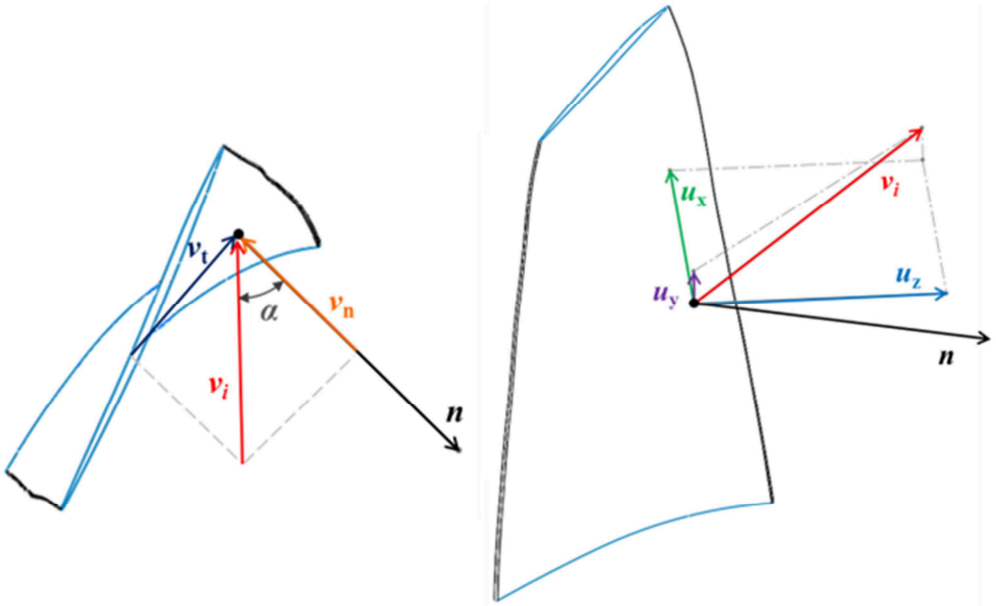

Figure 5.6 – Particle vectors velocity

Since the computational domain determined by the meshing process results in an approximation of the blade surfaces by means of a polygonal surface it is necessary to try to reconstruct the blade surface in order to calculate its normal unit vector in the collision point (i.e. not the normal of the cell face). Therefore, for each particle collision the algorithm starts by calculating a number of point which lay on the intersection of the polygonal surface and a right circular cylinder with radius r and axis parallel to the x-axis passing through the collision point as reported in Fig. 5.7. Then, it calculates an interpolating surface between these points and, finally, its normal unit vector. The accuracy of the surface reconstruction is determined by the radius, which should be high enough to avoid that all the points lay on a single cell surface but not too much to hide the actual blade surface curvature, and the number of point in the circumference. Once the normal unit vector is determined, the algorithm proceeds straightforward by determining the plane which contains the particle velocity and the normal unit vector, the inner angle between the two vectors and by decomposing the velocity in its tangential and normal components.

The particle velocity post-process is applied only for the Cases 1 – 5. These cases

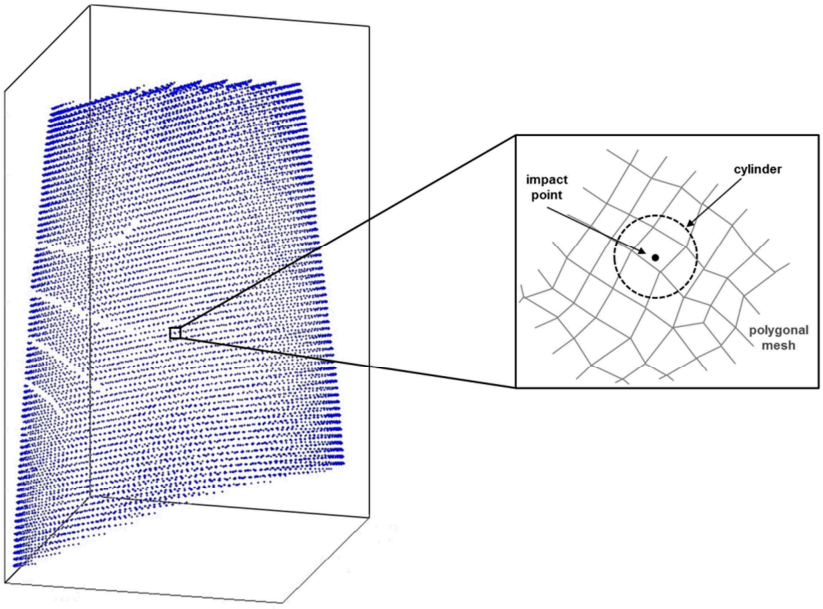

Figure 5.7 – Surface reconstruction

are considered the most interesting from a fouling point of view. The biggest particles dp = 2.00 µm (Case 6) are easily removed by a proper filtration systems (Wilcox *et al.*, 2009).

5.3 Particle impact angle

Thanks to the elaboration data realized by the aforementioned strategy, it is possible to calculate the impact angle and the two velocity component of the particle that impacts the blade surface. This paragraph focuses on the impact angle.

Figure 5.8 reports the overall representation of the impact angle for the transonic rotor. Each dots is colored by the impact angle and it is superimposed with respect to the mesh node that provide the blade shape.

In Figures 5.9 and 5.10, the particle impact angle for the pressure side of the 6th strip and for the suction side of the 10th strip (Case 2) are reported in the case of transonic rotor. In some instances the impact angle is higher than 90°. This is due to: (i) the surface local curvature (e.g. at the leading edge and on the trailing edge) and (ii) surface reconstruction approximation during the particle impact post-process. A deviation can arise from the fact that the surface is reconstructed by interpolating points on the mesh elements in the neighborhood of the point of impact. The approximation introduced by this procedure is considered acceptable by the author, allowing for a confidence band of ± 5° for all the results shown in this thesis.

Figures 5.9 and 5.10 illustrate the following observations:

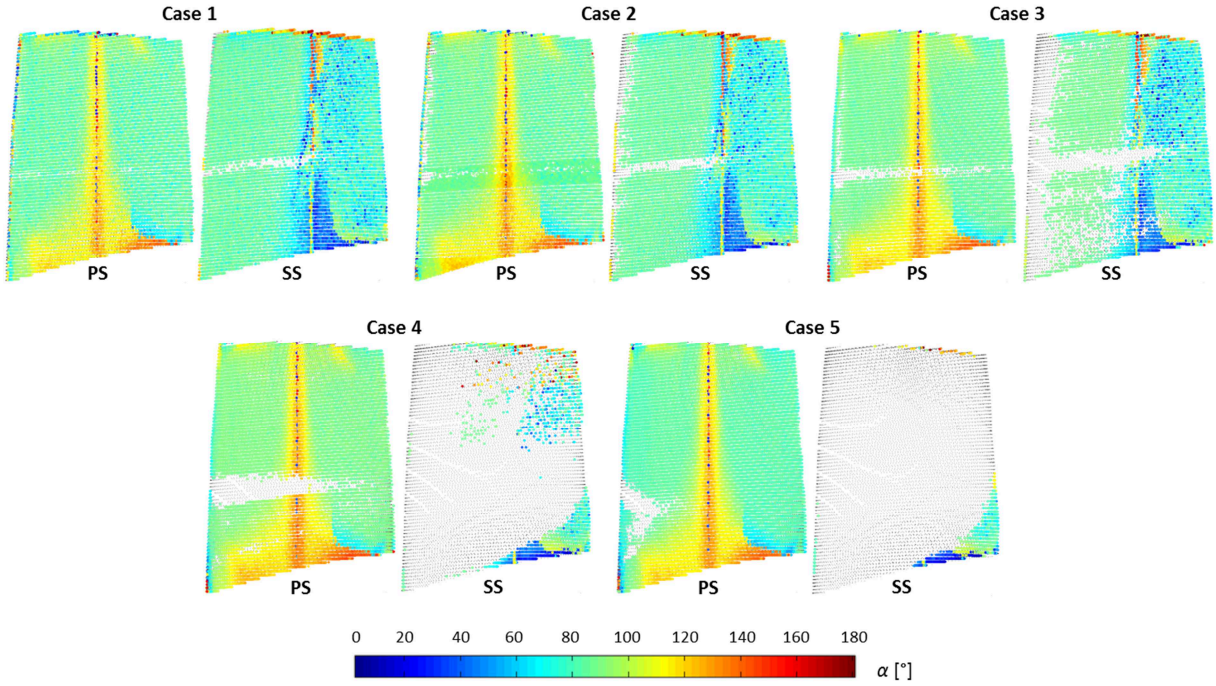

Figure 5.8 – Impact angle (transonic rotor)

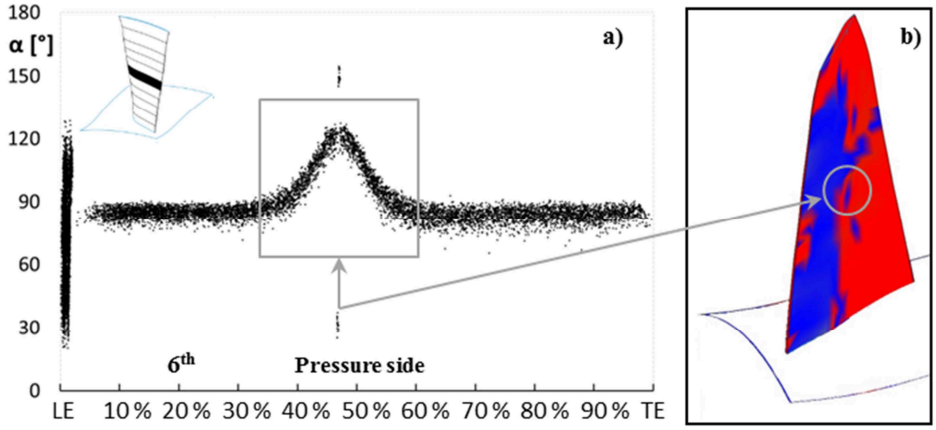

Figure 5.9 – a) Impact angle 6th strip, PS, Case 2 and b) contour plot of the pressure side curvature (transonic rotor)

- the impact angle at the leading edge (Fig. 5.9a) assumes different values from 30° to 120°;
- on the pressure side (Fig. 5.9a) the particle impact angle is very close to 90° (i.e. the particles are tangential to the blade surface) almost everywhere on the airfoil. A particular area can be noticed in the middle of the chord where the particle impact angle reaches 120°. This fact is consistent with Fig. 5.9b where the representation of the pressure side curvature is reported. The blue zone refers to a lower curvature while the red zone refers to higher curvature. The local variation of the impact angle (gray box) corresponds to the local variation of the surface curvature (gray circle). Thus, it is clearly shown that the local curvature of

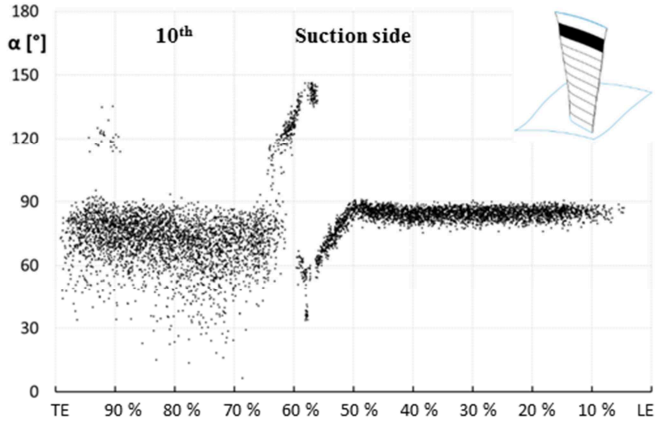

Figure 5.10 – Impact angle 10th strip, SS, Case 2 (transonic rotor)

the airfoil (e.g. dimples, surface damage, etc.) changes the particle impact angle in a significant way and, more generally, the local shape of the blade changes the particle deposition. A different impact angle can determine whether the particle sticks or slips and thus, the actual shape of the blade surface would determine the magnitude and the rate of the fouling. These findings represent a useful guide for blade surface treatment and control during the manufacturing and maintenance process. The same phenomenon can be noticed for all the strips;

- for the suction side there is also a variation of the particle impact angle in the middle of the chord due to the airfoil curvature. However, it is less noticeable than on the pressure side;
- on the suction side the particle impact angle is lower than the pressure side and this implies that the particle hits the surface with a value of normal velocity higher than the tangential velocity. This is noticeable in the last part of the chord where the flow is separated from the blade.

Figure 5.11 reports the overall representation of the impact angle for the subsonic rotor. Each dots is colored by the impact angle and it is superimposed with respect to the mesh node that provide the blade shape.

Figure 5.12 reports the impact angle analysis provided by the subsonic rotor. From Fig. 5.12 the following observation can be reported:

- the impact angle at the leading edge assumes different values from 0° to 180°;
- on the pressure side the particle impact angle is very close to 90° (i.e. the particles are tangential to the blade surface) almost everywhere on the airfoil. A particular area can be noticed in the middle of the chord where the particle impact angle range is wider. This local variation of the impact angle corresponds to the local variation of the blade surface curvature in similar manner to that influence the particle impact angle in the case of transonic rotor;

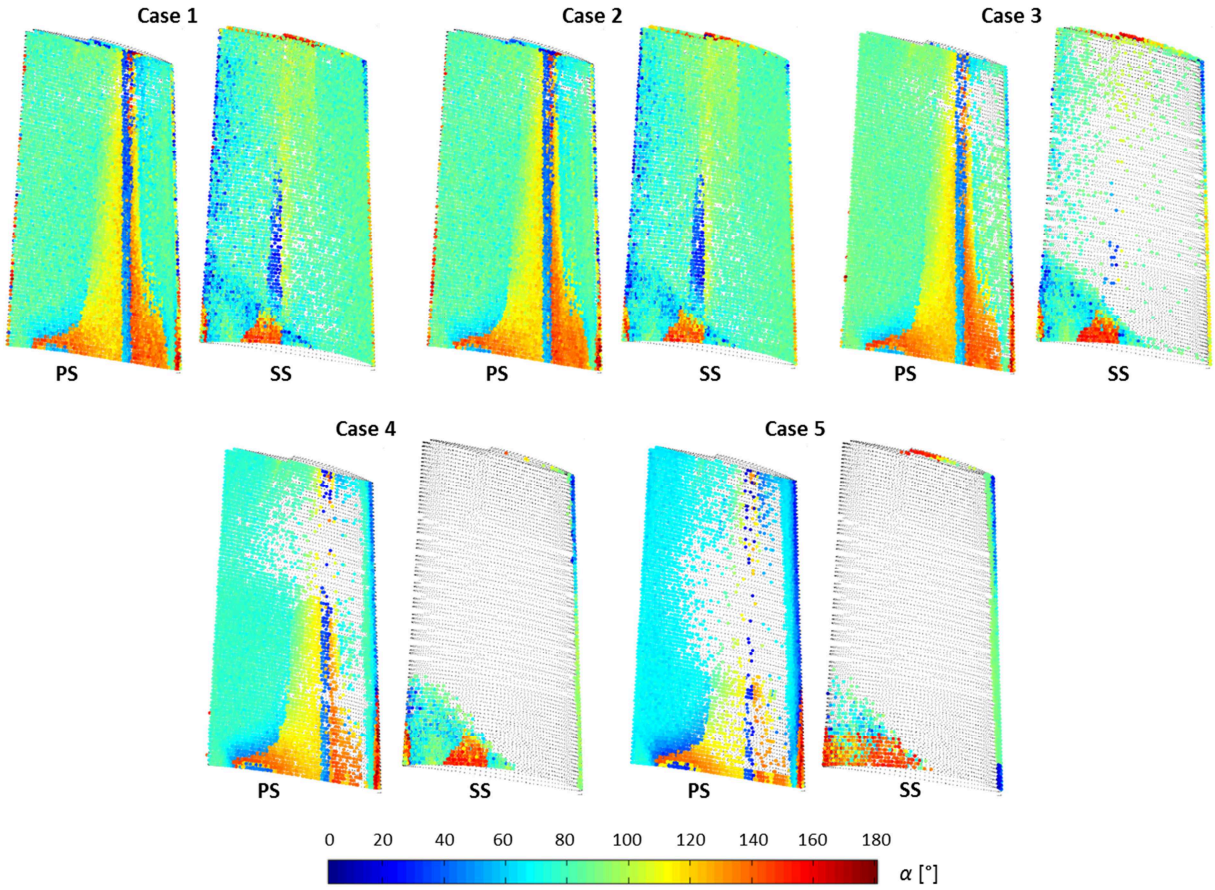

Figure 5.11 – Impact angle (subsonic rotor)

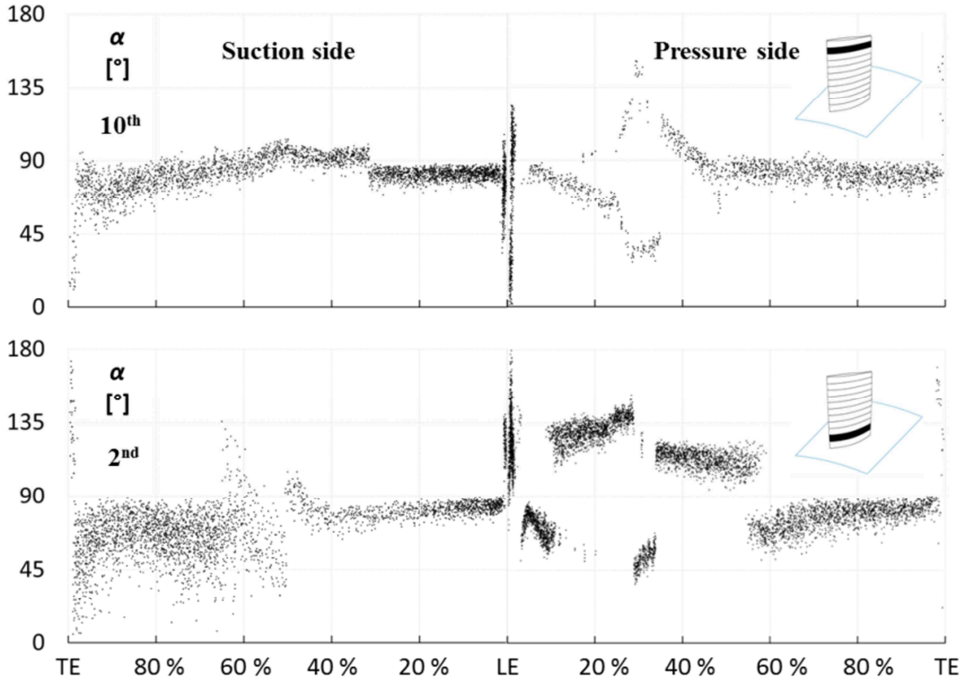

Figure 5.12 – Impact angle 2nd and 10th strip, Case 2 (subsonic rotor)

- for the suction side there is also a variation of the particle impact angle in the middle of the chord due to the airfoil curvature. However, it is less noticeable than on the pressure side;
- on the last part of chord on the suction side, the particle impact angle is lower than the pressure side and this implies that the particle hits the surface with a value of normal velocity which is higher than the tangential velocity. For the 2nd strip this fact is more evident because the air stream flow is separated from the blade.

In general way, areas characterized at the same time by very high tangential velocity and very low normal velocity (impact angle close to 90°) should not be subject to particle deposition because in this case the particles tend to slip on the blade surface. However, in the other areas with a lower impact angle, the normal velocity promotes particle sticking (e.g. in the case of ductile particles). Similar evaluations can be made for cases in which the blade surface is contaminated by water, oil or grease and in the case of viscous particles (e.g. oils, grease) that should stick to the blade surface more easily because of the high normal velocity.

As shown in the first paragraphs, the study of particle adhesion on a surface comprises a large number of aspects (materials and surface roughness among others) and probabilistic analyses are often used due to the unique nature of each contact. In this paper, the authors provide a quantitative analysis of particle adhesion by using the experimental results found in Poppe *et al.* (2000) in which particle velocity and materials are among the most similar to the particles causing fouling phenomena.

5.4 Sticking probability

The Sticking Probability (SP) analysis is closely related to the experimental results provided by Poppe *et al.* (2000). The sticking probability was calculated for each normal impact velocity v_n by sliding averaging in groups. The groups consisted of 11 collision events for the smallest and largest velocities respectively and of up to 71 collision events for the intermediate velocities, thus accounting for the uneven velocity distribution of the impacts. The upper and lower standard deviations (1σ) for the sticking probability are reported in Figs 5.13 and 5.14 (black continuous lines). The trends refer to irregular grains of silicon carbide ($\rho_p \approx 3{,}000$ kg/m^3, $E \approx 410$ GPa and hardness ≈ 2,800 kg/mm^2) with an average diameter equal to 0.37 μm and 0.64 μm that impacts a dry, polished silica surface. In Figs 5.13 and 5.14 SEM images of a silicon carbide sample are also reported. The sticking probability among the 11 slowest and the 11 fastest collisions is separately given as a constant value in the corresponding velocity interval (reported with a linear segment in Figs 5.13 and 5.14). The capture velocity is the velocity where the 1σ limits of the sticking

probability are 0.5. Such a definition results in a physically meaningful quantity only if the sticking probability behaves similarly to a step function. The particle characteristics used in Poppe *et al.* (2000) are quite different compared to the classic particle characteristics involved in fouling phenomena. In particular, the silicon carbide particles Poppe *et al.* (2000) have a very high level of hardness and this implies that the rebound properties could be different from those found in the real fouling applications. More details on materials and experimental results can be found in Poppe *et al.* (2000).

Some results related to the influence of the powder hardness on the deposition efficiency are reported in the cold spray deposition studies. A very complete analysis on this topic could be found in Papyrin *et al.* (2007). The authors report the influence of the powder hardness on deposition efficiency. The deposition efficiency for each powder was determined in separate tests by measuring the mass of powder deposited onto the planar Ti-CP substrate to the mass of powder loaded into the laboratory powder feeder. In these applications flow velocity and temperature play a key role in the deposition phenomena. Table 5.1 summarize the tests related to discover the influence of the powder hardness, then its ductility. The tests are conducted with a flow temperature equal to 550 °C. From the Table 5.1 is clearly the influence of the powder hardness. In fact, the hardest powder shows the lowest value of deposition efficiency. Size and shape of the powder do not influence the deposition results.

Table 5.1 – Powder characteristics and deposition efficiency measurements (Papyrin *et al.*, 2007)

Powder Type	Size [µm]	Hardness [VHN]	Shape	Deposition Efficiency [%]
Ti-6Al-4V, Gas Atomized	29.0	291	spherical	78
Ti-6Al-4V, Plasma Atomized	27.0	280	spherical	86
Ti-6Al-4V, HDH type	30.7	351	irregular	66
Ti (chemically pure), HDH type	21.0	153	irregular	85

With the experimental sticking probability trend reported in Fig. 5.13 and 5.14 it is possible to define representative trends for the correlation between the normal impact velocity v_n and the sticking probability. For the smaller silicon carbide particles (0.37 µm) reported in Fig. 5.13, the trend can be represented by two equations. The first one refers to the lower normal impact velocity (< 4 m/s)

$$\mathrm{SP} = -0.09\, v_n + 0.99 \tag{5.1}$$

and the second one refers to normal impact velocity in the range 4 – 90 m/s

$$\mathrm{SP} = 2 \cdot 10^{-6}\, v_n^3 - 0.000378 v_n^2 + 0.011800 v_n + 0.587100 \tag{5.2}$$

The results of Eq. (5.1) and (5.2) are reported in Fig. 5.13, with the experimental results obtained by Poppe *et al.* (2000) superimposed. As can be noticed from Eq. (5.1), in the case of the normal impact velocity equal to 0 m/s, the sticking probability is equal to 0.99.

In the same way, for the larger silicon carbide (0.64 µm) reported in Fig. 5.14, the trend can be represented by two equations. The first one refers to the lower normal impact velocity (< 4 m/s)

$$\mathrm{SP} = -0.112 v_{\mathrm{n}} + 0.990 \tag{5.3}$$

and the second one refers to normal impact velocity in the range 4 – 90 m/s

$$\mathrm{SP} = -6 \cdot 10^{-5}\, v_{\mathrm{n}}^2 - 6e-4\, v_{\mathrm{n}} + 0.545 \tag{5.4}$$

Again, the results of Eqs (5.3) and (5.4) are reported in Fig. 5.14, with the experimental results obtained by Poppe *et al.* (2000) superimposed. The threshold normal velocity (equal to 4 m/s) and the degree of the polynomials was chosen in order to better describe the experimental trend results.

With the definition of the sticking probability (Eqs (5.2) and (5.4)), for Cases 1 – 3 the SP = 0.5 is in correspondence to a normal impact velocity v_{n} equal to 48.35 m/s. However, for Case 3 and 4, the SP = 0.5 is in correspondence to a normal impact velocity v_{n} equal to 22.85 m/s. Thus, the smaller particles have a wider range of normal impact velocity for which particle impact with the blade surface becomes (with a high probability) a permanent adhesion.

Equations (5.1) – (5.4) are used to calculate the sticking probability for each particle stuck to the blade surface by using the normal impact velocity. For this reason, in Figs. 5.15 and 5.16 the overall representation of the normal impact velocity for the transonic and subsonic rotor respectively are reported.

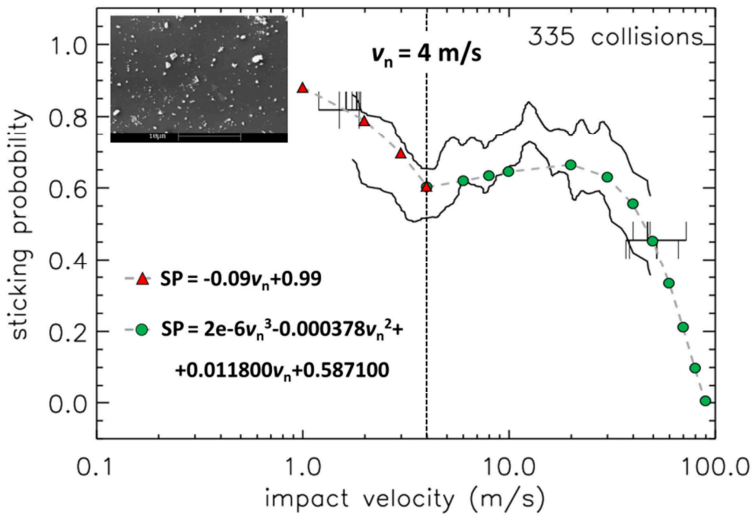

Figure 5.13 – Sticking probability vs normal impact velocity of silicon carbide particles, 0.37 µm on silica target (Poppe *et al.*, 2000) and trend of adopted equations superimposed

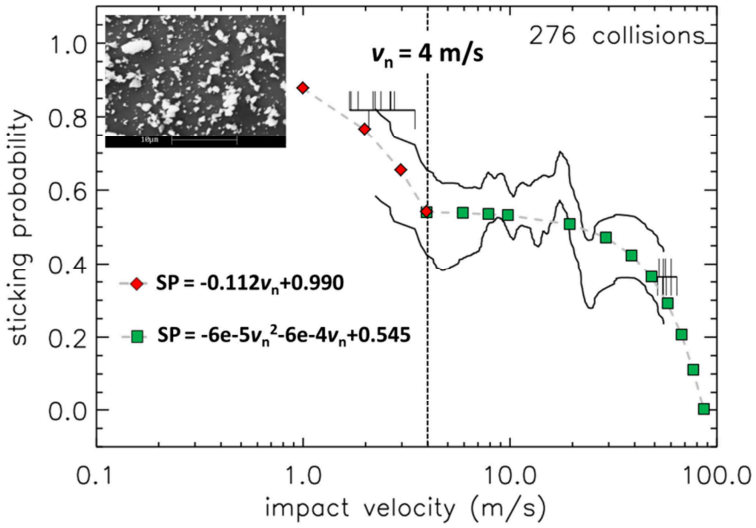

Figure 5.14 – Sticking probability vs normal impact velocity of silicon carbide particles, 0.64 µm on silica target (Poppe *et al.*, 2000) and trend of adopted equations superimposed

In Fig. 5.17 the sticking probability for the 6th strip (Case 2) are reported in the case of transonic rotor. Each dot on the graph represents a particle that hit the blade surface with a normal impact velocity less than 90 m/s. Only the particles with a normal velocity component towards the surface are taken into account. This procedure allows the identification of the dangerous particle (that will be able to stick) with respect to fouling phenomenon only. Fig. 5.17 illustrates that:

- the SS is completely covered by particles that have a sticking probability of about 0.7;

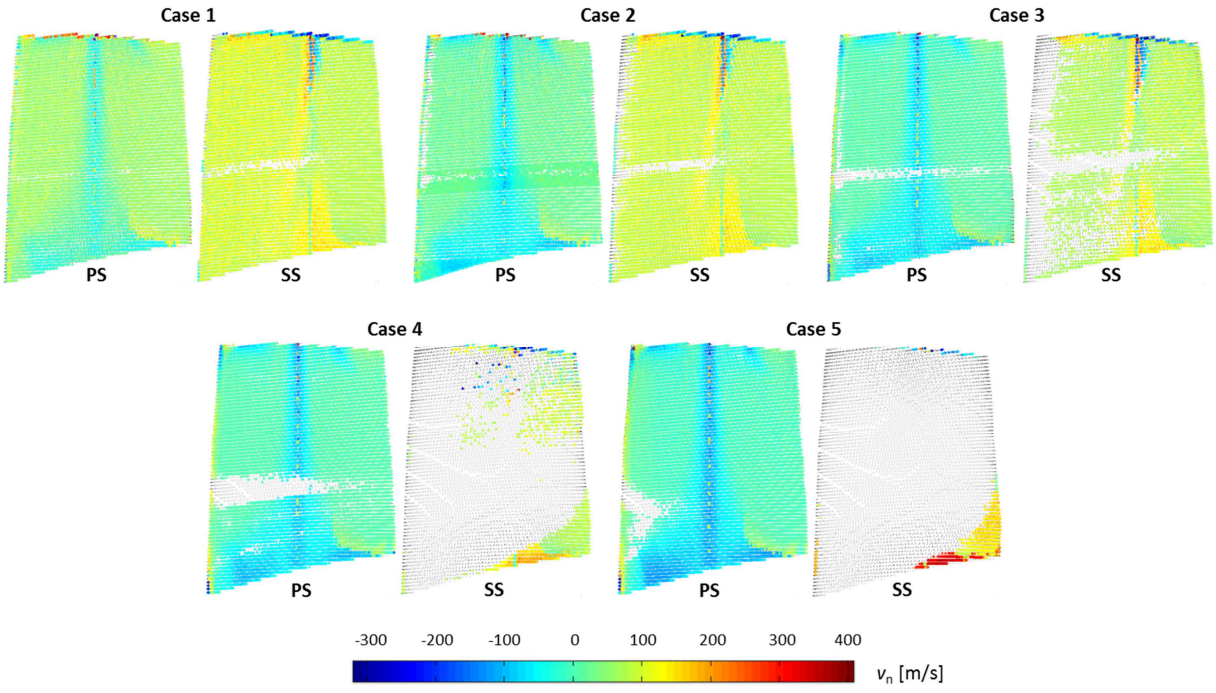

Figure 5.15 – Normal impact velocity (transonic rotor)

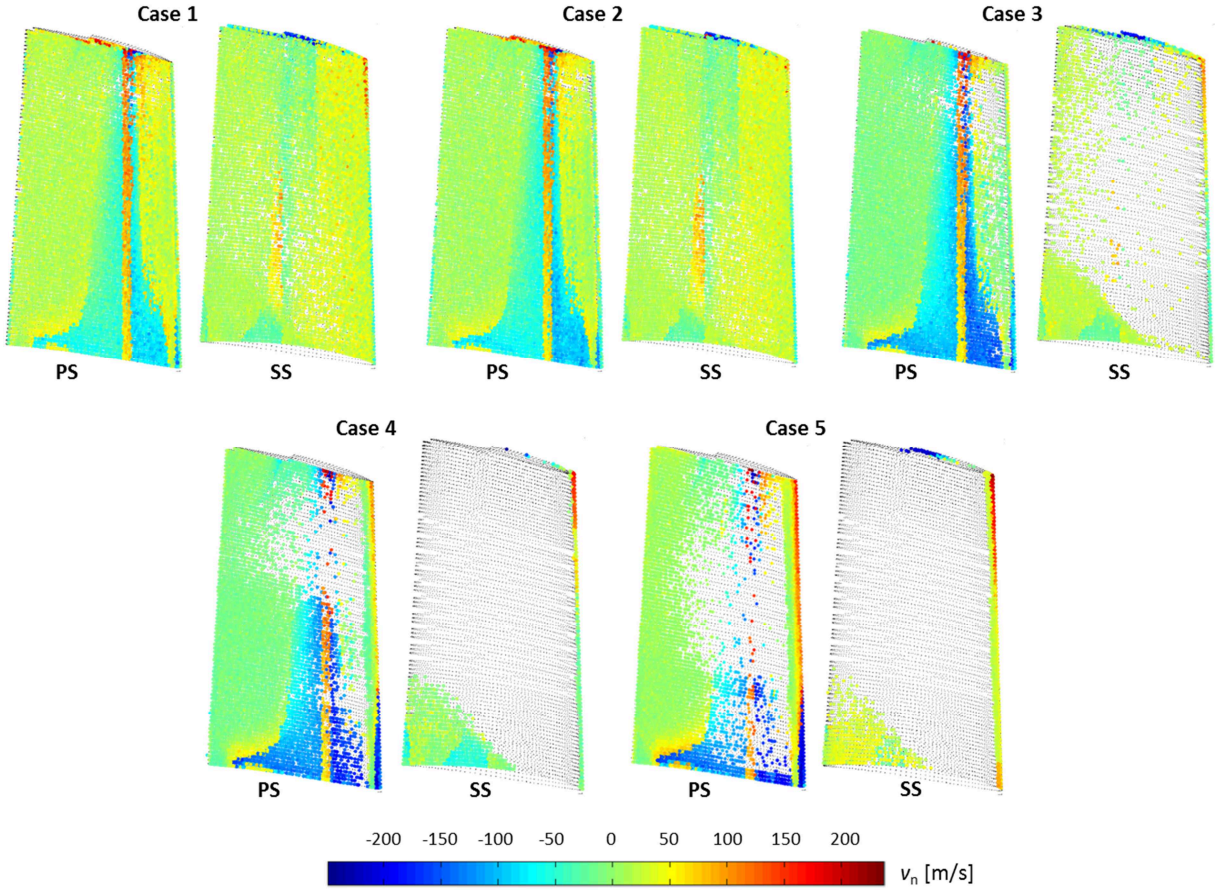

Figure 5.16 – Normal impact velocity (subsonic rotor)

- the pressure side shows an area, in the middle of the airfoil chord, in which the particles have a sticking probability equal to zero. This effect is due to the airfoil shape as highlighted in Fig. 5.9. For the other regions in the pressure side, the sticking probability is comparable with the sticking probability on the suction side, and in some cases reaches the unit;
- on the leading edge there are very dispersed values of sticking probability, probably due to the wide range of the impact angle.

The other strips show similar features. As mentioned above, the sticking probability defined in Poppe *et al.* (2000) only considers the normal impact velocity. However, in this application particular attention must be paid to the tangential impact velocity. In fact, as can be seen in Fig. 5.18 for the 6th strip, the magnitude of the tangential impact velocity is not negligible. The tangential impact velocity can reach 250 m/s or 400 m/s in the pressure side and suction side respectively. These very high values diminish the sticking probability and transform the adhesion-impact in to the slip-impact (specific studies on the interaction between normal impact velocity and tangential impact velocity are not available in literature). Conversely, it can be noted that in the separation zone on suction side, where the sticking probability is equal to 0.7, the tangential impact velocity is much smaller, thus limiting the

possibility of slip between the particle and blade surface. Regarding this aspect, some field data can be found in Silingardi *et al.* (2013), where the authors highlighted the higher deposition rate where the shear stress between air and blade surface is lower. This confirms the results obtained in this work by linking together the sticking probability data and the impact dynamic characteristics. In Fig. 5.19 the overall representation of the tangential impact velocity for the transonic rotor is reported.

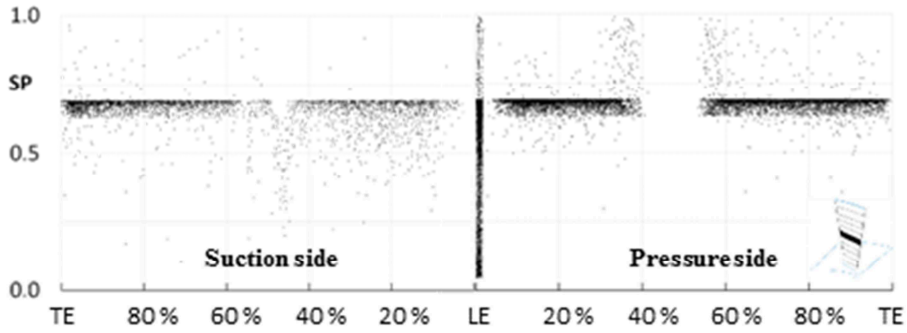

Figure 5.17 – Sticking probability, 6th strip, Case 2 (transonic rotor)

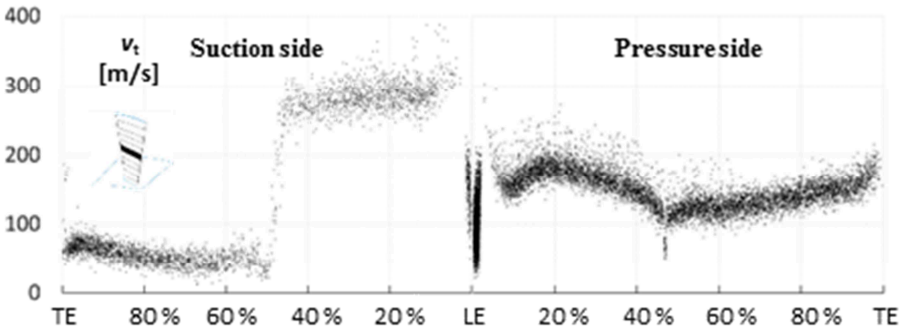

Figure 5.18 – Tangential velocity 6th strip, Case 2 (transonic rotor)

In Fig. 5.20 the sticking probability for the 2nd and 10th strips (Case 1) for the subsonic rotor are reported. Again, each dot on the graph represents a particle that hits the blade surface with a normal impact velocity of less than 90 m/s. Figure 5.20 illustrates that:

- the suction side is completely covered by particles that have a sticking probability of about 0.8;
- the pressure side shows an area, in the middle of the airfoil chord, in which the particles have a sticking probability equal to zero. This effect is due to the blade surface curvature mentioned above. For the other regions in the pressure side, the sticking probability is comparable with the sticking probability on the suction side;
- in the regions close to the leading edge there are very dispersed values of sticking probability, probably due to the wide range of the impact angle.

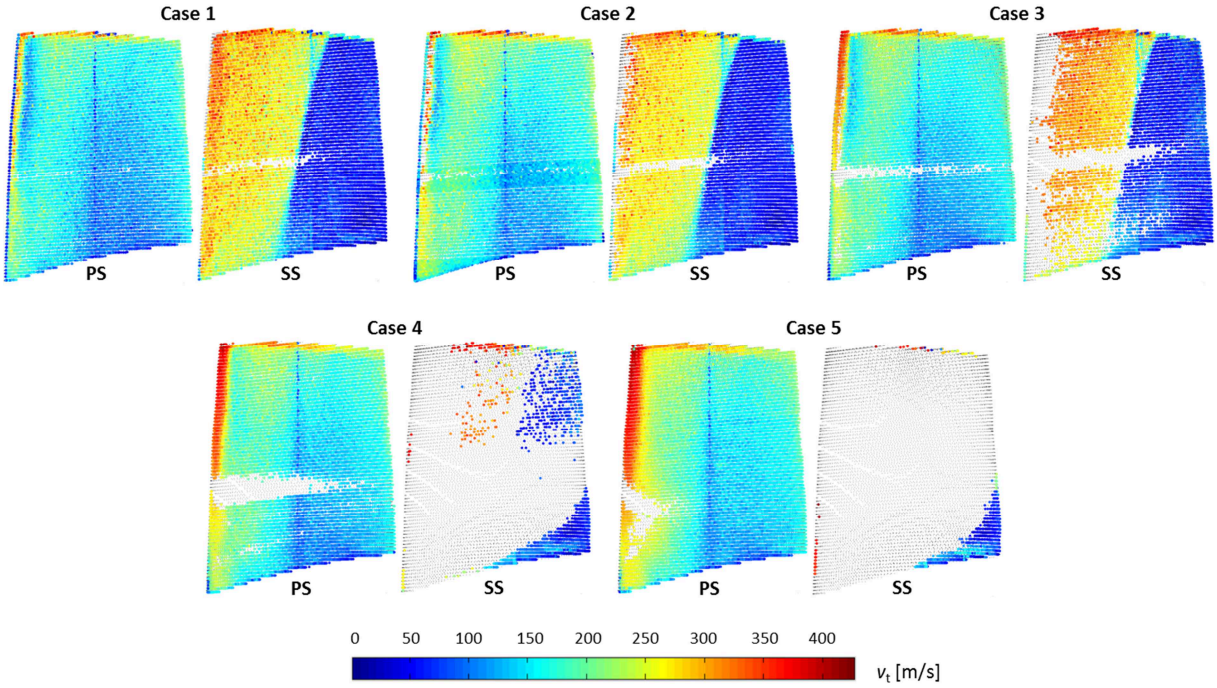

Figure 5.19 – Tangential impact velocity (transonic rotor)

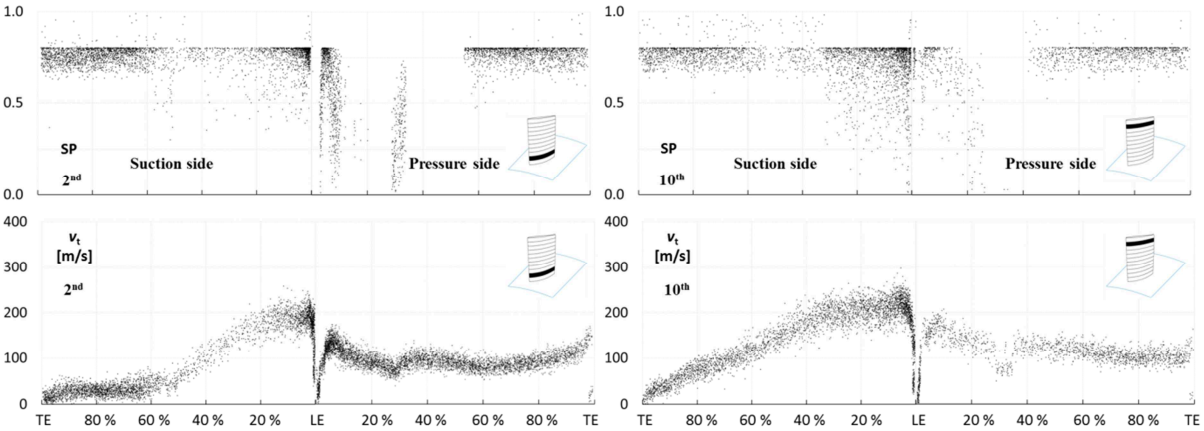

Figure 5.20 – Sticking probability and tangential velocity 2nd and 10th strip, Case 1 (subsonic rotor)

The other strips show similar features as well as for Case 2. Similar considerations, related to the tangential impact velocity, pointed out in the case of transonic rotor could be reported. Figure 5.21 reports the overall representation of the tangential impact velocity for the subsonic rotor. Also in this case, the flow separation that occurs in the suction side determines lower values of the tangential impact velocity.

The influence of the tangential velocity during the particle impact is not reported in literature. Only few studies are reported in the cold spray deposition research field. Li *et al.* (2005) show the influence of the spray angle on the deposition efficiency.

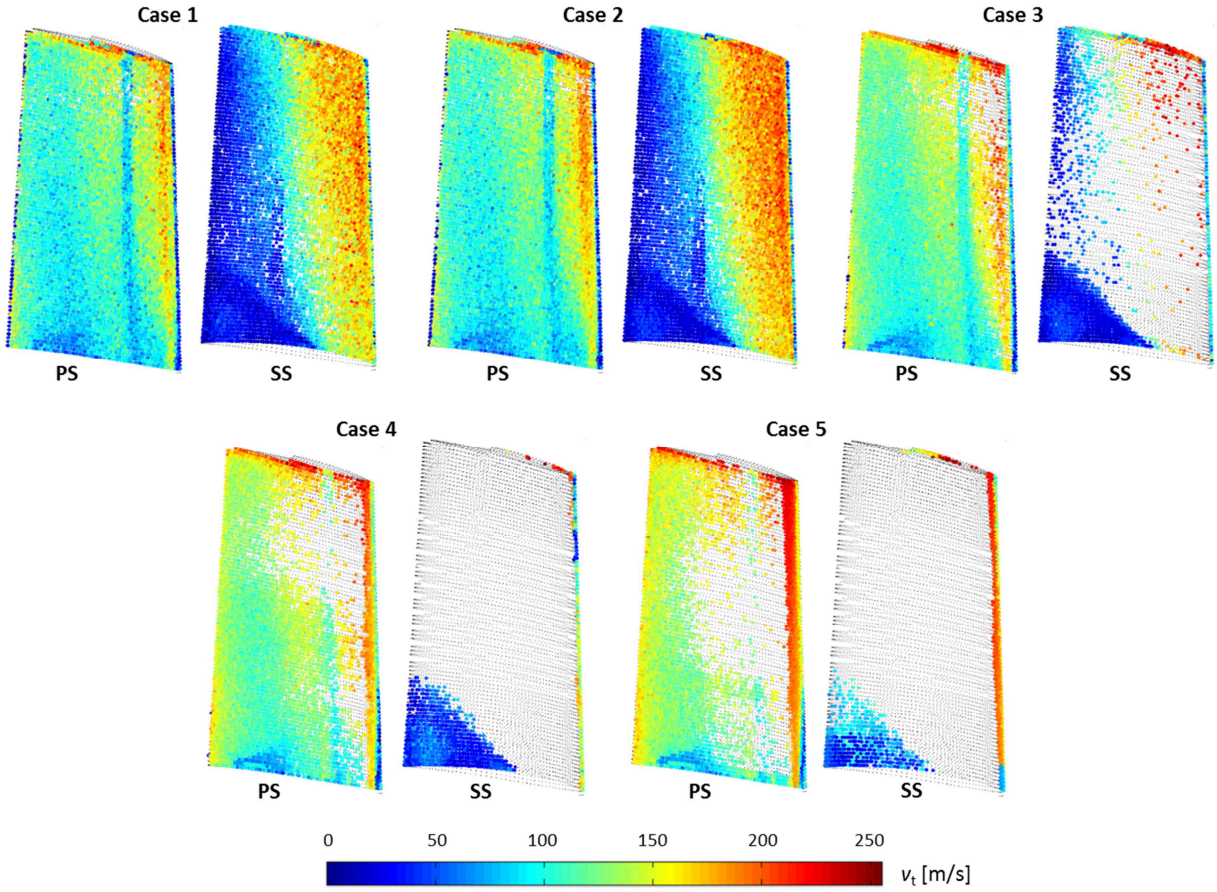

Figure 5.21 – Tangential impact velocity (subsonic rotor)

Figure 5.22 summarize the results obtained through the use of the experimental test bench reported in Fig. 5.22a. From Fig. 5.22b the maximum deposition region is around the vertical direction and its deposition efficiency reaches nearly 100 %. The particle approaching angle at which the maximum normal component is equal to the critical velocity is defined as the critical angle. The critical angle is a threshold, less than which no particle deposition occurs. The free of deposition region extends from zero degree to the critical angle. In the transient region, the deposition efficiency increases from 0 % to 100 %, depending on the velocity of the particles. These angle ranges depend mainly on the ratio of distribution of particle velocity to critical velocity for a given spray material.

Regarding the variation of the sticking probability due to a third substance at the interface between particle and surface some consideration can be done. Specific studies on the variation of the sticking probability due to the presence of a third material at the interface between surface and particle are not available in literature. Poppe *et al.* (2000) pointed out that the presence of hydrophobic silane coating did not change the collisional behavior with respect to another test in which the surface was only cleaned with alcohol and subsequently dried with pressurized air.

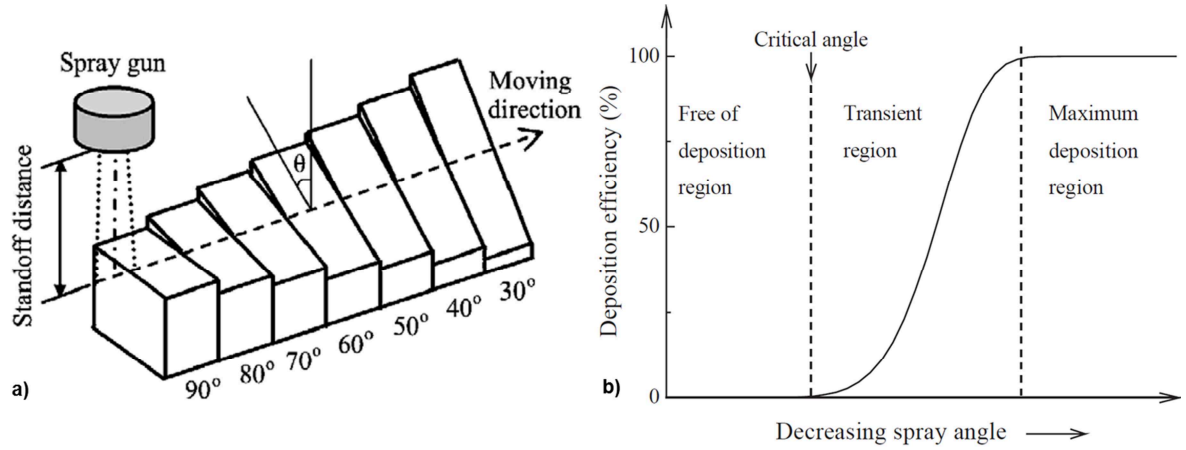

Figure 5.22 – a) sketch of the substrate fixture for spraying at different angles, b) schematic of effect of spray angle on deposition efficiency (Li *et al.*, 2005)

Generally, in the actual compressors, the presence of a third substance (such as oil, grease, etc.) on the blade surface could increase the sticking probability of the particle, but, at the moment, there are no specific studies that allow the quantification of this effect. In literature only the quantification of the influence of the presence of water at the particle-wall interface on the adhesion force are reported (see previous Chapters).

In order to better represent the evolution of the impact/adhesion phenomena, the particles are listed and subdivided by using a normal impact velocity criteria. In particular, the following three categories are defined:

- the particles that move away from the surface (called *Harmless*);
- the particles that have a normal impact velocity less than 90 m/s and for which it can be possible to define an sticking probability by using the Eqs (5.1) – (5.4);
- the particles that have an impact normal velocity higher than 90 m/s and for which the sticking probability is assumed equal to zero.

Special attention must be paid to the last category, characterized by an impact normal velocity higher than 90 m/s and an sticking probability equal to zero. These particles possess high kinetic energy that decreases by an order of magnitude during the first impact as reported in Poppe *et al.* (2000). This phenomenon implies that these particles will not be able to stick during the first contact but instead, it will most likely be during the second one. In fact, the decrease in kinetic energy is strongly related to the decrease in velocity and, consequently, an increase of sticking probability. A similar effect can also be found in turbomachinery applications. In Suzuki *et al.* (2008) the authors have described the poor erosion capacity shown by the particles during the second contact with the blade caused by a low level of kinetic energy that corresponds to that observed in Poppe *et al.* (2000). If this phenomenon is not important from an erosion point of view (due to the particle diameter lower than

10 µm), for the fouling problems a low particle kinetic energy during impact with the blade leads to a high sticking probability.

In the Appendix II and III all the impact characteristics are reported for Cases 1 – 5 for transonic and subsonic rotor respectively. Tables in the Appendix II and III show, for the transonic and subsonic rotor respectively, the all categories listed above: (i) the total number of particles N that have impacted on that side (pressure side or suction side) and on that strip (1^{st} – 11^{th}), (ii) the ratio n_{SIDE} between the total number N and the number of particles that impacted on that side of the blade and (iii) the ratio n_{hit} between the total number N and the number of injected particles. Thus, the ratio n_{SIDE} defines the kinematic characteristic distribution on one side of the blade for all the particles upon the impact and the ratio n_{hit} shows a global overview, in line with the fouling susceptibility criteria that consists of the ratio between the number of stuck particles and the number of particles injected in the flow path. In the tables N, n_{SIDE} and n_{hit} related to the particles characterized by an sticking probability equal to or greater than 0.5 are also reported. Finally, the rows grouped by the name SIDE contain the sum of the values reported for each strip. Thanks to the sum of the values N, n_{SIDE} and n_{hit} for the two sides of the blade, further analysis regarding particle-blade interaction is possible.

Figure 5.23 shows two bar charts relative to the sum of values for the ratio n_{SIDE}, reported for each strip, and indicated with the name n_{SIDE} for the transonic rotor. On the suction side, the percentage of particles with SP > 0.5 is greater than the pressure side for all cases even if, for Case 5, the phenomenon is much less obvious. This result shows how on the suction side there are some fluid dynamic conditions that make it more sensitive to particle sticking. On the suction side there are fewer particles than the pressure side but these particles have a higher sticking capacity. From the compressor performance point of view, the sensitivity to fouling of the suction side appears to be greater than the pressure side Morini *et al.* (2011), thus a greater particle tendency to stick to the suction side is an important result and focuses attention not only on the quantity of ingested contaminants but also to the fluid dynamic phenomena that characterize the flow around the blade. On the suction side, Case 1 is the most severe from a fouling point of view. The particles arrive with a normal impact velocity that makes it extremely effective in sticking to the blade surface. The percentage of particles with an SP > 0.5 reaches 80 %. On the pressure side the differences of the particle impact kinematics are less evident between the cases and all the percentages are quite similar to each other even if Case 5 uses a particle diameter ten times higher than Case 1. The pressure side, for all cases, shows a higher percentage for the *Harmless* particle category. This effect is directly related to the fact that in pressure side the separation that afflicts the suction side does not take place. For the pressure side and suction side it can be seen that the particle percentage of the v_n > 90 m/s category increases with the increase of the particle diameter and the sticking probability decreases as the diameter increases.

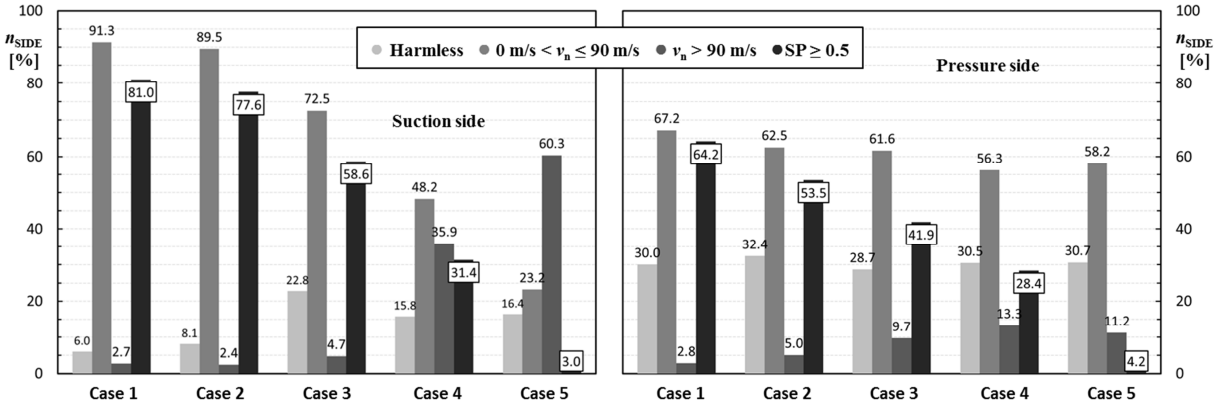

Figure 5.23 – Ratio n_{SIDE} for the SS and PS of Cases 1 – 5 (transonic rotor)

This phenomenon is the precursor of the erosive effects that are produced by the particles with a diameter greater than 10 µm, as reported in Ghenaiet (2012). In fact, the normal impact velocity increases with the increase of the particle diameter and, in the same way, the particles become less able to stick, although the impact is more dangerous for the blade surface.

Figure 5.24 shows two bar charts relative to the sum of values for the ratio n_{SIDE}, reported for each strip, and indicated with the name n_{SIDE} for the subsonic rotor. In this case, the particle percentage of the v_n > 90 m/s category represents a very small part of the impacting particles compared to the transonic case. For this reason, the impacting particles in a subsonic rotor are more dangerous because they are slower especially for the pressure side. For the case with the highest particle diameter (Case 5) the percentage of particles with an SP > 0.5 is very high (if compared with the transonic case) both in pressure side and suction side. This fact implies that the mass deposits on the blade surface could rapidly increase because bigger particles implies bigger values of mass of deposits. In general, the subsonic rotor collect less amount of contaminants but these contaminants have better chance to stick to blade surfaces (pressure ad suction side).

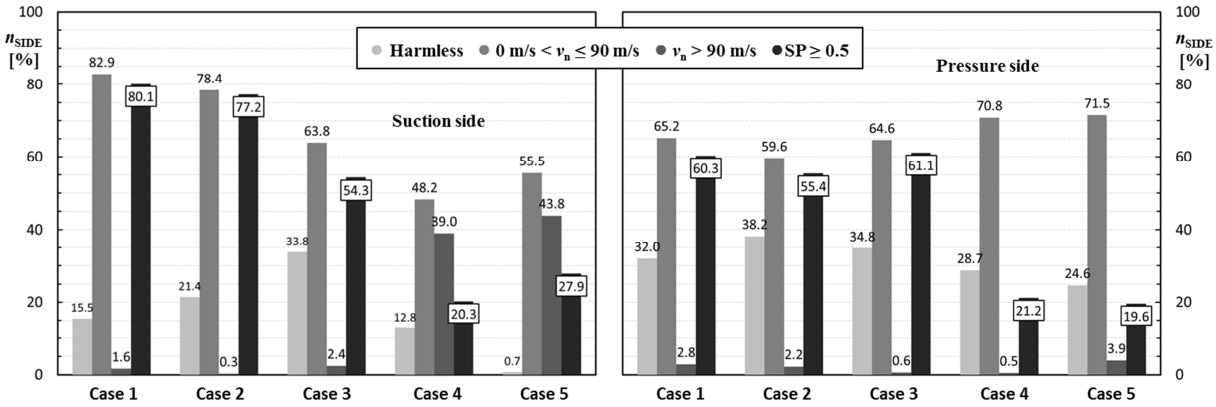

Figure 5.24 – Ratio n_{SIDE} for the SS and PS of Cases 1 – 5 (subsonic rotor)

The final analysis is related to the particles that have the SP > 0.5. In particular, in Fig. 5.25 the trend of the ratio $n_{hit,SP>0.5}$ (black continuous line) for the particles with SP > 0.5 superimposed with the trend of the η_{hit} (grey dotted line) is reported for the transonic rotor. The two trends refer to both sides of the blade (pressure side and suction side). As mentioned above η_{hit} represents the fouling susceptibility and its values represent a key result for gas turbine operators. As can be seen from Fig. 5.25, for the pressure side the trend of $n_{hit,PS,SP>0.5}$ does not follow the trend of $\eta_{hit,PS}$ unlike the trends reported for the suction side. For the pressure side the number of stuck particles is quite independent to the total number of particles that hit the blade and the $n_{hit,PS,SP<0.5}$ remains almost the same for the three considered cases. In this case the higher particles produce more fouling effects due to their higher diameter and thus the higher mass. For the suction side, the ratio $n_{hit,SS,SP>0.5}$ shows a very high percentage of particles able to stick for the smallest diameters compared to the total number of particles that hit the suction side.

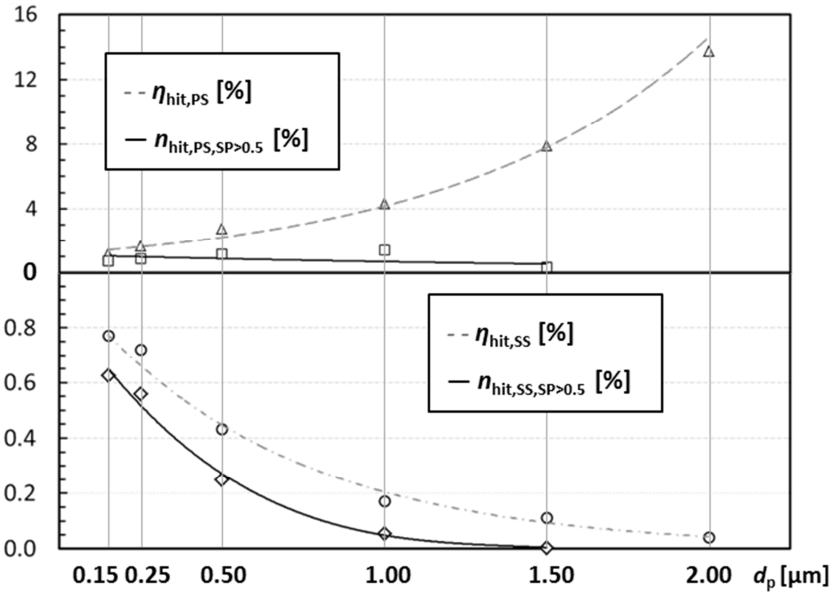

Figure 5.25 – Trends of the ratio $n_{hit,SP>0.5}$ and η_{hit} superimposed (transonic rotor)

Figure 5.26 reports the trend of the ratio $n_{hit,SP>0.5}$ (black continuous line) for the particles with SP > 0.5 superimposed with the trend of the η_{hit} (grey dotted line) for the subsonic rotor. As can be seen from Fig. 5.26, for the pressure side the trend of $n_{hit,PS,SP>0.5}$ does not follow the trend of $\eta_{hit,PS}$ unlike the trends reported for the suction side. For the pressure side the number of stuck particles is quite independent to the total number of particles that hit the blade and the $n_{hit,PS,SP>0.5}$ remains almost the same for the five considered cases. In this case the higher particles produce more fouling effects due to their higher diameter and thus higher mass. For the suction side, the ratio $n_{hit,SS,SP>0.5}$ shows a very high percentage of particles able to stick for the smallest diameters compared to the total number of particles that hit the

suction side.

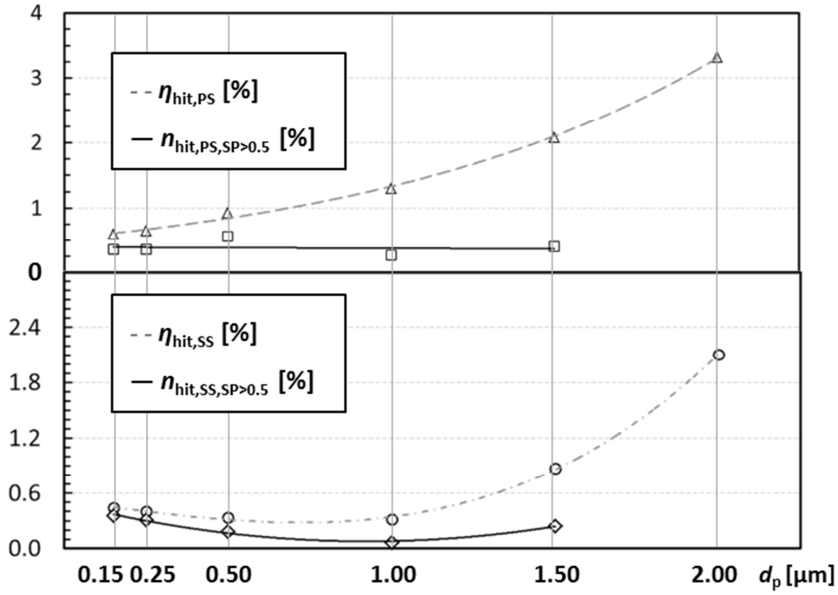

Figure 5.26 – Trends of the ratio $n_{hit,SP>0.5}$ and η_{hit} superimposed (subsonic rotor)

this page was intentionally left blank

Chapter 6

Quantitative Analysis of the Blade Contamination

In this chapter, the estimation of the actual deposits on the blade surface in terms of location and quantity are reported. The sticking property of the particles will combined with the actual contaminant concentration and filtration efficiency. A wide range of compressor working area and filtration efficiency have been considered. The blade zones affected by deposits are clearly reported by using easy-to-use contaminant maps realized on the blade surface in terms of contaminant mass per unit of time.

6.1 Contamination hypotheses

In this paragraph the data and the hypotheses used for the estimation of the mass deposits on a blade surface are reported. The data are directly related to the information and sources reported in the previous chapters. Tarabrin *et al*. (1998a) underline the importance of the climate condition and the efficiency of the inlet filtration system in order to limit the fouling issue of the compressor. For these reasons, specific air contamination data and filtration efficiency are chosen from different source.

By using the literature data reported in the previous chapters (Lü *et al*., 2012 and Lü *et al*., 2013), it is possible to define the air contaminant concentration at the inlet section of the air filtration system. Table 6.1 summarizes the literature data, in particular the table reports the mass concentration as a function of the particle diameter range and its average for Urban (U), Industrial Spring (IS) and Industrial Winter (IW) conditions.

By using the literature data reported in the previous chapters (Kurz and Brun, 2012 and Wilcox *et al*., 2010) it is possible to define the filtration efficiency as a function of the particle diameter. In this analysis, two conditions are taken into account: (i) Optimal Charge (OC) condition (high efficiency) and (ii) Poor Charge (PC) condition (low efficiency) of the electrostatic filters. The particle adhesion data refers to the results in the previous chapter, and for this reason, the filtration efficiency is defined

Table 6.1 – Mass concentration as a function of the particle diameter for U, IS and IW environment

d_{min} [µm]	d_{max} [µm]	d_{ave} [µm]	χ_U [µg/m^3]	χ_{IS} [µg/m^3]	χ_{IW} [µg/m^3]
0.010	0.018	0.014	2.50	16.50	2.00
0.018	0.032	0.025	1.50	18.50	2.00
0.032	0.056	0.044	2.00	35.00	2.00
0.056	0.100	0.078	2.50	33.00	2.50
0.100	0.180	0.140	3.25	39.00	2.00
0.180	0.320	0.250	6.75	26.00	3.00
0.320	0.560	0.440	11.00	19.50	13.00
0.560	1.000	0.780	12.00	72.00	15.25
1.000	1.800	1.400	6.00	35.00	21.50
1.800	3.200	2.500	7.00	13.50	8.00
3.200	5.600	4.400	10.25	11.50	10.00
5.600	10.000	7.800	11.00	9.50	14.00

for the analyzed particle diameter. Combining the mass concentration values (U, IS and IW) and the filtration efficiency (OC and PC), the contaminant concentration at the inlet section of the compressor can be calculated for the six considered cases (Tables 6.2 – 6.7).

Table 6.2 – Urban, optimal charge

d_p [µm]	χ_p @ air [#/m^3]	η_f [%]	χ_p @ inlet [#/m^3]
0.15	7.2e08	68	2.3e08
0.25	3.2e08	67	1.1e08
0.50	6.6e07	72	1.8e07
1.00	9.0e06	91	8.2e05
1.50	1.3e06	98	2.7e04

Table 6.3 – Industrial Spring, optimal charge

d_p [µm]	χ_p @ air [#/m^3]	η_f [%]	χ_p @ inlet [#/m^3]
0.15	8.6e09	68	2.7e09
0.25	1.2e09	67	4.1e08
0.50	1.2e08	72	3.2e07
1.00	5.4e07	91	4.9e06
1.50	7.7e06	98	1.5e05

Table 6.4 – Industrial Winter, optimal charge

d_p [µm]	χ_p @ air [#/m^3]	η_f [%]	χ_p @ inlet [#/m^3]
0.15	4.4e08	68	1.4e08
0.25	1.4e08	67	4.7e07
0.50	7.8e07	72	2.2e07
1.00	1.1e07	91	1.0e06
1.50	4.8e06	98	9.5e04

Table 6.5 – Urban, poor charge

d_p [µm]	χ_p @ air [#/m^3]	η_f [%]	χ_p @ inlet [#/m^3]
0.15	7.2e+8	49	3.7e08
0.25	3.2e08	47	1.7e08
0.50	6.6e07	54	3.0e07
1.00	9.0e06	82	1.6e06
1.50	1.3e06	93	9.5e04

Table 6.6 – Industrial Spring, poor charge

d_p [µm]	χ_p @ air [#/m^3]	η_f [%]	χ_p @ inlet [#/m^3]
0.15	8.6e09	49	4.4e09
0.25	1.2e09	47	6.6e08
0.50	1.2e08	54	5.3e07
1.00	5.4e07	82	9.6e06
1.50	7.7e06	93	5.5e05

Table 6.7 – Industrial Winter, poor charge

d_p [µm]	χ_p @ air [#/m^3]	η_f [%]	χ_p @ inlet [#/m^3]
0.15	4.4e08	0.49	2.3e08
0.25	1.4e08	0.47	7.6e07
0.50	7.8e07	0.54	3.5e07
1.00	1.1e07	0.82	2.0e06
1.50	4.8e06	0.93	3.4e05

In order to realize a comparative analysis, some hypotheses must be defined:

- the density of the contaminant is imposed equal to 3,000 kg/m^3. This value is obtained by a mass-weighted average of the air contaminant proposed in (Lü *et al.*, 2012 and Lü *et al.*, 2013);
- the filtration efficiency for the particles with d_p < 0.15 µm and d_p > 1.50 µm is imposed equal to 100 % (in agreement with Kurz and Brun, 2012 and Wilcox *et al.*, 2010);
- in order to calculate the number of particles swallowed by the compressor per unit of time, the volume flow rate at the best efficiency point is imposed.

As mentioned above, this analysis provides an estimation of the mass flow rate deposits (time-wise scenario) and for this reason, the results reported in the previous chapter must be processed in a different way. The results refer to the particle impact (instantaneous scenario) and, the sticking probability threshold limit imposed equal to 0.5 represents a useful discerning value to establish which particles stick or bounce.

In order to attribute the instantaneous scenario to the time-wise scenario the Dangerous Index (DI) is proposed. This new index refers to a specific amount of particles (that have a non-zero value of sticking probability) that impact on a specific blade area. The dangerous index is defined as the product between the ratio *n* and the average value of the particle sticking probability SP_{ave}. The ratio *n* is defined as the ratio between the amount of particles that hit the blade area with a SP > 0 and the amount of particles that enter the compressor. This definition is in agreement with the sticking coefficient reported by Ahluwalia *et al.* (1989) that represent the mass fraction of incident particles to a surface that are retained on that surface.

The approach used in this chapter is affected by two limitations:

- the particle characteristics used for the determination of the sticking probability (Poppe *et al.*, 2000) are quite different compared to the classic particle characteristics involved in fouling phenomena. In particular, the silicon carbide particles have a very high level of hardness and this implies that the rebound properties could be different from those found in the real fouling applications;
- the CFD numerical simulations refer to a particle density equal to 2,560 kg/m^3 instead of a density equal to 3,000 kg/m^3 assumed in this analysis. The different density allows the evaluation of the actual contaminant mass that afflicts the blade surface and at the same time, does not diminish the validity of the numerical results.

In the following paragraphs the deposits on the blade surface (for transonic and subsonic rotor) are analyzed in two different manners: (i) deposits divided by the blade side (pressure or suction) and (ii) deposits divided by a very fine discretization of the blade surface (mesh). In Fig. 6.1, the mesh realized on the blade surface is

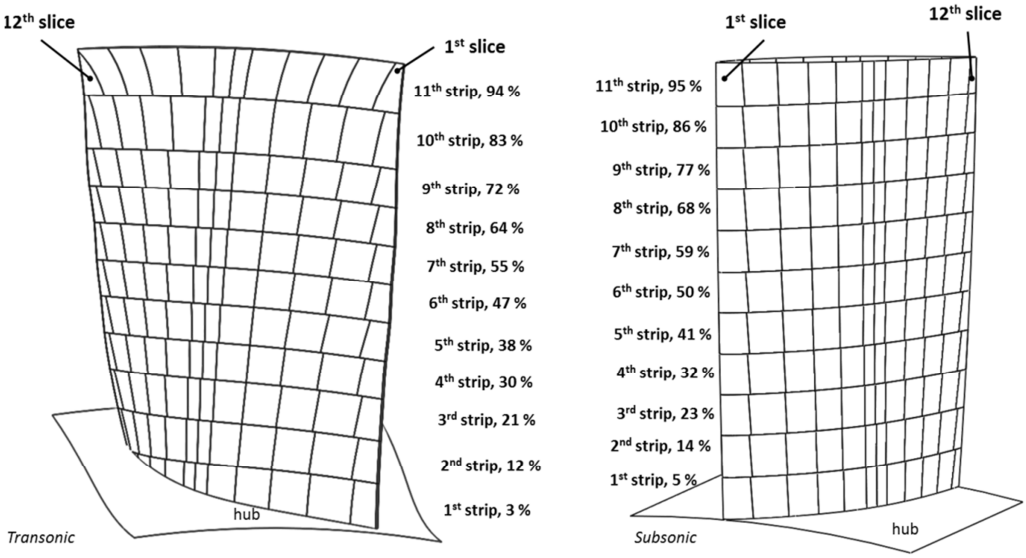

Figure 6.1 – Subdivision of the blade surface: eleven strips with its correspondent percentage of the blade span and twelve slices

reported. From Fig. 6.1, the subdivision of the blade surface is clearly seen as: from hub to shroud with eleven strips while from leading edge to trailing edge with twelve slices.

6.2 Transonic blade contamination

In this first section the analysis related to the deposits on the pressure and suction side, as a function of the conditions mentioned above are reported. The analysis refers to the quantification of the deposits on the blade surfaces in order to highlight which conditions are more dangerous for the compressor. As reported by Morini *et al*. (2011) the same deposits generate different performance drops as a function of the blade side. The deposits on the suction side are more dangerous than the deposits on the pressure side.

Table 6.8 reports the number of particles per unit of time that are swallowed by the transonic rotor. In particular, in line with the impact theory reported in Chapter 5, where the entering particles is the particle able to hit the blade surface, in this case, the considered volume flow rate, corresponds to the volume flow rate for a single passage vane at the best efficiency point. In this way, the number of particle per unit of time are the particles that have the chance to hit, and could stick, to the blade surface. For the transonic rotor, the volume flow rate at the best efficiency point for single passage vane are equal to 0.524 m^3/s.

In this paragraph the data related to the particles that stick to the pressure side or suction side as a function of the particle diameter are reported. For the data related

Table 6.8 – Number of particles per unit of time as function of: particle diameter, air contaminant and filtration efficiency (transonic rotor)

d_p [µm]	P (U, OC) [#/s]	P (IS, OC) [#/s]	P (IW, OC) [#/s]	P (U, PC) [#/s]	P (IS, PC) [#/s]	P (IW, PC) [#/s]
0.15	4.3e09	5.2e10	2.6e09	6.9e09	8.3e10	4.3e09
0.25	2.0e09	7.7e09	8.9e08	3.2e09	1.2e10	1.4e09
0.50	3.4e08	6.1e08	4.1e08	5.7e08	1.0e09	6.7e08
1.00	1.5e07	9.2e07	2.0e07	3.0e07	1.8e08	3.8e07
1.50	5.0e05	2.9e06	1.8e06	1.8e06	1.0e07	6.4e06

to the particles that stick to each cell of the blade mesh (Fig. 6.1), the data are reported in the Appendix IV, in order to improve the readability of the thesis. Table 6.9 reports the dangerous index, divided by the blade side. The values refer to per mil unit of measure.

Table 6.9 – DI for PS and SS, values refer to per mil unit (transonic rotor)

d_p [µm]	DI_{PS} [‰]	DI_{SS} [‰]
0.15	4.862	4.117
0.25	6.293	3.972
0.50	8.864	1.930
1.00	11.418	0.424
1.50	21.564	0.129

The first analysis is carried out in order to set the reference. In fact, the results reported in Figs 6.2 , 6.3 and 6.4 show the blade contamination in absence of the filtration systems. The values in Figs 6.2 – 6.4 are the results of the combination between the contaminant concentration in the air (Table 6.1) and the dangerous index values (Table 6.9). The values refer to mass per second that sticks to the blade surface. The considered particle diameters are those that have a filtration efficiency less than 100 %.

From Fig. 6.2 it is clearly visible that the pressure side is more contaminated than the suction side, in all conditions. In the pressure side the deposits generated by the Industrial Winter condition are higher than those generated by the Urban condition. In contrast, in suction side the Urban condition is more dangerous than the Industrial Winter condition. The higher deposition on the suction side corresponds to the Industrial Spring condition as well as on the pressure side.

In Figs 6.3 and 6.4 the differences in terms of particle diameter are reported for

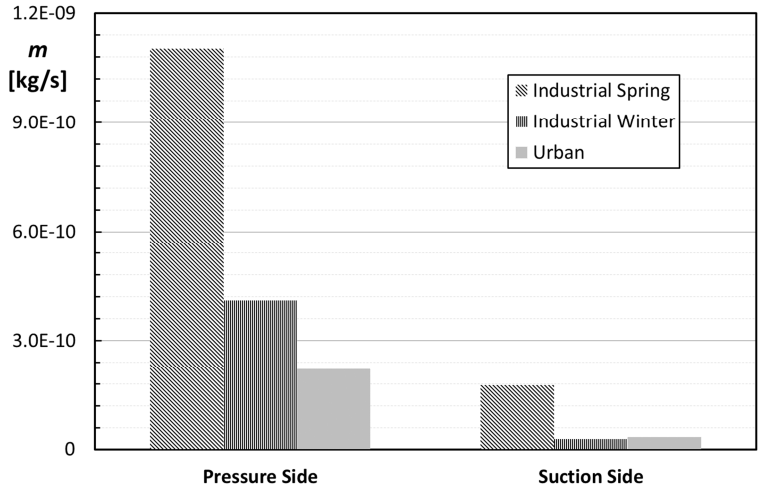

Figure 6.2 – Contaminant mass on the blade surface without filtration system (transonic rotor)

pressure side and suction side respectively. The pressure side is more contaminated by particles with a diameter equal to 1.00 µm in the Industrial Spring condition as well as the suction side in which the most dangerous particles have a diameter equal to 0.15 µm. In this case, it is clearly visible how the combination of the contaminant concentration and sticking probability values (represented by the dangerous index) determine different results as a function of the blade side. In the pressure side the bigger particles are responsible for higher blade side contamination. These particles (d_p = 1.00 µm and d_p = 1.50 µm) hit the pressure side with an SP_{ave} which is lower than the SP_{ave} of the smaller particles, but the higher number of impacts determine a very dangerous condition for this blade side. In the suction side the particle contributions are more similar and, fixing the condition, the dangerous diameter changes. In fact, the diameter of the dangerous particles for the Industrial Spring condition is 0.15 µm, but for the Industrial Winter condition it is 0.50 µm and finally, for the Urban condition it is 0.25 µm. These results confirm the requirement of (i) different filtration systems, in order to prevent the deposits in both of the blade sides at the same time and (ii) proper filtration system as a function of the location of the power unit, as reported in Wilcox *et al.* (2010).

Figure 6.5 reports the results related to the blade contamination with filtration systems. Two conditions are reported: optimal charge and poor charge of the filtration system. The charge level influences the overall mass deposits on both of the blade sides, in particular, the optimal charge allows a consistent reduction of the mass deposits. The reduction is in the range of (39 – 50) % depending on the environmental conditions.

These results highlight the importance of the presence of the filtration system and its efficiency:

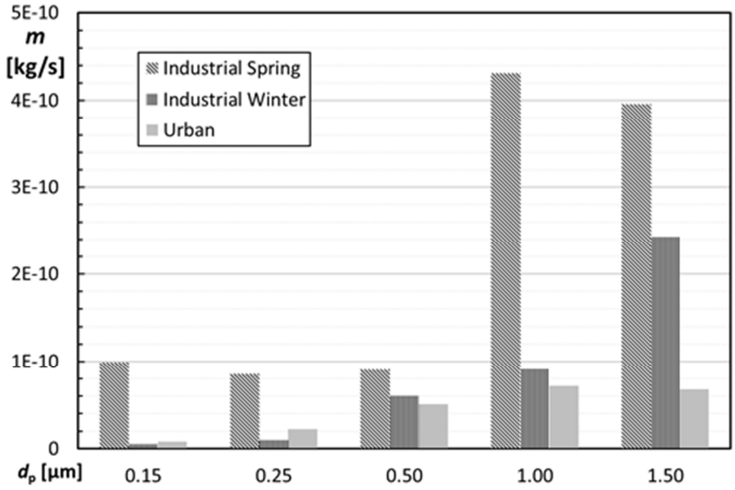

Figure 6.3 – Contaminant mass on the PS without filtration system (transonic rotor)

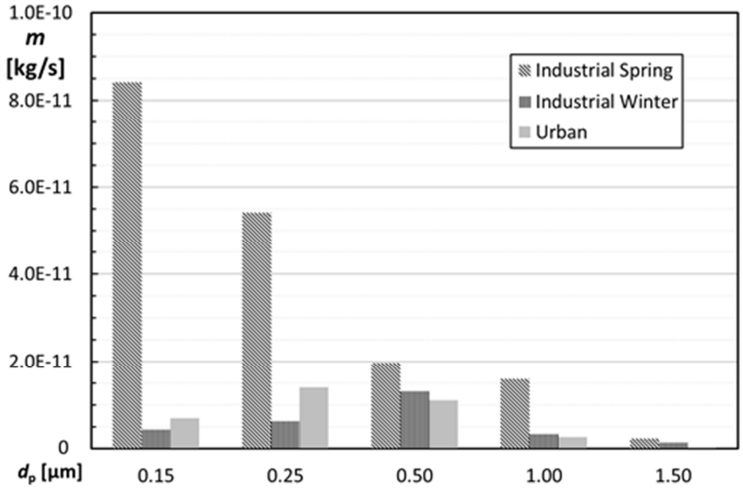

Figure 6.4 – Contaminant mass on the SS without filtration system (transonic rotor)

- the filtration system with poor charge reduces the mass contaminant by about 78 % on the pressure side and by about 54 % on the suction side with respect to the case without filtration system;
- the filtration system with optimal charge reduces the mass contaminant by about 88 % on the pressure side and by about 72 % on the suction side with respect to the case without filtration system.

Finally, it is possible to observe that the characterization of the contaminant concentration in the air is more important than the filter charge. In fact, Industrial Winter and/or Urban conditions in the case of poor charge, are less dangerous than the Industrial Spring condition in the case of optimal charge.

In Figs 6.6 and 6.7 the differences in terms of particle diameter are reported for pressure side and suction side respectively. The different charge condition

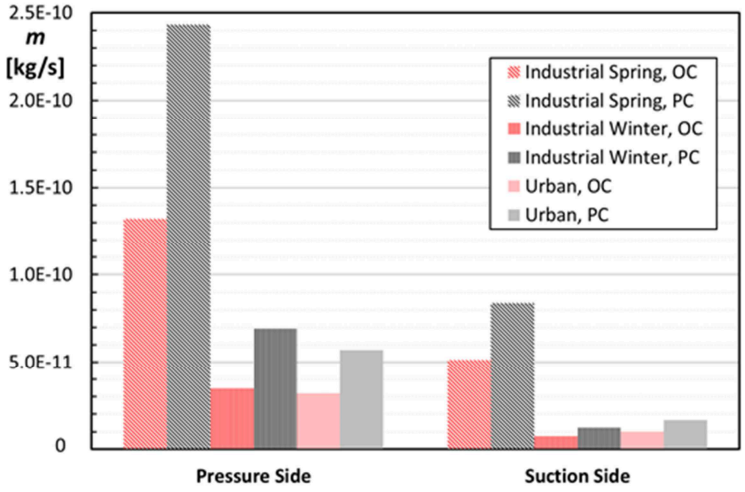

Figure 6.5 – Contaminant mass on the blade surface with filtration system (transonic rotor)

determines a more flat scenario with respect to the single particle diameter. This effect is more evident in pressure side than suction side. For example, for the Industrial Spring condition, in case of poor charge the highest contribution corresponds to d_p = 1.00 µm, while in case of optimal charge, the contributions of the particle with a diameter in the range 0.15 µm – 1.00 µm are quite similar. In suction side the higher contribution is related to particles with a diameter equal to 0.15 µm and 0.25 µm during the Industrial Spring condition. Regarding the suction side, it is important to emphasize that the smallest particles are the most dangerous only for the IS condition while, in the Industrial Winter and Urban conditions, the most dangerous particles are 0.50 µm and 0.25 µm respectively.

In this second section a specific analysis related to deposits on the blade surface are reported. As mentioned above, the blade surface was divided into eleven strips along the spanwise direction and into twelve slices along the chordwise direction.

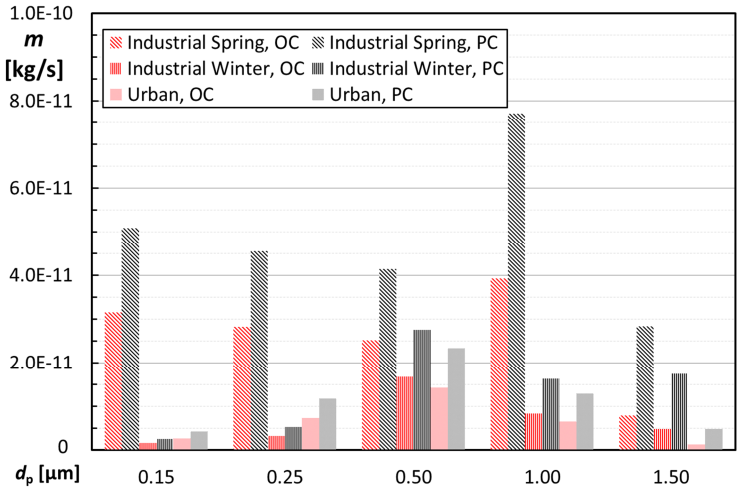

Figure 6.6 – Contaminant mass on the PS with filtration system (transonic rotor)

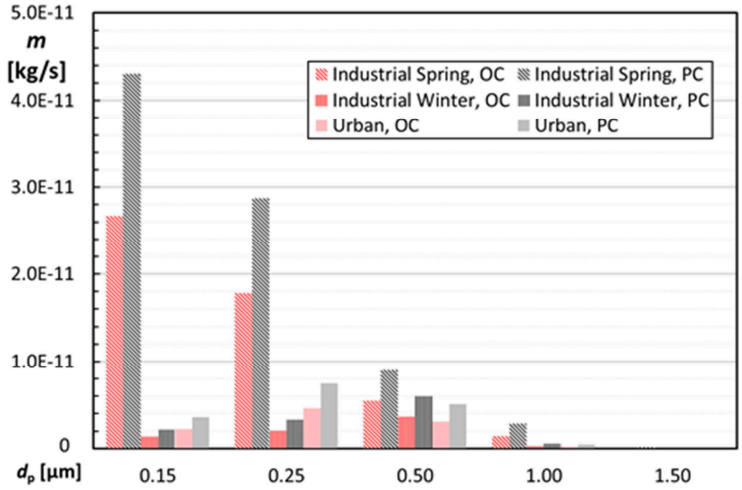

Figure 6.7 – Contaminant mass on the SS with filtration system (transonic rotor)

This very fine discretization of the blade surface allows the visualization of deposits which is quite similar to the real scenario. For each considered case, the localization of the contaminant peak on the pressure side ($m_{PS,peak}$) and suction side ($m_{SS,peak}$) is reported. The average values of contaminant at the pressure side ($m_{PS,ave}$), suction side ($m_{SS,ave}$), leading edge ($m_{LE,ave}$) and blade tip ($m_{TIP,ave}$) are also reported. The deposits on these blade areas in fact have the greatest influence in compressor performance degradation, as reported by Morini *et al.* (2011) and Aldi *et al.* (2014).

Without filtration system. In a similar manner to analyses reported in the previous paragraph, the first analysis is carried out in order to set the reference. In fact, the results reported in Fig. 6.8 show the blade contamination in absence of the filtration system. Figure 6.8 shows that deposits are concentrated in the first part of the airfoil chord on the pressure side. In particular the peak value is in correspondence with the leading edge: in pressure side at the 10th strip (83 % of the blade span) while in suction side it is at the 1st strip (3 % of the blade span). The deposits on the suction side are more distributed with respect to those on the pressure side, but the average value is an order of magnitude less than the pressure side. At the blade tip, the average value of deposit is higher than the average values of the suction side. This implies that the blade tip is more fouled with respect to the suction side.

Industrial Spring and poor charge. The second analysis refers to the most dangerous fouling operating condition: poor charge of the filtration system and Industrial Spring as the compressor work environment. Comparing this result to the case without filtration system, it is possible to understand the importance of the filtration system even if its efficiency is not optimal. This condition is usual in the case of fully loaded power units for which the shut-off is not possible. Figure 6.9 shows the deposits on the blade surface. The colorbar values are different from the previous case in order to improve the contour plot readability. The colorbar values used for

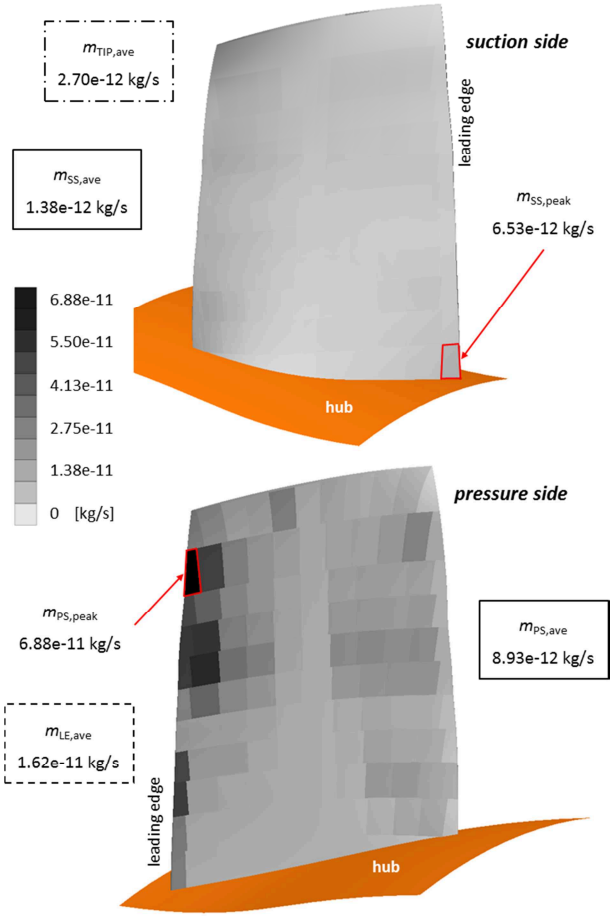

Figure 6.8 – Overall deposits on the blade surface without filtration system (transonic rotor)

this analysis will be held constant for all the following analyses. The peak value in the pressure side is located in the same area as the previous case with a reduction in mass contaminant of about 80 %. In the suction side, the deposit peak is located in the rear part of the airfoil chord at the 3rd strip (21 % of the blade span) with a reduction of about 72 % with respect to the case without a filtration system. Regarding the average values of the deposits in pressure side and suction side, it can be noticed that the filtration system with a poor charge realizes a reduction of about 78 % of the mass deposits on the pressure side while, in suction side the reduction is only about 52 %. Finally, the filtration system seems to determine a spreading of deposits in the suction side. In fact, the peak value and the average one are closer to each other and the difference is only about 64 % with respect to the peak value.

Industrial Spring and optimal charge. The third analysis is conducted in order to emphasize the performance and the benefits deriving from the proper management of the filtration system. Figure 6.10 shows the deposits on the blade surface in the case of Industrial Spring environment with optimal charge conditions. As mentioned above, the filtration system charge reduces the amount of deposits on the blade

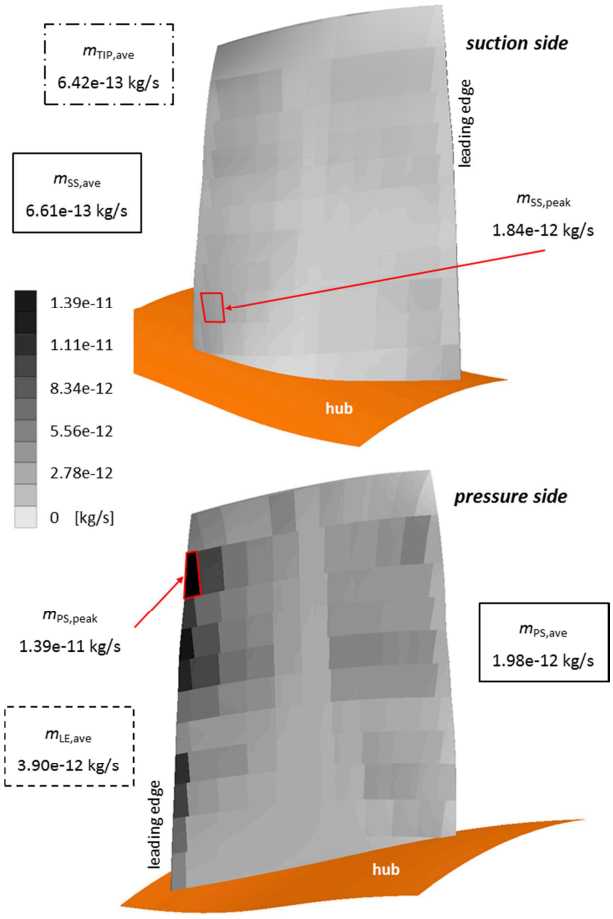

Figure 6.9 – Overall deposits on the blade surface: Industrial Spring and poor charge (transonic rotor)

surface. For the pressure side the average reduction is about 46 % while for the suction side the reduction is about 39 % with respect to the case with the poor charge condition. Again, the influence of the filtration system is higher for the pressure side than suction side. The peak values in the pressure side and suction side are in the same blade areas with respect to the previous cases (without filtration system, and Industrial Spring with poor charge). Once again, the suction side appears uniformly contaminated and the spread effect due to the filtration system is present. The difference between the peak value and the average value on the suction side is similar to the previous case (about 63 % with respect to the peak value). On the suction side, the blade area close to the blade tip (10^{th} strip, 83 % of the blade span) is also affected by deposits in a similar way to the peak value area.

Industrial Winter and optimal charge. The last analysis refers to the least heavy operating condition: Industrial Winter environment with optimal charge conditions. Figure 6.11 shows the deposits on the blade surface. As mentioned above, this condition is the least heavy of those considered. In this case, the contaminant concentration in the ingested air has a greater influence for the deposits in suction side: the reduction of the peak value is equal to 78 % for the suction side (with

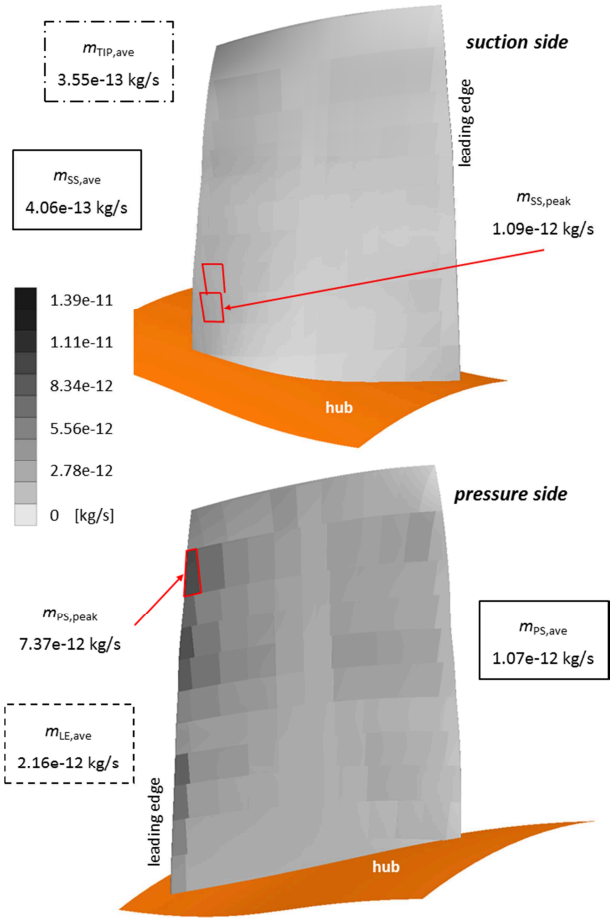

Figure 6.10 – Overall deposits on the blade surface: Industrial Spring and optimal charge (transonic rotor)

respect to the peak value resulting for the case Industrial Spring with optimal charge), while in the pressure side the reduction of the peak value is about 67 % (with respect to the peak value resulting for the case Industrial Spring with optimal charge). The same trend can be obtained by using the average values.

For these reasons, air contamination plays a key role in the performance degradation because the deposits on the suction side have a greater influence on the compressor performance drop (Morini *et al.*, 2011). In the light of this consideration, Fig. 6.12 shows which suction side areas are interested by the deposits (dark-grey colored) and the blade areas not interested by the deposits (pale-grey colored). Figure 6.12a represents the first three cases: (i) Industrial Spring without filtration system, (ii) Industrial Spring with poor charge and (iii) Industrial Spring with optimal charge while Fig. 6.12b represents the last case: Industrial Winter with optimal charge. As mentioned above air contamination has the greatest influence for the suction side. In fact, as can be seen in Fig. 6.12, only the variation of the air contaminant concentration can influence the pattern of deposits on the suction side.

Considering all the analyses some general rules can be drawn:

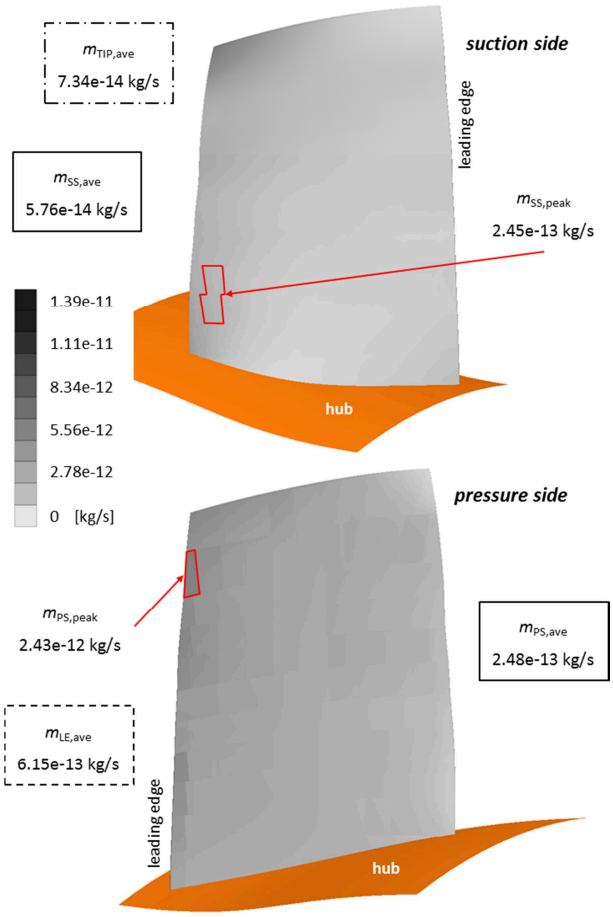

Figure 6.11 – Overall deposits on the blade surface: Industrial Winter and optimal charge (transonic rotor)

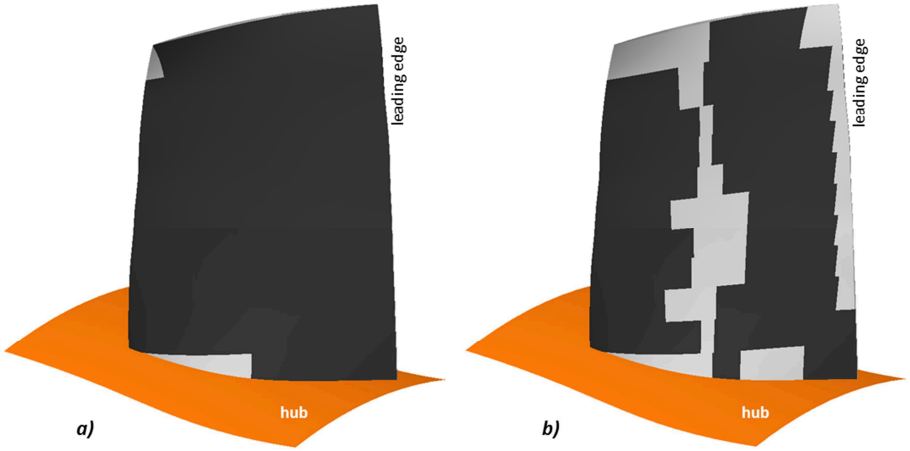

Figure 6.12 – Deposits pattern on the SS: a) IS without filtration system, IS with PC and IS with OC; b) IW with OC

- the pressure side is more affected by the deposits in the first part of airfoil chord (close to the leading edge) at the top of the blade (about 80 % of blade span). On this side the deposits do not cover the entire surface and some blade areas remain almost completely free from deposits (especially in the midchord zone, full

span);
- the suction side are more affected by the deposits in the areas close to the hub for the full chord length. On this side the deposits appear much more uniform and there is not an preferable blade area interested by the contaminant;
- the filtration system influences the deposition rate: the presence and/or the operating conditions of the filtration system determines the amount of deposit that affected each blade area. Its influence appears more relevant for the pressure side deposition rate;
- the work environment of the compressor determines which blade areas are interested by the deposits. Different air contaminant concentrations lead to different fouled blade areas. Their influence appears more relevant for the suction side deposition rate.

6.3 Subsonic blade contamination

Similarly to the transonic rotor, in this paragraph the particle deposition in the case of subsonic rotor is reported. The first section refers to the deposits on the pressure and suction side, as a function of the conditions mentioned above. Table 6.10 reports the number of particles per unit of time that are swallowed by the subsonic rotor. In this case, the volume flow rate at the best efficiency point for single passage vane are equal to 0.686 m^3/s.

Table 6.10 – Number of particles per unit of time as function of: particle diameter, air contaminant and filtration efficiency (subsonic rotor)

d_p [µm]	*P* (U, OC) [#/s]	*P* (IS, OC) [#/s]	*P* (IW, OC) [#/s]	*P* (U, PC) [#/s]	*P* (IS, PC) [#/s]	*P* (IW, PC) [#/s]
0.15	1.3e08	1.6e09	8.2e07	2.1e08	2.6e09	1.3e08
0.25	6.2e07	2.4e08	2.8e07	1.0e08	3.9e08	4.4e07
0.50	1.1e07	1.9e07	1.3e07	1.8e07	3.1e07	2.1e07
1.00	4.8e05	2.9e06	6.1e05	9.4e05	5.6e06	1.2e06
1.50	1.6e04	9.1e04	5.6e04	5.6e04	3.2e05	2.0e05

In this paragraph the data related to the particles that stick to the pressure side or suction side as a function of the particle diameter are reported. For the data related to the particles that stick to each cell of the mesh, the data are reported in the Appendix V, in order to improve the readability of the thesis. Table 6.11 reports the dangerous index, divided by the blade side. The values refer to per mil unit of measure.

Figures 6.13 , 6.14 and 6.15 show the blade contamination in absence of the

Table 6.11 – DI for PS and SS, values refer to per mil unit (subsonic rotor)

d_p [µm]	DI_{PS} [‰]	DI_{SS} [‰]
0.15	2.789	2.733
0.25	2.806	2.369
0.50	4.318	1.445
1.00	4.026	0.727
1.50	5.454	2.094

filtration systems. The values in Figs 6.13 – 6.15 are the results of the combination between the contaminant concentration in the air (Table 6.1) and the dangerous index values (Table 6.11). The values refer to mass per second that sticks to the blade surface. The considered particle diameters are those that have a filtration efficiency less than 100 %.

Even in this case (subsonic rotor) from Fig. 6.13 it is clearly visible that the pressure side is more contaminated than the suction side, in all conditions. The higher deposition on the suction side corresponds to the Industrial Spring condition as well as on the pressure side. In this case the seasons influence in similar manner both blade side: Industrial Spring is the most dangerous while the Urban condition is the least. In the case of subsonic rotor, the differences in the deposits rate between pressure side and suction side, for a fixed season, is less accentuated with respect to the case with transonic rotor.

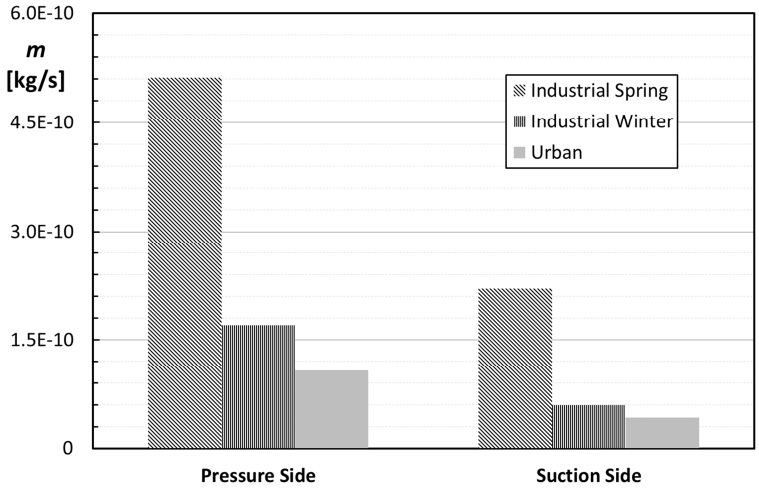

Figure 6.13 – Contaminant mass on the blade surface without filtration system (subsonic rotor)

In Figs 6.14 and 6.15 the differences in terms of particle diameter are reported for pressure side and suction side respectively. The pressure side is more contaminated

by particles with a diameter equal to 1.00 µm in the Industrial Spring condition as well as the suction side in which the most dangerous particles have a diameter equal to 0.15 µm. Also in this case, it is clearly visible how the combination of the contaminant concentration and sticking probability values (represented by the dangerous index) determine different results as a function of the blade side. In the pressure side the bigger particles are responsible for higher blade side contamination. These particles (d_p in the range of 0.50 µm to 1.50 µm) hit the pressure side with an SP_{ave} which is lower than the SP_{ave} of the smaller particles, but the higher number of impacts determine a very dangerous condition for this blade side. In the suction side the particle contributions are more similar and, fixing the condition, the dangerous diameter changes. In fact, the diameter of the dangerous particles for the Industrial Spring condition is 0.15 µm, but for the Industrial Winter condition it is 1.50 µm and finally, for the Urban condition it is 0.50 µm. Subsonic suction side appear more prone to collect particles that have a wide diameter range. These results confirm the requirement of a specific design of the filtration systems related to the power plant location (Wilcox *et al.*, 2010).

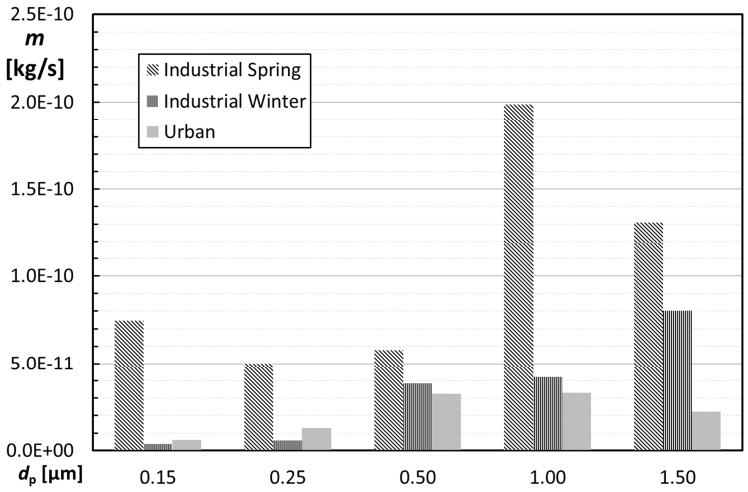

Figure 6.14 – Contaminant mass on the PS without filtration system (subsonic rotor)

Figure 6.16 reports the results related to the blade contamination with filtration systems. Two conditions are reported: optimal charge and poor charge of the filtration system. In this case, the reduction, by using a filter with optimal charge (optimal charge conditions), is in the range of (41 – 46) % depending on the environmental conditions.

These results highlight the importance of the presence of the filtration system and its efficiency:

- the filtration system with poor charge reduces the mass contaminant by about 74 % on the pressure side and by about 68 % on the suction side with respect to the case without filtration system;

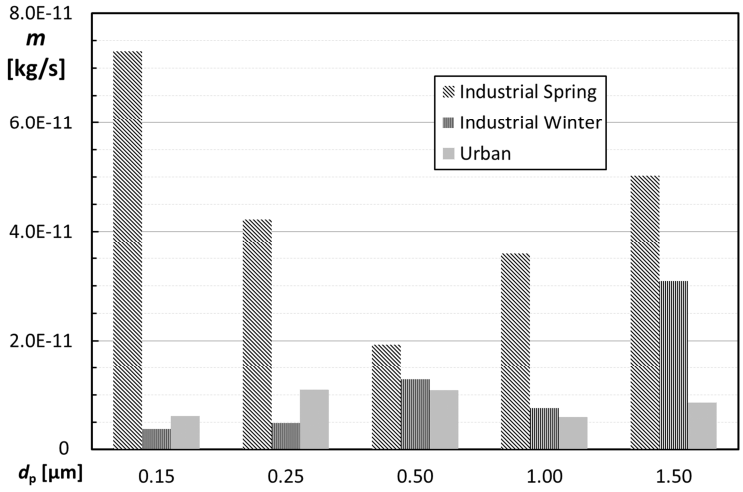

Figure 6.15 – Contaminant mass on the SS without filtration system (subsonic rotor)

- the filtration system with optimal charge reduces the mass contaminant by about 85 % on the pressure side and by about 81 % on the suction side with respect to the case without filtration system.

Finally, it is possible to observe that the characterization of the contaminant concentration in the air is more important than the filter charge. In fact, Industrial Winter and/or Urban conditions in the case of poor charge, are less dangerous than the Industrial Spring condition in the case of optimal charge. The same results were found in the case of transonic rotor.

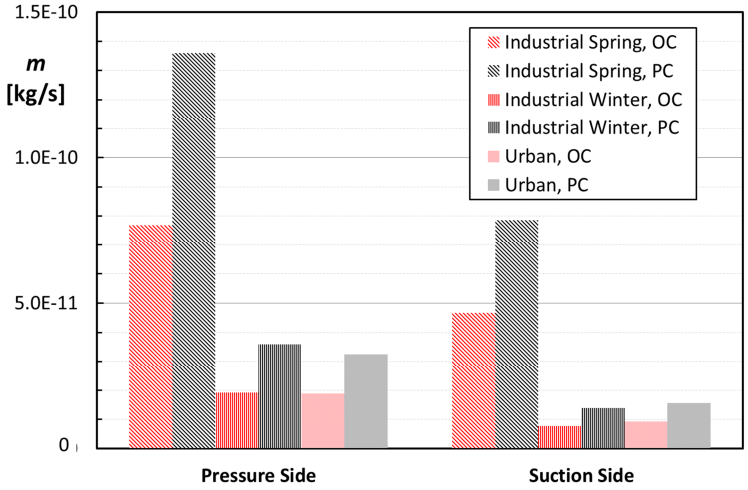

Figure 6.16 – Contaminant mass on the blade surface with filtration system (subsonic rotor)

In Figs 6.17 and 6.18 the differences in terms of particle diameter are reported for pressure side and suction side respectively. The different charge condition determines a more flat scenario with respect to the single particle diameter. This

effect is more evident in pressure side than suction side. For example, for the Industrial Spring condition, in case of poor charge the highest contribution corresponds to d_p equal to 0.15 µm and 1.00 µm, while in case of optimal charge, the contributions of the particle with a diameter in the range (0.15 – 1.00) µm are quite similar. In suction side the higher contribution is related to particles with a diameter equal to 0.15 µm and 0.25 µm during the Industrial Spring condition. Regarding the suction side, it is important to emphasize that the smallest particles are the most dangerous only for the Industrial Spring condition while, in the Industrial Winter and Urban conditions, the most dangerous particles are 0.50 µm and 0.25 µm respectively. Subsonic blade appear less sensitive to the particle diameter, and in contrast, all particle could determine a fouling issue. The subsonic suction side is contaminated in similar manner with respect to the pressure side (the peak values are quite similar) instead of the situation highlighted for the transonic suction side in which the peak values were always less than the pressure side peak values.

In this second section, the deposit patterns in the case of subsonic rotor are

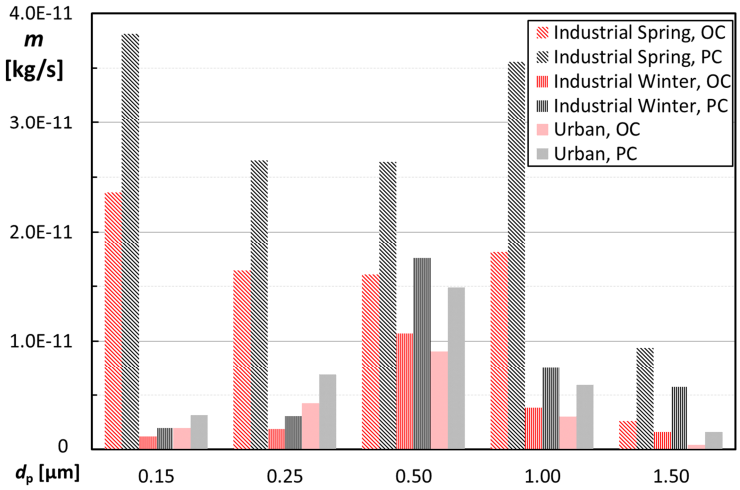

Figure 6.17 – Contaminant mass on the PS with filtration system (subsonic rotor)

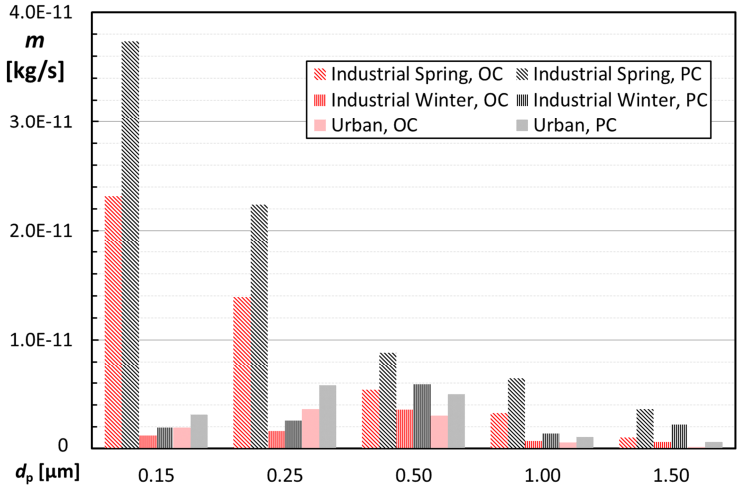

Figure 6.18 – Contaminant mass on the SS with filtration system (subsonic rotor)

reported. The fine discretization is reported in Fig. 6.1 and it is composed of eleven strips along the spanwise direction and twelve slices along the chordwise direction. For each considered case, the localization of the contaminant peak on the pressure side ($m_{PS,peak}$) and suction side ($m_{SS,peak}$) is reported. The average values of contaminant at the pressure side ($m_{PS,ave}$), suction side ($m_{SS,ave}$), leading edge ($m_{LE,ave}$) and blade tip ($m_{TIP,ave}$) are reported like transonic rotor analysis.

Without filtration system. In a similar manner to analyses reported above, the first analysis is carried out in order to set the reference. In fact, the results reported in Fig. 6.19 show the blade contamination in absence of the filtration system. Figure 6.19 shows that deposits are concentrated in the first part of the airfoil chord on the pressure side. In particular the peak values is in correspondence with the leading edge: in pressure side and suction side at the 7th (59 % of the blade span) strip and 9th (77 % of the blade span) respectively. The deposits on the suction side are more distributed with respect to those on the pressure side, but the average value is about 50 % of the magnitude less than the pressure side. In the case of subsonic rotor the average values of the blade sides are more close to each other with respect to the transonic rotor. At the blade tip, the average value of deposit is higher than the average values of the suction side. This implies that the blade tip is more fouled with respect to the suction side.

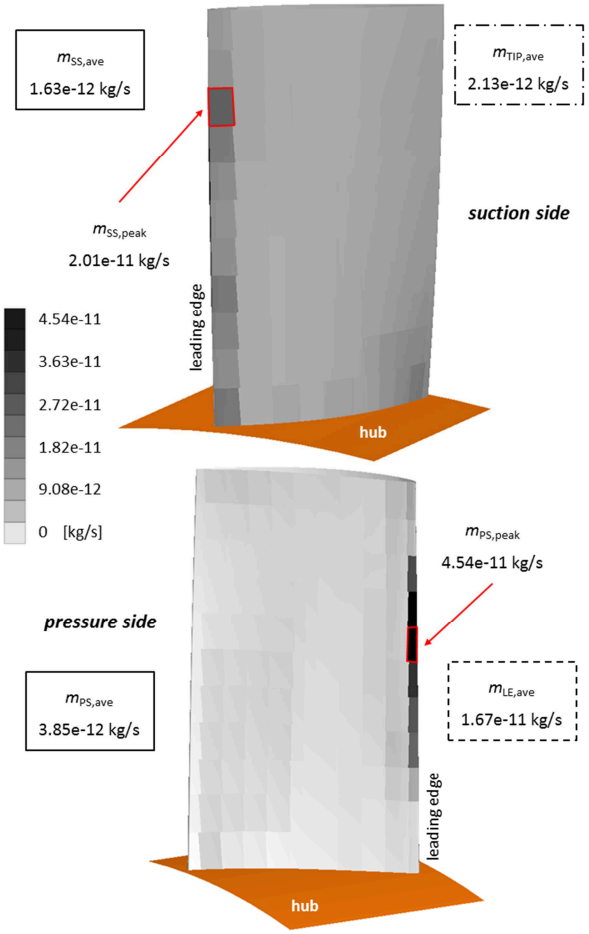

Figure 6.19 – Overall deposits on the blade surface without filtration system (subsonic rotor)

Industrial Spring and poor charge. The second analysis refers to the most dangerous fouling operating condition: poor charge of the filtration system and Industrial Spring as the compressor work environment. Figure 6.20 shows the deposits on the blade surface. The colorbar values are different from the previous case in order to improve the contour plot readability. The colorbar values used for this analysis will be held constant for all the following analyses. The peak value in the pressure side is located in the 8th strip (68 % of the blade span) with a reduction in mass contaminant of about 79 %. In the suction side, the deposit peak is located in the same region of the previous case with a reduction of about 71 % with respect to the case without a filtration system. Regarding the average values of the deposits in pressure side and suction side, it can be noticed that the filtration system with a poor charge realizes a reduction of about 73 % of the mass deposits on the pressure side while, in suction side the reduction is only about 65 %.

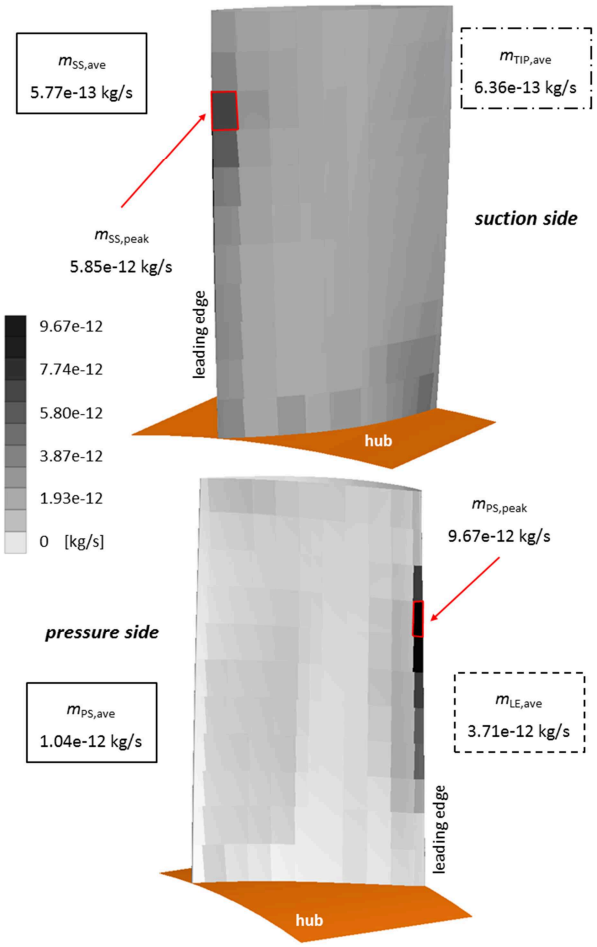

Figure 6.20 – Overall deposits on the blade surface: Industrial Spring and poor charge (subsonic rotor)

Industrial Spring and optimal charge. Figure 6.21 shows the deposits on the blade surface in the case of Industrial Spring environment with optimal charge conditions. As mentioned above, the filtration system charge reduces the amount of deposits on

the blade surface. For the pressure side the average reduction is about 43 % while for the suction side the reduction is about 41 % with respect to the case with the poor charge condition. The peak values in the pressure side and suction side are in the same blade areas with respect to the previous cases (without filtration system, and Industrial Spring with poor charge). On the suction side, the blade area close to the leading edge is affected by deposits in a similar way to rear part of the airfoil chord. This phenomenon is due to the flow separation in the corner of the flow passage vane.

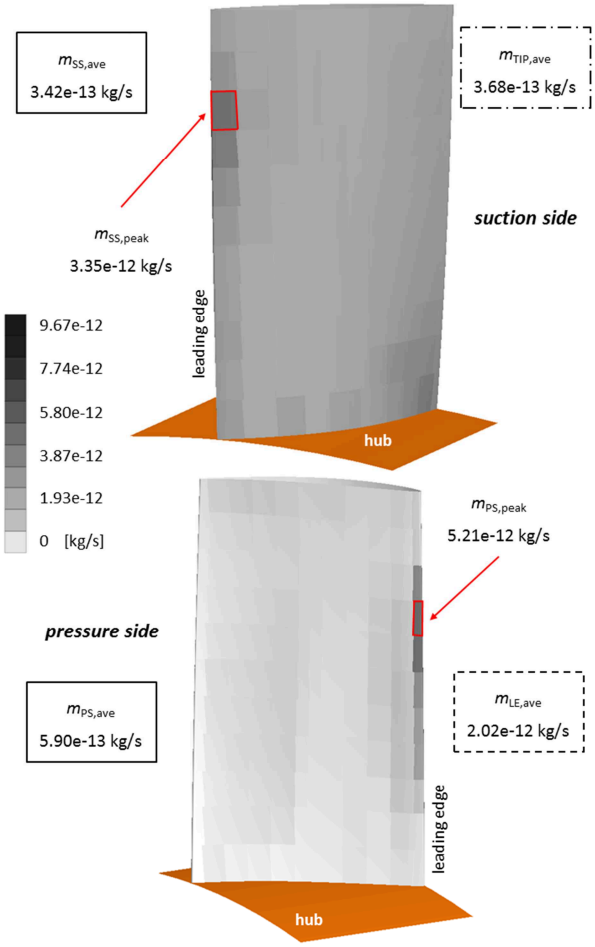

Figure 6.21 – Overall deposits on the blade surface: Industrial Spring and optimal charge (subsonic rotor)

Industrial Winter and optimal charge. The last analysis refers to the least heavy operating condition: Industrial Winter environment with optimal charge conditions. Figure 6.22 shows the deposits on the blade surface. As mentioned above, this condition is the least heavy of those considered. In this case, the contaminant concentration in the ingested air has a greater influence for the deposits in suction side: the reduction of the peak value is equal to 69 % for the suction side (with respect to the peak value resulting for the case Industrial Spring with optimal charge), while in the pressure side the reduction of the peak value is about 67 % (with respect

to the peak value resulting for the case Industrial Spring with optimal charge). The same trend can be obtained by using the average values. In this case, the season, and then the work environment of the compressor influence the deposits in suction side strongly.

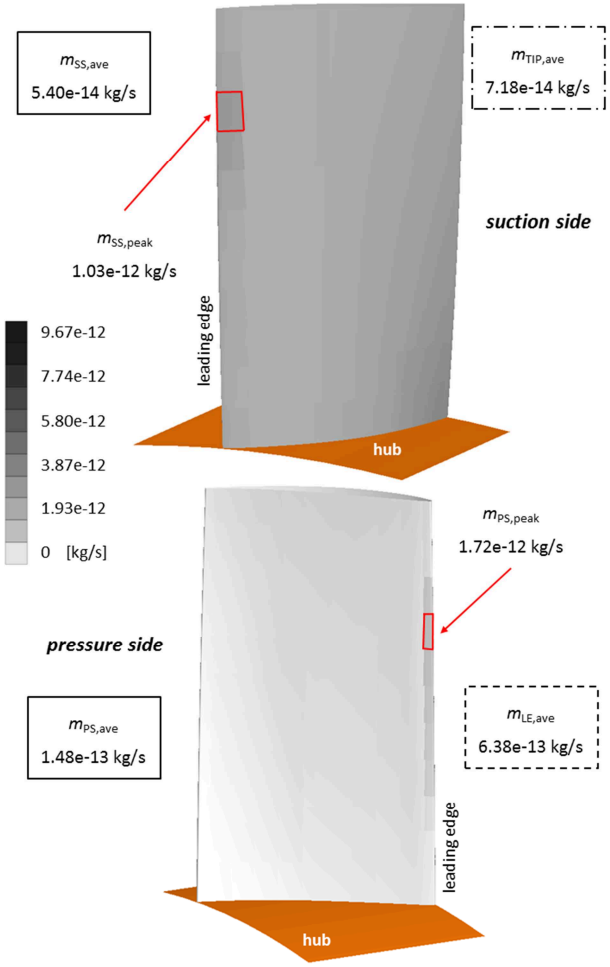

Figure 6.22 – Overall deposits on the blade surface: Industrial Winter and optimal charge (subsonic rotor)

6.4 Particle adhesion: observations

The mass deposits reported in the previous paragraphs highlight that, for both rotors, the pressure side is more contaminated by the deposits than the suction side. The mass deposit rate reported for the blade side and, through the contour, for each region, combines the sticking characteristics of the particles and the air contamination data. Mass deposits are influenced in a greater manner by bigger particles (d_p = 1.00 µm and d_p = 1.50 µm) inasmuch as the mass deposits are related to (i) particle diameter, (ii) number of particles and (iii) the average value of the sticking probability because the particle density is kept constant. These assumptions,

added to the limitations reported at the beginning of this work, determine that the higher values of mass deposits are localized in the pressure side and, as a result, the pressure side is more contaminated than the suction side.

The values of mass deposits presented in this thesis are directly related to the calculated dangerous index, as reported in this chapter. As mentioned above, this index is strongly related to the sticking coefficient reported in Ahluwalia *et al.* (1989). By using the dangerous index it is possible to highlight some considerations regarding particle adhesion on the pressure and suction sides for both rotors and compare the results with the discussion reported by Ahluwalia *et al.* (1989). Despite the fact that in Ahluwalia *et al.*'s work the cascade under investigation refers to a gas turbine, some general hints could be used to explain the results presented in this thesis.

Figure 6.23 shows the relationship between the dangerous index and the particle diameter for the pressure side and suction side for both rotors. The different effects of the flow field on particle deposition are clearly visible. As reported in Ahluwalia *et al.* (1989) inertial deposition takes a place on the pressure surface for diameters greater than 1 µm while, by contrast, the suction side is affected by a diffusion deposition provided by diameters less than 1 µm.

In the transonic rotor, where the flow field is greatly different from the pressure side and suction sides, the DI assumes different values and for the suction side its values are very low for bigger diameters. In the suction side in fact, the separation due to the shock wave determines a turbulent and thicker boundary layer. This condition allows the diffusion-deposition condition and, as reported in literature, this condition influences the deposition of the smaller particles (Parker and Lee, 1972). On the pressure side, the inertia deposition takes place, and for this reason, the dangerous index increases as the particle diameter increases.

In the subsonic rotor, the flow field on the pressure side and on the suction side is more comparable than in the case of the transonic rotor. This situation results in a

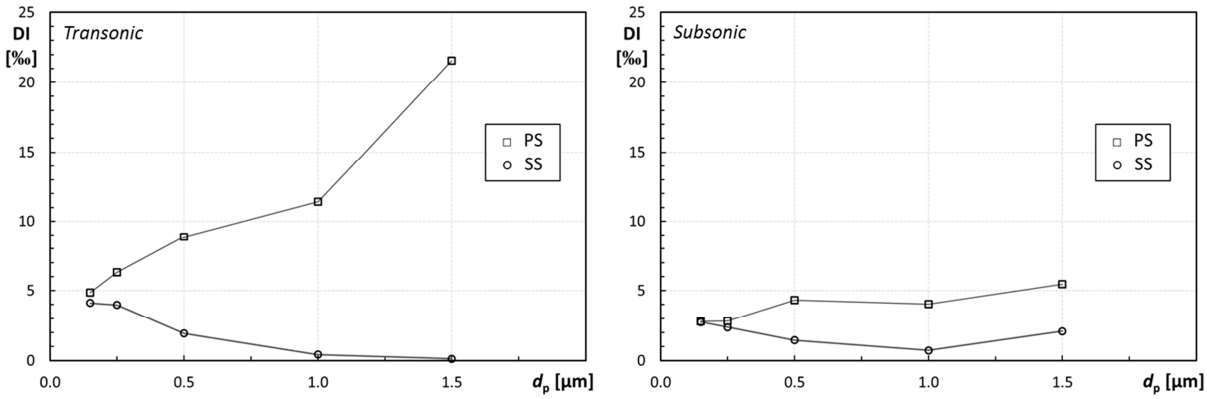

Figure 6.23 – DI vs particle diameter

dangerous index trend which is very similar for the pressure side and suction side. The separation and diffusion phenomena take place only in a small portion of the suction side close to the hub and both blade sides show that the inertial deposition is the major contributor to the composition of the deposits. In particular, as shown above, the deposition is concentrated on the leading edge area and the particle surrounds the leading edge from suction side to pressure side.

Experimental results reported by Tarabrin *et al.* (1998b) show that the rotor of the first stage of a 16 stage axial compressor is more highly contaminated by the deposits on the suction side (convex side) rather than the pressure side (concave side). By contrast, the rotor of the second stage is more greatly affected on the pressure side. Figure 6.24 depicts the experimental results from Tarabrin *et al.* (1998b).

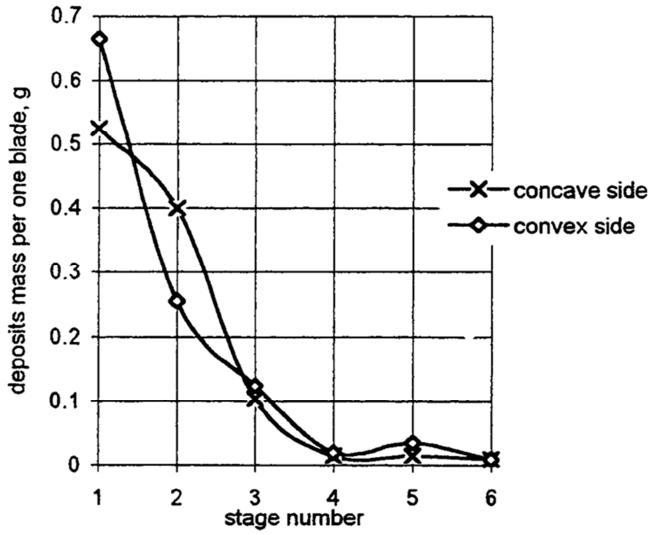

Figure 6.24 – Weight distribution of deposits on the convex and concave sides of the axial compressor rotor blades (Tarabrin *et al.*, 1998b)

The comparison of the numerical results provided by this thesis and the experimental results provided by an experimental evaluation of the blade deposit mass highlights that the fouling phenomenon is strongly related to power plant management (filtration systems and air contaminant concentration) and to the design characteristics of the axial compressor. Data taken from Tarabrin *et al.* (1998b) demonstrate that each stage should be specifically characterized for the fouling issue.

The last analysis refers to particle deposition on the blade tip. Table 6.12 reports the average values of contaminants at the blade tip. Deposits determine a greater boundary layer due to the increase in surface roughness. As stated in Aldi *et al.* (2014) blade surface roughness generates a variation in work and loss

distributions along the spanwise direction. In particular, the presence of greater roughness on the blade tip reflects greater work at the top of the blade. This effect is probably due to the different interaction between: (i) the boundary layer on the pressure surface, (ii) the tip gap and (iii) the main flow on the suction side. The interaction and the mixing phenomena that occur between the tip leakage vortex and the main flow are responsible for the losses in an axial compressor (Denton, 1993) and for this reason the difference in the magnitude of the tip leakage vortex determines differences in losses. Therefore, a different surface roughness at the top of the blade, corresponding to particle deposition at the blade tip, could determine differences in the cascade load and in particular, determine a greater load at the top of the blade. This fact, which could be positive at first glance, determines, in the case of multistage compressors, a stage rematch and, in some cases could determine the reduction of the stall margin for the successive stage due to the higher blade load at the blade tip in the first stage.

Table 6.12 – The average values of contaminant [kg/s] at the blade tip

Condition	Transonic	Subsonic
without filtration system	2.70e-12	2.13e-12
Industrial Spring, Poor Charge	6.42e-13	6.36e-13
Industrial Spring, Optimal Charge	3.68e-13	3.68e-13
Industrial Winter, Optimal Charge	7.34e-14	7.18e-14

Chapter 7

Guidelines and Final Remarks

7.1 Overall comparison between transonic and subsonic rotor

The study of particle impact/adhesion for axial compressors comprises countless phenomena and aspects, ranging from materials to the compressor's design characteristics. In this paragraph a brief summary of the results related to both rotors is reported. In particular, the comparison is presented in qualitative form and represents an easy-to-use statement of the particle impact/adhesion in axial compressors. The comparison related to particle impact behavior can be summarized as follows:

- for both rotors the percentage of the particles that hit the blade surface increases with the diameter of the particles but the transonic rotor is more affected by the particle impact (the mass flow rates swallowed by the two rotors as well as the amount of the contaminant are in the same order of magnitude). Some relations have been proposed in order to link the capture efficiency and the particle's characteristics as well as the compressor's characteristics;
- for both rotors, by increasing particle diameter, the pressure side is more affected by the impacts, thus the particles tend to hit the pressure side in increasing quantities as the particle diameter increases. On the other hand, the smaller particles surround the blade surfaces entirely;
- for the suction side, by increasing the particle diameter the suction side is less affected by the impacts in the case of the transonic rotor, while in the case of the subsonic rotor, by increasing the particle diameter the number of particles that hit the blade decreases to d_p = 1.00 µm, while the number of impacts that take place on the suction side increases from d_p = 1.00 µm to d_p = 2.00 µm. For these reasons, the subsonic rotor shows a more distributed particle impact pattern;
- the major differences in the particle impact pattern between the rotors are localized in the leading edge zone. The particles can surround the subsonic leading edge (from pressure side to suction side) because it is thicker than the transonic leading edge while, in the case of the transonic rotor, the thinner

leading edge only allows particle impact on the pressure side. This phenomenon could dramatically influence the performance drops of the subsonic rotor;

- the maximum value of the fouling index is an order of magnitude higher in the case of the transonic rotor (3.09 compared to 0.39 for the subsonic rotor).
- The comparison related to particle adhesion behavior can be summarized as follows:
- the particle impact velocity is lower in the case of the subsonic rotor due to the lower peripheral velocity. This implies that the particles impacting on the subsonic blade could have a greater probability of sticking because sticking probability is related to the normal impact velocity magnitude;
- the flow separation in the suction side influences particle adhesion in both rotors. In particular the separation reduces the magnitude of the air velocity field around the blade and this implies that the particle impact decreases, determining the aforementioned effect. The reduction regards, in particular, the values of the tangential impact velocity which are an order of magnitude less than those taking place before the separation line;

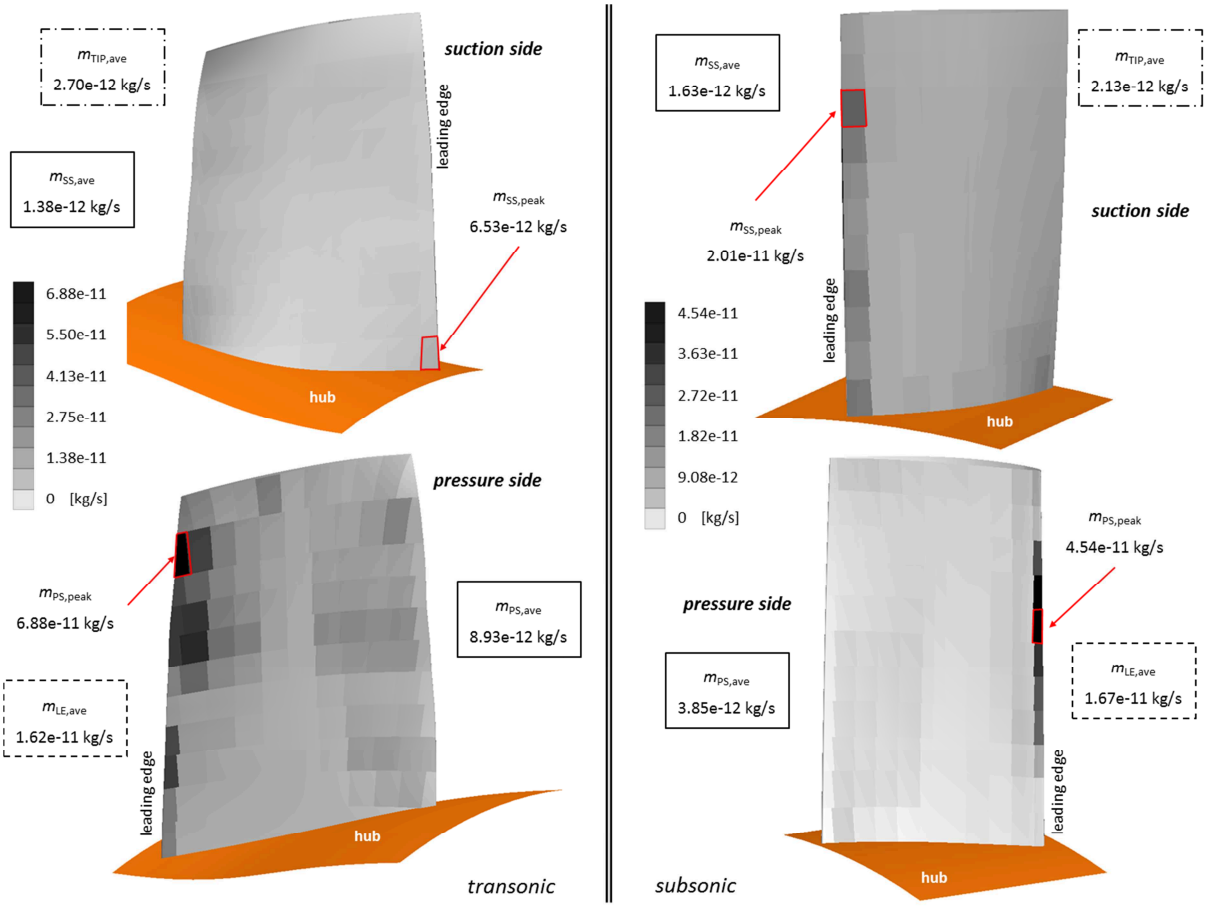

Figure 7.1 – Overall deposits on the blade surface: without filtration system (transonic and subsonic rotor)

- the trend of the percentage of the particles that could stick in the pressure side ($n_{hit,PS,SP>0.5}$) for the transonic rotor are almost independent with respect to the particle while, in the case of the subsonic rotor, this percentage decreases with the particle diameter. Thus, the bigger particles that impact in the pressure side are more dangerous in the case of the transonic rotor. The trend of the percentage of particles that could stick in the suction side ($n_{hit,SS,SP}$>0.5) follows the trend of the capture efficiency in both rotors;
- the amount of contaminant that sticks on the blade surfaces is almost the same for the two rotors. Figure 7.1 reports the comparison between the overall deposits on the blade surface for the rotors without filtration system. The order of magnitude of the contaminant is the same especially for the pressure side. In the suction side, the subsonic rotor shows a higher peak of contaminant located in the leading edge areas near the blade tip. In this case, the smaller capture efficiency value calculated for the subsonic rotor must be related to the smaller value of the particle impact velocity that leads to a higher value of sticking probability. However, transonic blade surfaces appear more contaminated in the pressure side as well as in the suction side, excluding the leading edge area. The shape of the subsonic airfoils could be responsible for the higher concentration of contaminants in the leading edge areas but, at the same time, the thicker leading edge could determine fewer deposits on the rest of the blade surface.

7.2 Conclusions

This thesis reports an extensive study of the micro-particle ingestion/adhesion by two different compressor rotors. Small particles overpassing the filtration systems and sticking to the blade surface determine the fouling problems. According to the objectives reported at the beginning of this thesis, the conclusions can be summarized according to the following points:

- the kinematic characteristics for the impacting particles are obtained by a numerical model validated by data from literature and are used in order to describe for the first time how the sub micro-size particles hit the blade surface. Special attention was given to the particle-blade interaction in terms of impact velocity and impact angle;
- numerous relation was given to quantify the amount of particles that impact the blade surfaces compared to the injected one. Particular attention was given to subdividing the particles that impact on the pressure side with those impacted on the pressure side because deposits in the pressure side determine fewer performance drops compared to the same deposits located in the suction side;

- general relations that link the compressor's capture efficiency with the compressor's design characteristics were given. Pressure and flow coefficients are directly related to the capability of the compressor to collect the particles dragged by the airflow;
- specific software was created in order to establish the kinematic characteristic of the impacting particles: impact angle, normal and tangential impact velocity were calculated for each particle that impacted on the blade surfaces. Thanks to literature data, the kinematic characteristics of the particles are linked with the sticking probability;
- numerical results and the post elaboration data have allowed the identification of the amount of contaminant that afflicts the blade surface as a function of the contamination of the compressor work environment and the efficiency of the filtration systems. Patterns reporting the mass flow rate of contaminants that afflict the blade surface were carried out as a function of the environment contamination and filtration efficiency.

7.3 Prospective

The understanding of fouling mechanisms in compressors is still a challenge for manufacturers and users. An increase in the knowledge of fouling through the use of numerical codes may therefore constitute a decisive element for better planning of the maintenance of turbomachinery. The computational fluid dynamic numerical simulations link the design characteristic of the machine and the fluid dynamic phenomena. As shown in this work these two items determine particle deposition on the blade surface and thus the fouling phenomena. In this sense, studies (experimental and numerical) dedicated to the interaction between the particles responsible for fouling (in terms of size and material) with blade surfaces are fundamental in order to allow for better simulations with numerical codes.

Through these analyses it is possible to determine the evolution of the fouling phenomenon through the integration of interdisciplinary studies: (i) CFD numerical simulation (that provides the match between the design characteristic of the machine and the fluid dynamic phenomena), (ii) particle-adhesion characteristics and (iii) power plant characteristics (air contaminant concentrations and the efficiency of filtration systems). The integration of these research fields could represent a valuable support for the investigation of the relationship between compressor airfoil design and fouling rate. In the future, this approach could be a support in the preliminary power plant design phase, in order to establish, a priori, the cost management due to the maintenance of filtration systems, the interval for washing operations as a function of the axial compressor and the air contaminant concentration that characterizes the power plant location.

List of Symbols

Normal letters

A	area
a, b, c, d, e, f, g	coefficient (referred to the Buckingham Pi Theorem)
a_1, a_2, a_3	model coefficient
B	function (referred to erosion model)
b	bounce (average)
C	function
d	diameter
d_{ij}	deformation tensor
E	Young module
e	restitution coefficient
F	force
f	function (referred to impact angle)
g	gravity acceleration
H	fouling index
He	head (referred to a rotor performance)
h_f	mass transfer coefficient
K	model constant
k	turbulent kinetic energy
L	dimensional characteristic of compressor
M	mass
m	mass flow rate
N	total number (referred to particles)
n	ratio
P	number of particle
p	pressure
q	volume flow rate
r	radius
Re	Reynolds number
St	Stokes number
T	temperature
t	time
U	averaged velocity
u	velocity component

u_t	shear velocity
V	axial component of absolute velocity
v	velocity
W	variable (referred to the filtration efficiency)
X	particle concentration (blade)
$y+$	non-dimensional distance

Greek letters

α	impact angle
β	compression ratio
ε	dissipation rate of turbulent kinetic energy
η	efficiency
λ	molecular mean free path
μ	dynamic viscosity
ν	kinematic viscosity
Π	dimensionless group
ρ	density
σ	standard deviation
τ	shear stress
$\tau+$	non-dimensional particle relaxation time
Φ	flow coefficient
χ	particle concentration (air)
ψ	pressure coefficient
ω	angular velocity

Subscripts and superscripts

ave	average value
B	Brownian
b	bounce
C	Cunningham
c	contaminant
D	drag
f	filtration system
g	gauge
h	hydraulic
hit	hit (referred to particle-blade interaction)
i	impact
j,k,l	indices
max	maximum value
min	minimum value
n	normal direction
p	particle
peak	peak value
S	Saffman
SIDE	side (referred to the side of the blade)
sh	shear
SLICE	slice (referred to chordwise division)
STRIP	strip (referred to spanwise division)
t	tangential
TT	total-to-total
w	wall
0	total
1	inlet
2	outlet
—	average
~	weighted-area average
*	peak
x,y,z	axis coordinate

Acronyms

AC	Accretion Rate
AFM	Atomic Force Microscopy
CFD	Computational Fluid Dynamics
CP	Chemical Pure (referred to the cold spray deposition)
DI	Dangerous Index
DPM	Discrete Phase Model
DRW	Discrete Random Walk
IS	Industrial Spring
ISF	Index of compressor Sensitivity to Fouling
IW	Industrial Winter
FDS	Flux-Difference Splitting
HDH	Hydride-DeHydride (referred to the cold spray deposition)
LE	Leading Edge
OC	Optimal Charge
PC	Poor Charge
PS	Pressure Side
SEM	Scanning Electron Microscope
SP	Sticking Probability
SS	Suction Side
STW	STandard Wall function
TE	Trailing Edge
U	Urban

this page was intentionally left blank

References

Abd-Elhady, M. S., Rindt, C.C.M., Wijers, J. G., van Steenhoven, A. A., 2006, "Modelling the impaction of a micron particle with a powdery layer", *Powder Technology*, **168**, pp. 111–24

Adi, S., Adi, H., Chan, H. K., Tong, Z., Yang, R., Yu, A., 2013, "Effects of mechanical impaction on aerosol performance of particles with different surface roughness", *Powder Technology*, **236**, pp. 164–170

Ahlert, K., 1994, "Effects of Particle Impingement Angle and Surface Wetting on Solid Particle Erosion of AISI 1018 Steel", M.S. Thesis, Department of Mechanical Engineering, The University of Tulsa, Tulsa, Oklahoma, US

Ahluwalia, R. K., Im, K. M., Wenglarz, R. A., 1989, " Flyash Adhesion in Simulated Coal-Fired Gas Turbine Environment", *Journal of Engineering for Gas Turbine and Power*, **111**, pp. 672–678

Alkhimov, A. P., Kosarev, V. F., Papyrin, A. N., 1990, "A method of "cold" gas-dynamic spraying", *Soviet Physics Doklady*. **35**, pp. 1047–1049

Alkhimov, A. P., Kosarev, V. F., Papyrin, A. N., 1992, "New Materials and Technologies, Theory and Practice of Materials Hardening in Extremal Processes", Novosibirsk: Nauka, (in Russian)

Aldi, N., Morini, M., Pinelli, M., Spina, P. R., Suman, A., Venturini, M., 2014, "Performance Evaluation of Non-Uniformly Fouled Axial Compressor Stages by Means of Computational Fluid Dynamics Analyses," *Journal of Turbomachinery*, **136**(2), p. 021016

Andreasen, A. (1939), Op. Cit. Fuchs (1964), Ref. 558

ANSYS Fluent, 2012 , User Manual, ANSYS, Inc., Canonsburg, Pennsylvania, US

ASHRAE 52.2 – Method of Testing General Ventilation Air-Cleaning Devices for Removal Efficiency by Particle Size, American Society of Heating, Refrigeration and Air-Conditioning Engineers, Inc., 2007

Back, S. C., Hobson, G. V., Song, S. J., Millsaps, K. T., 2010, "Effect of Surface Roughness Location and Reynolds Number on Compressor Cascade Performance", ASME Paper GT2010-22208

Balan, C., Tabakoff, W., 1984, “Axial flow compressor performance deterioration”, 20th Joint Propulsion Conference, June 11-13, 1984, Cincinnati, Ohio, US

Bammert, K., Woelk, G. U., 1980, “ The Influence of the Blading Surface Roughness on the Aerodynamic Behavior and Characteristic of an Axial Compressor”, *Journal of Engineering for Power*, **102**, pp. 283–287

Birmili, W., Tomsche, L., Sonntang, A., Opelet, C., Weinhold, K., Nordmann, S., Schmidt, W., 2013, “Variability of aerosol particles in the urban atmosphere of Dresden (Germany): Effects of spatial scale and particle size”, *Meteorologische Zeitschrift*, **22**(2), pp. 195–211

Bons, J. P., 2010, “A Review of Surface Roughness Effects in Gas Turbines”, *Journal of Turbomachinery*, **132**, p. 021004

Borello, D., Rispoli, F., Venturini, P., 2012, “An Integrated Particle-Tracking Impact/Adhesion Model for the Prediction of Fouling in a Subsonic Compressor”, *Journal of Engineering for Gas Turbine and Power*, **134**, p. 092002

Boyle, R. J., 1994, “Prediction of Surface Roughness and Incidence Effects on Turbine Performance”, *Journal of Turbomachinery*, **123**, pp. 70–77

Brach, R. M., Dunn, P. F., 2007, “A Mathematical Model of the Impact and Adhesion of Microsphers”, *Aerosol Science and Technology*, **16**(1), pp. 51–64

Brake, C., 2007, “Identifying areas prone to dusty winds for gas turbine inlet specification”, Proceedings of ASME Paper GT2007-27820

Brice, T., “Atmospheric Aerosols: physical properties; chemical composition; health & environmental effects”, Department of Chemistry, UCC, Ireland

Brun, K., Foiles, W. C., Grimley, T. A:, Kurz, R., 2013, “Experimental Evaluation of the Effectiveness of Online Water-Washing in Gas Turbine Compressors”, Proceedings of the Forty-Second Turbomachinery Symposium September 30-October 3, 2013, Houston, Texas, US

Brun, K., Nored, M., Kurz, R., 2012, “Analysis of Solid Particle Surface Impact Behavior in Turbomachines to Asses Blade Erosion and Fouling”, Proceedings of the Forty-First Turbomachinery Symposium September 24-27, 2012, Houston, Texas, US

Buckingham, E., 1914, “On Physically Similar Systems; Illustrations of the Use of Dimensional Equations”, *Physical Review*, **4**, pp. 345–376

camfil FARR, 2013, Technical report

Casaday, B., Prenter, R., Bonilla, C., Lawrence, M., Clum, C., Ameri, A. A., Bons, J.

P., 2014, “Deposition With Hot Streaks in an Uncooled Turbine Vane Passage”, *Journal of Turbomachinery*, **136**, p. 041017

Clift, R., Grace, J. R., and Weber, M. E., 1978, "Bubbles, Drops, and Particles," ACADEMIC PRESS, New York, US

Cumpsty, N. A., (1989), Compressor Aerodynamics, Longman Scientific & Technical, Harlow, UK

Day, I., Williams, J., Freeman, C., 2008, “Rain Ingestion in Axial Flow Compressors at Part Speed”, *Journal of Turbomachinery*, **130**, p. 011024

Denton, J. D., 1993, “Loss Mechanism in Turbomachines”, The 1993 IGTI Scholar Lecture, *Journal of Turbomachinery*, **115**(4), pp. 621–656

Delimont, J. M., Murdock, M. K., Ng, W. F., Ekkad, S. V., 2014, “Effect of Near Melting Temperatures on Microparticle Sand Rebound Characteristics at Constant Impact Velocity”, ASME Paper GT2014-25686

Derjaguin, B. V., Muller, V. M., Toporov, Yu. P. Yu. P. Yu. P., 1975, “Effect of contact deformations on the adhesion of particles”, *Journal of Colloid Interface*, **53**(2), pp. 314–326

Diakunchak, I. S., 1992, “Performance Deterioration in Industrial Gas Turbines”, *Journal of Engineering for Gas Turbine and Power*, **114**, pp. 161–168

Dykhuizen, R. C:, Smith, M. F., 1998, “Gas Dynamic Principles of Cold Spray“, Journal of Thermal Spray Technology, **7**(2), pp. 205–212

El-Batsh, H., Haselbacher, H., 2000, “Effect of Turbulence Modeling on Particle Dispersion and Deposition on Compressor and Turbine Blade Surfaces“, ASME Paper GT2000-0519

Elrod, C. E., Bettner, J. L., 1983, “Experimental Verification of an Endwall Boundary Layer Prediction Method”, Report No. AGRAD CP-351

EN 779:2012 - Dust air filters for general ventilation - Determining the filtering performance

Forder, A., Thew, M., Harrison, D., 1998, “A Numerical Investigation of Solid Particle Erosion Experienced Whithin Oilfield Control Valves”, *Wear*, **216**, pp. 184–193

Fottner, L., 1989, “Review of Turbomachinery Blading Design Problems,” Report No. AGARD-LS-167

Fuchs, N. A., 1964, “The Mechanics of Aerosols”, Dover Publications, Inc., New York, US

Gbadebo, S. A., Cumpsty, N. A., Hynes, T. P., 2005, Three-Dimensional Separations in Axial Compressors, *Journal of Turbomachinery*, **127**, pp. 331–339

Gbadebo, S. A., Hynes, T. P., Cumpsty, N. A., 2004, "Influence of Surface Roughness on Three-Dimensional Separation in Axial Compressors," *Journal of Turbomachinery*, **126**(4), pp. 455–463

Ghenaiet, A., 2012, "Study of Sand Particle Trajectories and Erosion Into the First Compression Stage of a Turbofan", *Journal of Turbomachinery*, **134**, p. 051025

Gotoh, K., Masuda, M., Higashitani, K., 1997, Powder Technology Handbook, 2nd Ed. Marcel Dekker, New York, US

Guha, A., 2008, "Transport and Deposition of Particles in Turbulent and Laminar Flow", *Annual review of fluid mechanics*, **40**, pp. 311–341

Gupta, P. K., Pagalthivarthi, K. V., 2006, "A comparative study of the effect of model lift coefficients on particle trajectory", *Indian Journal of Engineering & Materials Sciences*, **13**, pp. 293–306

Hamaker, H. C., 1937, "The London-Van Der Walls Attraction Between Spherical Particles", Physica, **4**(10), pp. 1058–1072

Hamed, A. A., Tabakoff, W., Rivir, R. B., Das, K., Arora, P., 2005, "Turbine Blade Surface Deterioration by Erosion", *Journal of Turbomachinery*, **127**, pp. 445–452

Hamed, A., Tabakoff, W., Singh, D., 1998, "Modeling of Compressor Performance Deterioration Due to Erosion", International Journal of Rotating Machinery, **4**(4), pp. 243–248

Hamed, A., Tabakoff, W., Wenglarz, R., 2006, "Erosion and Deposition in Turbomachinery", *Journal of Propulsion and Power*, **22**(2), pp. 350–360

Heim, L. O., Blum, J., Preuss, M., Butt, H. J., 1999, "Adhesion and Friction Forces between Spherical Micrometer-Sized Particles", *Physical Review Letters*, **83**(16), pp. 3328–3331

Hepperle, N., Therkorn, D., Schneider, E., 2011, „Assessment of Gas Turbine and Combined Cycle Power Plant Performance Degradation", ASME Paper GT2011-45375

Hertz, H., 1896, "Miscellaneous Papers," MACMILLAN AND CO., LTD., London, UK (Authorised english Translation), pp. 146–183

Hoeft, R. F., 1993, "Heavy Duty Gas Turbine Operating and Maintenance Considerations", GER-3620B, GE I&PS

Hummel, F., Ltzerich, M., Cardamone, P., Fottner, L., 2005, "Surface Roughness Effects on Turbine Blade Aerodynamics", *Journal of Turbomachinery*, **127**, pp. 453–461

Jacobs, G. B., Don, W. S:, Dittmann, T., 2012, "High-order resolution Eulerian–Lagrangian simulations of particle dispersion in the accelerated flow behind a moving shock", *Theoretical and Computational Fluid Dynamics*, **26**, pp. 37–50

Johnson, K. L., Kendall, K., Roberts, A. D., 1971, "Surface Energy and the Contact of Elastic Solids", Proceedings of the Royal Society of London. Series A, Mathematical and Physical, **324**(1558), pp. 301–313

Khan, J. R., Wang, T., 2011, " Three-Dimensional Modeling for Wet Compression in a Single Stage Compressor Including Liquid Particle Erosion Analysis", *Journal of Engineering for Gas Turbine and Power*, **133**, p. 012001

Kind, R. J., Serjak, P. J., Abbott, M. W. P., 1998, "Measurements and Prediction of the Effects of Surface Roughness on Profile Losses and Deviation in a Turbine Cascade", *Journal of Turbomachinery*, **120**, pp. 20–27

Klinkov, S. V., Kosarev, V., F., Rein, M., 2005, "Cold spray deposition: Significance of particle impact phenomena", *Aerospace Science and Technology*, **9**, pp. 582-591

Krupp, H., 1967, "Particle Adhesion Theory and Experiment", *Advances in Colloid and Interface Science*, **1**, pp. 111–239

Kumar, A., Nair, P. B., Keane, A. J., Shahpar, S., 2005, "Probabilistic performance analysis of eroded compressor blades", Proceedings of ASME Power Conference, Chicago, 5-7 April, 2005, Chicago, Illinois, US

Kurz, R., Brun, K, 2012, "Fouling Mechanism in Axial Compressor", *Journal of Engineering for Gas Turbine and Power*, **134**, p. 032401

Kurz, R., Brun, K., Meher-Homji, C., Moore, J., 2012, „Gas Turbine Performance and Maintenance", Proceedings of the Forty-First Turbomachinery Symposium September 24-27, 2012, Houston, Texas, US

Kurz, R., Brun, K., Wollie, M., 2008, "Degradation Effects on Industrial Gas Turbine", ASME Paper GT2008-50020

Lee, B. E., Tu, J. Y., Fletcher, C. A. J., 2002, "On numerical modeling of particle–wall impaction in relation to erosion prediction: Eulerian versus Lagrangian method", *Wear*, **252**, pp. 179–188

Li, C. J., Li, W. Y., Wang, Y. Y., Yang, G. J., Fukanuma, H., 2005, "A theoretical model for prediction of deposition efficiency in cold spraying", *Thin Solid Films*, **489**,

pp. 79–85

Liu, Y. J., Harrison, R. M., 2011, “Properties of coarse particles in the atmosphere of the United Kingdom”, *Atmospheric Environment*, **45**, pp. 3267–3276

Lü, S., Yi, F., Hao, X., Yu, S., Ren, J., Wu, M., Jialiang, F., Yonemochi, S., Wang, Q., 2013, “Physicochemical properties and ability to generate free radicals of ambient coarse, fine, and ultrafine particles in the atmosphere of Xuanwei, China, an area of high lung cancer incidence”, *Atmospheric Environment*, **97**, pp. 519–528

Lü, S., Zhang, R., Yao, Z., Yi, F., Ren, J., Wu, M., Feng, M., Wang, Q., 2012, “Size distribution of chemical elements and their source apportionment in ambient coarse, fine, and ultrafine particles in Shanghai urban summer atmosphere”, *Journal of Environmental Sciences*, **24**(5), pp. 882–890

Mangwandi, C., Cheonga, Y. S., Adamsb, M. J., Hounslowa, M. J., Salmana, A. D., 2007, “The coefficient of restitution of different representative types of granules”, *Chemical Engineering Science*, **62**, pp. 437–450

Maugis, D., Pollock, H. M., 1984, “Surface forces, deformation and adherence at metal microcontacts”, Acta Metallurgica, **32**(9), pp. 1323–1334

Meher-Homji, C., Bromley, A., 2004, “Gas Turbine Compressor Fouling and Washing”, Proceedings of the Thirty-Third Turbomachinery Symposium September, 2004, Houston, Texas, US

Meher-Homji, C. B., Chaker, M. A., Bromley, A. F., 2009, “The Fouling of Axial Flow Compressors — Causes, Effects, Susceptibility and Sensitivity,” ASME Paper No. GT2009-59239

Meher-Homji, C. B., Chaker, M. A:, Motiwala, H., 2001, “Gas turbine performance deterioration”, Proceedings of the Thirty Turbomachinery Symposium, September 12-15, 2011, Houston, Texas, US

Morini, M., Pinelli, M., Spina, P. R., Venturini, M., 2010a, “Influence of Blade Deterioration on Compressor and Turbine Performance”, *Journal of Engineering for Gas Turbine and Power*, **132**, p. 072401

Morini, M., Pinelli, M., Spina, P. R., Venturini, M., 2010b, “Computational Fluid Dynamics Simulation of Fouling on Axial Compressor Stages”, *Journal of Engineering for Gas Turbine and Power*, **132**, p. 072401

Morini, M., Pinelli, M., Spina, P. R., Venturini, M., 2011, “Numerical Analysis of the Effects of Non-Uniform Surface Roughness on Compressor Stage Performance”, *Journal of Engineering for Gas Turbine and Power*, **133**(7), p. 072402

Morsi, S. A., Alexander, A. J., 1972, "An Investigation of Particle Trajectories in Two-Phase Flow Systems", *Journal of Fluid Mechanics*, **55**(2), pp. 193–208

Muller, V. M., Yushchenko, V. S., Derjaguin, B. V., 1980, “On the influence of molecular forces on the deformation of an elastic sphere and its sticking to a rigid plane”, *Journal of Colloid Interface*, **77**(1), pp. 91–101

Mund, F. C., Pilidis, P., 2006, “Gas Turbine Compressor Washing: Historical developments, Trends and Main design Parameters for Online Systems“, *Journal of Engineering for Gas Turbine and Power*, **128**, pp. 344–353

Mustafa, Z., Pilidis, P., Amaral Teixeira, J. A., Arifin Ahmad, K., 2006, “CFD Aerodynamic investigation of air-water trajectories on rotor-stator blade of an axial compressor for online washing”, ASME Paper GT2006-90745

Nicholson, G., 1990, “Gas Turbine Cleaning at the Utrecht Site of Dutch Utility Company", *Turbomachinery International*, May/June

Papyrin, A. N., Kosarev, V. F., Klinkov, S., Alkhimov, A. P., Fomin, V., 2007, “Cold Spray Technology”, Elsevier, Oxford, UK

Reagle, C. J., Delimont, J. M., Ng, W. F., Ekkad, S. V., 2014, “Study of Microparticle Rebound Characteristics Under High Temperature Conditions”, *Journal of Engineering for Gas Turbine and Power*, **136**, p. 011501

Parker, G. J., Lee, P., 1972, “Studies of the Deposition of Sub-Micron Particles on Turbine Blades”, Proceedings of the Institution of Mechanical Engineers, **186**(1), pp. 519–526

Poppe, T., Blum, J., 1997, “Experimental on pre-planetary grain growth”, *Advances in Space Research*, **20**(8), pp. 1595–1604

Poppe, T., Blum, J., Henning, T., 2000, “Analogous experiments on the stickiness of micron-sized preplanetary dust”, *The Astrophysical Journal*, **533**, pp. 454–471

Reid, L., Moore, R.D., 1978, “Design and overall performance of four highly-loaded, high-speed inlet stages for an advanced high-pressure-ratio core compressor”, NASA TP 1337

Reid, L., Urasek, D. C., 1973, “Experimental Evaluation of the Effects of a Blunt Leading Edge on the Performance of a Transonic Rotor”, *Journal of Engineering for Gas Turbine and Power*, **95**(3), pp. 199–204

Saffman, P. G., 1965, "The Lift on a Small Sphere in a Slow Shear Flow", *Journal of Fluid Mechanics*, **22**(2), pp. 385–400

Samsher, R. L., 2007, “Comparison between loss coefficients of smooth, smooth-thickened, and rough-thickened axial turbine blades”, Proceedings of the Institution of Mechanical Engineers, **221**, A, pp. 575–582

Schroth, T., Cagna, M., 2008, “Economical Benefits of Highly Efficient Three-Stage Intake Air Filtration for Gas Turbines”, Proceedings of ASME Paper GT2007-50280

Schurovsky, V.A., Levikin, A.P., 1986, "Fouling and Cleaning of Gas Turbine Axial Compressor Flow Path", Moscow, series, *Transport and Gas Conservation*, **11**

Scott, J. N., 1979, “Axial Compressor Monitoring by Measuring Air Intake Depression”, Third Symposium on Gas Turbine Operations and Maintenance, National research Council of Canada, September 1979

Silingardi, A., Astrua, P., Piola, S., Ventrucci, I., 2013, “A Method for a Reliable Prediction of Heavy Duty Gas Turbines Performance Degradation due to Compressor Aging Employing Field Test Data,” Power Gen Europe, June 4-6, 2013, Messe, Wien, Austria

Song, Q. L., Li, C., Wei, Y., Chen, J., 2013, “Numerical and experimental study of particle deposition on inner wall of 180° bend”, *Powder Technology*, **237**, pp. 241–254

Stalder, J. -P., 2001, “Gas Turbine Compressor Washing State of the Art: Field Experiences”, *Journal of Engineering for Gas Turbine and Power*, **123**, pp. 363–370

Suder, K. L., Chima, R. V., Strazisar, A. J., Roberts, W. B., 1995, “The Effect of Adding Roughness and Thickness to a Transonic Axial Compressor rotor”, *Journal of Turbomachinery*, **117**(4), pp. 491–505

Suzuki, M., Inaba, K., Yamamoto, M., 2008, “Numerical Simulation of Sand Erosion Phenomena in Rotor/Stator Interaction of Compressor”, *Journal of Thermal Science*, **17**(2), pp. 125–133

Suzuki, M., Yamamoto, M., 2011, “Numerical Simulation of Sand Erosion Phenomena in a Single-Stage Axial Compressor”, *Journal of Fluid Science and Technology*, **6**(1), pp. 98–113

Syverud, E., Brekke, O., Bakken, L. E., 2005, “Axial Compressor deterioration caused by Saltwater Ingestion”, ASME Paper GT2005-68701

Tarabrin, A. P., Schurovsky, V. A., Boldrov, A. I., Stalder, J. -P, 1998a, “An Analysis of Axial Compressor Fouling and a Blade Cleaning Method“, *Journal of Turbomachinery*, **120**, pp. 256–261

Tarabrin, W. P., Schurovsky, V. A., Bodrov, A. I., Stalder, J.-P., 1998b, “Influence of Axial Compressor Fouling on Gas Turbine Unit Performance Based on Different Schemes and With Different Initial Parameters”, ASME Paper 98-GT-416

Thornton, C., Ning, Z., 1998, “A theoretical model for the stick/bounce behavior of adhesive elastic-plastic spheres”, *Powder Technology*, **99**, pp. 154–162

Tian, T., Ahmadi G., 2007, “Particle deposition in turbulent duct flows—comparisons of different model predictions”, *Journal of Aerosol Science*, **38**, pp. 377–397

Tomas, J., 2006, “Mechanics of particle Adhesion”, Mechanical Process Engineering, Department of Process Engineering and Systems Engineering, Otto-von-Guericke-University, Magdeburg, Germany

Vigueras Zuniga, M. O., 2007, “Analysis of Gas Turbine Compressor Fouling and Washing on Line”, Ph. D. Thesis, Cranfield University, UK

Wall, S., John, W., Wang, H. C., Goren, S. L., 1990, “Measurements of Kinetic Energy Loss for Particles Impacting Surfaces”, *Aerosol Science and Technology*, **12**(4), pp. 926–946

Wang, G. H., Zhou, B. H., Cheng, C. L., Cao, J. J., Li, J. J., Meng, J. J., Tao, J., Zhang, R. J., Fu, P. Q., 2013, “Impact of Gobi desert dust on aerosol chemistry of Xi’an, inland China during spring 2009: differences in composition and size distribution between the urban ground surface and the mountain atmosphere”, *Atmospheric Chemistry and Physics*, **13**, pp. 819–835

Wang, T., Dhanasekaran, T. S., 2008, “Calibration of CFD Model for Mist/Steam Impinging Jets Cooling”, ASME Paper No. GT2008-50737

Wilcox, M., Baldwin, R., Garcia-Hernandez, A., Brun, K., 2010, “Guideline for gas turbine inlet air filtration systems”, Gas Machinery Research Council Southwest Research Institute, Release 1.0

Wilcox, M., Kurz, R., Brun, K., 2011, ”Successful Selection and Operation of Gas Turbine Inlet Filtration Systems”, Proceedings of the Fortieth Turbomachinery Symposium, September 12-15, 2011, Houston, Texas, US

Zaba, T, 1980, “Losses in Gas Turbines Due to Deposits on the Blading”, *Brown Boveri review*, **67**(12), pp. 715–722

Zender, C. S., Bian, H., Newman, D., 2003, “Mineral Dust Entrainment and Deposition (DEAD) model: Description and 1990s dust climatology”, *Journal of Geophysical research*, **108**(D14)

Zhang, Z., Chen, Q., 2006, “Experimental measurements and numerical simulations of particle transport and distribution in ventilated rooms”, *Atmospheric Environment*, **40**, pp. 3396–3408

Zhu, Y., Hinds, W. C., Kim, S., Sioutas, C., 2011, “Concentration and Size Distribution of Ultrafine Particles Near a Major Highway”, *Journal of the Air & Waste Management Association*, **52**, pp. 1032–1042

Zohdi, T. I., 2004, “Modeling and direct simulation of near-field granular flows”, *International Journal of Solid and Structures*, **42**, pp. 539–564

Acknowledgements

I thank my advisor Professor Michele Pinelli and Professor Pier Ruggero Spina for their continuous guidance, advice and for giving me the opportunities to improve my knowledge.

I thank Dr. Rainer Kurz and Dr. Klaus Brun for their availability, useful ideas and curiosity that pushed me to enhance the quality of the analyses and the comprehension of the results.

I thank the staff of the Fluid Machinery Research Group at the University of Ferrara who have challenged me and pushed my work forward.

Finally, I thank my family for their invaluable support.

this page was intentionally left blank

List of papers

1- Suman, A., Kurz, R., Aldi, N., Morini, M., Brun, K., Pinelli, M., Spina, P. R., 2015, "Quantitative CFD Analyses of Particle Deposition on an Axial Compressor Blade, Part I: Particle Zones Impact", *Journal of Turbomachinery*, **137**, p. 021009

- Presented at the ASME Turbo Expo 2014: Turbine Technical Conference and Exposition GT2014-25282, June 16 – 20, 2014, Düsseldorf, Germany

2- Suman, A., Morini, M., Kurz, R., Aldi, N., Brun, K., Pinelli, M., Spina, P. R., 2015, "Quantitative CFD Analyses of Particle Deposition on an Axial Compressor Blade, Part II: Impact Kinematics and Particle Sticking Analysis", *Journal of Turbomachinery*, **137**, p. 021010

- Presented at the ASME Turbo Expo 2014: Turbine Technical Conference and Exposition GT2014-25473, June 16 – 20, 2014, Düsseldorf, Germany
- Paper awarded by Best Paper Award by Oil & Gas Committee

3- Aldi, N., Morini, M., Pinelli, M., Spina, P. R., Suman, A., 2015, "Comparative Analyses of Micro-Particle Impact Between Transonic and Subsonic Axial Compressors", Proceedings of European Turbomachinery Conference, March 23 – 26, 2015, Madrid, Spain

4- Suman, A., Kurz, R., Aldi, N., Morini, M., Brun, K., Pinelli, M., Spina, P. R., 2015, "Quantitative CFD Analyses of Particle Deposition on a Subsonic Axial Compressor Blade", Proceedings of ASME Turbo Expo, Paper GT2015-42685, June 15 – 19, 2015, Montreal, Canada

5- Suman, A., Morini, M., Kurz, R., Aldi, N., Brun, K., Pinelli, M., Spina, P. R., 2015, "Estimation of the Particle Deposition on a Transonic Axial Compressor Blade", Proceedings of ASME Turbo Expo, Paper GT2015-42689, June 15 – 19, 2015, Montreal, Canada

this page was intentionally left blank

Appendix I

Overall Impact Patterns

Figure AI.1 – Spanwise subdivision (left side) and overall impact patterns (transonic rotor)

All the particle impact patterns are reported in Figs. AI.1 and AI.2 for transonic and subsonic rotor respectively. Each pattern represents the projection of the fouled airfoil into a perpendicular plane with respect to the spanwise direction. On the left side the spanwise station and the correspondent percentage of the blade span is reported. The blade was divided by 11 strips along the spanwise direction and each dot on the graph represents a single particle that has hit the blade surface. For the transonic case, due to the shape of the hub, which develops along the streamwise direction with different diameters, the projection of the first strip is not complete and only the first half of the airfoil can be represented.

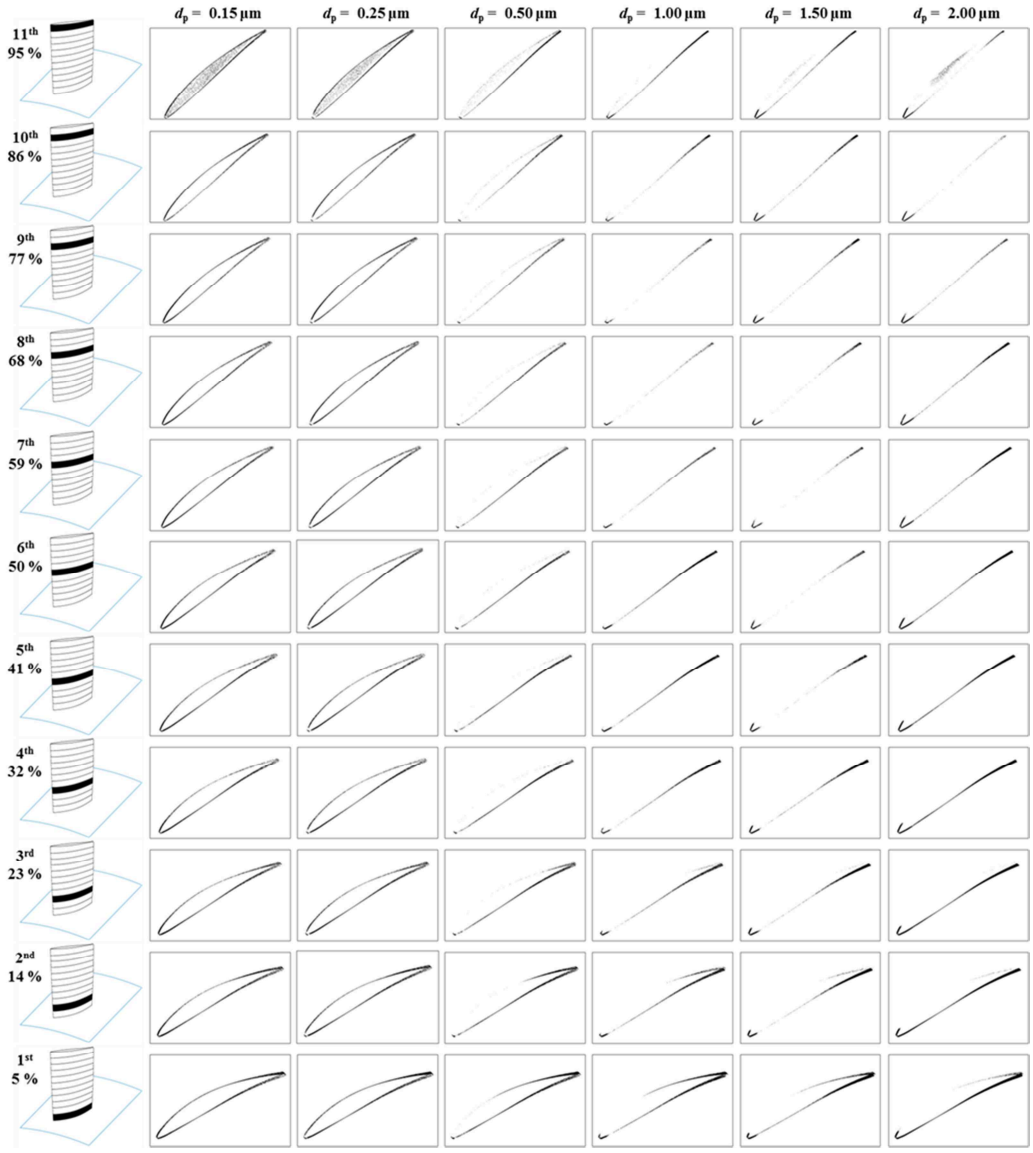

Figure AI.2 – Spanwise subdivision (left side) and overall impact patterns (subsonic rotor)

Appendix II

Particle Blade Interaction – Transonic Rotor

Table AII.1 – Particle-blade interaction, Cases 1 and 2 (transonic rotor)

		Case 1 (d_p = 0.15 µm)						Case 2 (d_p = 0.25 µm)					
		Pressure side			Suction side			Pressure side			Suction side		
		N	n_{SIDE} [%]	n_{hit} [%]	N	n_{SIDE} [%]	n_{hit} [%]	N	n_{SIDE} [%]	n_{hit} [%]	N	n_{SIDE} [%]	n_{hit} [%]
11th	*Harmless*	4,299	4.39	0.05	1,852	2.83	0.02	8,004	5.69	0.09	1,333	2.18	0.02
	0 < v_n ≤ 90 m/s	4,195	4.28	0.05	3,300	5.04	0.04	4,392	3.12	0.05	2,678	4.38	0.03
	v_n > 90 m/s	756	0.77	0.01	613	0.94	0.01	283	0.20	0.00	328	0.54	0.00
	SP ≥ 0.5	3,836	3.92	0.05	2,265	3.46	0.03	4,045	2.88	0.05	1,717	2.81	0.02
10th	*Harmless*	1,998	2.04	0.02	345	0.53	0.00	5,606	3.99	0.07	335	0.55	0.00
	0 < v_n ≤ 90 m/s	11,142	11.38	0.13	8,185	12.49	0.10	15,102	10.74	0.18	6,385	10.44	0.08
	v_n > 90 m/s	137	0.14	0.00	228	0.35	0.00	669	0.48	0.01	191	0.31	0.00
	SP ≥ 0.5	10,120	10.33	0.12	7,426	11.34	0.09	11,943	8.49	0.14	5,951	9.73	0.07
9th	*Harmless*	970	0.99	0.01	72	0.11	0.00	2,249	1.60	0.03	71	0.12	0.00
	0 < v_n ≤ 90 m/s	8,099	8.27	0.10	5,978	9.13	0.07	11,079	7.88	0.13	5,011	8.20	0.06
	v_n > 90 m/s	313	0.32	0.00	120	0.18	0.00	1,216	0.86	0.01	113	0.18	0.00
	SP ≥ 0.5	7,849	8.02	0.09	5,579	8.52	0.07	9,049	6.43	0.11	4,729	7.73	0.06
8th	*Harmless*	1386	1.42	0.02	100	0.15	0.00	2,159	1.53	0.03	385	0.63	0.00
	0 < v_n ≤ 90 m/s	9,042	9.23	0.11	7,225	11.03	0.09	13,206	9.39	0.16	6,724	11.00	0.08
	v_n > 90 m/s	345	0.35	0.00	60	0.09	0.00	1,403	1.00	0.02	35	0.06	0.00
	SP ≥ 0.5	8,906	9.09	0.10	6,704	10.23	0.08	11,711	8.33	0.14	6,321	10.34	0.07
7th	*Harmless*	2,149	2.19	0.03	93	0.14	0.00	2,974	2.11	0.04	319	0.52	0.00
	0 < v_n ≤ 90 m/s	8,897	9.09	0.10	5,549	8.47	0.07	13,162	9.36	0.16	4,969	8.13	0.06
	v_n > 90 m/s	333	0.34	0.00	13	0.02	0.00	1,032	0.73	0.01	1	0.00	0.00
	SP ≥ 0.5	8,816	9.00	0.10	5,226	7.98	0.06	12,071	8.58	0.14	4,749	7.77	0.06
6th	*Harmless*	2,141	2.19	0.03	77	0.12	0.00	2,785	1.98	0.03	381	0.62	0.00
	0 < v_n ≤ 90 m/s	7,367	7.52	0.09	3,823	5.84	0.05	9,623	6.84	0.11	3,184	5.21	0.04
	v_n > 90 m/s	288	0.29	0.00	5	0.01	0.00	539	0.38	0.01	1	0.00	0.00
	SP ≥ 0.5	7,265	7.42	0.09	3,629	5.54	0.04	8,711	6.19	0.10	3,063	5.01	0.04
5th	*Harmless*	1,838	1.88	0.02	51	0.08	0.00	1,967	1.40	0.02	65	0.11	0.00
	0 < v_n ≤ 90 m/s	4,179	4.27	0.05	4,794	7.32	0.06	4,646	3.30	0.05	4,785	7.83	0.06
	v_n > 90 m/s	117	0.12	0.00	14	0.02	0.00	350	0.25	0.00	0	0.00	0.00
	SP ≥ 0.5	4,102	4.19	0.05	4,587	7.00	0.05	4,127	2.93	0.05	4,624	7.56	0.05
4th	*Harmless*	3,480	3.55	0.04	80	0.12	0.00	5,202	3.70	0.06	115	0.19	0.00
	0 < v_n ≤ 90 m/s	6,362	6.50	0.07	5,890	8.99	0.07	8,021	5.70	0.09	6,057	9.91	0.07
	v_n > 90 m/s	91	0.09	0.00	16	0.02	0.00	254	0.18	0.00	12	0.02	0.00
	SP ≥ 0.5	6,221	6.35	0.07	5,389	8.23	0.06	7,411	5.27	0.09	5,393	8.82	0.06
3rd	*Harmless*	3,461	3.53	0.04	192	0.29	0.00	4,840	3.44	0.06	311	0.51	0.00
	0 < v_n ≤ 90 m/s	3,428	3.50	0.04	7,367	11.25	0.09	4,205	2.99	0.05	7,074	11.57	0.08
	v_n > 90 m/s	162	0.17	0.00	139	0.21	0.00	526	0.37	0.01	123	0.20	0.00
	SP ≥ 0.5	3,319	3.39	0.04	6,356	9.70	0.07	3,731	2.65	0.04	5,940	9.71	0.07
2nd	*Harmless*	5,308	5.42	0.06	756	1.15	0.01	6,703	4.77	0.08	1,372	2.24	0.02
	0 < v_n ≤ 90 m/s	2,391	2.44	0.03	5,897	9.00	0.07	3,350	2.38	0.04	6,497	10.63	0.08
	v_n > 90 m/s	180	0.18	0.00	545	0.83	0.01	669	0.48	0.01	656	1.07	0.01
	SP ≥ 0.5	1,866	1.91	0.02	4,193	6.40	0.05	2,130	1.51	0.03	3,632	5.94	0.04
1st	*Harmless*	2,394	2.44	0.03	308	0.47	0.00	3,133	2.23	0.04	250	0.41	0.00
	0 < v_n ≤ 90 m/s	658	0.67	0.01	1,821	2.78	0.02	1,170	0.83	0.01	1,385	2.27	0.02
	v_n > 90 m/s	21	0.02	0.00	1	0.00	0.00	148	0.11	0.00	0	0.00	0.00
	SP ≥ 0.5	530	0.54	0.01	1,734	2.65	0.02	712	0.51	0.01	1,345	2.20	0.02

SIDE	*Harmless*	29,424	30.05	0.35	3,926	5.99	0.05	45,622	32.43	0.54	4,937	8.07	0.06
	$0 < v_n \leq 90$ m/s	65,760	67.15	0.77	59,829	91.33	0.71	87,956	62.53	1.04	54,749	89.54	0.65
	$v_n > 90$ m/s	2,743	2.80	0.03	1,754	2.68	0.02	7,089	5.04	0.08	1460	2.39	0.02
	SP ≥ 0.5	62,830	64.16	0.74	53,088	81.04	0.63	75,641	53.77	0.89	47,464	77.62	0.56

Table AII.2 – Particle-blade interaction, Cases 3 and 4 (transonic rotor)

		Case 3 (d_p = 0.50 µm)						Case 4 (d_p = 1.00 µm)					
		Pressure side			Suction side			Pressure side			Suction side		
		N	n_{SIDE} [%]	n_{hit} [%]	N	n_{SIDE} [%]	n_{hit} [%]	N	n_{SIDE} [%]	n_{hit} [%]	N	n_{SIDE} [%]	n_{hit} [%]
11th	*Harmless*	17,091	7.32	0.20	423	1.15	0.00	29,258	8.00	0.35	118	0.81	0.00
	$0 < v_n \leq 90$ m/s	3,600	1.54	0.04	1,074	2.92	0.01	7,259	1.99	0.09	96	0.66	0.00
	$v_n > 90$ m/s	290	0.12	0.00	102	0.28	0.00	357	0.10	0.00	13	0.09	0.00
	SP ≥ 0.5	3,354	1.44	0.04	828	2.25	0.01	4,337	1.19	0.05	44	0.30	0.00
10th	*Harmless*	11,646	4.99	0.14	157	0.43	0.00	13,168	3.60	0.16	84	0.58	0.00
	$0 < v_n \leq 90$ m/s	21,913	9.39	0.26	3,278	8.92	0.04	33,297	9.11	0.39	78	0.54	0.00
	$v_n > 90$ m/s	83	0.04	0.00	97	0.26	0.00	146	0.04	0.00	1	0.01	0.00
	SP ≥ 0.5	18,183	7.79	0.21	3,065	8.34	0.04	22,125	6.05	0.26	64	0.44	0.00
9th	*Harmless*	1,851	0.79	0.02	50	0.14	0.00	17,070	4.67	0.20	151	1.04	0.00
	$0 < v_n \leq 90$ m/s	18,876	8.09	0.22	2,849	7.75	0.03	5,985	1.64	0.07	32	0.22	0.00
	$v_n > 90$ m/s	1,784	0.76	0.02	52	0.14	0.00	7,658	2.10	0.09	0	0.00	0.00
	SP ≥ 0.5	12,442	5.33	0.15	2,634	7.17	0.03	159	0.04	0.00	29	0.20	0.00
8th	*Harmless*	1,996	0.85	0.02	90	0.24	0.00	2,544	0.70	0.03	0	0.00	0.00
	$0 < v_n \leq 90$ m/s	24,456	10.48	0.29	4,011	10.91	0.05	35,757	9.78	0.42	207	1.42	0.00
	$v_n > 90$ m/s	3,462	1.48	0.04	11	0.03	0.00	9,268	2.54	0.11	0	0.00	0.00
	SP ≥ 0.5	13,522	5.79	0.16	3,704	10.08	0.04	18,874	5.16	0.22	126	0.87	0.00
7th	*Harmless*	3,203	1.37	0.04	63	0.17	0.00	5,041	1.38	0.06	8	0.05	0.00
	$0 < v_n \leq 90$ m/s	24,158	10.35	0.28	2,159	5.87	0.03	43,160	11.81	0.51	65	0.45	0.00
	$v_n > 90$ m/s	3,440	1.47	0.04	5	0.01	0.00	9,057	2.48	0.11	1	0.01	0.00
	SP ≥ 0.5	17,038	7.30	0.20	2,001	5.44	0.02	26,929	7.37	0.32	36	0.25	0.00
6th	*Harmless*	2,087	0.89	0.02	15	0.04	0.00	3,275	0.90	0.04	0	0.00	0.00
	$0 < v_n \leq 90$ m/s	11,885	5.09	0.14	845	2.30	0.01	18,351	5.02	0.22	1	0.01	0.00
	$v_n > 90$ m/s	3,000	1.29	0.04	1	0.00	0.00	1,207	0.33	0.01	0	0.00	0.00
	SP ≥ 0.5	8,282	3.55	0.10	810	2.20	0.01	14,195	3.88	0.17	1	0.01	0.00
5th	*Harmless*	665	0.28	0.01	21	0.06	0.00	219	0.06	0.00	0	0.00	0.00
	$0 < v_n \leq 90$ m/s	4,649	1.99	0.05	1,718	4.67	0.02	1,131	0.31	0.01	7	0.05	0.00
	$v_n > 90$ m/s	1,504	0.64	0.02	2	0.01	0.00	999	0.27	0.01	0	0.00	0.00
	SP ≥ 0.5	2,192	0.94	0.03	1,642	4.47	0.02	968	0.26	0.01	5	0.03	0.00
4th	*Harmless*	5,787	2.48	0.07	33	0.09	0.00	1,823	0.50	0.02	0	0.00	0.00
	$0 < v_n \leq 90$ m/s	15,357	6.58	0.18	1,938	5.27	0.02	17,564	4.81	0.21	222	1.52	0.00
	$v_n > 90$ m/s	553	0.24	0.01	22	0.06	0.00	723	0.20	0.01	0	0.00	0.00
	SP ≥ 0.5	11,720	5.02	0.14	1,722	4.68	0.02	3,321	0.91	0.04	22	0.15	0.00
3rd	*Harmless*	7,866	3.37	0.09	576	1.57	0.01	6,359	1.74	0.08	46	0.32	0.00
	$0 < v_n \leq 90$ m/s	8,848	3.79	0.10	2,664	7.25	0.03	24,561	6.72	0.29	1,416	9.73	0.02
	$v_n > 90$ m/s	4,149	1.78	0.05	39	0.11	0.00	3,112	0.85	0.04	0	0.00	0.00
	SP ≥ 0.5	6,281	2.69	0.07	2,510	6.83	0.03	10,785	2.95	0.13	1,326	9.11	0.02
2nd	*Harmless*	8,021	3.44	0.09	5,601	15.24	0.07	18,922	5.18	0.22	1,774	12.19	0.02
	$0 < v_n \leq 90$ m/s	7,879	3.37	0.09	5,557	15.12	0.07	13,813	3.78	0.16	2,322	15.95	0.03
	$v_n > 90$ m/s	3,524	1.51	0.04	1,409	3.83	0.02	10,017	2.74	0.12	5,217	35.84	0.06
	SP ≥ 0.5	4,166	1.78	0.05	2,133	5.80	0.03	1567	0.43	0.02	692	4.75	0.01
1ts	*Harmless*	6,765	2.90	0.08	1,339	3.64	0.02	13,741	3.76	0.16	120	0.82	0.00
	$0 < v_n \leq 90$ m/s	2,240	0.96	0.03	560	1.52	0.01	4,753	1.30	0.06	2,578	17.71	0.03
	$v_n > 90$ m/s	834	0.36	0.01	0	0.00	0.00	5,924	1.62	0.07	1	0.01	0.00
	SP ≥ 0.5	691	0.30	0.01	508	1.38	0.01	566	0.15	0.01	2,227	15.30	0.03

SIDE	*Harmless*	66,978	28.69	0.79	8,368	22.76	0.10	111,420	30.48	1.31	2,301	15.81	0.03
	$0 < v_n \leq 90$ m/s	143,861	61.62	1.70	26,653	72.50	0.31	205,631	56.26	2.43	7,024	48.25	0.08
	$v_n > 90$ m/s	22,623	9.69	0.27	1,740	4.73	0.02	48,468	13.26	0.57	5,233	35.95	0.06
	SP ≥ 0.5	97,871	41.92	1.15	21,557	58.64	0.25	103,826	28.41	1.22	4,572	31.41	0.05

Table AII.3 – Particle-blade interaction, Case 5 (transonic rotor)

		Case 5 (d_p = 1.50 µm)					
		Pressure side			Suction side		
		N	n_{SIDE} [%]	n_{hit} [%]	N	n_{SIDE} [%]	n_{hit} [%]
11th	*Harmless*	60,502	9.06	0.71	36	0.38	0.00
	$0 < v_n \leq 90$ m/s	24,549	3.68	0.29	1	0.01	0.00
	$v_n > 90$ m/s	559	0.08	0.01	0	0.00	0.00
	SP ≥ 0.5	2,682	0.40	0.03	0	0.00	0.00
10th	*Harmless*	15,056	2.25	0.18	0	0.00	0.00
	$0 < v_n \leq 90$ m/s	55,794	8.36	0.66	0	0.00	0.00
	$v_n > 90$ m/s	155	0.02	0.00	0	0.00	0.00
	SP ≥ 0.5	4,174	0.63	0.05	0	0.00	0.00
9th	*Harmless*	2,096	0.31	0.02	0	0.00	0.00
	$0 < v_n \leq 90$ m/s	36,850	5.52	0.43	0	0.00	0.00
	$v_n > 90$ m/s	8,821	1.32	0.10	0	0.00	0.00
	SP ≥ 0.5	2,712	0.41	0.03	0	0.00	0.00
8th	*Harmless*	3,778	0.57	0.04	0	0.00	0.00
	$0 < v_n \leq 90$ m/s	63,010	9.44	0.74	0	0.00	0.00
	$v_n > 90$ m/s	20,544	3.08	0.24	0	0.00	0.00
	SP ≥ 0.5	3,511	0.53	0.04	0	0.00	0.00
7th	*Harmless*	7,216	1.08	0.09	0	0.00	0.00
	$0 < v_n \leq 90$ m/s	72,497	10.86	0.85	0	0.00	0.00
	$v_n > 90$ m/s	12,271	1.84	0.14	0	0.00	0.00
	SP ≥ 0.5	6,202	0.93	0.07	0	0.00	0.00
6th	*Harmless*	6,072	0.91	0.07	0	0.00	0.00
	$0 < v_n \leq 90$ m/s	41,234	6.18	0.49	0	0.00	0.00
	$v_n > 90$ m/s	425	0.06	0.01	0	0.00	0.00
	SP ≥ 0.5	4,092	0.61	0.05	0	0.00	0.00
5th	*Harmless*	6,483	0.97	0.08	44	0.46	0.00
	$0 < v_n \leq 90$ m/s	14,626	2.19	0.17	13	0.14	0.00
	$v_n > 90$ m/s	32	0.00	0.00	0	0.00	0.00
	SP ≥ 0.5	1,800	0.27	0.02	2	0.02	0.00
4th	*Harmless*	4,891	0.73	0.06	0	0.00	0.00
	$0 < v_n \leq 90$ m/s	21,789	3.26	0.26	196	2.07	0.00
	$v_n > 90$ m/s	63	0.01	0.00	0	0.00	0.00
	SP ≥ 0.5	928	0.14	0.01	18	0.19	0.00
3rd	*Harmless*	16,827	2.52	0.20	13	0.14	0.00
	$0 < v_n \leq 90$ m/s	33,102	4.96	0.39	747	7.88	0.01
	$v_n > 90$ m/s	5,497	0.82	0.06	0	0.00	0.00
	SP ≥ 0.5	754	0.11	0.01	183	1.93	0.00
2nd	*Harmless*	50,486	7.56	0.60	1,458	15.38	0.02
	$0 < v_n \leq 90$ m/s	14,998	2.25	0.18	1,240	13.08	0.01
	$v_n > 90$ m/s	14,015	2.10	0.17	5,720	60.33	0.07
	SP ≥ 0.5	496	0.07	0.01	80	0.84	0.00
1ts	*Harmless*	31,246	4.68	0.37	0	0.00	0.00
	$0 < v_n \leq 90$ m/s	9,970	1.49	0.12	0	0.00	0.00
	$v_n > 90$ m/s	12,490	1.87	0.15	0	0.00	0.00
	SP ≥ 0.5	776	0.12	0.01	0	0.00	0.00
SIDE	*Harmless*	204,653	30.65	2.41	1,551	16.36	0.02
	$0 < v_n \leq 90$ m/s	388,419	58.17	4.58	2,197	23.17	0.03
	$v_n > 90$ m/s	74,872	11.21	0.88	5,720	60.33	0.07
	SP ≥ 0.5	28,127	4.21	0.33	283	2.98	0.00

this page was intentionally left blank

Appendix III

Particle Blade Interaction – Subsonic Rotor

Table AIII.1 – Particle-blade interaction, Cases 1 and 2 (subsonic rotor)

		Case 1 (d_p = 0.15 µm)						Case 2 (d_p = 0.25 µm)					
		Pressure side			Suction side			Pressure side			Suction side		
		N	n_{SIDE} [%]	n_{hit} [%]	N	n_{SIDE} [%]	n_{hit} [%]	N	n_{SIDE} [%]	n_{hit} [%]	N	n_{SIDE} [%]	n_{hit} [%]
11th	*Harmless*	690	1.35	0.01	1,554	4.09	0.02	733	1.31	0.01	1,407	4.10	0.02
	$0 < v_n \leq 90$ m/s	2,887	5.65	0.03	2,468	6.49	0.03	2,785	4.99	0.03	2,406	7.01	0.03
	$v_n > 90$ m/s	592	1.16	0.01	164	0.43	0.00	365	0.65	0.00	78	0.23	0.00
	SP ≥ 0.5	2,536	4.96	0.03	2,278	5.99	0.03	2,515	4.50	0.03	2,280	6.64	0.03
10th	*Harmless*	265	0.52	0.00	462	1.21	0.01	393	0.70	0.00	596	1.74	0.01
	$0 < v_n \leq 90$ m/s	1,407	2.75	0.02	3,277	8.62	0.04	1,567	2.81	0.02	2,856	8.32	0.03
	$v_n > 90$ m/s	43	0.08	0.00	72	0.19	0.00	64	0.11	0.00	2	0.01	0.00
	SP ≥ 0.5	1,346	2.64	0.02	3,120	8.20	0.04	1,513	2.71	0.02	2,830	8.24	0.03
9th	*Harmless*	581	1.14	0.01	580	1.52	0.01	903	1.62	0.01	765	2.23	0.01
	$0 < v_n \leq 90$ m/s	2,148	4.21	0.03	3,956	10.40	0.05	2,351	4.21	0.03	3,304	9.62	0.04
	$v_n > 90$ m/s	92	0.18	0.00	34	0.09	0.00	107	0.19	0.00	0	0.00	0.00
	SP ≥ 0.5	2,030	3.97	0.02	3,766	9.90	0.04	2,271	4.07	0.03	3,289	9.58	0.04
8th	*Harmless*	998	1.95	0.01	516	1.36	0.01	1,450	2.60	0.02	873	2.54	0.01
	$0 < v_n \leq 90$ m/s	3,241	6.35	0.04	3,315	8.72	0.04	3,187	5.71	0.04	2,675	7.79	0.03
	$v_n > 90$ m/s	164	0.32	0.00	1	0.00	0.00	215	0.39	0.00	0	0.00	0.00
	SP ≥ 0.5	3,109	6.09	0.04	3,236	8.51	0.04	3,113	5.57	0.04	2,663	7.75	0.03
7th	*Harmless*	1,187	2.32	0.01	383	1.01	0.00	1,538	2.75	0.02	655	1.91	0.01
	$0 < v_n \leq 90$ m/s	3,707	7.26	0.04	2,667	7.01	0.03	3,637	6.51	0.04	2,172	6.32	0.03
	$v_n > 90$ m/s	188	0.37	0.00	1	0.00	0.00	206	0.37	0.00	0	0.00	0.00
	SP ≥ 0.5	3,580	7.01	0.04	2,604	6.85	0.03	3,530	6.32	0.04	2,157	6.28	0.03
6th	*Harmless*	1,352	2.65	0.02	440	1.16	0.01	1,860	3.33	0.02	676	1.97	0.01
	$0 < v_n \leq 90$ m/s	3,851	7.54	0.04	2,443	6.42	0.03	3,888	6.96	0.05	1,790	5.21	0.02
	$v_n > 90$ m/s	123	0.24	0.00	8	0.02	0.00	117	0.21	0.00	1	0.00	0.00
	SP ≥ 0.5	3,713	7.27	0.04	2,393	6.29	0.03	3,710	6.64	0.04	1,757	5.12	0.02
5th	*Harmless*	1,443	2.83	0.02	205	0.54	0.00	1,937	3.47	0.02	222	0.65	0.00
	$0 < v_n \leq 90$ m/s	3,974	7.78	0.05	1,906	5.01	0.02	3,947	7.07	0.05	1,515	4.41	0.02
	$v_n > 90$ m/s	95	0.19	0.00	6	0.02	0.00	76	0.14	0.00	4	0.01	0.00
	SP ≥ 0.5	3,744	7.33	0.04	1,850	4.86	0.02	3,648	6.53	0.04	1,474	4.29	0.02
4th	*Harmless*	1,771	3.47	0.02	140	0.37	0.00	2,327	4.17	0.03	129	0.38	0.00
	$0 < v_n \leq 90$ m/s	3,973	7.78	0.05	1,778	4.67	0.02	4,057	7.26	0.05	1,356	3.95	0.02
	$v_n > 90$ m/s	64	0.13	0.00	7	0.02	0.00	52	0.09	0.00	5	0.01	0.00
	SP ≥ 0.5	3,701	7.25	0.04	1,725	4.54	0.02	3,692	6.61	0.04	1,290	3.76	0.02
3rd	*Harmless*	2,027	3.97	0.02	235	0.62	0.00	2,923	5.23	0.03	157	0.46	0.00
	$0 < v_n \leq 90$ m/s	3,441	6.74	0.04	2,485	6.53	0.03	3,175	5.69	0.04	2,008	5.85	0.02
	$v_n > 90$ m/s	47	0.09	0.00	2	0.01	0.00	23	0.04	0.00	0	0.00	0.00
	SP ≥ 0.5	3,054	5.98	0.04	2,424	6.37	0.03	2,863	5.13	0.03	1,964	5.72	0.02
2nd	*Harmless*	2,511	4.92	0.03	284	0.75	0.00	3,293	5.90	0.04	256	0.75	0.00
	$0 < v_n \leq 90$ m/s	2,754	5.39	0.03	3,464	9.11	0.04	2,718	4.87	0.03	3,172	9.24	0.04
	$v_n > 90$ m/s	26	0.05	0.00	1	0.00	0.00	12	0.02	0.00	0	0.00	0.00
	SP ≥ 0.5	2,313	4.53	0.03	3,429	9.01	0.04	2,358	4.22	0.03	3,165	9.22	0.04
1ts	*Harmless*	3,518	6.89	0.04	1,097	2.88	0.01	3,978	7.12	0.05	1,607	4.68	0.02
	$0 < v_n \leq 90$ m/s	1,911	3.74	0.02	3,771	9.91	0.04	1,952	3.50	0.02	3,657	10.65	0.04
	$v_n > 90$ m/s	8	0.02	0.00	315	0.83	0.00	8	0.01	0.00	0	0.00	0.00
	SP ≥ 0.5	1,658	3.25	0.02	3,659	9.62	0.04	1,699	3.04	0.02	3,655	10.64	0.04

SIDE	*Harmless*	16,343	32.00	0.19	5,896	15.50	0.07	21,335	38.20	0.25	7,343	21.38	0.09
	$0 < v_n \leq 90$ m/s	33,294	65.18	0.39	31,530	82.89	0.37	33,264	59.57	0.39	26,911	78.36	0.31
	$v_n > 90$ m/s	1,442	2.82	0.02	611	1.61	0.01	1,245	2.23	0.01	90	0.26	0.00
	SP ≥ 0.5	30,784	60.27	0.36	30,484	80.14	0.36	30,912	55.35	0.36	26,524	77.23	0.31

Table AIII.2 – Particle-blade interaction, Cases 3 and 4 (subsonic rotor)

		Case 3 (d_p = 0.50 µm)						Case 4 (d_p = 1.00 µm)					
		Pressure side			Suction side			Pressure side			Suction side		
		N	n_{SIDE} [%]	n_{hit} [%]	N	n_{SIDE} [%]	n_{hit} [%]	N	n_{SIDE} [%]	n_{hit} [%]	N	n_{SIDE} [%]	n_{hit} [%]
11th	*Harmless*	683	0.86	0.01	191	0.67	0.00	392	0.36	0.00	13	0.05	0.00
	$0 < v_n \leq 90$ m/s	3,350	4.23	0.04	1,345	4.70	0.02	4,426	4.04	0.05	19	0.07	0.00
	$v_n > 90$ m/s	118	0.15	0.00	630	2.20	0.01	113	0.10	0.00	4,391	16.47	0.05
	SP ≥ 0.5	3,143	3.97	0.04	309	1.08	0.00	2,286	2.08	0.03	11	0.04	0.00
10th	*Harmless*	136	0.17	0.00	40	0.14	0.00	64	0.06	0.00	0	0.00	0.00
	$0 < v_n \leq 90$ m/s	2,788	3.52	0.03	2,640	9.22	0.03	3,260	2.97	0.04	282	1.06	0.00
	$v_n > 90$ m/s	22	0.03	0.00	45	0.16	0.00	3	0.00	0.00	5,992	22.47	0.07
	SP ≥ 0.5	2,615	3.30	0.03	1,336	4.67	0.02	1,009	0.92	0.01	5	0.02	0.00
9th	*Harmless*	313	0.39	0.00	61	0.21	0.00	25	0.02	0.00	0	0.00	0.00
	$0 < v_n \leq 90$ m/s	5,270	6.65	0.06	3,772	13.18	0.04	12,161	11.09	0.14	3,898	14.62	0.05
	$v_n > 90$ m/s	26	0.03	0.00	0	0.00	0.00	4	0.00	0.00	0	0.00	0.00
	SP ≥ 0.5	4,927	6.22	0.06	3,437	12.01	0.04	603	0.55	0.01	334	1.25	0.00
8th	*Harmless*	937	1.18	0.01	703	2.46	0.01	42	0.04	0.00	2	0.01	0.00
	$0 < v_n \leq 90$ m/s	5,959	7.52	0.07	3,339	11.66	0.04	14,197	12.95	0.17	2,451	9.19	0.03
	$v_n > 90$ m/s	69	0.09	0.00	0	0.00	0.00	1	0.00	0.00	14	0.05	0.00
	SP ≥ 0.5	5,858	7.39	0.07	3,298	11.52	0.04	581	0.53	0.01	86	0.32	0.00
7th	*Harmless*	1,219	1.54	0.01	1,578	5.51	0.02	168	0.15	0.00	15	0.06	0.00
	$0 < v_n \leq 90$ m/s	5,953	7.51	0.07	1,371	4.79	0.02	12,280	11.20	0.15	579	2.17	0.01
	$v_n > 90$ m/s	67	0.08	0.00	0	0.00	0.00	12	0.01	0.00	0	0.00	0.00
	SP ≥ 0.5	5,856	7.39	0.07	1,370	4.79	0.02	1,607	1.47	0.02	114	0.43	0.00
6th	*Harmless*	1,596	2.01	0.02	2,158	7.54	0.03	835	0.76	0.01	140	0.53	0.00
	$0 < v_n \leq 90$ m/s	6,579	8.30	0.08	336	1.17	0.00	7,520	6.86	0.09	168	0.63	0.00
	$v_n > 90$ m/s	38	0.05	0.00	0	0.00	0.00	20	0.02	0.00	0	0.00	0.00
	SP ≥ 0.5	6,463	8.15	0.08	334	1.17	0.00	4,286	3.91	0.05	136	0.51	0.00
5th	*Harmless*	1,967	2.48	0.02	867	3.03	0.01	504	0.46	0.01	345	1.29	0.00
	$0 < v_n \leq 90$ m/s	6,781	8.55	0.08	53	0.19	0.00	5,739	5.23	0.07	315	1.18	0.00
	$v_n > 90$ m/s	23	0.03	0.00	0	0.00	0.00	14	0.01	0.00	0	0.00	0.00
	SP ≥ 0.5	6,224	7.85	0.07	43	0.15	0.00	3,804	3.47	0.05	315	1.18	0.00
4th	*Harmless*	2,346	2.96	0.03	327	1.14	0.00	525	0.48	0.01	175	0.66	0.00
	$0 < v_n \leq 90$ m/s	6,492	8.19	0.08	49	0.17	0.00	7,135	6.51	0.08	139	0.52	0.00
	$v_n > 90$ m/s	58	0.07	0.00	0	0.00	0.00	326	0.30	0.00	0	0.00	0.00
	SP ≥ 0.5	5,771	7.28	0.07	45	0.16	0.00	3,062	2.79	0.04	139	0.52	0.00
3rd	*Harmless*	5,670	7.15	0.07	490	1.71	0.01	6,541	5.97	0.08	498	1.87	0.01
	$0 < v_n \leq 90$ m/s	3,666	4.62	0.04	461	1.61	0.01	5,382	4.91	0.06	552	2.07	0.01
	$v_n > 90$ m/s	4	0.01	0.00	0	0.00	0.00	2	0.00	0.00	0	0.00	0.00
	SP ≥ 0.5	3,493	4.41	0.04	458	1.60	0.01	2,173	1.98	0.03	543	2.04	0.01
2nd	*Harmless*	6,539	8.25	0.08	626	2.19	0.01	11,566	10.55	0.14	482	1.81	0.01
	$0 < v_n \leq 90$ m/s	2,507	3.16	0.03	1,914	6.69	0.02	2,977	2.71	0.04	1,153	4.32	0.01
	$v_n > 90$ m/s	0	0.00	0.00	0	0.00	0.00	0	0.00	0.00	0	0.00	0.00
	SP ≥ 0.5	2,357	2.97	0.03	1,914	6.69	0.02	2,459	2.24	0.03	1,003	3.76	0.01
1ts	*Harmless*	6,207	7.83	0.07	2,635	9.20	0.03	10,857	9.90	0.13	1,743	6.54	0.02
	$0 < v_n \leq 90$ m/s	1,837	2.32	0.02	2,997	10.47	0.03	2,562	2.34	0.03	3,296	12.36	0.04
	$v_n > 90$ m/s	46	0.06	0.00	0	0.00	0.00	0	0.00	0.00	0	0.00	0.00
	SP ≥ 0.5	1,727	2.18	0.02	2,991	10.45	0.03	1,379	1.26	0.02	2,714	10.18	0.03

SIDE	*Harmless*	27,613	34.84	0.32	9,676	33.80	0.11	31,519	28.74	0.37	3,413	12.80	0.04
	$0 < v_n \leq 90$ m/s	51,182	64.57	0.60	18,277	63.84	0.21	77,639	70.80	0.92	12,852	48.20	0.15
	$v_n > 90$ m/s	471	0.59	0.01	675	2.36	0.01	495	0.45	0.01	10,397	39.00	0.12
	SP ≥ 0.5	48,434	61.10	0.57	15,535	54.27	0.18	23,249	21.20	0.28	5,400	20.25	0.06

Table AIII.3 – Particle-blade interaction, Case 5 (subsonic rotor)

		Case 5 (d_p = 1.50 µm)					
		Pressure side			Suction side		
		N	n_{SIDE} [%]	n_{hit} [%]	N	n_{SIDE} [%]	n_{hit} [%]
11th	*Harmless*	192	0.11	0.00	81	0.11	0.00
	$0 < v_n \leq 90$ m/s	11,825	6.63	0.14	2,072	2.76	0.02
	$v_n > 90$ m/s	1,295	0.73	0.02	8,382	11.15	0.10
	SP ≥ 0.5	3,907	2.19	0.05	1,094	1.46	0.01
10th	*Harmless*	129	0.07	0.00	0	0.00	0.00
	$0 < v_n \leq 90$ m/s	7,178	4.03	0.08	1,746	2.32	0.02
	$v_n > 90$ m/s	476	0.27	0.01	11,517	15.32	0.13
	SP ≥ 0.5	4,056	2.28	0.05	667	0.89	0.01
9th	*Harmless*	54	0.03	0.00	0	0.00	0.00
	$0 < v_n \leq 90$ m/s	9,790	5.49	0.11	1,718	2.28	0.02
	$v_n > 90$ m/s	1,073	0.60	0.01	9,224	12.27	0.11
	SP ≥ 0.5	2,909	1.63	0.03	415	0.55	0.00
8th	*Harmless*	30	0.02	0.00	0	0.00	0.00
	$0 < v_n \leq 90$ m/s	12,000	6.73	0.14	3,079	4.10	0.04
	$v_n > 90$ m/s	173	0.10	0.00	3,690	4.91	0.04
	SP ≥ 0.5	1,190	0.67	0.01	142	0.19	0.00
7th	*Harmless*	25	0.01	0.00	0	0.00	0.00
	$0 < v_n \leq 90$ m/s	14,080	7.90	0.16	3,185	4.24	0.04
	$v_n > 90$ m/s	3	0.00	0.00	124	0.16	0.00
	SP ≥ 0.5	715	0.40	0.01	240	0.32	0.00
6th	*Harmless*	18	0.01	0.00	1	0.00	0.00
	$0 < v_n \leq 90$ m/s	17,868	10.02	0.21	2,631	3.50	0.03
	$v_n > 90$ m/s	1	0.00	0.00	0	0.00	0.00
	SP ≥ 0.5	846	0.47	0.01	662	0.88	0.01
5th	*Harmless*	25	0.01	0.00	20	0.03	0.00
	$0 < v_n \leq 90$ m/s	16,854	9.46	0.20	3,380	4.50	0.04
	$v_n > 90$ m/s	2	0.00	0.00	0	0.00	0.00
	SP ≥ 0.5	2,572	1.44	0.03	2,379	3.16	0.03
4th	*Harmless*	373	0.21	0.00	13	0.02	0.00
	$0 < v_n \leq 90$ m/s	15,624	8.77	0.18	7,669	10.20	0.09
	$v_n > 90$ m/s	2,212	1.24	0.03	0	0.00	0.00
	SP ≥ 0.5	5,172	2.90	0.06	7,400	9.84	0.09
3rd	*Harmless*	9,156	5.14	0.11	8	0.01	0.00
	$0 < v_n \leq 90$ m/s	9,388	5.27	0.11	4,906	6.53	0.06
	$v_n > 90$ m/s	1,685	0.95	0.02	0	0.00	0.00
	SP ≥ 0.5	4,728	2.65	0.06	4,144	5.51	0.05
2nd	*Harmless*	16,712	9.38	0.20	13	0.02	0.00
	$0 < v_n \leq 90$ m/s	6,495	3.64	0.08	3,574	4.75	0.04
	$v_n > 90$ m/s	1	0.00	0.00	0	0.00	0.00
	SP ≥ 0.5	5,222	2.93	0.06	98	0.13	0.00
1ts	*Harmless*	17,198	9.65	0.20	380	0.51	0.00
	$0 < v_n \leq 90$ m/s	6,319	3.54	0.07	7,774	10.34	0.09
	$v_n > 90$ m/s	0	0.00	0.00	0	0.00	0.00
	SP ≥ 0.5	3,658	2.05	0.04	3,721	4.95	0.04
SIDE	*Harmless*	43,912	24.63	0.51	516	0.69	0.01
	$0 < v_n \leq 90$ m/s	127,421	71.48	1.49	41,734	55.51	0.49
	$v_n > 90$ m/s	6,921	3.88	0.08	32,937	43.81	0.38
	SP ≥ 0.5	34,975	19.62	0.41	20,962	27.88	0.24

this page was intentionally left blank

Appendix IV

Dangerous Index Values: Transonic Rotor

The Tables AIV.1 – AIV.10 summarize the DI related to the particles that stick to each cell of the mesh reported in Chapter 6. The blade span is divided into eleven strips, while the blade chord is divided into twelve slice. In each table, the strip number (rows) and the chord percentage (column) are reported.

Table AIV.1 – DI for SS, Case 1, values refer to per mil unit (transonic rotor)

	Suction side, DI [‰]											
11	0.000	0.004	0.007	0.010	0.003	0.013	0.011	0.024	0.024	0.031	0.040	0.014
10	0.033	0.074	0.068	0.049	0.004	0.014	0.024	0.053	0.062	0.077	0.090	0.025
9	0.029	0.058	0.058	0.033	0.018	0.004	0.013	0.032	0.044	0.055	0.062	0.023
8	0.026	0.070	0.065	0.052	0.028	0.004	0.015	0.039	0.052	0.070	0.075	0.024
7	0.023	0.049	0.026	0.046	0.023	0.010	0.007	0.026	0.039	0.049	0.063	0.018
6	0.027	0.042	0.032	0.025	0.015	0.005	0.005	0.015	0.022	0.030	0.047	0.016
5	0.031	0.063	0.053	0.047	0.031	0.008	0.008	0.009	0.019	0.029	0.041	0.017
4	0.034	0.067	0.064	0.062	0.039	0.013	0.015	0.014	0.022	0.035	0.041	0.013
3	0.031	0.055	0.057	0.044	0.023	0.007	0.016	0.030	0.037	0.059	0.102	0.036
2	0.011	0.040	0.025	0.020	0.012	0.005	0.012	0.032	0.027	0.047	0.080	0.032
1	0.000	0.000	0.000	0.000	0.000	0.000	0.000	0.007	0.012	0.002	0.054	0.033
Slice	**TE**	**95**	**85**	**75**	**65**	**55**	**50**	**45**	**35**	**25**	**15**	**5**

Strip ↑

Table AIV.2 – DI for PS, Case 1, values refer to per mil unit (transonic rotor)

	Pressure side, DI [‰]											
11	0.042	0.066	0.024	0.027	0.046	0.002	0.001	0.036	0.022	0.018	0.019	0.002
10	0.104	0.147	0.107	0.081	0.051	0.000	0.005	0.061	0.060	0.073	0.082	0.027
9	0.129	0.074	0.076	0.059	0.033	0.000	0.008	0.054	0.055	0.053	0.047	0.018
8	0.247	0.072	0.067	0.055	0.030	0.000	0.004	0.051	0.051	0.052	0.051	0.017
7	0.170	0.083	0.082	0.068	0.031	0.000	0.005	0.065	0.062	0.058	0.052	0.019
6	0.110	0.088	0.065	0.054	0.020	0.000	0.005	0.056	0.054	0.051	0.050	0.020
5	0.062	0.054	0.045	0.036	0.004	0.000	0.001	0.024	0.033	0.027	0.027	0.011
4	0.106	0.097	0.078	0.043	0.002	0.000	0.001	0.024	0.049	0.042	0.040	0.011
3	0.042	0.053	0.028	0.004	0.000	0.000	0.000	0.008	0.041	0.036	0.035	0.013
2	0.076	0.020	0.000	0.000	0.000	0.000	0.000	0.000	0.005	0.017	0.026	0.007
1	0.036	0.008	0.000	0.000	0.000	0.000	0.000	0.000	0.000	0.000	0.000	0.000
Slice	**5**	**15**	**25**	**35**	**45**	**50**	**55**	**65**	**75**	**85**	**95**	**TE**

Strip ↑

Table AIV.3 – DI for SS, Case 2, values refer to per mil unit (transonic rotor)

	Suction side, DI [‰]											
11	0.000	0.004	0.010	0.012	0.005	0.015	0.017	0.029	0.027	0.029	0.017	0.002
10	0.033	0.085	0.078	0.063	0.005	0.016	0.025	0.055	0.053	0.046	0.023	0.000
9	0.030	0.073	0.055	0.037	0.023	0.005	0.015	0.036	0.045	0.039	0.023	0.001
8	0.030	0.083	0.079	0.060	0.032	0.006	0.017	0.051	0.051	0.063	0.037	0.003
7	0.021	0.058	0.060	0.051	0.029	0.012	0.007	0.026	0.040	0.042	0.032	0.002
6	0.029	0.044	0.032	0.027	0.017	0.005	0.005	0.014	0.024	0.025	0.021	0.002
5	0.037	0.074	0.060	0.050	0.041	0.011	0.008	0.010	0.021	0.029	0.027	0.003
4	0.035	0.068	0.070	0.069	0.044	0.016	0.002	0.018	0.031	0.038	0.033	0.004
3	0.038	0.074	0.062	0.049	0.024	0.007	0.022	0.035	0.044	0.064	0.072	0.013
2	0.020	0.056	0.035	0.024	0.020	0.008	0.020	0.043	0.031	0.048	0.055	0.005
1	0.000	0.000	0.000	0.000	0.000	0.000	0.000	0.000	0.014	0.026	0.044	0.008
Slice	**TE**	**95**	**85**	**75**	**65**	**55**	**50**	**45**	**35**	**25**	**15**	**5**

Strip ↑

Table AIV.4 – DI for PS, Case 2, values refer to per mil unit (transonic rotor)

	Pressure side, DI [‰]											
11	0.122	0.037	0.016	0.020	0.048	0.001	0.000	0.026	0.013	0.026	0.029	0.002
10	0.287	0.127	0.123	0.095	0.064	0.000	0.003	0.075	0.070	0.082	0.100	0.033
9	0.218	0.077	0.092	0.067	0.039	0.000	0.005	0.069	0.065	0.066	0.065	0.020
8	0.403	0.080	0.091	0.072	0.038	0.000	0.003	0.070	0.065	0.067	0.064	0.016
7	0.337	0.084	0.108	0.091	0.033	0.000	0.003	0.086	0.081	0.071	0.068	0.023
6	0.217	0.073	0.077	0.069	0.015	0.000	0.003	0.063	0.058	0.063	0.061	0.018
5	0.109	0.040	0.041	0.031	0.002	0.000	0.000	0.021	0.032	0.029	0.027	0.012
4	0.191	0.100	0.099	0.032	0.000	0.000	0.000	0.022	0.059	0.049	0.044	0.015
3	0.073	0.056	0.025	0.002	0.000	0.000	0.000	0.007	0.046	0.046	0.040	0.015
2	0.128	0.009	0.000	0.000	0.000	0.000	0.000	0.000	0.007	0.024	0.031	0.009
1	0.069	0.001	0.000	0.000	0.000	0.000	0.000	0.000	0.000	0.000	0.000	0.000
Slice	**5**	**15**	**25**	**35**	**45**	**50**	**55**	**65**	**75**	**85**	**95**	**TE**

Strip ↑

Table AIV.5 – DI for SS, Case 3, values refer to per mil unit (transonic rotor)

	Suction side, DI [‰]											
11	0.000	0.003	0.006	0.005	0.003	0.009	0.009	0.016	0.013	0.008	0.001	0.000
10	0.019	0.050	0.050	0.036	0.002	0.009	0.015	0.030	0.023	0.012	0.002	0.000
9	0.022	0.046	0.038	0.024	0.013	0.003	0.008	0.022	0.022	0.016	0.003	0.000
8	0.021	0.056	0.056	0.041	0.022	0.002	0.009	0.030	0.032	0.027	0.008	0.000
7	0.008	0.027	0.029	0.025	0.014	0.005	0.003	0.015	0.019	0.014	0.003	0.000
6	0.013	0.019	0.009	0.007	0.003	0.002	0.001	0.004	0.004	0.004	0.001	0.000
5	0.014	0.031	0.025	0.019	0.014	0.003	0.003	0.004	0.007	0.008	0.004	0.000
4	0.023	0.028	0.025	0.027	0.012	0.004	0.004	0.003	0.006	0.007	0.004	0.000
3	0.048	0.078	0.039	0.012	0.003	0.001	0.003	0.004	0.005	0.006	0.003	0.000
2	0.035	0.076	0.042	0.021	0.019	0.008	0.023	0.019	0.003	0.003	0.002	0.008
1	0.000	0.000	0.000	0.000	0.000	0.000	0.000	0.019	0.007	0.005	0.004	0.006
Slice	**TE**	**95**	**85**	**75**	**65**	**55**	**50**	**45**	**35**	**25**	**15**	**5**

Strip ↑

Table AIV.6 – DI for PS, Case 3, values refer to per mil unit (transonic rotor)

	Pressure side, DI [‰]											
11	0.073	0.037	0.009	0.007	0.046	0.000	0.000	0.018	0.008	0.029	0.051	0.004
10	0.706	0.190	0.116	0.096	0.050	0.000	0.001	0.059	0.067	0.101	0.156	0.050
9	0.494	0.101	0.099	0.073	0.031	0.000	0.002	0.073	0.082	0.088	0.092	0.024
8	0.559	0.149	0.130	0.093	0.035	0.000	0.000	0.090	0.086	0.091	0.100	0.025
7	0.491	0.156	0.147	0.126	0.033	0.000	0.001	0.143	0.145	0.130	0.131	0.038
6	0.187	0.080	0.069	0.063	0.006	0.000	0.001	0.070	0.080	0.083	0.090	0.030
5	0.121	0.010	0.013	0.008	0.000	0.000	0.000	0.009	0.023	0.021	0.025	0.011
4	0.662	0.065	0.079	0.008	0.000	0.000	0.000	0.018	0.073	0.060	0.061	0.017
3	0.282	0.033	0.012	0.000	0.000	0.000	0.000	0.011	0.072	0.064	0.068	0.023
2	0.313	0.000	0.000	0.000	0.000	0.000	0.000	0.000	0.016	0.040	0.059	0.011
1	0.096	0.000	0.000	0.000	0.000	0.000	0.000	0.000	0.000	0.000	0.000	0.000
Slice	**5**	**15**	**25**	**35**	**45**	**50**	**55**	**65**	**75**	**85**	**95**	**TE**

Strip ↑

Table AIV.7 – DI for SS, Case 4, values refer to per mil unit (transonic rotor)

	Suction side, DI [‰]											
11	0.000	0.000	0.001	0.000	0.000	0.001	0.001	0.001	0.001	0.000	0.000	0.000
10	0.000	0.002	0.001	0.001	0.000	0.000	0.000	0.000	0.000	0.000	0.000	0.000
9	0.002	0.003	0.002	0.001	0.000	0.000	0.000	0.001	0.000	0.000	0.000	0.000
8	0.001	0.003	0.003	0.002	0.001	0.000	0.000	0.001	0.001	0.000	0.000	0.000
7	0.000	0.001	0.001	0.001	0.001	0.000	0.001	0.000	0.000	0.000	0.000	0.000
6	0.000	0.000	0.000	0.000	0.000	0.000	0.000	0.000	0.000	0.000	0.000	0.000
5	0.000	0.000	0.000	0.000	0.000	0.000	0.000	0.000	0.000	0.000	0.000	0.000
4	0.011	0.003	0.000	0.000	0.000	0.000	0.000	0.000	0.000	0.000	0.000	0.000
3	0.028	0.048	0.019	0.001	0.000	0.000	0.000	0.000	0.000	0.000	0.000	0.000
2	0.017	0.034	0.015	0.002	0.001	0.005	0.007	0.004	0.000	0.000	0.000	0.000
1	0.000	0.000	0.000	0.000	0.000	0.000	0.000	0.007	0.000	0.000	0.000	0.151
Slice	**TE**	**95**	**85**	**75**	**65**	**55**	**50**	**45**	**35**	**25**	**15**	**5**

Strip ↑

Table AIV.8 – DI for PS, Case 4, values refer to per mil unit (transonic rotor)

	Pressure side, DI [‰]											
11	0.097	0.062	0.001	0.007	0.102	0.001	0.000	0.036	0.006	0.044	0.086	0.005
10	0.855	0.525	0.122	0.052	0.031	0.000	0.000	0.019	0.037	0.088	0.191	0.061
9	0.471	0.319	0.113	0.066	0.019	0.000	0.001	0.059	0.077	0.083	0.096	0.033
8	0.478	0.464	0.148	0.103	0.029	0.000	0.000	0.091	0.108	0.097	0.123	0.037
7	0.518	0.576	0.199	0.167	0.021	0.000	0.000	0.163	0.189	0.172	0.197	0.062
6	0.124	0.196	0.084	0.068	0.001	0.000	0.000	0.097	0.129	0.151	0.162	0.067
5	0.001	0.000	0.000	0.000	0.000	0.000	0.000	0.003	0.012	0.015	0.024	0.010
4	0.566	0.039	0.042	0.001	0.000	0.000	0.000	0.003	0.019	0.016	0.022	0.010
3	0.828	0.030	0.004	0.000	0.000	0.000	0.000	0.005	0.083	0.117	0.033	0.196
2	0.262	0.000	0.000	0.000	0.000	0.000	0.000	0.001	0.036	0.082	0.115	0.020
1	0.178	0.000	0.000	0.000	0.000	0.000	0.000	0.000	0.000	0.000	0.000	0.000
Slice	**5**	**15**	**25**	**35**	**45**	**50**	**55**	**65**	**75**	**85**	**95**	**TE**

Strip ↑

Table AIV.9 – DI for SS, Case 5, values refer to per mil unit (transonic rotor)

	Suction side, DI [‰]											
11	0.000	0.000	0.000	0.000	0.000	0.000	0.000	0.000	0.000	0.000	0.000	0.000
10	0.000	0.000	0.000	0.000	0.000	0.000	0.000	0.000	0.000	0.000	0.000	0.000
9	0.000	0.000	0.000	0.000	0.000	0.000	0.000	0.000	0.000	0.000	0.000	0.000
8	0.000	0.000	0.000	0.000	0.000	0.000	0.000	0.000	0.000	0.000	0.000	0.000
7	0.000	0.000	0.000	0.000	0.000	0.000	0.000	0.000	0.000	0.000	0.000	0.000
6	0.000	0.000	0.000	0.000	0.000	0.000	0.000	0.000	0.000	0.000	0.000	0.000
5	0.001	0.000	0.000	0.000	0.000	0.000	0.000	0.000	0.000	0.000	0.000	0.000
4	0.010	0.003	0.000	0.000	0.000	0.000	0.000	0.000	0.000	0.000	0.000	0.000
3	0.018	0.029	0.005	0.000	0.000	0.000	0.000	0.000	0.000	0.000	0.000	0.000
2	0.007	0.011	0.003	0.000	0.000	0.004	0.000	0.000	0.000	0.000	0.000	0.036
1	0.000	0.000	0.000	0.000	0.000	0.000	0.000	0.000	0.000	0.000	0.000	0.000
Slice	**TE**	**95**	**85**	**75**	**65**	**55**	**50**	**45**	**35**	**25**	**15**	**5**

Strip ↑

Table AIV.10 – DI for PS, Case 5, values refer to per mil unit (transonic rotor)

	Pressure side, DI [‰]											
11	0.348	0.226	0.001	0.065	0.530	0.000	0.000	0.062	0.008	0.081	0.156	0.008
10	1.266	0.784	0.322	0.087	0.031	0.000	0.000	0.012	0.051	0.164	0.395	0.129
9	0.499	0.614	0.250	0.118	0.022	0.000	0.000	0.061	0.112	0.124	0.151	0.066
8	0.551	1.333	0.377	0.196	0.038	0.000	0.000	0.146	0.200	0.182	0.218	0.078
7	0.595	1.376	0.525	0.324	0.027	0.000	0.000	0.215	0.301	0.285	0.334	0.132
6	0.135	0.840	0.336	0.128	0.000	0.000	0.000	0.165	0.249	0.297	0.327	0.144
5	0.000	0.031	0.080	0.052	0.000	0.000	0.000	0.093	0.215	0.202	0.213	0.088
4	0.336	0.002	0.002	0.000	0.000	0.000	0.000	0.023	0.232	0.238	0.279	0.086
3	0.360	0.002	0.001	0.000	0.000	0.000	0.000	0.034	0.300	0.361	0.435	0.145
2	0.126	0.014	0.000	0.000	0.000	0.000	0.000	0.001	0.063	0.154	0.224	0.052
1	0.483	0.025	0.000	0.000	0.000	0.000	0.000	0.000	0.000	0.000	0.000	0.000
Slice	**5**	**15**	**25**	**35**	**45**	**50**	**55**	**65**	**75**	**85**	**95**	**TE**

Strip ↑

this page was intentionally left blank

Appendix V

Dangerous Index Values: Subsonic Rotor

The Tables AV.1 – AV.10 summarize the DI related to the particles that stick to each cell of the mesh reported in Chapter 6. The blade span is divided into eleven strips, while the blade chord is divided into twelve slice. In each table, the strip number (rows) and the chord percentage (column) are reported.

Table AV.1 – DI for SS, Case 1, values refer to per mil unit (subsonic rotor)

	Suction side, DI [‰]											
11	0.006	0.018	0.019	0.016	0.013	0.003	0.002	0.007	0.017	0.026	0.038	0.042
10	0.015	0.026	0.028	0.021	0.015	0.002	0.003	0.010	0.021	0.030	0.045	0.063
9	0.010	0.023	0.023	0.018	0.015	0.002	0.004	0.012	0.021	0.038	0.066	0.107
8	0.009	0.018	0.018	0.015	0.011	0.001	0.002	0.012	0.017	0.027	0.050	0.109
7	0.007	0.012	0.013	0.010	0.010	0.001	0.003	0.010	0.014	0.023	0.039	0.090
6	0.008	0.011	0.011	0.011	0.009	0.001	0.002	0.009	0.011	0.018	0.038	0.085
5	0.007	0.011	0.012	0.009	0.007	0.001	0.002	0.007	0.009	0.013	0.026	0.062
4	0.006	0.009	0.010	0.010	0.007	0.000	0.002	0.006	0.009	0.011	0.024	0.060
3	0.014	0.031	0.019	0.013	0.007	0.001	0.003	0.007	0.009	0.012	0.030	0.068
2	0.021	0.041	0.047	0.044	0.024	0.005	0.002	0.008	0.008	0.012	0.030	0.063
1	0.022	0.062	0.043	0.035	0.023	0.014	0.026	0.027	0.013	0.088	0.020	0.040
Slice	**TE**	**95**	**85**	**75**	**65**	**55**	**50**	**45**	**35**	**25**	**15**	**5**

Strip →

Table AV.2 – DI for PS, Case 1, values refer to per mil unit (subsonic rotor)

	Pressure side, DI [‰]											
11	0.010	0.020	0.010	0.001	0.018	0.017	0.016	0.025	0.037	0.037	0.032	0.011
10	0.012	0.014	0.006	0.000	0.002	0.004	0.007	0.014	0.017	0.020	0.018	0.008
9	0.041	0.042	0.014	0.000	0.001	0.007	0.008	0.013	0.016	0.017	0.017	0.007
8	0.048	0.074	0.028	0.001	0.002	0.011	0.014	0.027	0.024	0.022	0.018	0.009
7	0.054	0.079	0.035	0.001	0.001	0.010	0.019	0.035	0.028	0.027	0.024	0.010
6	0.055	0.084	0.042	0.002	0.000	0.005	0.015	0.033	0.030	0.029	0.029	0.010
5	0.061	0.083	0.033	0.004	0.000	0.002	0.015	0.035	0.034	0.030	0.031	0.011
4	0.056	0.086	0.023	0.006	0.000	0.001	0.011	0.040	0.038	0.036	0.030	0.010
3	0.048	0.070	0.006	0.009	0.000	0.000	0.004	0.035	0.036	0.038	0.028	0.008
2	0.034	0.034	0.000	0.010	0.000	0.000	0.000	0.029	0.035	0.035	0.031	0.010
1	0.026	0.019	0.000	0.011	0.000	0.000	0.000	0.004	0.019	0.026	0.034	0.012
Slice	**5**	**15**	**25**	**35**	**45**	**50**	**55**	**65**	**75**	**85**	**95**	**TE**

Strip →

Table AV.3 – DI for SS, Case 2, values refer to per mil unit (subsonic rotor)

		Suction side, DI [‰]											
	11	0.007	0.021	0.021	0.014	0.012	0.002	0.001	0.005	0.015	0.028	0.035	0.044
	10	0.012	0.028	0.023	0.019	0.012	0.002	0.002	0.006	0.020	0.034	0.045	0.048
	9	0.013	0.022	0.023	0.024	0.016	0.002	0.002	0.010	0.023	0.037	0.059	0.064
	8	0.009	0.014	0.018	0.017	0.014	0.002	0.003	0.012	0.018	0.030	0.046	0.056
	7	0.005	0.013	0.013	0.015	0.010	0.000	0.002	0.011	0.017	0.026	0.037	0.041
	6	0.005	0.011	0.011	0.012	0.010	0.001	0.002	0.009	0.014	0.020	0.031	0.032
	5	0.005	0.011	0.009	0.010	0.009	0.001	0.002	0.008	0.011	0.015	0.028	0.023
	4	0.005	0.011	0.010	0.010	0.007	0.001	0.002	0.008	0.010	0.014	0.020	0.020
	3	0.014	0.028	0.021	0.011	0.010	0.003	0.001	0.009	0.010	0.016	0.028	0.025
Strip ↑	**2**	0.026	0.044	0.050	0.049	0.019	0.005	0.003	0.010	0.010	0.015	0.027	0.022
	1	0.020	0.072	0.050	0.025	0.006	0.008	0.030	0.035	0.013	0.018	0.029	0.021
Slice		**TE**	**95**	**85**	**75**	**65**	**55**	**50**	**45**	**35**	**25**	**15**	**5**

Table AV.4 – DI for PS, Case 2, values refer to per mil unit (subsonic rotor)

		Pressure side, DI [‰]											
	11	0.019	0.016	0.010	0.001	0.014	0.015	0.015	0.026	0.034	0.040	0.033	0.009
	10	0.027	0.010	0.006	0.000	0.002	0.005	0.007	0.017	0.014	0.020	0.020	0.009
	9	0.065	0.029	0.017	0.000	0.002	0.008	0.009	0.016	0.018	0.015	0.016	0.006
	8	0.055	0.056	0.033	0.000	0.001	0.012	0.017	0.027	0.022	0.022	0.021	0.010
	7	0.057	0.056	0.043	0.001	0.000	0.010	0.018	0.035	0.031	0.029	0.025	0.010
	6	0.047	0.071	0.047	0.003	0.000	0.006	0.017	0.038	0.032	0.031	0.031	0.012
	5	0.060	0.069	0.036	0.005	0.000	0.002	0.014	0.036	0.037	0.031	0.030	0.010
	4	0.054	0.075	0.026	0.009	0.000	0.001	0.012	0.042	0.038	0.042	0.031	0.010
	3	0.027	0.065	0.006	0.010	0.000	0.000	0.003	0.040	0.037	0.036	0.030	0.010
Strip ↑	**2**	0.020	0.035	0.000	0.012	0.000	0.000	0.000	0.032	0.039	0.038	0.031	0.011
	1	0.023	0.016	0.000	0.013	0.000	0.000	0.000	0.004	0.021	0.027	0.037	0.013
Slice		**5**	**15**	**25**	**35**	**45**	**50**	**55**	**65**	**75**	**85**	**95**	**TE**

Table AV.5 – DI for SS, Case 3, values refer to per mil unit (subsonic rotor)

	Suction side, DI [‰]											
11	0.002	0.006	0.003	0.001	0.000	0.000	0.000	0.000	0.001	0.003	0.002	0.034
10	0.003	0.006	0.004	0.001	0.001	0.000	0.000	0.000	0.001	0.001	0.001	0.135
9	0.003	0.005	0.003	0.002	0.000	0.000	0.000	0.000	0.001	0.000	0.000	0.289
8	0.001	0.003	0.001	0.001	0.000	0.000	0.000	0.000	0.000	0.000	0.000	0.285
7	0.002	0.002	0.001	0.001	0.000	0.000	0.000	0.000	0.000	0.000	0.000	0.117
6	0.001	0.002	0.001	0.001	0.000	0.000	0.000	0.000	0.000	0.000	0.000	0.025
5	0.001	0.001	0.001	0.000	0.000	0.000	0.000	0.000	0.000	0.000	0.000	0.001
4	0.001	0.001	0.001	0.000	0.000	0.000	0.000	0.000	0.000	0.000	0.000	0.000
3	0.010	0.018	0.008	0.001	0.001	0.000	0.000	0.000	0.000	0.000	0.000	0.000
2	0.022	0.048	0.049	0.038	0.008	0.000	0.000	0.000	0.000	0.000	0.000	0.000
1	0.027	0.085	0.055	0.030	0.003	0.004	0.025	0.025	0.002	0.001	0.001	0.006
Slice	**TE**	**95**	**85**	**75**	**65**	**55**	**50**	**45**	**35**	**25**	**15**	**5**

Strip ↑

Table AV.6 – DI for PS, Case 3, values refer to per mil unit (subsonic rotor)

	Pressure side, DI [‰]											
11	0.084	0.004	0.004	0.000	0.005	0.009	0.009	0.017	0.036	0.048	0.045	0.021
10	0.131	0.000	0.001	0.000	0.000	0.004	0.004	0.010	0.015	0.025	0.025	0.018
9	0.354	0.001	0.001	0.000	0.000	0.005	0.004	0.011	0.013	0.016	0.019	0.012
8	0.396	0.003	0.004	0.000	0.000	0.004	0.008	0.022	0.021	0.022	0.024	0.012
7	0.367	0.004	0.006	0.001	0.000	0.003	0.011	0.026	0.027	0.032	0.028	0.012
6	0.406	0.004	0.007	0.001	0.000	0.001	0.011	0.030	0.034	0.034	0.033	0.012
5	0.369	0.006	0.007	0.004	0.000	0.000	0.009	0.035	0.039	0.039	0.037	0.016
4	0.308	0.007	0.006	0.006	0.000	0.000	0.009	0.043	0.045	0.044	0.043	0.014
3	0.113	0.006	0.001	0.007	0.000	0.000	0.001	0.040	0.044	0.042	0.044	0.013
2	0.003	0.004	0.000	0.010	0.000	0.000	0.000	0.039	0.052	0.049	0.043	0.014
1	0.007	0.004	0.000	0.013	0.000	0.000	0.000	0.006	0.028	0.034	0.047	0.014
Slice	**5**	**15**	**25**	**35**	**45**	**50**	**55**	**65**	**75**	**85**	**95**	**TE**

Strip ↑

Table AV.7 – DI for SS, Case 4, values refer to per mil unit (subsonic rotor)

		Suction side, DI [‰]											
	11	0.000	0.000	0.000	0.000	0.000	0.000	0.000	0.000	0.000	0.000	0.000	0.001
	10	0.000	0.000	0.000	0.000	0.000	0.000	0.000	0.000	0.000	0.000	0.000	0.002
	9	0.000	0.000	0.000	0.000	0.000	0.000	0.000	0.000	0.000	0.000	0.000	0.216
	8	0.000	0.000	0.000	0.000	0.000	0.000	0.000	0.000	0.000	0.000	0.000	0.080
	7	0.000	0.000	0.000	0.000	0.000	0.000	0.000	0.000	0.000	0.000	0.000	0.029
	6	0.000	0.000	0.000	0.000	0.000	0.000	0.000	0.000	0.000	0.000	0.000	0.011
	5	0.000	0.000	0.000	0.000	0.000	0.000	0.000	0.000	0.000	0.000	0.000	0.023
	4	0.000	0.000	0.000	0.000	0.000	0.000	0.000	0.000	0.000	0.000	0.000	0.011
	3	0.002	0.004	0.002	0.000	0.000	0.000	0.000	0.000	0.000	0.000	0.000	0.033
Strip ↑	**2**	0.006	0.014	0.016	0.009	0.002	0.000	0.000	0.000	0.000	0.000	0.000	0.032
	1	0.015	0.050	0.029	0.012	0.001	0.001	0.008	0.007	0.000	0.000	0.000	0.091
Slice		**TE**	**95**	**85**	**75**	**65**	**55**	**50**	**45**	**35**	**25**	**15**	**5**

Table AV.8 – DI for PS, Case 4, values refer to per mil unit (subsonic rotor)

		Pressure side, DI [‰]											
	11	0.066	0.009	0.002	0.000	0.001	0.002	0.001	0.004	0.018	0.037	0.044	0.034
	10	0.060	0.002	0.000	0.000	0.000	0.001	0.001	0.002	0.005	0.015	0.018	0.023
	9	0.411	0.001	0.000	0.000	0.000	0.000	0.001	0.002	0.003	0.007	0.010	0.014
	8	0.645	0.002	0.000	0.000	0.000	0.000	0.001	0.001	0.003	0.005	0.008	0.008
	7	0.593	0.002	0.000	0.000	0.000	0.000	0.002	0.006	0.009	0.015	0.021	0.010
	6	0.268	0.014	0.001	0.000	0.000	0.000	0.004	0.015	0.031	0.041	0.059	0.024
	5	0.125	0.018	0.002	0.001	0.000	0.000	0.003	0.021	0.034	0.053	0.065	0.028
	4	0.192	0.005	0.000	0.001	0.000	0.000	0.002	0.015	0.024	0.045	0.053	0.024
	3	0.129	0.004	0.000	0.001	0.000	0.000	0.000	0.013	0.024	0.035	0.045	0.018
Strip ↑	**2**	0.022	0.004	0.000	0.002	0.000	0.000	0.000	0.015	0.030	0.040	0.050	0.025
	1	0.022	0.007	0.000	0.003	0.000	0.000	0.000	0.002	0.016	0.027	0.063	0.014
Slice		**5**	**15**	**25**	**35**	**45**	**50**	**55**	**65**	**75**	**85**	**95**	**TE**

Table AV.9 – DI for SS, Case 5, values refer to per mil unit (subsonic rotor)

		Suction side, DI [‰]											
	11	0.000	0.000	0.000	0.000	0.000	0.000	0.000	0.000	0.000	0.000	0.000	0.111
	10	0.000	0.000	0.000	0.000	0.000	0.000	0.000	0.000	0.000	0.000	0.000	0.093
	9	0.000	0.000	0.000	0.000	0.000	0.000	0.000	0.000	0.000	0.000	0.000	0.064
	8	0.000	0.000	0.000	0.000	0.000	0.000	0.000	0.000	0.000	0.000	0.000	0.063
	7	0.000	0.000	0.000	0.000	0.000	0.000	0.000	0.000	0.000	0.000	0.000	0.109
	6	0.000	0.000	0.000	0.000	0.000	0.000	0.000	0.000	0.000	0.000	0.000	0.144
	5	0.000	0.000	0.000	0.000	0.000	0.000	0.000	0.000	0.000	0.000	0.000	0.207
	4	0.000	0.000	0.000	0.000	0.000	0.000	0.000	0.000	0.000	0.000	0.000	0.471
	3	0.000	0.001	0.001	0.000	0.000	0.000	0.000	0.000	0.000	0.000	0.000	0.294
Strip ↑	**2**	0.002	0.004	0.005	0.004	0.000	0.000	0.000	0.000	0.000	0.000	0.000	0.203
	1	0.013	0.029	0.013	0.006	0.002	0.001	0.001	0.001	0.000	0.000	0.000	0.352
	Slice	**TE**	**95**	**85**	**75**	**65**	**55**	**50**	**45**	**35**	**25**	**15**	**5**

Table AV.10 – DI for PS, Case 5, values refer to per mil unit (subsonic rotor)

		Pressure side, DI [‰]											
	11	0.285	0.177	0.002	0.000	0.000	0.000	0.000	0.000	0.006	0.022	0.038	0.035
	10	0.145	0.154	0.001	0.000	0.000	0.001	0.000	0.001	0.005	0.017	0.023	0.034
	9	0.121	0.097	0.000	0.000	0.000	0.000	0.001	0.003	0.005	0.013	0.020	0.035
	8	0.220	0.021	0.000	0.000	0.000	0.000	0.000	0.001	0.002	0.009	0.018	0.022
	7	0.365	0.010	0.000	0.000	0.000	0.000	0.000	0.000	0.001	0.005	0.015	0.012
	6	0.603	0.006	0.000	0.000	0.000	0.000	0.000	0.001	0.002	0.007	0.020	0.014
	5	0.612	0.019	0.000	0.000	0.000	0.000	0.000	0.001	0.005	0.013	0.036	0.027
	4	0.401	0.087	0.000	0.000	0.000	0.000	0.000	0.007	0.018	0.042	0.086	0.047
	3	0.107	0.027	0.000	0.000	0.000	0.000	0.000	0.009	0.024	0.060	0.120	0.062
Strip ↑	**2**	0.040	0.009	0.000	0.000	0.000	0.000	0.000	0.009	0.033	0.082	0.144	0.075
	1	0.070	0.020	0.000	0.002	0.000	0.000	0.000	0.002	0.022	0.059	0.157	0.040
	Slice	**5**	**15**	**25**	**35**	**45**	**50**	**55**	**65**	**75**	**85**	**95**	**TE**

this page was intentionally left blank

An innovative methodology for the analysis of micro-particle deposits in transonic and subsonic blades for the assessment of compressor degradation

Alessio Suman

this page was intentionally left blank